CRYOGENIC ENERGY FOR INDIRECT FREEZE DESALINATION – NUMERICAL AND EXPERIMENTAL INVESTIGATION

By

HARITH ERANGA JAYAKODY

Thesis submitted to the University of Birmingham for the
Degree of Doctor of Philosophy

School of Engineering
Department of Mechanical Engineering
College of Engineering and Physical Sciences
The University of Birmingham
Edgbaston, Birmingham, UK
March – 2019

UNIVERSITY OF BIRMINGHAM

University of Birmingham Research Archive

e-theses repository

ABSTRACT

Due to the increasing demand for fresh water, desalination of sea water is viewed as a potential solution to overcome potable water shortages; therefore desalination technologies have been continuously developed. Renewed interest in freeze desalination has emerged due to its advantages over other desalination technologies. A major advantage of the freeze desalination technology over the evaporative methods is its lower energy consumption (latent heat of freezing is 333.5 kJ/kg and latent heat of evaporation is 2256.7 kJ/kg). Cryogenic fluids like LN_2/L_{Air} are emerging as an effective energy storage medium to maximise utilisation of intermittent renewable energy sources. The recovery of this stored cold energy has the potential to be used for freeze desalination. Computational Fluid Dynamics (CFD) is a powerful technique that allows investigating complex thermodynamic processes, including freeze desalination and evaporation of LN_2.

CFD modelling was developed to simulate the freeze desalination process in terms of the dynamics of ice layer growth and salt separation to investigate the amount of ice formed and salinity of the remaining brine at different operating conditions. The developed CFD model was validated by experiments conducted using a Peltier device and an ice maker machine showing good agreement with maximum deviation of less than 16.9%. Parametric analysis was then carried out using the validated CFD models, showing that as the freezing temperature decreased, the ice production increased due a faster rate of freezing of salt water. The initial salinity of salt water had a significant effect on the volume of ice produced and the output salinity. Therefore, different stages of freezing were needed to produce water

with a salinity level below the required 0.1% recommended by the WHO as safe to drink. Parametric analysis was carried out on the geometry of the freezing tubes in the ice maker machine, where increasing the diameter and the length of the freezing tube, increased the volume of ice produced as this increased the total freezing surface area but this also increased the heat transfer rate and power consumption. It is seen that, the 20mm diameter with a 15mm length is the best geometry to use with a low heat transfer rate producing a higher volume of ice.

Regarding the use of cryogenic fluids, the validated CFD model for freeze desalination was integrated with CFD modelling of liquid nitrogen evaporation, to investigate the feasibility of using cryogenic energy for freeze desalination. This integrated CFD model was validated using experimental heat exchanger test facility constructed, to evaporate liquid nitrogen to supply the cooling required for freezing. Tests were conducted without and with a copper mesh being inserted in the liquid nitrogen tube, where inserting the mesh improved the heat transfer rate to produce more desalinated water. The percentage of energy lost by water to form ice from liquid nitrogen increased significantly for the tests carried out with the mesh inserted as it was 70% and 63% compared to only 25% and 21% for the tests conducted without the mesh. The heat exchanger effectiveness improved considerably when the mesh was inserted as it was about 3.65 times more compared to the tests carried out without using a mesh. Parametric study on the LN_2 flow rate to observe the volume of ice obtained was also examined using CFD, where increasing the velocity of LN_2 by 6 times, increased the volume of ice obtained by 4.3times.

A number of freezing stages were required in order to reduce the ice salinity from 1.5% down to 0.1% as regarded by the WHO as safe to drink. Hence, the overall efficiency was 0.12 for the ice maker machine to reduce the ice salinity from 1.5% to less than 0.1%. In the cryogenic desalination test rig, approximately 1.35 litres of liquid nitrogen was required to reduce the ice salinity from 1.5% to less than 0.1% with an overall efficiency of 0.23. Therefore, it is seen that the cryogenic desalination test rig had a better efficiency. Furthermore, the above results illustrate the potential of using the cold energy of cryogenic fluids such as LNG and LN_2/L_{Air} for freeze desalination applications as most cold energy during LNG regasification has been unexploited today.

ACKNOWLEDGMENTS

CONTENTS

LIST OF FIGURES

xv

LIST OF TABLES

NOMENCLATURE

Symbols

A	surface area (m^2)
A_{mush}	mushy zone constant (-)
C_{min}	smaller heat capacity (J.kg/K.s)
$coeff$	Coefficient (-)
Cp_1	initial specific heat capacity (J/K)
Cp_2	final specific heat capacity (J/K)
d_b	bubble diameter (m)
$D_{i,m}$	mass diffusion coefficient for species (m^2/s)
E_{LN2}	Total energy in a known volume of liquid nitrogen (J)
E_k	total energy of phase k (J)
$\vec{F}$	body force (N)
$\vec{F}_s$	solutal buoyancy body forces (N)
$\vec{g}$	gravity (m/s^2)
h_k	sensible enthalpy for phase k [energy/mass or mol (J/kg), (J/mol)]
H	enthalpy [energy/mass (J/kg), energy/mole (J/mol)]
H_1	inlet enthalpy (J/kg)
H_2	outlet enthalpy (J/kg)
$\vec{J_i}$	diffusion flux of the species (kg/m^2-s)
k	mass transfer coefficient (-)
k_{eff}	effective conductivity (W/m-K)

K_i	partition coefficient of the solute (-)
k_k	thermal conductivity of phase k (W/m-K)
k_t	turbulent thermal conductivity (W/m-K)
l	level of fluid in inclined ruler (m)
L	latent heat (J/kg)
L_f	latent heat of fusion (J/kg)
m	mass (kg)
$\dot{m}$	mass flow rate (kg/s)
$\dot{m}_{qp}$	rate of mass transfer from phase q to phase p (kg/s)
$\dot{m}_{pq}$	rate of mass transfer from phase p to phase q (kg/s)
$\dot{m}_{lv}$	rate of mass transfer due to evaporation (kg/s)
$\dot{m}_{vl}$	rate of mass transfer due to condensation (kg/s)
m_i	slope of the liquidus surface (K)
n	number of phases (-)
N_s	number of species (-)
N	number of data points in the sample (-)
p	pressure (Pa)
Q_{brine}	energy lost by brine remaining (J)
Q_{ice}	energy loss by ice (J)
$Q_{ice-maker}$	total energy output by the ice maker (J)
Q_{water}	energy loss by water (J)
R	universal gas constant (8.31447x10^3 J/kmol-K)
S_E	other volumetric heat sources (-)

S_{α_q}	Source term (-)
S_h	influences from radiations and any other volumetric heat sources (-)
$S_{\hat{x}}$	mean deviation (-)
$t_{N-1.95\%}$	student distribution factor for a degree of freedom N-1 (-)
T	temperature (K)
T_{W1}	inlet water temperature (K)
T_{W2}	outlet water temperature (K)
T_{N1}	inlet nitrogen temperature (K)
T_{N2}	inlet nitrogen temperature (K)
U	overall heat transfer coefficient (W/m^{2}K)
U_{random}	random errors (-)
$U_{systematic}$	systematic errors (-)
$U_{overall}$	overall uncertainty (-)
$\vec{v}$	velocity (m/s)
$\vec{v}_{dr,k}$	drift velocity of phase k (m/s)
$\vec{v}_k$	velocity of phase k (m/s)
$\overrightarrow{v_m}$	mixture velocity (m/s)
$y_{l,i}$	mass fraction of the liquid phase (-)
Y_i	mass fraction of the solute (-)

Greek symbols

α	volume fraction (-)
β	liquid volume fraction (-)

β	accommodation coefficient (-)
$\beta_{s,i}$	solutal expansion coefficient (K^{-1})
ε	mall number (0.001) (-)
ε	effectiveness of the heat exchanger (-)
θ	angle of inclination (deg.)
μ	viscosity of the fluid (Pa-s)
μ_k	viscosity of phase k (Pa-s)
μ_m	mixture viscosity (Pa-s)
ρ	density of fluid (kg/m^3)
ρ_m	mixture density (kg/m^3)

Acronyms

Ads	adsorption technology
CFD	computational fluid dynamics
ED	electro-dyalysis
FD	freeze desalination
FO	forward osmosis
Frz	freezing
G.Hyd	gas hydrate
HDH	humidification - dehumidification desalination
I.Ex	ion-exchange desalination
LLE	liquid–liquid extraction
LMTD	logarithmic mean temperature difference
LNG	liquefied natural gas

MED	multiple-effect distillation
MSF	multi-stage flash
MVC	vapour compression distillation
NF	nano filtration
NTU	number of transfer units
RO	reverse osmosis
SD	solar distillation
VCD	vapour compression desalination
F.P	freezing point

Subscripts

b	bubble
Eut	eutectic
i	solute
dr	drift
k	phase k
l	liquid
liq	liquid
$liquidus$	liquid
m	mixture
$melt$	melting
N	nitrogen
p	secondary phase p
q	q^{th} phase

ref	reference
s	species
sat	saturated
sol	solid
solidus	solid
t	turbulent
v	vapour
w	water

Superscripts

*	*
T	*T*

LIST OF PUBLICATIONS

I.   Journal Papers

1. H. Jayakody, R. Al-Dadah, and S. Mahmoud, "Computational fluid dynamics investigation on indirect contact freeze desalination," *Desalination*, vol. 420, pp. 21–33, 2017.

2. H. Jayakody, R. Al-Dadah, and S. Mahmoud, "Numerical investigation of indirect freeze desalination using an ice maker machine," *Energy Convers. Manag.*, vol. 168, 2018.

3. H. Jayakody, R. Al-Dadah, and S. Mahmoud, "Cryogenic energy for indirect freeze desalination – numerical and experimental investigation," – under preparation.

II.   Conference Papers

1. H. Jayakody, R. Al-Dadah, and S. Mahmoud, "Indirect contact freeze water desalination for an ice maker machine - CFD simulation," in *E3S Web of Conferences*, 2017, vol. 22.

2. A.K. Almajri, S. Mahmoud, R. Al-Dadah, S. Alfarawi, H. Jayakody, "CFD Parametric Study of Alpha Stirling Engine Performance," in *Proceedings of the 17th International Stirling Engine Conference, Northumbria University, Newcastle,* 2016.

CHAPTER 1

1. INTRODUCTION

1.1 Background

Sustainable resources of water and energy are essential for social, economic and human wellbeing in the modern world [1]. The basic substance for life is water and it is progressively becoming a scarce resource where half of the world population of about 88 developing countries are affected by water shortages [2]. In these developing countries, 80-90% of all diseases are caused by poor water quality and 30% deaths are also due to poor water quality [2]. The people affected by harsh water shortages are projected to rise in the next 25 years due to the growth in population and the demands of industrialization [3]. At present, the rate of increase of water consumption is twice the rate of population growth, where it doubles every 20 years [4]. There is a vast amount of water available on Earth, about $1,400,000,000 \text{ km}^3$ [4]. However, less than 3% of this amount is fresh water, about $35,000,000 \text{ km}^3$. Majority of this of about $24,000,000 \text{ km}^3$ is not accessible due to it being located in ice caps and glaciers as shown in Figure 1-1. Approximately, $11,000,000 \text{ km}^3$ of the Earth's water is retained as groundwater, plants, atmosphere and surface water in rivers, lakes, etc. [5]. Majority of this water has slowly accrued over time and it is not considered to be renewable [2].
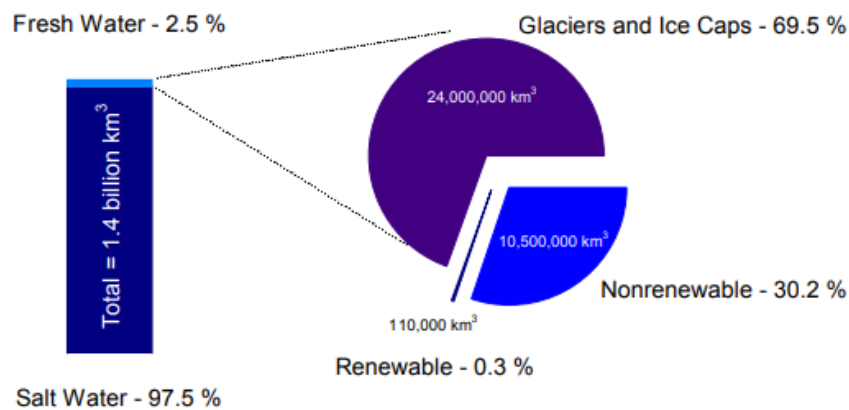
Figure 1-1: World's water distribution [2], [5]

Freshwater production by the removal of dissolved minerals from sea water is known as desalination; as it verifies to be an answer to the water shortage issue [6], [7]. Cost-effective and possibly climate independent water resources can be produced by desalination technologies for agricultural uses [8]. Figure 1-2 shows that in order to address the water shortage issue, sea water is the leading feed water in the world for installed desalination techniques, thus making it the most applied solution [8].
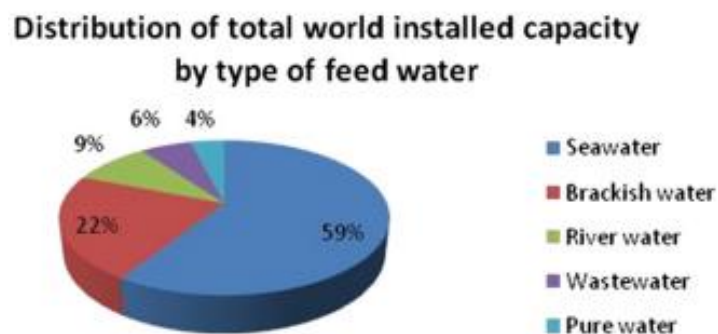
Figure 1-2: Total capacity of installed desalination techniques in the world [8]

Freeze desalination is an evolving desalination technology due to its low energy usage. The process of freezing an aqueous salt solution results in ice crystals that are of pure water in the solid phase, this process is the physical principle of freeze desalination [9]. Another key

advantage of the freeze desalination process is its low operating cost of 0.34$/m^3 compared to 0.75$/m^3 for the commonly used Reverse Osmosis desalination technology, as shown in Figure 1-3.
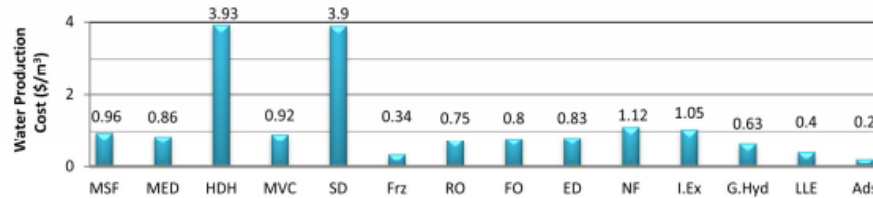
Figure 1-3: The water production cost for various desalination technologies [10]

A key advantage of the freeze desalination technology is the ability to utilize the cold energy from the regasification of liquefied natural gas (LNG). This high quality cold energy source can be used to freeze salt water in the freeze desalination process, but most cold energy during LNG regasification has been unexploited until today. Approximately 830kJ/kg of cold energy is released during LNG regasification and this cryogenic exergy can be used for the freeze desalination process [11]. Due to the on-going energy supply-demand disparity, augmenting these technologies can aid in providing solutions for this, and in improving the economics of the renewable energy powered desalination systems, as desalination capacity is escalating worldwide [12].

1.2 Aim and objectives

This research aims to investigate the potential of the indirect contact freeze seawater desalination using an ice maker machine and stored cryogenic energy by CFD modelling and experimental testing in terms of salinity and water production, through the following objectives:

1. Carry out a comprehensive literature review on; (a) the water crisis and the importance of water and how desalination is a significant solution to the shortage of water, (b) comparison of current desalination technologies (c) the process of freeze desalination and its advantages, (d) the major freeze desalination techniques, (f) numerical modelling of freeze desalination and (e) cryogenic energy storage and its use for freeze desalination.

2. Develop a numerical model for freeze desalination using computational fluid dynamics (CFD) taking into account the salt separation process.

3. Validate the CFD model through experimental testing using a Peltier cooling device and carry out parametric analysis to predict the effects of freezing temperature, solution salinity and the direction of freezing, on the freezing time, ice production and its salinity.

4. Assess the performance of an ice making machine for freeze desalination in terms of ice production, salinity and energy consumption using experimental testing and the validated CFD model.

5. Investigate the use of cryogenic energy storage (evaporation of liquid nitrogen) for saline water freeze desalination using CFD modelling and experimental testing.

1.3 Thesis outline

This thesis has been divided into six chapters and they are summarised as follows:
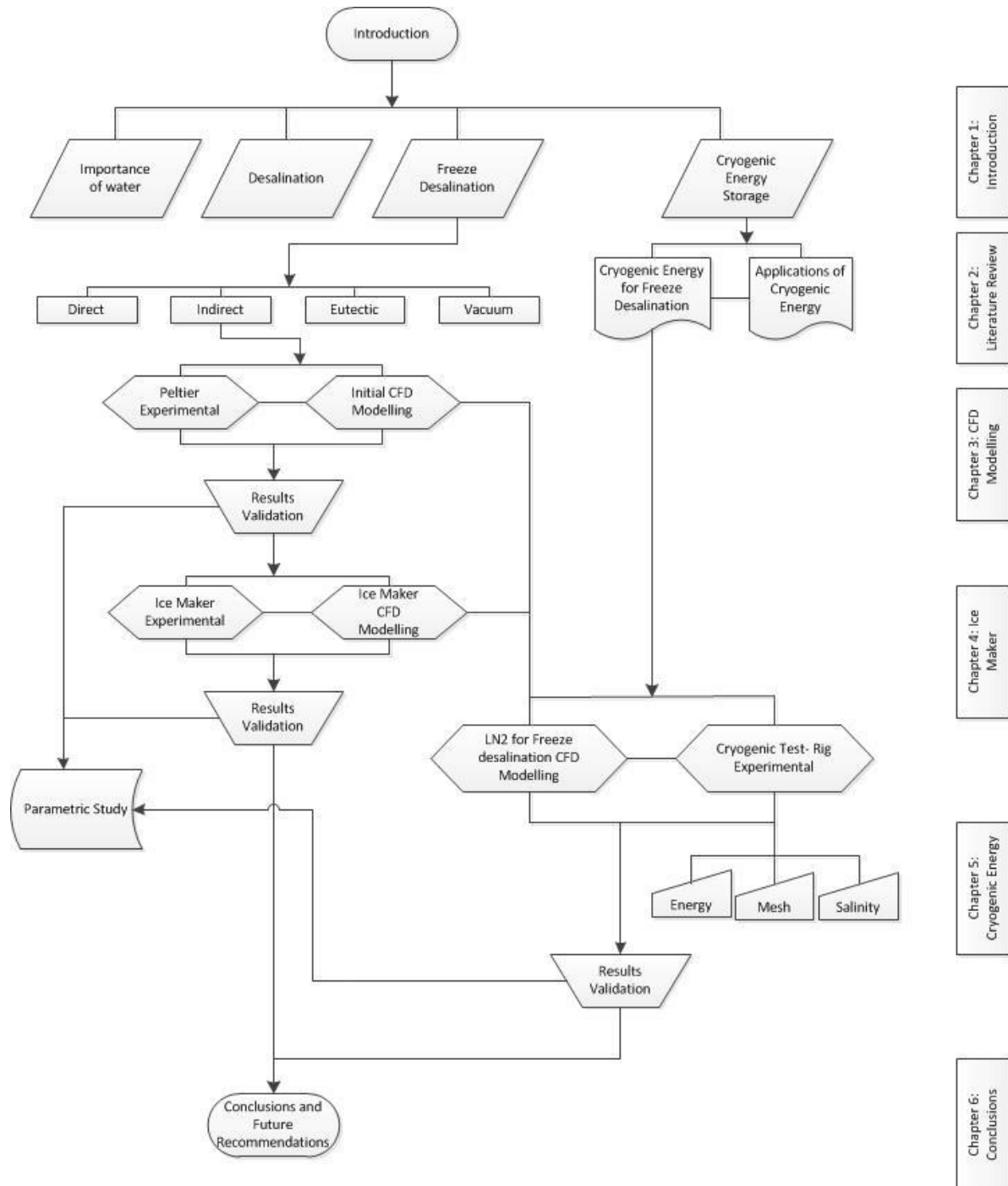
Figure 1-4: Thesis structure flow chart

1 **CHAPTER ONE:** Introduction of the background to this research where the significance of water is discussed. Desalination, a solution to the water shortage issue and freeze desalination proving to use less energy consumption is discussed. The use of cryogenics for freeze desalination is also briefly discussed. The aim and objectives of this research are stated.

2 **CHAPTER TWO:** A thorough literature review predominantly focused on freeze desalination and the use of cryogenics for freeze desalination was carried out. The importance of water with an economic background is concisely discussed. A brief history and the benefits and drawbacks of this technique is also stated. The process of freeze desalination is also presented in this chapter with a thorough analysis of various available freeze desalination techniques. A comprehensive study on cryogenic energy storage and its applicability to freeze desalination is also specified in this chapter. Numerical analysis (CFD) on the freeze desalination process is also discussed in this chapter. This chapter also includes a 'Research motivation and contribution' section where, the novelty of the research and the three different types of experiments conducted are summarised.

3 **CHAPTER THREE:** This chapter is primarily acquired from the journal paper of "Computational Fluid Dynamics Investigation on Indirect Contact Freeze Desalination" by Jayakody et al. [12] which is published in the Desalination Journal. A detailed Computational Fluid Dynamics (CFD) modelling of the freeze desalination process is explained. The theory and model set-up methodology of the CFD modelling to simulate the salt separation process of freeze desalination is discussed. The CFD model has then been validated through experimental testing using a Peltier cooling

device. Additionally, in this chapter, measuring devices calibration and uncertainty analysis are also explained. The developed CFD model has been used to carry out parametric analysis to predict the effects of freezing temperature, solution salinity and the direction of freezing; on the freezing time, ice production and its salinity. Overall, in this chapter, the fundamentals of the CFD modelling of the freeze desalination process was carried out and investigated.

4 **CHAPTER FOUR:** This chapter is primarily acquired from the journal paper of "Numerical Investigation of Indirect Freeze Desalination using an Ice Maker Machine" by Jayakody et al. [7] which is published in the Journal of Energy Conversion and Management. The feasibility of using an ice maker machine as a portable freeze desalination method is investigated in this chapter. A commercially available ice maker machine has been used to carry out experimental work and CFD modelling has been conducted. Further parametric analysis was also carried out numerically using the validated CFD model in order to observe the effects of the freeze tube temperature and the initial salinity of salt water on ice production and the final salinities of ice and brine. A second stage freezing process was then done in order to obtain fresh water with pure ice crystals with salinities below the 0.1% mark which is regarded as fresh and safe to drink by the WHO [13]. Additionally, parametric study was carried out on the geometry of the freezing tubes in the ice maker machine. Overall, in this chapter, the fundamentals of the CFD modelling process investigated in chapter 3 was used to improve the CFD model and to develop it for an ice maker machine to assess the feasibility of using an ice maker for freeze desalination as a domestic application.

5 **CHAPTER FIVE:** The use of cryogenic energy storage for freeze desalination has been investigated using CFD modelling and experimental testing. The numerical modelling of evaporation of liquid nitrogen is explained with the theory and methodology. CFD modelling of the evaporation of liquid nitrogen to carry out freeze desalination process is conducted to investigate the feasibility of using cryogenic energy for freeze desalination. This CFD model was then validated using experimental test facility constructed to evaporate liquid nitrogen to supply the cooling required for freezing. In this chapter, the experimental heat exchanger test rig has been comprehensively explained with the experimental test facility descriptions, measuring devices, experimental calculations, etc. Furthermore, parametric analysis was also conducted on CFD by changing the flow rate of liquid nitrogen in order to observe the volume of ice obtained. Overall, in this chapter, the CFD modelling process investigated in chapters 3 and 4 was used to combine with the CFD modelling of the LN_2 evaporation process to assess the feasibility of using cryogenic energy for freeze desalination.

6 **CHAPTER SIX:** Conclusions from the research is discussed and the major outcomes of the research carried out is presented in this chapter. Future developments and recommendations are also stated here.

CHAPTER 2

2. LITERATURE REVIEW

2.1 Introduction

In this chapter a comprehensive literature review is presented and predominantly focused on freeze desalination and the use of cryogenics for freeze desalination. The importance of water and how desalination is a key solution for the water shortage is discussed. The process of freeze desalination and the benefits of this method are explained. Furthermore, the major freeze desalination technologies are detailed. Cryogenic energy storage and the use of cryogenic energy for freeze desalination is discussed.

Certain information are taken from the published papers; "Computational Fluid Dynamics Investigation on Indirect Contact Freeze Desalination" by Jayakody et al [12], "Numerical Investigation of Indirect Freeze Desalination using an Ice Maker Machine" by Jayakody et al [7] and "Indirect contact freeze water desalination for an ice maker machine – CFD simulation" by Jayakody et al [14].

2.1.1 Importance of water

There are several necessities for life on Earth, where water is one of them and it is becoming scarce [2]. Water is an essential element for all inhabitants of this earth, and it plays a major role in the development of any human society [12], [15], [16]. On this planet, water is an

abundant natural resource and it is an essential nutrient to all living beings. Studies have shown that the freshwater supply is approximately only about 3% of the entire water supply on Earth. The World Water Council has stated that by 2020, the world will be short of approximately 17% of freshwater that is required for the increasing world population [17]. Over the past decades, population growth, changes in socioeconomic conditions, increased water demands for agricultural and industrial use, and climatic change have increased water consumption and created growing water scarcity problems in many parts of the world [16], [18]–[22]. Given the current situation of mismanagement and increased use of water resources, the World Economic Forum identified water scarcity issue as the third highest risk of global concern [23].

Many developing and third world countries are affected by water shortages, causing a large number of losses of about 80-90% caused by diseases and 30% of that is caused by poor water quality [1]. Therefore, desalination becomes an important process in order to obtain freshwater using seawater, as a substitute solution to the rapid shortage in freshwater [24]. Advancement in technology has enabled the growth of processes, for improving water quality over the past few decades [12], [25].

2.1.2 Desalination

The process of desalination is used in order to purify water containing dissolvable substances, which are eliminated by being fed into a system [26]. Desalination is used to produce fresh water from sea water by removal of dissolved minerals and has been acknowledged as the answer for water shortages in many countries [6], [7]. Hence,

desalination is a relevant and practical method in order to obtain a large amount of pure water. Correspondingly, seawater desalination is a key system used for the supply of water in coastal regions. During the years 2008 to 2013, the world capacity to produce desalinated water has risen by 57% annually. In the year 2013, 300 million people were served desalinated water as 1700 plants were used to produce 80million m^3/day [6], [27]. The water shortage issues are significantly reduced and the quality of water is enhanced thus in turn bettering the quality of life and economic status by desalination technologies [7], [28]. Selecting a correct method for desalination can be challenging [29]. There are various methods of desalination available where the primary objective is to eliminate salts from saline water by producing freshwater from saltwater as shown in Figure 2-1. Freshwater is produced from this process with a low concentration of salt, leaving a waste product called brine with a high concentration of salt.
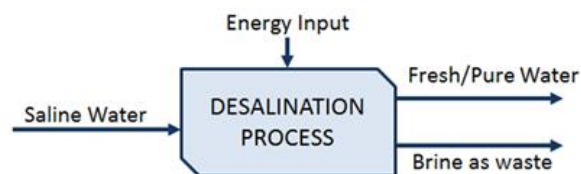
Figure 2-1: The desalination process principle

2.1.3 Different types of desalination processes

On the basis of thermal distillation, membrane separation, freezing, electro dialysis, several desalination technologies have been developed over the years [30]. The main desalination processes are; multi-stage flash distillation, multiple-effect distillation, vapour compression distillation, reverse osmosis, freeze desalination and solar evaporation. Worldwide, there

are two processes that are widely used to desalinate water, the thermal and membrane methods [30], [31]. Thermal methods include multiple-effect distillation (MED) and multi-stage flash (MSF) desalination. In membrane methods, where permeable membranes are used to separate solutes from water, the reverse osmosis (RO) technology is most widely used. However, these processes face the challenges of high-energy consumption for thermal processes and severe membrane fouling for the membrane ones [31]–[36]. For small-scale desalination applications the vapour compression technology (VCD) is used where the heat required to evaporate the feed water is derived from the vapour compression process [27]. Vast amount of energy (heat demand/high-pressure demand) and high operating costs (scaling and fouling maintenance) are required in order to carry out these types of desalination processes [12], [37], [38]. Thus, the rise in desalination plants which uses fossil fuels, considerably increased the air pollution [7], [39]. Intensive pre-treatment and chemical requirement are needed in the reverse osmosis process and this process yields high concentrated brine that is harmful to the environment [40].

Detailed parametric analysis was conducted by Youssef et al [10], which compared the performance of various desalination technologies, and presented that freeze desalination releases CO_2 emissions of about 5.5kg/m^3 as shown in Figure 2-2. It also demonstrated that water production costs were only 0.34\$/m^3; comparatively lower in relation to other desalination technologies as shown in Figure 1-3. [7] It is seen in Figure 2-3, that freeze desalination systems require high electrical energy of about 11.9kWh/m^3 with no thermal energy required. The high energy consumption is due to the use of electricity driven mechanical vapour compression refrigeration systems to produce the cooling required for freeze desalination. Figure 2-4 displays the salt water feed in salinity and the produced

water salinity in various desalination technologies. It is seen that freeze desalination is able to reduce the salt content at a great deal but not as much in comparison to desalination methods such as multi stage flash, reverse osmosis, adsorption, etc.
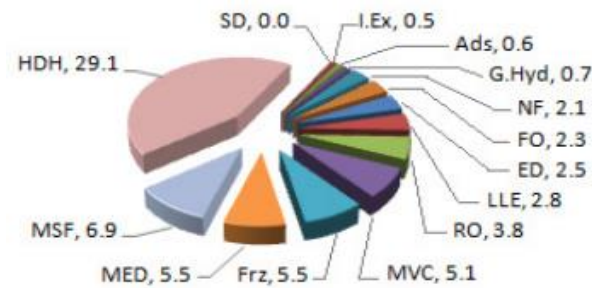
Figure 2-2: CO_2 released amount for various desalination methods measured in kg/m^3 [10]
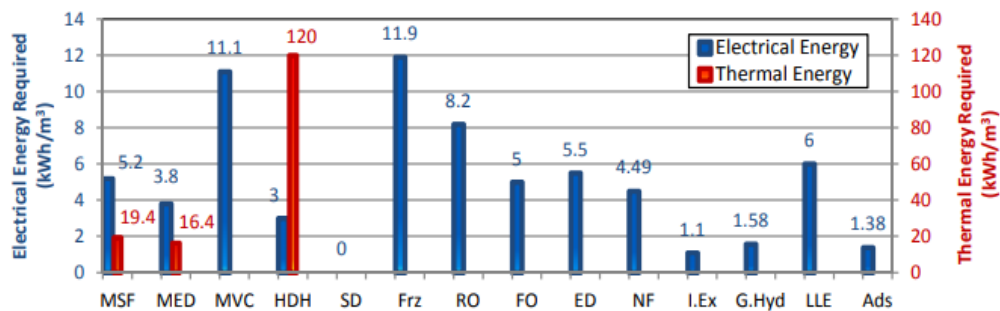
Figure 2-3: Various desalination methods' energy requirements [10]
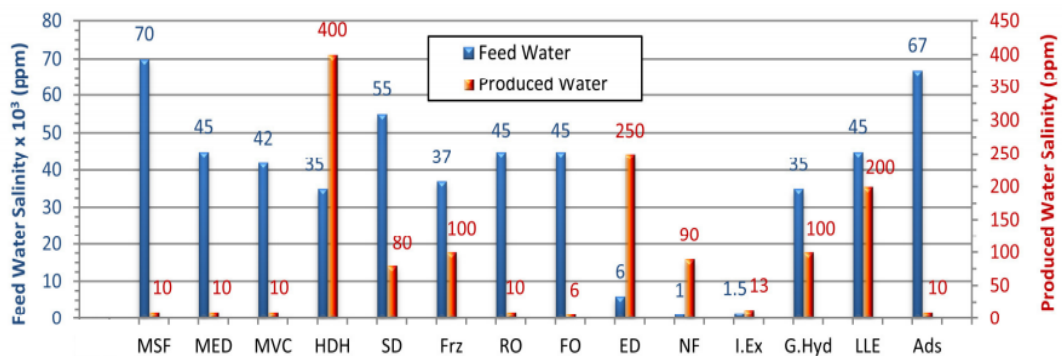
Figure 2-4: The feed salt water salinity and the produced water salinity in different desalination technologies [10]

2.2 Freeze desalination

Ice crystallization of pure water occurs when temperatures of saline water is decreased to reach its freezing point, thus causing desalination to occur by the freezing process [41]. The principle of freeze desalination process is based on water solidification phenomena, where the growing small ice crystal lattice prevents the inclusion of any solutes. Therefore, during ice crystal formation, salts are rejected by the nature of ice crystal lattice, which is formed from pure water [12], [42], [43]. Freeze desalination uses the fact that; salts are insoluble in ice as a base to carry out the process [29]. The process of freezing an aqueous salt solution results in ice crystals that are of pure water in the solid phase. Hence, the ice crystals must be separated from the brine and the adhering salts on the crystal surface must also be detached from the ice crystals by cleaning.

2.2.1 Advantages and disadvantages of freeze desalination

<u>**Advantages**</u>

Recently, renewed interest in freeze desalination (FD) has emerged due to its potential advantages over current desalination technologies [12], [35], [41]–[45]. The main advantage of freeze desalination technology is its lower energy requirement in comparison to other desalination processes that uses evaporative methods; since the latent heat of freezing is low (333.5 kJ/kg) compared to the latent heat of evaporation (2256.7 kJ/kg) [12], [44], [45]. Hence, it is clearly shown that a lower amount of energy is required for the freeze desalination process. Approximately, the ratio of latent heat of vaporisation of water to the latent heat of freezing is 6.5:1. Hence, evaporating 1kg of water will create 6.5kg of ice [46], thus enabling an increased production of ice and an increased efficiency. Important

issues with all types of distillation processes are the scale formation and corrosion; but since freeze desalination is operated at low temperatures, these issues are minimized. There is also minimal corrosion and metallurgical problems and requires almost no pre-treatment. Therefore, an extensive range of materials and construction methods can be used [45]. The freezing process is suitable for substances that even the membrane process cannot desalt, including industrial or wastewater, or brackish water that has a high salt content. This is because the freezing process enables the feed water to undertake properties with different concentrations or types of substances [12], [41].

Youssef et al [10] carried out detailed parametric analysis to compare the performance of various desalination technologies, and showed that freeze desalination releases CO_2 emissions of about 5.5kg/m^3 and the cost of water production is only 0.34\$/m^3, which are low compared to other desalination technologies. Another major advantage of the freeze desalination technology is the ability to exploit the cold energy from the regasification of liquefied natural gas (LNG) [35]. This high quality energy source can be used to cool the feed sea water in the freeze desalination process, but most cold energy during LNG regasification has been wasted until today [32]. Due to the on-going energy supply-demand disparity, enhancing these technologies can aid in providing solutions for this, and in improving the economics of the renewable energy powered desalination systems, as desalination capacity is rising worldwide [12], [47]. An adsorption system can also be used to conduct freeze desalination as Dakkama et al [48] investigated a novel vacuum-direct freezing technique using an adsorption system for freeze desalination by using sea water as refrigerant [7].

Disadvantages

Despite of lower energy consumption, good separation efficiency and high product quality; the widespread use of freeze desalination is still limited due to a number of technical issues like the formation of ice scale layer on the cooling surfaces in the indirect freeze system [49]. The thermal conductivity of ice is very low ($2.16\ \text{W.m}^{-1}.\text{K}^{-1}$) [50] compared with those materials used in heat exchangers like copper or stainless steel. Therefore, the formation of such ice layer on the heat exchanger walls will significantly reduce its efficiency and production rate, particularly as the ice layer thickness increases [12], [51], [52].

In theory, the freeze desalination process is predicted to produce ice crystals which are pure but the ice quality is affected by many aspects during the freezing process. It was suggested that the ions could be expelled into brine of slight quantities of moderately frozen or completely unfrozen. Occasionally, these ions do get trapped into the ice crystal, in qualitative concurrence with the low solubility of salts in ice [53]. Luo et al [54] conducted a research on factors that affected the ice crystal quality during freezing where it was concluded that the rate of freezing, solid fraction, temperature of freezing and the concentration of the solution affected the ice quality [7]. The separation of ice crystals from the concentrated brine is a challenge in the freeze desalination process. Higher initial investment, capital costs and higher operating costs during the ice separation process are also further drawbacks of this process. Other disadvantages include: build-up of the initial feed saline water that contains unnecessary aromas and flavours into the produced water [31]. Growing, handling and washing of ice crystals are involved in the freeze desalination process. Furthermore, mechanical vapour compressors which consume significant amount of electrical energy are used in this system. Additionally, due to the high complexity of the

unit operations involved in the melting unit, freezing unit, and wash-separation column, it is unlikely that large plants will be designed and operated, causing a major drawback in the freezing process [31].

Crushing and recrystallization of ice are two processes that are required during freeze desalination due to the salt solution being confined in the ice. In distillation and other evaporation processes, low quality energy is used, however for freeze desalination, high quality energy is essential. There are several key processes that require a substantial amount of awareness such as, practicalities of handling ice slurries, ice crystallization and growth in the slurry system, hydration behaviour, and also methods for the separation of brine from ice. This will assist in understanding that when reducing the salt content in the water produced, it is achieved by needing a certain amount of fresh water to wash the ice [31]. A few freeze desalination plants that have been manufactured in the past 40 years, have not been commercially practical; thus causing some of these plants to have been abandoned [29].

2.2.2 History of freeze desalination

The ice formed in seawater is essentially fresh clean water and after melting, it can be used as pure water. During the second part of the seventeenth century, sailors have used this method in order to obtain fresh water from ice. In 1661, Thomas Bartholinu, a Danish physician was the first to state that the ice formed in the sea was fresh and melting this ice would give pure water [55]. Robert Boyle also confirmed the observation that ice in

seawater can be used to obtain freshwater [56]. The basis of why ice in sea water is pure was then discussed by Jesuit Athanasios Kircher [57].

Anton Maria Lorgna, an Italian scientist in the late 1700's, came up with a technique to purify seawater by the freezing process, where the saltwater was frozen and then the ice crystals formed, were melted to obtain pure water [58], [59]. Freeze water refinement was not a practical solution in the early days as it was only feasible in the cold climatic conditions [59]. In the late 1930s, the interest in freeze desalination process was renewed, leading to construction of an experimental desalting plant near Rome that functioned for some years [59]. This was due to the revolution of refrigeration machines. The urge to develop this process then faded. However in the 1950's, 1960's and 1970's several researchers consistently analysed this process, resulting in creating ideas and improvements for this method [60]–[67].

In the 1970s, a crude oil boom occurred, which resulted in more energy being accessible, hence evaporation and RO processes regained interest. This later resulted in the freeze desalination process, fading again [45]. Nevertheless, in the food industry, the freeze desalination process has been extensively used and various other developments that can be used for freeze desalination have been discussed by Sanchez et al. [67], [68].

2.2.3 The process of freeze desalination

The fundamental idea of the freeze desalination process is freezing of saline solutions to form ice crystals from water to separate it from the salts. This is due to the fact that the ice

crystals formed contain pure water and are free of salts. When sea water is partially frozen, the ice crystals can then be separated from the residual concentrated brine by physically separating the two, and then melting the ice to form pure water [31].

Williams et al. [45] proved the process of desalination by conducting a small experiment, where a methylene blue dye solution was placed in a metal beaker and was frozen. This was carried out in a regular freezer for a few hours. The water and dye then separated in a gentle de-freezing progression. From this experiment, it was observed that the concentrated brine was collected in the middle of the ice and at the edge of the ice, was pure water as shown in Figure 2-5. Later the dye pockets were washed and the ice was melted in order to obtain pure water. Hence, Williams et al. [45], proved that by removing heat to form ice, separating the ice from brine and melting this ice to obtain pure water, were the primary steps in the freeze desalination process.
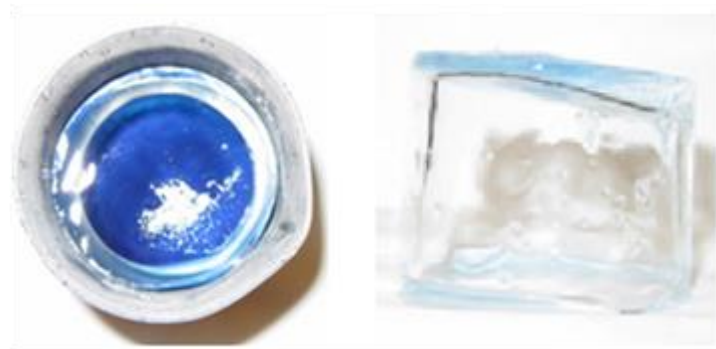
Figure 2-5: Freeze separation with methylene blue dye [45]

Rahman et al. [31] also concluded that the 'ice crystallisation' and the 'separation and melting' of the ice are the two primary steps of the freeze desalination process as shown in Figure 2-6. Nucleation arises in the first step, at an appropriate super cooling temperature. Thus, large ice crystals are then formed as the nuclei in the solution develop. In the second stage, a separator divides the ice crystals from the concentrate. Therefore, melting these ice

18

crystals results in pure water. Overall, the pre-cooler cools the feed water and then in the crystallisation unit, adequate heat is taken out from the process in order to form ice crystals, which are then separated from the concentrated brine that is not frozen. These crystals are then washed with pure water to remove any adhering brine concentrate from the crystals' surface.
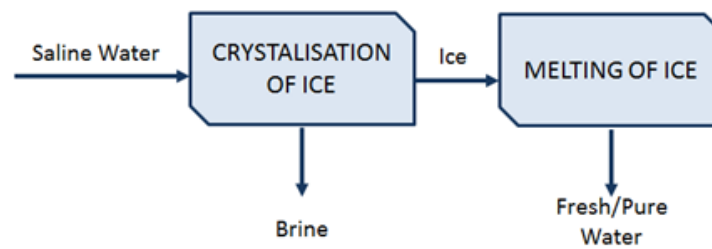
Figure 2-6: A basic freeze desalination process

Lu and Xu [41] suggested four mechanisms for the freeze desalination process which are; freezer, washer, melting unit and the heat elimination system. There are many designs for the freeze desalination process and the way the freezing and melting takes place differs in various processes. As the heat is removed from the salt water, ice crystals are formed; and there are many different ways to conduct freezing. Thus, these crystals are then simply moved, removed, detached, cleansed and melted. During the freezing process, the extracted heat is generally recovered on for the melting of ice at the end of the process, in order to optimise the efficiency. The amount of heat that is added to the melting unit is principally almost equivalent to the amount of heat extracted from the freezing component. By transferring the heat removed from the brine in the washer during crystallization, into the melter will allow the ice to melt [41]. The temperatures at which the freezing processes occur are lower than the ambient; hence the heat must be extracted from the system

continuously. Freeze desalination processes differ in the various methods of heat elimination.

Figure 2-7 shows the basic process of freeze desalination. As the salt water enters the crystallizer, the solution is frozen and the ice crystals are formed. This is the primary section of the process and the way the freezing is completed can be different to many freeze desalination processes. In the separator, the ice and the brine slurry mixture is separated. Washing of the ice crystals also occurs at this stage, where a small amount of clean water obtained from the product is used to clean the ice crystals from the entrained brine. Pure water is then finally obtained after melting the ice.
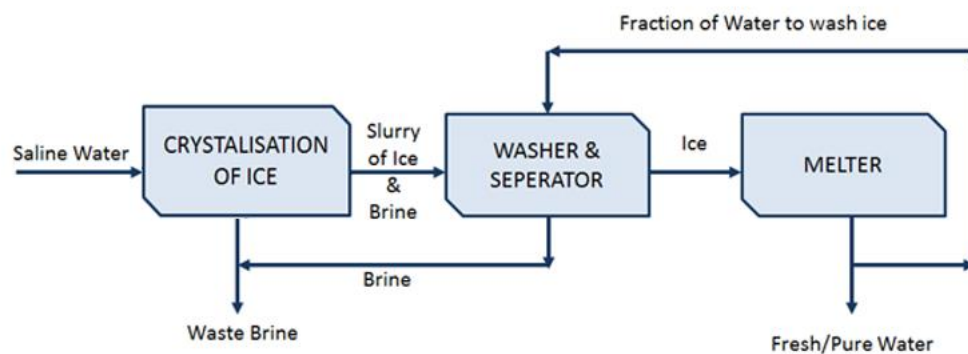
Figure 2-7: An advanced freeze desalination process

2.3 Different types of freeze desalination processes

There are various types of freeze desalination processes and a small number of freeze desalination demonstration plants that has been built over the past 40 years [29]. The main types of freeze desalination processes that are discussed in this chapter are summarised in Figure 2-8.
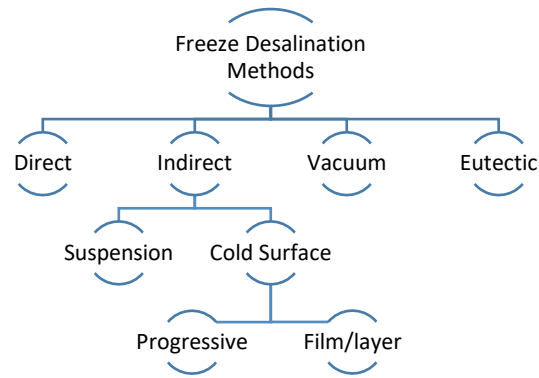
Figure 2-8: Different freeze desalination methods

2.3.1 Direct contact freezing process

In direct contact freezing, the direct-contact crystallisers mix the saltwater solution and the refrigerant. Saline water and a non-miscible refrigerant of liquid hydrocarbon like butane; are directly made in contact with each other and is then vaporised. Under high pressure, the refrigerant in a liquid form is expanded through a nozzle into the product liquid. Afterwards at low pressure, it then vaporizes. A refrigeration effect is then occurred due to this vaporization, thus causing ice formation and solute crystal formation within the saline water [31]. The ice and brine slurry must then be separated as it is propelled to a wash column and subsequently sent for melting [45].

The main stages of direct contact freezing consists of nucleation of ice, a crystalliser permitting the progress of these nuclei up to an appropriate size for separation, and a separator to separate the ice crystals from brine [69]. The appropriate size for separation is determined by the critical size of the crystals and these crystals have to be bigger than the

critical size for them to grow and not melt [69]. Moreover, an ice crystal washer and an ice-melting unit are needed to obtain pure water. Figure 2-9 displays the basic direct contact freezing process [70].
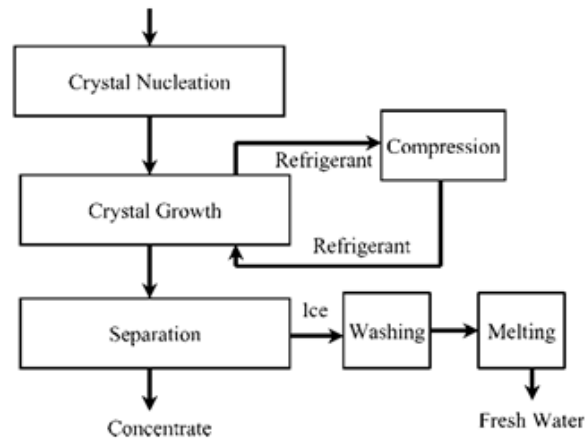
Figure 2-9: Direct contact freezing process [31]

Williams et al. [45] suggested that in the freezer, the hydrocarbon vapour is compressed and heated; this heated vapour is then sent to the ice melting unit, as shown in Figure 2-10, to be used for melting the ice. At high pressure, the compression and condensation of the butane vapour will occur and is recycled back to the freezer. The heat exchanger is there to regain a low amount of heat from the seawater that is entering into the system using the cooled water and brine.
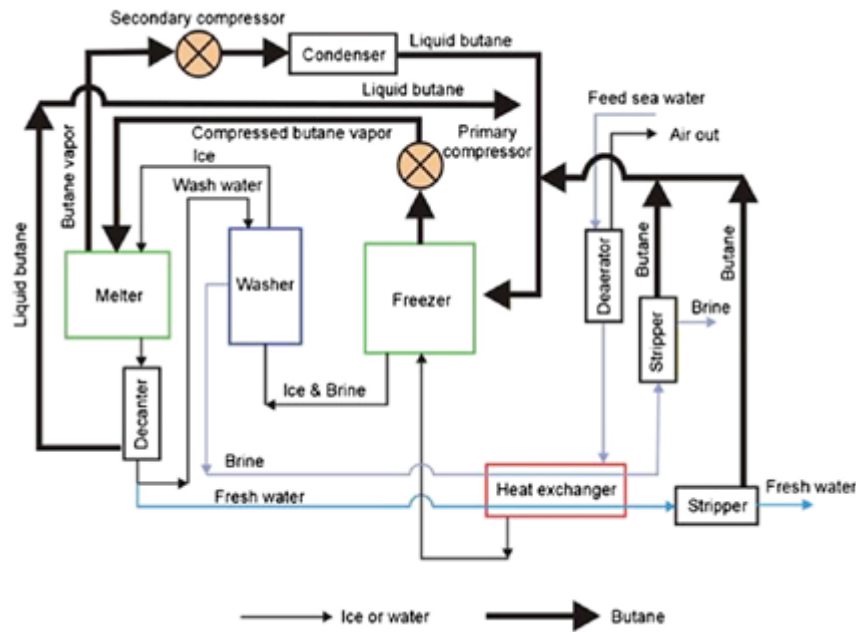
Figure 2-10: Direct contact freezing process - schematic diagram [41]

The primary benefits of this method are; that the consumption of power is low due to the lack of a heat transfer surface in the system, the nonexistence of moving parts, that it is a compact and an efficient system and most importantly occurs at a small driving force and has a high production rate per unit volume [71]. Moreover, this only needs a small amount of work per unit of freshwater produced, due to the fact that the compressor functions over a small temperature range [72]. Furthermore, using butane as the refrigerant benefits greatly, by not having to be vacuum tight.

Conversely, a critical drawback of this process is that the water attained is non-potable, due to the partial retention of the refrigerant in the ice made. Additionally, there are many issues with the compressors where these compressors require lubrication that could result in the water being infected unless demisters are included in the plant. Furthermore, compressors that work with low-pressure refrigerants like butane have not been tested and are

unattainable. Thermally driven adsorption heat pumps, can substitute the compressor driven refrigeration cycle as a possible answer to the issue and this could also surge the effectiveness and efficiency [72]. An alternative answer to the issue can be, the application of a hydraulic refrigerant compressor that uses a liquid stream, such as water, that is flowing and a hydrostatic head to compress the refrigerant [73]. Other disadvantages of the direct contact freezing process are because of practical considerations, including functioning and controlling the solids handling operations [2].

2.3.2 Vacuum freezing process

The simultaneous occurrence of evaporation and freezing is the base of the vacuum freezing process. The saltwater enters the system as the ice, brine slurry, and water vapour are drawn out. The refrigerant in the vacuum freezing process can be water itself [74]. Initially, using a high vacuum, water is vaporized, thus resulting in the refrigeration effect and the water temperature being reduced, causing ice crystals to form. The ice crystals are then washed and melted by condensing the water vapour in the melting-condensing section as shown in Figure 2-11. The compression of the vapour is the primary energy requirement in this process and energy is also required to drive the vacuum pump. As shown in Figure 2-11, the dissolved gasses are removed using the deaerator as these gases would affect the general operation of the process.
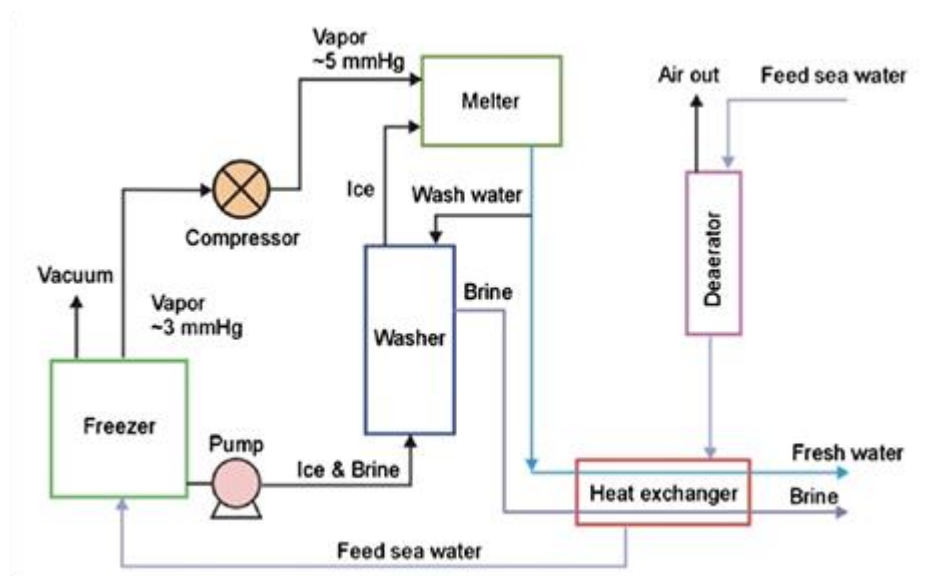
Figure 2-11: Vacuum freeze desalination process - schematic diagram [41]

Research conducted by Rane and Padiya [75] concluded that 3.5% salt by weight can be obtained at 0.0051bar and −2.1°C which is the triple point of seawater. The seawater surface is maintained below this triple point value in the vacuum freezing technique [75]. Major issues are reduced when using water as the refrigerant. Thus, this benefits the system as the cost is reduced and the supply is available. Contamination of the product is avoided and the separation of the ice becomes easy in comparison to direct contact freezing.

Vacuum flash freeze desalination is mostly applied to small-scale desalination plants due to its simplicity and ease [76]. This process is mainly based on heat transfer that is controlled; needing stirring and the residence time is not a crucial variable. Furthermore, for the elimination of the non-condensable gas in the system, an efficiently designed melting component is required [77]. A major drawback of vacuum freeze desalination is the fact that, due to the high specific volume of the water vapour, the design of the compressor is challenging. Alternative solutions include, vacuum-freezing high pressure

ice melting (VFHPIM) processes and vacuum-freezing vapour adsorption (VFVA), where the vacuuming process have been designed to avoid the challenges involved [41].

2.3.3 Eutectic freezing process

Barduhn was the first to create the eutectic freezing process [78] which was then first tested by Pangborn [79]. Schroeder [80] concluded that if the eutectic freezing process was enhanced, it could be a very significant process in the future.

The fundamental idea of the eutectic freezing process is the fact that the product water will separate as ice and the salts as solids by taking advantage of the difference in the densities of ice and salt. The growth of the crystals of ice and salt occur individually, which can then be separated quite simply due to the fact that the ice will float and the salt will sink. These aqueous solutions are frozen to obtain pure water as ice and salt which precipitate when sufficiently concentrated. Hence, one ends up with no brine product [31]. The temperature at which both the ice and the salt will crystallise is called the eutectic point. The extraction of heat at around -20°C (eutectic point) causes the precipitation of the ice and $NaCl.2H_2O$ crystals. The saltwater when frozen, forms pure water as ice crystals on the surface and the brine is then concentrated in the rest of the solution. The pure ice crystals can then be separated from the solution and then washed to clean. These ice crystals are then melted to obtain the pure water. The solution nevertheless would still contain pure salt that will crystallise at the eutectic point.

A salt filter and an ice-salt separator exists in the eutectic freezing process and this distinguishes it from ordinary freezing processes as concluded by Van der Ham et al. [81] and shown in Figure 2-12. The key difference in the eutectic freezing process compared to conventional freezing processes is the stirred tank crystalliser used in eutectic freezing. Additionally, a hydro-cyclone separator and a floating wash column are used in the eutectic freezing process [82].
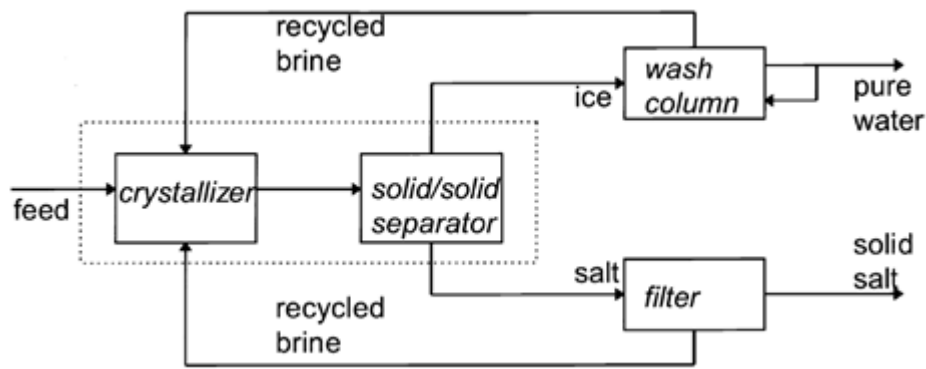
Figure 2-12: Eutectic freezing process - schematic diagram [81]

Figure 2-13 shows a disk column crystalliser (CDCC) that allows the separation of ice and salt solids simultaneously, built by Van der Ham et al [83]. Cooled Disk Column Crystallizer (CDCC) system utilizes 2 'cooling disks' that is fed with coolant solution in an indirect manner to cool the salt water to freeze [45]. The saltwater is directed into the centre of the column and when the freezing process arises, the salt travels to the bottom and the ice rises to the top of the column. Van der Ham et al. [84] and Himawan et al. [85] developed a detailed cooled disk column crystalliser model and a eutectic freeze crystallizer model respectively, by creating computer based dynamic models to simulate their transient behaviour.
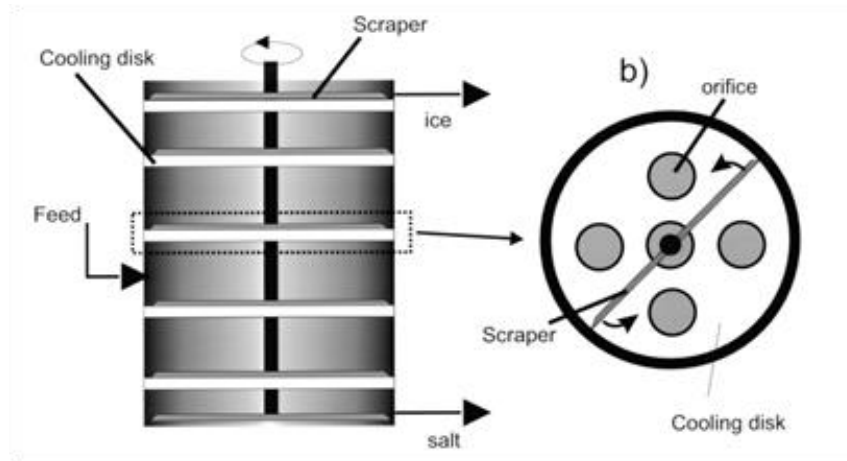
Figure 2-13: Cooled disk column crystallizer side view (left) and top view (right) [83]

Disposal of brine and concentration of industrial wastes, are key issues, where the continuous use of eutectic freezing could assist in eliminating these problems [82]. The discarding of brine issue can be solved using the eutectic freezing process as the ice crystals and salt solids are separated simultaneously. Hence, the salt that is precipitated can also be a by-product of this process. A great benefit of the technology involved in this process is that, theoretically in a binary system, a 100% yield can be achieved [45]. Conversely, the eutectic freezing process requires much more energy for freezing, due to the fact that this operates at around -25°C compared to other freezing processes, which operate at around -5°C.

2.3.4 Indirect contact freezing process

Indirect contact freezing process contains a wall or a physical barrier separating the sea water and the refrigerant used for cooling. The main difference in indirect freezing in comparison to direct contact freezing is the fact that the saltwater and the refrigerant do not

directly come into contact. Mechanical refrigeration or various other means cause the ice to form on the surface. The transfer of heat must be passed through a firm barrier and the refrigeration energy is delivered through a type of heat exchanger [9], [86].

Similar to direct contact freezing process, saline water enters the system by passing through a heat exchanger in order to lower its temperature. Hereafter, it enters the freezer where it is frozen to produce the ice crystals. The brine and the ice formed are then separated after passing through the washer. Ice is then melted by passing through the melter using the energy obtained from the heat released by condensation of the refrigerant, which is then compressed in the compressor. The fresh water obtained is then collected and stored. During the process of storing, it is passed through the heat exchanger to cool the incoming saline water. A small amount of the produced freshwater is sent to the washer to wash and clean the ice crystals as shown in Figure 2-14. The volume of water needed for washing the ice does not surpass 5% of the total output water [45]. Lastly, the waste brine product from the washer is then rejected. While in the process of being discarded, it is passed through the heat exchanger for further cooling of the incoming saltwater. Therefore, it can be concluded that energy retrieval from the freshwater and the reject brine by precooling the saline water can be carried out through the heat exchanger [72].
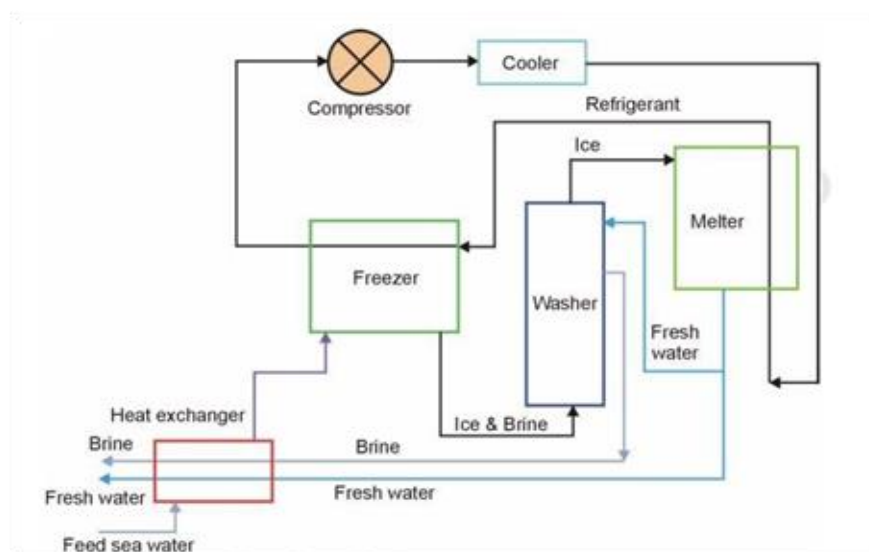
Figure 2-14: Indirect freezing process - schematic diagram [41]

There are two types of indirect freezing processes, which differ by the way cooling takes place, i.e. internally or externally [31]. Kadi et al. [87] confirmed that there are two types of indirect freezing processes; suspension freezing and freezing on a cold plate [88], [89]. Ice particles are formed in two stages in the suspension of the mother liquor (brine) in suspension freezing. The first crystals that are formed in the ice nucleator is moved to the re-crystalliser where the petite crystals develop into bigger crystals by the Ostwald ripening mechanism [88]. Suspension freezing is mainly used in the food concentration industry [31], and has many drawbacks such as; complexity, cost, difficult nucleation and crystal growth control [90]–[92]. On the other hand, freezing on a cold surface method works by formation of a single crystal layer on the surface that is being cooled. This process can be in the form of progressive freezing or falling film method [87]. The key advantage of using this method is that the ice forms in a one dimensional direction where the crystallization forms layer by layer [54]. Thus, less impurities can be trapped in-between ice crystals. If a stirrer is used in this process, it reduces the impurities near the surface of the ice growth. This process is also easy to scale-up.

30

The uncomplicated and straightforward process of indirect freezing also has a few drawbacks [93], [94]. Firstly, heat transfer surfaces, which are big and metallic, are required to freeze and melt; these apparatuses can be expensive and complex. This requires a high amount of energy due to the fact that, a resistance exists between the refrigerant and the salt water. The process can be very complicated in operating and in maintaining the ideal operating conditions [95].

Fujioka et al. [43] and Miyawaki et al. [96] conducted an indirect contact freeze desalination process for a progressive freeze- concentration that is commonly used in the food industry to be used for freeze desalination. Fujioka et al. [43] conducted laboratory experiments for the indirect contact freeze desalination and investigated the effect of the advanced speed of ice, initial concentration and the circumferential velocity of stirrer on freeze desalination. Miyawaki et al. [96] investigated the effective partition constant in the progressive freeze-concentration mathematically. It was concluded that the freeze concentration performance was improved when the rate of stirring was increased; where, increasing the stirring rate from 650RPM to 1400RPM, lowered the effective partition constant from 0.7 to 0.55 thus increasing the freeze concentration performance.

Rich et al. [97] conducted indirect contact freezing process in three experiments to produce water with salinities below 0.5g/kg that satisfies the standard of drinking water. The complete process included the freezing step that involves the crystallisation and then the sweating steps to purify the ice layer by melting the impure locations. It was concluded that using severe sweating conditions lead to obtaining water salinities lower than 0.5g/kg, fulfilling the drinking water standards [97].

Williams et al. [98] and Cao et al. [35] conducted research on indirect contact freeze desalination using an ice maker machine. Williams et al. [98] studied experimentally the potential of using an ice maker (Figure 2-15) for freeze desalination by desalting sodium chloride solutions, Arabian Gulf seawater and reverse osmosis brines. It was concluded that this is a less complicated method in comparison to conventional freeze desalination methods due to the fact that mechanical movable parts and the complicated separation and post-treatment processes are excluded.
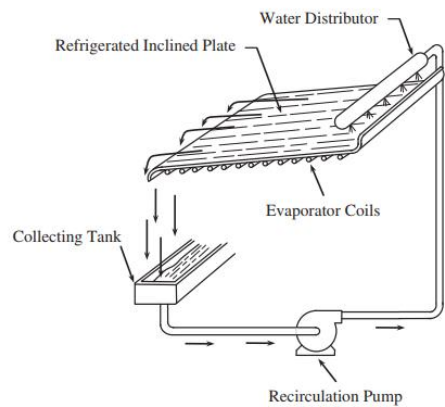
Figure 2-15: Schematic diagram of ice maker freeze desalination process by Williams et al. [98]

Indirect contact freeze desalination has been chosen for the three different types of experiments discussed in this thesis in chapters 3, 4 and 5 due to the ease in manufacturing this system and also due to less impurities being trapped in the crystallisation, thus providing more pure water.

2.4 Cryogenic energy storage

This section describes cryogenic energy storage and the importance of cryogenic energy for various applications. The advantages of cryogenic energy and the use of cryogenic energy in combination with freeze desalination are also introduced.

Energy storage is a vital part of energy production using renewable energy sources [99]. Cryogenic energy offers potential for enhancing renewable energy utilisation, due to the fact that liquid nitrogen and liquid air have high energy density.

Cryogenic energy storage uses surplus electricity to cool air to liquefy it and then it is stored in tanks. Liquid air can be stored in a compact manner in small tanks because of the energy density and pressure. In low pressure insulated tanks, these cryogenic fluids can be stored for months with losses as small as 0.005% volume per day [100]. When needed, the liquid air is pressurized and transformed into gaseous state (evaporated), usually using waste heat from another process (higher temperature source). This gas is then expanded to run a turbine to generate electricity [100], [101].

2.4.1 Advantages

Cryogenic energy storage has many advantages [102] such as:

- Cryogenic technology has been proven as it has been there for many years.
- There are cryogenic storage regulations that exist already.
- Tanks are cheap due to the fact that the liquid air storage is at low pressure.
- The energy density of liquid air is four times the energy density of compressed air.

- Air is not toxic, and it does not explode.

- Liquid air is plentiful and cheap and safe energy vector to store such energy [103].

Most importantly, the low boiling temperatures of cryogenic fluids inspired researchers to investigate the use of cryogenic energy especially in cooling as well as in power generation.

2.4.2 Applications of cryogenic energy storage

Liquid nitrogen and liquid air have caught the attention of many researchers to use it in power generation, energy storage and also in domestic applications for cooling, primarily due to the low boiling points of cryogenic fluids. Due to the key benefit of using liquid nitrogen or liquid air as energy carriers, many researchers have still investigated the potential of using liquid nitrogen and liquid air energy to deliver power [104], [105] or cooling [106]–[108] or both [109]–[111] for domestic use.

The regasification process of LNG to recover the cold energy allows to generate power and cooling, although the plants that does this are only situated in certain places due to safety reasons, making it difficult for domestic application. Additionally, the gasification process generates 840 kJ/kg of low temperature energy [112], [113], allowing this cold energy to be used in applications like frozen food production, frozen food storage and to produce fresh water through freeze desalination [114]. The use of cryogenic energy for some important applications are discussed below.

Dearman engine technology

Dearman [115] developed an engine to be used in transport refrigeration vehicles, for power generation and cooling. Figure 2-16 explains how the Dearman engine works for cooling and power generation. Liquid air or liquid nitrogen is vaporised and expanded to drive a novel piston engine to generate power and produce clean cold [110].
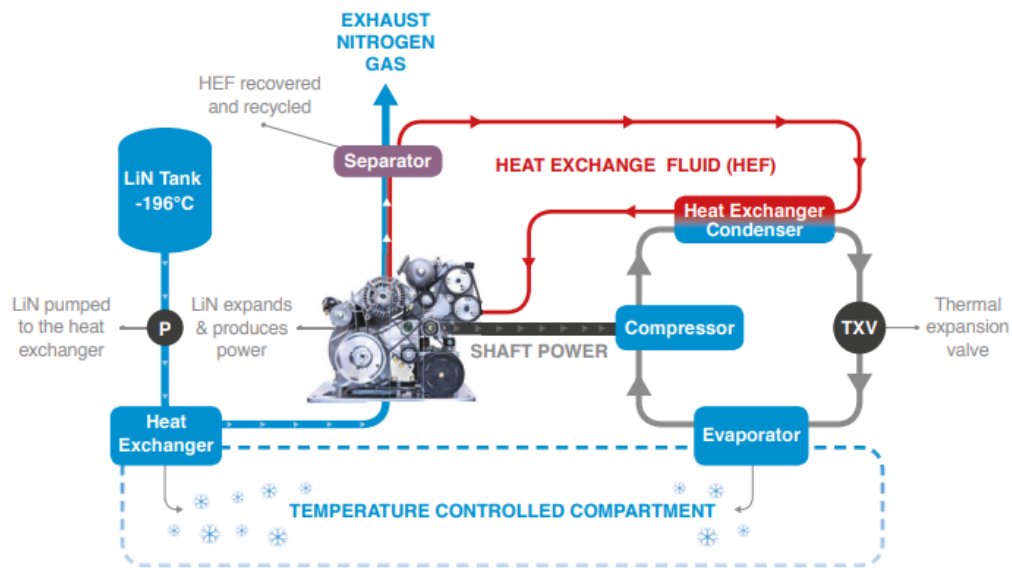
Figure 2-16: How the Dearman engine works in the transport refrigeration [115]

The Dearman engine works at near isothermal expansion where firstly, the LN_2 is entered into a heat exchanger providing cooling to the temperature controlled locations as shown in Figure 2-17. The Dearman engine is then used to expand the LN_2 by mixing it with heat exchanger fluid to improve the efficiency and power. A secondary refrigeration system is driven by the engine for further cooling. The heat exchanger fluid of glycol/water is recovered and recycled [115].
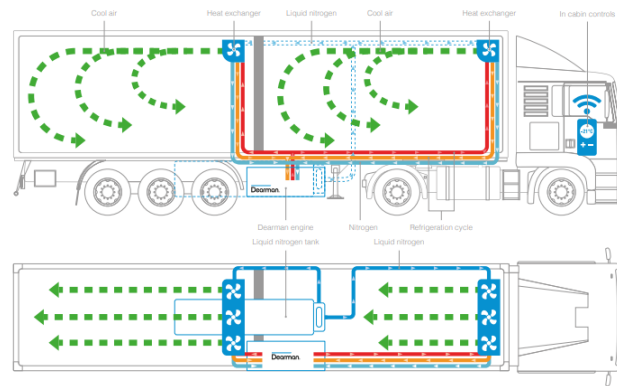
Figure 2-17: Dearman clean cold and power transport refrigeration unit [115]

The key benefits of this engine are; the zero local emissions, quiet, superior performance, cost comparable and 'easy and safe' operation. In comparison to commercially available battery systems, this system's capital cost is much lower. The total cost over 5 years is slightly higher of about 9% in comparison to diesel engines, however the CO_2 emissions and fuel consumption are 22% and 32% less, respectively [103], [110], [115].

Stirling engine

Wang et al. [109] numerically modelled a gamma type Stirling engine, cooled by the very low temperatures of LN_2. Figure 2-18 shows the engine mechanism where; the engine efficiency is enhanced due to the very low temperature of the cold side, as this ensures a larger hot-cold temperature difference [109], [116].
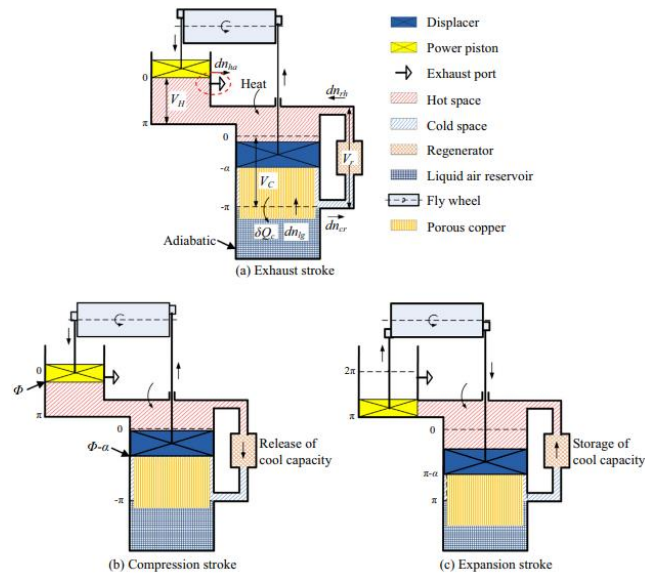
Figure 2-18: Open-closed hybrid cycle engine mechanism [109], [116]

Liquid nitrogen powered vehicle

A closed Brayton cycle with a liquid nitrogen power system is introduced by Ordonez [117]. A numerical model of combining an open LN_2 power cycle to drive a closed Brayton cycle was developed. The thermodynamic analysis proved that the closed Brayton cycle system could reach a specific energy which is 10 times larger than the 'CooLN$_2$Car' open cycle system introduced by Plummer et al. [118] and 4 times greater than the GM EV1 battery power system [117]. Liquid nitrogen was used to power a zero emission vehicle using the closed Brayton cycle cryogenic heat engine. It is expected to have a capital cost less than battery powered vehicles and a fuel cost not larger than gasoline fuelled vehicles [117].

Figure 2-19 shows the working mechanism of the LN_2 fuelled closed Brayton cycle cryogenic heat engine where it is divided into two parts '(a)' and '(b)' as shown in the schematic diagram.

1	LN$_2$ reducing the temperature of the working fluid, nitrogen gas, by heat exchange.
2	Compression.
3	Counter-flowing gas increasing the temperature by heat exchange.
4	Atmospheric air increasing the temperature by heat exchange.
5	Expansion.
6	Counter-flowing gas reducing the temperature by heat exchange.
(a)	Compression.
(b)	Atmospheric air increasing the temperature of the cold gas by heat exchange.
(c)	Release into atmosphere after expansion.

Figure 2-19: LN$_2$ fuelled closed Brayton cycle cryogenic heat engine (a) and an open cycle subsystem (b) [117]

The closed Brayton cycle includes; cooling, compression, heat recovery, heat input, expansion and precooling processes which are numbered from 1 to 6 as shown in

Figure 2-19. Evaporation, compression, heat input and expansion processes are identified by a, b and c of the LN$_2$ open cycle subsystem. The open cycle subsystem maintains the LN$_2$ pressure low at atmospheric pressure and the processes are explained in

Figure 2-19.

Other cryogenic applications

A food transport vehicle using cryogenic energy has been patented by Newman and McCormick [119]. This patent claims that liquid nitrogen and LNG fluids are both used to cool and power the food transport vehicle [119]. Garlov et al. [120] patented a food transport vehicle that sprayed LN$_2$ directly into the food space. This patent claims that when

the spraying of LN_2 is stopped, it passes through a heat exchanger to a space with ambient air, where the ambient air releases the nitrogen gas from the space allowing the space to be in a breathable atmosphere [120]. Directly releasing LN_2 from a high pressure vessel to a space for cooling was patented by Dakhil et al. [107]. This invention allows the release of liquid nitrogen into nitrogen gas which is mixed with warmer air to create a cool air mixture, which is then directed to the space to be cooled [107]. A cooled beverage dispenser using cryogenic energy was invented by Skobel et al. [106]. This patent claims that the liquid (slush) is rapidly cooled with a counter flowing flow of liquid nitrogen in a heat exchanger, where the liquid comes from a reservoir to a dispenser [106].

Chen et al. [104] conducted numerical analysis to compare the performance of two types of air fuelled engines for a typical small scale passenger car; compressed air and liquid air as shown in Figure 2-20. The comparison has been carried out in terms of output work, energy density, efficiency and cooling capacity. It was concluded that when the working temperature and pressure were increased, the shaft work output and the coolth of both fluids increased. However, it was stated that liquid air powered engines have lower specific work outputs in comparison to compressed air powered engines [104].
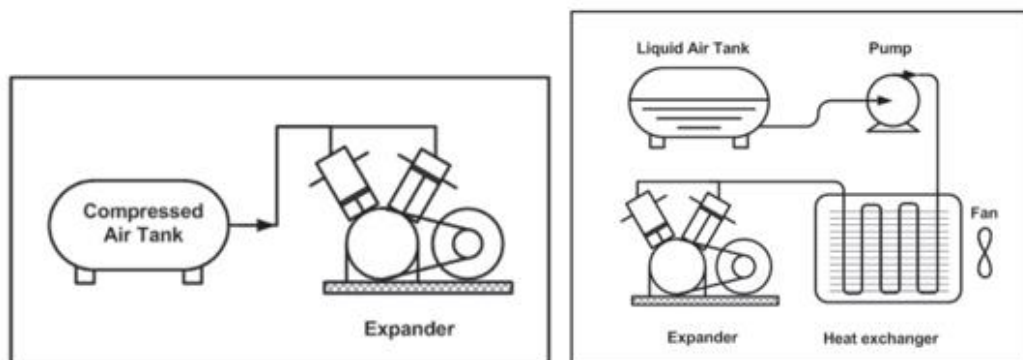
Figure 2-20: Engine systems schematic diagrams: compressed air engine (left), liquid air engine (right) [104]

Knowlen et al. [105] studied the use of liquid nitrogen to fuel a car engine where heat exchangers at ambient temperature were used to power the engine. The temperature at ambient was used to evaporate liquid nitrogen in a heat exchanger, before expanding it in an isothermal expander, which employs a secondary warming fluid that adds heat to the nitrogen throughout the expansion procedure to sustain a nearly constant temperature. It was concluded that the cryogenic propulsion system would deliver better automotive ranges and lesser operating costs in comparison to electric vehicles at present; if adequate heat input during the expansion process can be achieved [105]. Ordonez and Plummer [121] investigated the different cryogenic fluids such as neon, helium, air, nitrogen, etc. to generate power to drive a car and concluded that the high energy density of 0.75MJ/kg in LN_2 made it the most suitable [121]. It was also stated that for a LN_2 energy system, there are no risks of chemical explosions, by-products that are toxic or emissions of low-frequency electromagnetic field [121].

2.4.3 Applications of cryogenics for freeze desalination

There are many uses for cryogenic energy as explained above and desalinating sea water by freezing is one important process that can benefit from cryogenic energy storage. The vast amount of cold energy obtained from the regasification of liquid nitrogen/air allows freeze desalination techniques to be investigated [114].

Few researchers have investigated the use of cryogenic fluids for freeze desalination. Lin et al. [11] designed and manufactured a prototype of a freeze desalination system exploiting the cold energy from LNG as shown in Figure 2-21. It was concluded that due to this cold

energy being available at no cost, the freeze desalination process can become economical and environmentally friendly. 2kg of fresh water per kilogram of LNG was achieved but the salt removal rate was only 50%, which is quite low in comparison to certain desalination techniques such as multi-stage flash, reverse osmosis, adsorption, etc. as was shown in Figure 2-4.
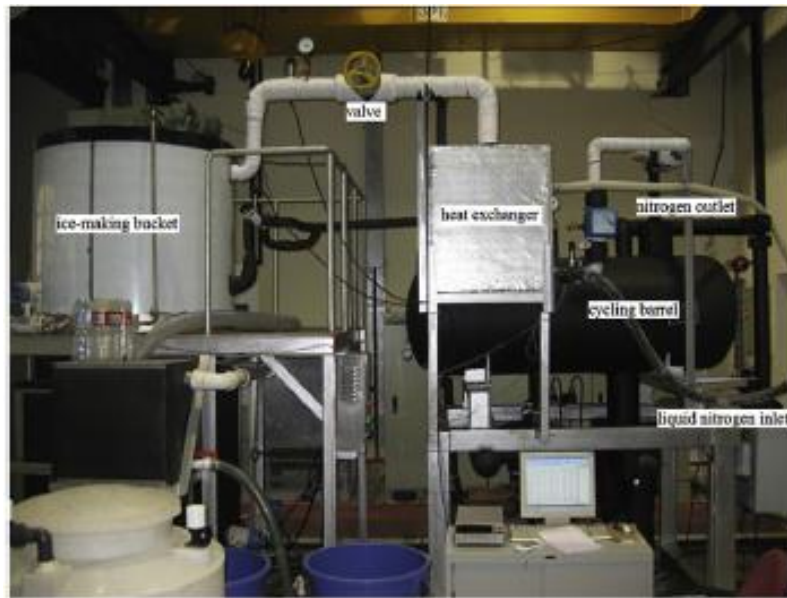
Figure 2-21: Freeze desalination prototype system developed by Lin et al. [11]

Wang et al. [89] designed and systematically investigated a hybrid freeze desalination system and concluded that the utilization of LNG cold energy could greatly reduce the total energy consumption. Cao et al. [35] designed and simulated on HYSYS software, freeze desalination using a flake ice maker using LNG cold energy. From the calculations, it was found that using 1kg of LNG, 2kg of fresh water was obtained.

Chang et al. [32] investigated and optimised the operating parameters of the indirect contact freeze desalination process using LNG by developing an indirect contact freeze

desalination unit as shown in Figure 2-22. In one hour, 520-525g of ice was obtained from a 1kg of feed in solution, thus giving a recovery rate of 26%; due to the fact that the volume of wash water required was improved to be 50% of the weight of raw ice. Hence, it was concluded that the process parameters optimised in the study can be directly used for the freeze desalination process of sea water.
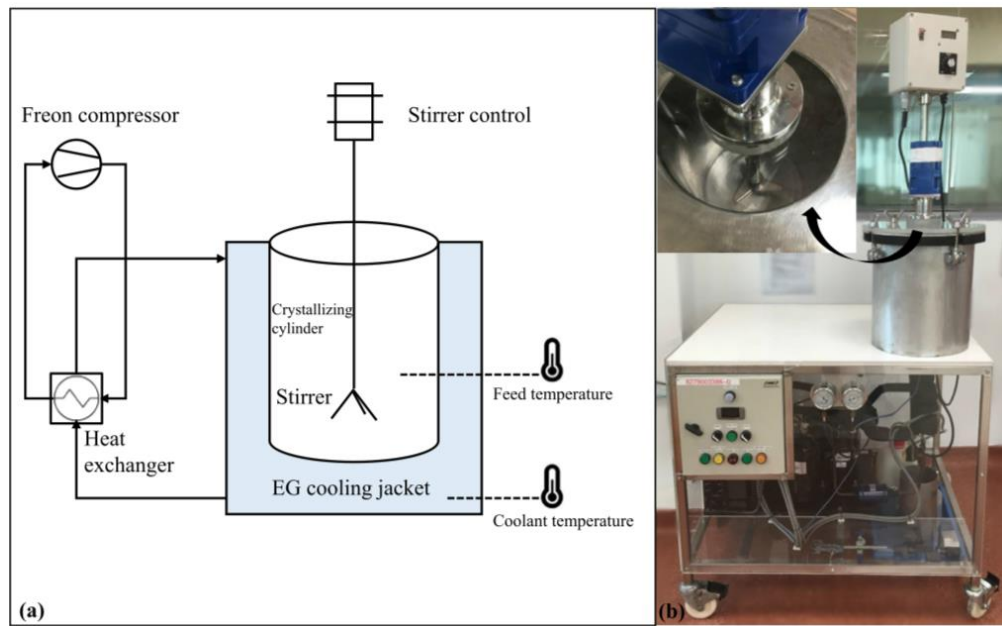
Figure 2-22: Indirect contact freeze desalination unit developed by Chang et al. [32]

Kalista et al. [40] and Williams et al. [45] also stated that the combination of freeze desalination process with regasification of liquified natural gas could solve the energy consumption issue, thus lowering its costs. Therefore, this shows great potential of using cryogenic energy for freeze desalination.

2.5 Numerical analysis (CFD) of freeze desalination

Literature on computational fluid dynamics to conduct freeze desalination is very limited. Research has been conducted numerically on the formation of ice on subcooled surfaces for the rate of ice growth and conditions for controlling [122], distribution of temperature [123], heat transfer coefficient [124], unsteady heat transfer [125], and ice growth kinetics for a continuous freezing process [126], [127]. Nevertheless, these studies did not examine the progression of salt separation and the rise of the salinity of the brine solution [7].

The separation of binary mixture freezing for salt water desalination was numerically studied by Abid et al. [128], nonetheless the effect of ice growth dynamics was not taken into consideration [7]. Abid et al. [128] used ANSYS Fluent [129] to demonstrate the freeze desalination process in a rectangular enclosure and conducted parametric study to observe the effect of altering the direction of freezing. The 35g/l initial salinity saltwater reduced to 7g/l, 1g/l and 0.5g/l when freezing was done from bottom, top and lateral sides respectively. Therefore, it was concluded that freezing from lateral sides was the best as it allowed to reduce the ice salinity the most. Jaouahdou et al. [130] numerically demonstrated the freeze desalination process using the CFD software ANSYS Fluent [129] where the freezing occurred around a cylindrical copper tube. It was concluded that by using a vertical tube enabled a faster and efficient freezing process in comparison to using a horizontal tube. Khadije et al. [87] also briefly conducted CFD analysis on freeze desalination and concluded that the use of CFD allows giving a clear understanding of the overall crystallisation of the freeze desalination process. The separation of salt from ice after the freezing process and the increase of the salinity in the remaining brine have not been investigated by any other researchers [7].

In theory, the freeze desalination process is predicted to produce ice crystals which are pure but the ice quality is affected by many aspects during the freezing process. It was suggested that the ions could be expelled into brine of slight quantities of moderately frozen or completely unfrozen. Occasionally, these ions do get trapped into the ice crystal, in qualitative concurrence with the low solubility of salts in ice [53]. Vrbka and Jungwirth [131] have studied molecular dynamics simulations of freezing an aqueous sodium chloride solution. Freezing has been studied at a molecular level and the rejection of brine from the salt solution of NaCl after freezing was witnessed. A PMEMD program based on the software package AMBER 7 was used to carry out the molecular dynamics simulations in terms of time evolution of density profiles and patterns of hydrogen bonding [7]. Additionally, Vrbka and Jungwirth [53] did further research of molecular dynamics (MD) simulations using the PMEMD program to understand the molecular mechanism of brine rejection. It was concluded that increasing the initial salt concentration, increased the time scales of the freezing process from approximately 250ns in pure water to more than 0.5µs for the most concentrated NaCl solution. It was also concluded that at higher initial salt water concentrations, NaCl ions can get trapped in the ice crystal due to the qualitative concurrence with the low solubility of salts in ice as shown in Figure 2-23.
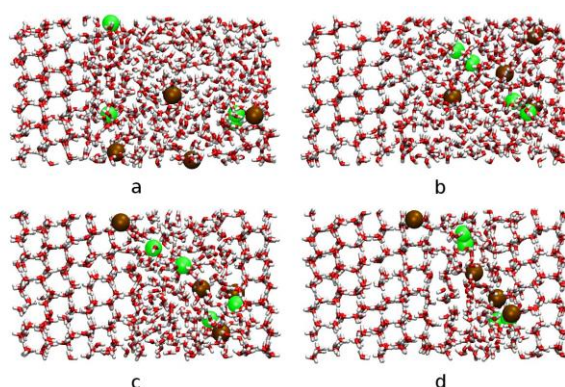
Figure 2-23: Freezing simulation results at (a) 1ns, (b) 200ns, (c) 400ns and (d) 600ns of the NaCl solution [53]

Cao et al. [35] conducted numerical analysis to simulate the freeze desalination process of a flake ice maker using the cold energy from LNG by using the software HYSYS. The freezing section's dynamic model was simulated by gPROMS software where the conservation laws of mass and heat were applied. It was concluded that the rate of ice growth reduced more quickly as the ice thickness increased. The numerical analysis showed that, 2 kg of fresh water was obtained by using 1kg of LNG. Interestingly, Srinophakun et al. [132] investigated freeze desalination using a horizontal hydroclone by CFD analysis. Thus, concluded that the horizontal hydroclone successfully separated ice from a brine slurry and the salt separation efficiency was enhanced by the increase of inlet velocity and by lowering the solid concentration. The high inlet velocity of the horizontal hydroclone created a higher centrifugal force thus increasing the separation rate.

In this thesis, the novelty of this research is the use of computational fluid dynamics to model the salt separation process for freeze desalination. The salt separation process during freeze desalination has not yet been simulated accurately using CFD. The separation of brine from the ice layer allowing the ice formed to be of pure water and the brine that is being rejected to the rest of the solution with high concentration which was missing in the literature, was also investigated in this thesis [7]. The use of cryogenic energy where the evaporation of liquid nitrogen to provide the cooling required for freeze desalination was also modelled using CFD.

2.6 Research motivation and contribution

Due to the increasing demand for fresh water, desalination of sea water is viewed as a potential solution to overcome potable water shortages; therefore, desalination technologies have been continuously developed. Currently, almost all desalination processes used are based on evaporative approaches where extensive thermal energy is used, leading to high fossil fuel consumption and CO_2 emissions. Freeze desalination has become an important process due to the lower energy consumption compared to other desalination processes; since the latent heat of freezing is low (333.5 kJ/kg) compared to the latent heat of evaporation (2256.7 kJ/kg) [12], [44], [45].

Computational fluid dynamics (CFD) is a powerful technique that permits to investigate thermodynamic processes, including freeze desalination. Literature on computational fluid dynamics studies for freeze desalination is very limited; therefore, the research conducted is primarily focused on developing CFD modelling of indirect contact freeze desalination. Hence, the novelty of this research is developing a three-dimensional computational fluid dynamics model (CFD) to simulate the salt separation process and the dynamics of ice layer growth to investigate the amount of ice (fresh water) generated and, salinity of the remaining brine at various operating conditions. The main knowledge gap of this research is the modelling of the salt separation process during freeze desalination. By conducting CFD modelling of the freeze desalination process, it helps to further understand the process and it also allows for optimization using advanced simulations. This will allow in creating an effective freeze desalination system with less energy consumption to produce more ice/pure water.

Initially, the salt separation process of freeze desalination by computational fluid dynamics (CFD) is carried out. The CFD model was then validated by carrying out experiments using a Peltier cooling device to conduct freezing. The effect of freezing temperature, salinity of salt water, direction of freezing has been investigated as a parametric study.

A commercially available ice maker machine has then been used to simulate the freeze desalination process to assess the feasibility of freeze desalination as a small scale portable desalination system that offers potential in domestic applications. CFD modelling using the ice maker geometry is then carried out and validated using experimental testing. Investigations of further freezing stages were conducted to obtain fresh water with salinities regarded as fresh and safe to drink by the WHO. Parametric analysis was then carried out on the geometry of the freezing tubes in the ice maker machine, on ice production.

Evaporation of liquid nitrogen has been utilized to assess the feasibility of using cryogenic energy for freeze desalination. CFD modelling of the evaporation of liquid nitrogen for freeze desalination was carried out. A test rig has been developed, where it has been used to validate the CFD model and to study the use of cryogenic energy for freeze desalination. Furthermore, altering the liquid nitrogen flow rate was investigated using CFD on ice production.

2.7 Summary

Freeze desalination is the process of separating water from salt by freezing salt water to obtain pure water. Ice crystals are created from pure water when salt water is frozen; pure water in the form of ice is separated from the brine. An in-depth literature review was conducted on freeze desalination and the significance of this process was thoroughly analyzed. The key steps of the freeze desalination process were thoroughly explained. The main stages involved in the freeze desalination process are, 'Ice crystallization' and 'Separation and Melting'. The first stage consists of the freezing of the salt water in order to form the ice crystals. In the latter stages, washing, cleaning and melting of the ice crystals follow, towards obtaining pure water. The main freeze desalination processes were explained whilst acknowledging the benefits and drawbacks of these processes explained and highlighted. In indirect freezing, less impurities gets trapped in the crystallization process, thus generating more pure ice in comparison to other freeze desalination techniques and also this type of freeze desalination technique is less complex to manufacture. Hence, indirect contact freeze desalination has been selected for the three different types of experiments discussed in this thesis in chapters 3, 4 and 5. Therefore, the indirect contact freeze desalination process has been discussed in 'Chapter 3 - Computational Fluid Dynamics Investigation on Indirect Contact Freeze Desalination', where CFD modelling has been carried out to simulate the freeze desalination process and validated using experimental testing. Literature conducted on freeze desalination using ice maker machines enabled to investigate this technique which has been discussed in 'Chapter 4 – Numerical Investigation of Indirect Freeze Desalination using an Ice Maker Machine', where CFD modelling and experimental testing has been conducted for a commercially

available ice maker machine to assess the feasibility of using an ice maker machine as a portable device in domestic applications.

Recently, liquid nitrogen and liquid air were identified as important energy carriers for cryogenic energy storage in renewable energy systems due to their high energy density and availability. Consequently, a thorough literature review was done on cryogenic energy storage and its applications. The use of cryogenic energy for freeze desalination showed potential due to the lower energy consumption. Hence, a literature review was carried out regarding the use of cryogenics for freeze desalination. The use of cryogenics for freeze desalination was investigated and discussed in 'Chapter 5 – Evaporation of Liquid Nitrogen for Freeze Desalination', where CFD modelling has been carried out of the evaporation of liquid nitrogen for the freeze desalination process. An experimental test-rig has been developed to validate the CFD model and to understand this process further.

CHAPTER 3

3. COMPUTATIONAL FLUID DYNAMICS INVESTIGATION OF INDIRECT CONTACT FREEZE DESALINATION

3.1 Introduction

This chapter is based on the published paper "Computational Fluid Dynamics Investigation on Indirect Contact Freeze Desalination" by Jayakody et al [12]. Contents such as texts, figures, graphs and tables are taken from the above mentioned paper [12].

Computational Fluid Dynamics is a powerful tool for simulation of various complex fluid dynamic phenomena. Literature on CFD simulation of freeze desalination is very limited and the salt separation process during freeze desalination has not yet been simulated using CFD [12]. Therefore, in this research work, CFD modelling of the freeze desalination process which allows the salt separation was developed.

Various researchers have experimentally and numerically investigated the formation of ice on subcooled surfaces in terms of ice growth rate and conditions for controlling [122], temperature distribution [123], heat transfer coefficient [124], unsteady heat transfer [125], and ice growth kinetics for a continuous freezing process [126], [127]. However, these research work did not investigate the salt separation process and increasing the salinity of the aqueous solution. Abid et al. [128] numerically studied the separation of binary mixture

freezing for seawater desalination application, but did not include the effect of ice growth dynamics on the cooling surface [12]. Moreover, Vrbka and Jungwirth [131] have studied molecular dynamics simulations of freezing an aqueous sodium chloride solution. Freezing has been studied at a molecular level and the rejection of brine from the salt solution of NaCl after freezing was observed. A PMEMD program based on the software package AMBER 7 was used to carry out the molecular dynamics simulations in terms of time evolution of density profiles and patterns of hydrogen bonding.

In this chapter, a 3D CFD model is developed to simulate the salt separation process and the dynamics of ice layer growth to investigate the amount of ice (fresh water) generated and salinity of the remaining brine at various operating conditions. ANSYS Fluent software was used to develop a 3D CFD model of the freeze desalination process using species transport, solidification/melting and energy modules. Furthermore, a representative prototype was developed and experimental testing was carried out to validate the CFD model. The validated CFD model has been used to conduct parametric analysis to predict the effects of freezing temperature, solution salinity and the direction of freezing; on the freezing time, ice production and its salinity. [12]

3.2 CFD theory of the freeze desalination process

Firstly, the theoretical background of the CFD simulation of the freeze desalination process is discussed in this chapter. In order to simulate the freeze desalination process, energy (heat transfer), species transport and solidification/melting modules were utilised. Modules of solidification/melting and species transport were used to allow the pure water (as ice)

separation from the rejected brine solution [12]. The solidification process has been modelled using an enthalpy – porosity technique in ANSYS Fluent where a porous zone is incorporated at the liquid-solid mushy zone, using liquid fraction corresponding to the porosity value [133]–[135]. Therefore, in the model, a measure called the liquid fraction indicating the cell volume fraction, which is in liquid form, is linked with every cell in the domain individually. Based on the enthalpy balance, at each iteration the liquid fraction is computed. The liquid fraction lies between zero and one in a region called the mushy zone. This zone is modelled as a "pseudo" porous medium where, as the material solidifies, a reduction of porosity from one to zero is reached. The porosity becomes zero when the material is fully solidified in a cell and thus the velocities also drops to zero [136]. A pressure drop occurs when the water freezes and in order to predict this pressure drop, momentum sink terms are incorporated in the momentum equation [136].

The energy equation for solidification problems with the inclusion of species transport is written as [12]:

$$\frac{d}{dt}(\rho H) + \nabla \cdot (\rho \vec{v} H) = \nabla \cdot (k\nabla T) + \frac{(1-\beta)^2}{(\beta^2+\varepsilon)} A_{mush}\vec{v} \qquad \text{3-1}$$

where, T is the temperature, k is the mass transfer coefficient, H is the enthalpy and $\vec{v}$ is the velocity. The term $\frac{d}{dt}(\rho H)$, represents the energy stored and the body forces. $\nabla \cdot (\rho \vec{v} H)$, term represent the surface forces and $\nabla \cdot (k\nabla T)$ is the heat flux term. The term $\frac{(1-\beta)^2}{(\beta^2+\varepsilon)} A_{mush}\vec{v}$, represents the momentum sink term added to the equation to represent the porosity in the mushy zone where β, is the liquid volume fraction. A_{mush}, is the mushy zone constant and ε is a small number (0.001) given to prevent it being divided by zero when $\beta = 0$ [12].

The material's enthalpy is calculated from equation (3-2):

$$H = h + \Delta H \qquad\qquad 3\text{-}2$$

where ΔH is the latent heat of solidification and h is the sensible enthalpy calculated by equation (3-3):

$$h = h_{ref} + \int_{T_{ref}}^{T} C_p dT \qquad\qquad 3\text{-}3$$

where, h_{ref} and T_{ref} are the reference enthalpy and reference temperature respectively. C_p is the specific heat at constant pressure.

The liquid fraction, β is determined as [7]:

$$\beta = \frac{T - T_{solidus}}{T_{liquidus} - T_{solidus}}, \text{ when } T_{solidus} < T < T_{liquidus} \qquad\qquad 3\text{-}4$$

$\beta = 0$, when $T < T_{solidus}$

$\beta = 1$, when $T > T_{liquidus}$

The latent heat content is shown in terms of the latent heat of the material and the liquid volume fraction β, in equation (3-5).

$$\Delta H = \beta L \qquad\qquad 3\text{-}5$$

With values of β ranging from 0 to 1, this latent heat content can differ from 0 (solid) to L (liquid). Iteration between the energy equation (3-1) and liquid fraction equation (3-4) will provide a solution for the temperature. However, a poor convergence of the energy equation is seen when equation (3-4) is used directly to update the liquid fraction [137]. Hence, to update the liquid fraction, the method recommended by Swaminathan and Voller [137] is used as discussed below. [7]

In order to understand the species equations for solidification and melting of a pure substance, the temperatures T_{melt}, $T_{liquidus}$ and $T_{solidus}$ are studied. T_{melt} is the apparent

melting temperature where phase change arises for solidification of a pure substance. A mushy freeze/melt region happens amongst a higher liquidus ($T_{liquidus}$) temperature and a lower solidus temperature ($T_{solidus}$) for a multicomponent mixture [135]. The solidification effect of a multicomponent liquid allows the solutes to diffuse from solid phase to liquid phase. [7], [123]

$$T_{solidus} = T_{melt} + \Sigma_{solutes} \, m_i Y_i / K_i \tag{3-6}$$

$$T_{liquidus} = T_{melt} + \Sigma_{solutes} \, m_i Y_i \tag{3-7}$$

Y_i is the mass fraction of the solute and the slope of the liquidus surface is m_i with respect to Y_i. The partition coefficient of solute i is K_i. It is vital to consider when calculating the solidus and liquidus temperatures; if the value of the mass fraction Y_i surpasses the eutectic mass fraction $Y_{i,Eut}$, then the mass fraction Y_i is replaced by $Y_{i,Eut}$. An assumption has been made that, the last species material of the mixture is taken as the solvent and the solutes are the other species in the mixture. The solid ice formed is of pure water during freezing, without any salt content. Hence for species segregation, the 'scheil' rule has been sourced at the micro-scale due to the fact that it assumes no diffusion of solute species in the solid. [7], [138] Thus, when using the Scheil rule, the species transport equation (3-8) is given as [7]:

$$\frac{d}{dt}\left(\rho Y_{i,liq}\right) + \nabla \cdot \left(\rho\left[\beta \overrightarrow{v_{liq}} Y_{i,liq} + (1-\beta) Y_{i,sol}\right]\right) = \nabla \cdot \left(\rho \beta D_{i,m,liq} \nabla Y_{i,liq}\right) -$$

$$K_i Y_{i,liq} \frac{d}{dt}\left(\rho(1-\beta)\right) + \frac{d}{dt}\left(\rho(1-\beta) Y_{i,liq}\right) \tag{3-8}$$

Mass fractions of liquid $Y_{i,liq}$ and solid $Y_{i,sol}$ are related using K_i, the partition coefficient as [7],

$$Y_{i,sol} = K_i Y_{i,liq} \tag{3-9}$$

Consequently, it is seen that, $Y_{i,liq}$ is solved as the dependant variable in ANSYS Fluent when the scheil rule is utilized. Furthermore, the liquid velocity is denoted as $\overrightarrow{v_{liq}}$ in the mixture and $D_{i,m}$ for species, is the mass diffusion coefficient. [7] For the Scheil rule, T^*, the temperature at the interface is calculated as shown in equation (3-10) [7]:

$$T^* = T_{melt} + \sum_{i=0}^{N_S-1} m_i Y_i \beta^{K_i-1} \qquad \text{3-10}$$

where, N_s denotes the number of species.

As density varies with temperature and species composition, buoyancies tend to occur when there is more than one species in the mixture. Thermal buoyancy occurs due to the variations in density with temperature and is calculated using natural convection flows. On the other hand, solutal buoyancy occurs when density varies with species composition. Hence, solutal buoyancy body forces are calculated using equation (3-11). [12]

$$\vec{F}_s = \rho_{ref}\vec{g} \sum_{i=0}^{N_S} \beta_{s,i}(Y_{l,i} - Y_{ref,i}) \qquad \text{3-11}$$

where, ρ_{ref} is the reference density and $\vec{g}$ is the gravity. The solutal expansion coefficient is $\beta_{s,i}$ and the total number of solute species is N_s. $Y_{l,i}$ and $Y_{ref,i}$ are the mass fraction of the liquid phase and the reference mass fraction respectively. Thermal and solutal buoyancy together is the total body force. The overall solidification behaviour of salt water can be correctly predicted by modelling the thermal and solutal buoyancies. Hence, the Boussinesq approach has been used to model the buoyancy induced flows in solidification problems with multi-components such as freezing of salt water. [12]

The conservation equation of mass and momentum are used to solve for chemical species and the local mass fraction of each species by ANSYS Fluent. This is done by solving a convection-diffusion as shown in equation (3-12). [12]

$$\frac{d}{dt}(\rho Y_i) + \nabla \cdot (\rho \vec{v} Y_i) = -\nabla \cdot \vec{J_i} \qquad\qquad 3\text{-}12$$

where, $\vec{J_i}$ is the diffusion flux of the species, this occurs as the concentration and temperature gradients change. In this domain, the momentum equation (3-13) is solved between the phases and the subsequent velocity is shared [12]:

$$\frac{d}{dt}(\rho \vec{v}) + \nabla \cdot (\rho \vec{v} \vec{v}) = -\nabla p + \mu \nabla^2 \vec{v} + \rho \vec{g} \qquad\qquad 3\text{-}13$$

where, μ is the viscosity of the fluid, p is the pressure and the momentum equation is reliant on the volume fractions of all phases [12].

3.3 CFD modelling

A 3D CFD model has been developed using ANSYS Fluent version 16.2 [129] to understand the freeze desalination process. An investigation was conducted on the separation of brine from the ice layer allowing the ice formed to be of pure water and the brine that is being rejected to the rest of the solution with high concentration. The CFD modelling includes a number of main steps namely; geometry generation, meshing, model setup and solution. The model set-up involves creating the materials, setting the boundary conditions and modelling physics. The solution process is then carried out where the results are obtained and analysed in the post processing step. A summary of the full CFD simulation procedure is shown in Figure 3-1 and the steps are described in detail in the following sections.
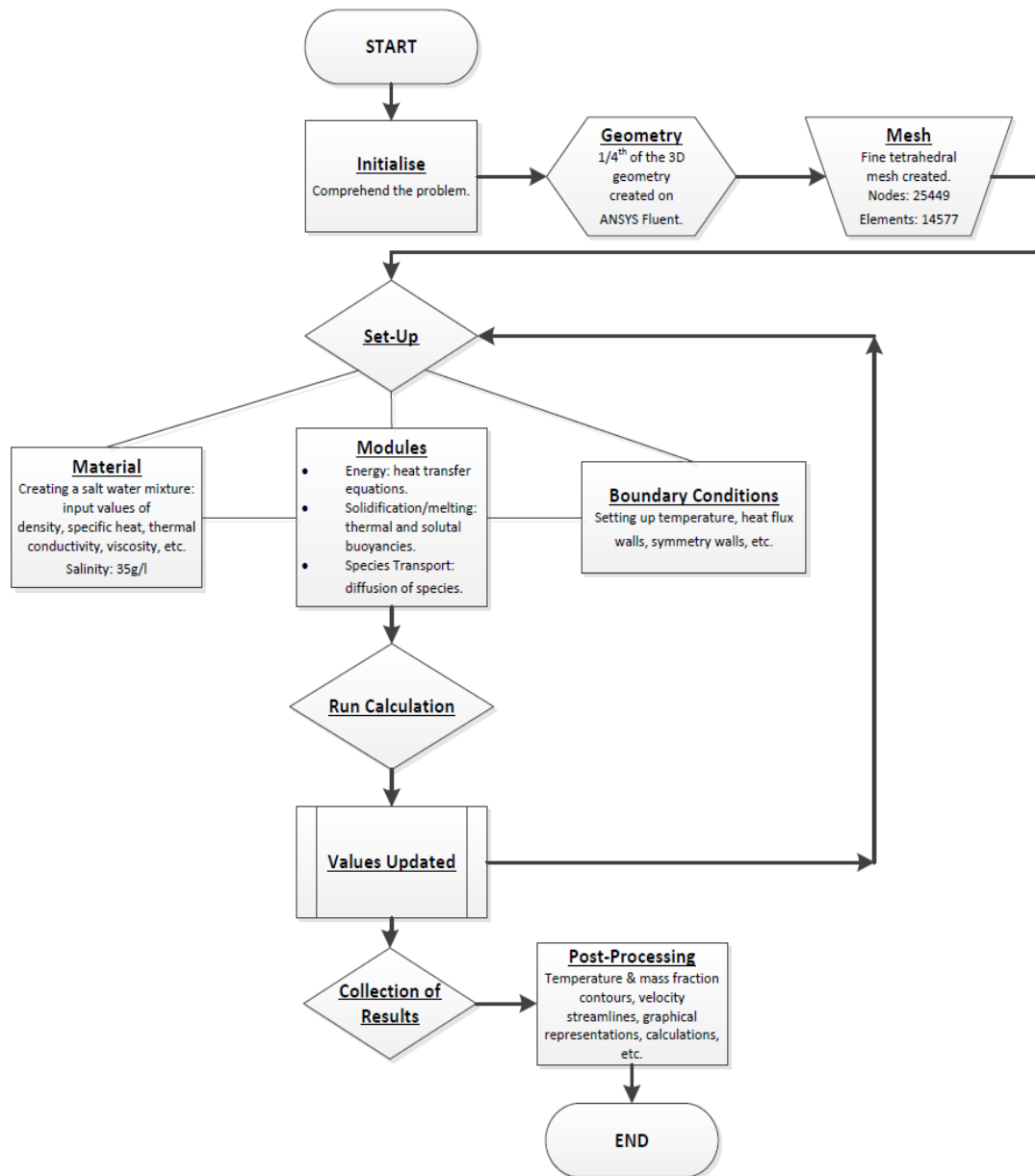
Figure 3-1: CFD process flow chart [12]

3.3.1 Geometry generation

The geometry has been created using ANSYS geometry modeller to represent a stainless steel frustum shaped container of 36mm top diameter, 20mm bottom diameter and 42mm height which was used in the experimental testing. Using symmetry, a quarter of the 3D frustum geometry was used in the modelling to reduce the simulation time.

57

3.3.2 Mesh

A fine tetrahedral mesh has been created using 'ANSYS Meshing', where edge sizing feature has been used at appropriate locations to ensure accurate results. Mesh independency study has been investigated by using edge sizing to give coarser and finer meshes to select the appropriate mesh as shown in Table 3-1. The time-step size was kept constant at 0.001s in the mesh independency study. The predicted ice salinity has been compared to those obtained from experimental testing to select the appropriate mesh that produces results comparable to the experimental results. Increasing the mesh density would increase the computational time but produce more accurate results. Therefore, the mesh has been selected accordingly and is shown in Figure 3-2. It consists of 25449 nodes and 14577 elements [12].

Table 3-1: Mesh Independency [7]

Mesh Type	Nodes	Elements	Salinity-Experimental (%)	Salinity-CFD (%)	Percentage of Error (%)
Coarse	15202	3363	1.4	1.61	13.04
Selected Mesh	25449	14577	1.4	1.43	2.10
Fine	47324	10846	1.4	1.42	1.41
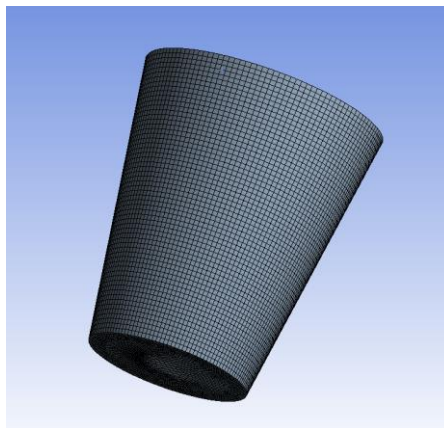
Figure 3-2: Tetrahedral mesh used for the frustum shaped container

3.3.3 Model set-up

The selected mesh was then imported into 'ANSYS Fluent Setup' to set the boundary conditions, solution methods, materials, modules/equations, discretization settings, etc. Laminar incompressible flow conditions, pressure based solver, solidification/melting and species transport modules were used to simulate the physics of the freeze desalination process. The residuals used for continuity, velocity and saltwater mass fraction were $1x10^{-9}$ and for energy was $1x10^{-11}$. Transient analysis was carried out for 30 minutes of real time. In order to obtain the most accurate results in less computational time, a suitable time step was selected by conducting time step size independency tests as shown in Table 3-2. Increasing the time step size, decreased the computational time; however, decreasing the time step size, improved the results' accuracy and avoided many errors in the ANSYS Fluent software. Table 3-2 showed that the time step size of 0.001 can be used to obtain accurate results. [12] This was the optimum time step size that could be used; where increasing this time step size produced less accurate results and produced many errors such as 'floating point exception' to appear in the 'ANSYS Fluent Solution', resulting in the system crashing, while decreasing this time step produced longer computational time.

Table 3-2: Time-step size independency [7]

Time-step size (s)	Salinity-Experimental (%)	Salinity-CFD (%)	Percentage of Error (%)
0.01	1.4	System-error	-
0.001	1.4	1.43	2.10
0.0001	1.4	1.41	0.71

The three major modules used in the simulation were; energy (heat transfer), species transport and solidification/melting and the combination of species transport with the

solidification/melting module will allow the separation of pure water (in the form of ice) and the brine as the rejected solution. ANSYS Fluent uses an enthalpy-porosity technique to model the solidification process, where a porous zone is included at the liquid-solid mushy zone, using liquid fraction equivalent to the porosity value. As the water freezes and solidifies a pressure drop takes place, and to predict this pressure drop, momentum sink terms are included in the momentum equation. [12], [136] The modules used and the CFD modelling process is summarised in Table 3-3.

Table 3-3: Summary of the physics used in the ANSYS Fluent set-up [12]

Modules	Key Factors and Equations
Energy	• Main equations used: 1. $\frac{d}{dt}(\rho H) + \nabla \cdot (\rho \vec{v} H) = \nabla \cdot (k \nabla T) + \frac{(1-\beta)^2}{(\beta^2+\varepsilon)} A_{mush} \vec{v}$
Species Transport	• Mixture created with salt water and pure water for different concentration levels of 25g/L, 35g/L, 45g/L and 55g/L. • Diffusion energy source selected. • Main equations used: 1. $T_{solidus} = T_{melt} + \sum_{solutes} m_i Y_i / K_i$ 2. $T_{liquidus} = T_{melt} + \sum_{solutes} m_i Y_i$
Solidification/Melting	• 'Scheil' rule has been selected. • Thermal and Solutal buoyancies have been activated. • Main equations used: 1. $T^* = T_{melt} + \sum_{i=0}^{N_s-1} m_i Y_i \beta^{K_i-1}$ 2. $\frac{d}{dt}(\rho Y_{i,liq}) + \nabla \cdot (\rho[\beta \overrightarrow{v_{liq}} Y_{i,liq} + (1-\beta)Y_{i,sol}]) = \nabla \cdot (\rho \beta D_{i,m,liq} \nabla Y_{i,liq}) - K_i Y_{i,liq} \frac{d}{dt}(\rho(1-\beta)) + \frac{d}{dt}(\rho(1-\beta)Y_{i,liq})$ 3. $\vec{F_s} = \rho_{ref} \vec{g} \sum_{i=0}^{N_s} \beta_{s,i}(Y_{l,i} - Y_{ref,i})$

Mass fraction is integrated into the model when the modules 'Species Transport' and 'Solidification/Melting' are both used. This enables to create a mixture of two species, in

this case 'Pure water' and 'Salt water' with different concentrations resulting in a salt water mixture of known concentration. The different salt water concentrations are created by editing the properties of water in the ANSYS fluent material setup, where the density, specific heat, thermal conductivity, viscosity, etc. are written as a piecewise-linear function of temperature and concentration as shown in Table 3-4. Consequently, this mixture is then separated with pure water as ice and salt water as the remaining brine after the freezing process. [12]

Table 3-4: Creating the salt water mixture in the ANSYS Fluent material set-up [12]

Mixture of Salt Water and Pure Water			
Salt Water Properties		**Pure Water Properties**	
Density (kg/m³)	Piecewise-linear function	*Density (kg/m³)*	Piecewise-linear function
Cp Specific Heat (J/kg.K)	Piecewise-linear function	*Cp Specific Heat (J/kg.K)*	Piecewise-linear function
Thermal Conductivity (W/m.K)	Piecewise-linear function	*Thermal Conductivity (W/m.K)*	Piecewise-linear function
Viscosity (kg/m.s)	Piecewise-linear function	*Viscosity (kg/m.s)*	Piecewise-linear function
Molecular Weight (kg/kgmol)	18.63 (constant)	*Molecular Weight (kg/kgmol)*	18.02 (constant)

Figure 3-3 shows the boundary conditions used in modelling sea water in a container at a fixed initial temperature of 298K and 35g/L of initial salt water concentration. The container is made of stainless steel with thermally insulated walls but being cooled at the base to maintain a constant temperature of 260K. A top lid was also used to ensure thermal insulation from the top. [12]
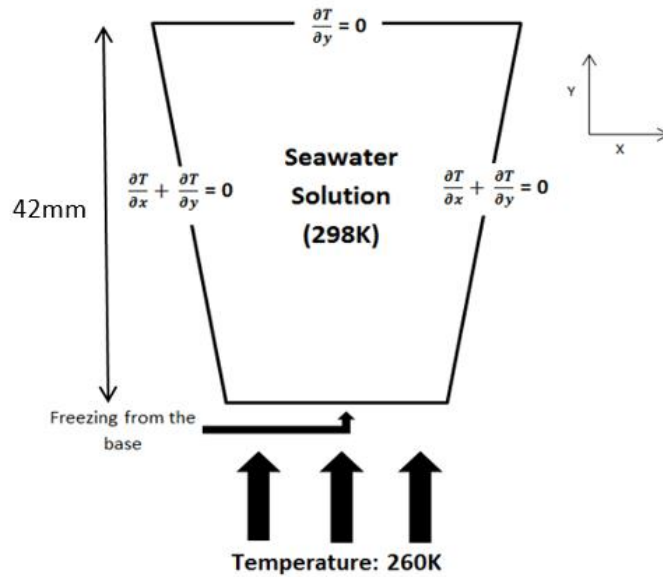
Figure 3-3: Schematic diagram of the problem [12]

3.4 CFD results

Figure 3-4(a) displays the temperature contours in the container, with 260K next to the base signifying the direction of freezing. Figure 3-4(b) shows the temperature distribution with distance from the container base at mid-section for the 42mm distance shown in Figure 3-3 after 30 minutes of freezing. It is clear from Figure 3-4(a) and (b) that a solid ice layer of 4mm thickness is formed at the base and the ice temperature is varying from 260K at the lower edge of the ice layer to 270K at the top edge. Figure 3-4(b) also indicates that the ice temperature is increasing from the lower edge of the ice layer (in contact with the freezing surface); to the top edge of the ice layer (in contact with brine solution) and then remains constant throughout the brine solution. [12]

62
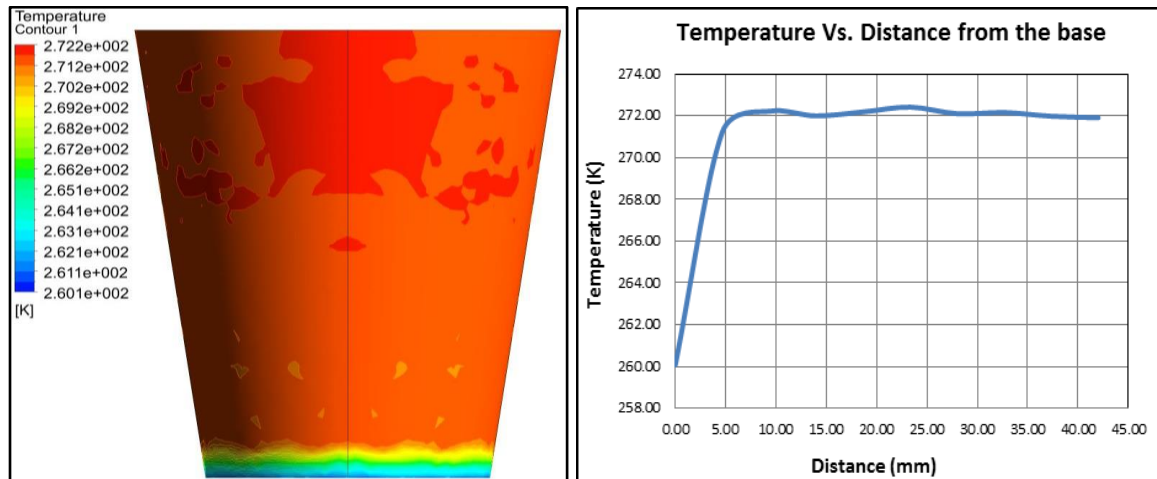
Figure 3-4: (a) Temperature contours (left) and (b) temperature vs. distance from the base (right) after 30 minutes of real time freezing [12]

Figure 3-5(a) displays the solidification of the solution in terms of the liquid phase mass fraction. Mass fraction contours refer to the mass fraction of solidification where the blue region represents the ice formed, the red/orange region representing the remaining brine and the intermediate colours representing the solid/liquid mushy region. In Figure 3-5(a), the blue thick layer indicates minimum liquid fraction, which is the solid ice and the rest of the solution in red/yellow indicates high amount of liquid fraction, which is the brine solution. Figure 3-5(b) shows the liquid fraction distribution with distance from the container base at mid-section. It is evident from this figure that through the 4mm thickness of ice, the liquid fraction changes from 0 to 0.2. [12]
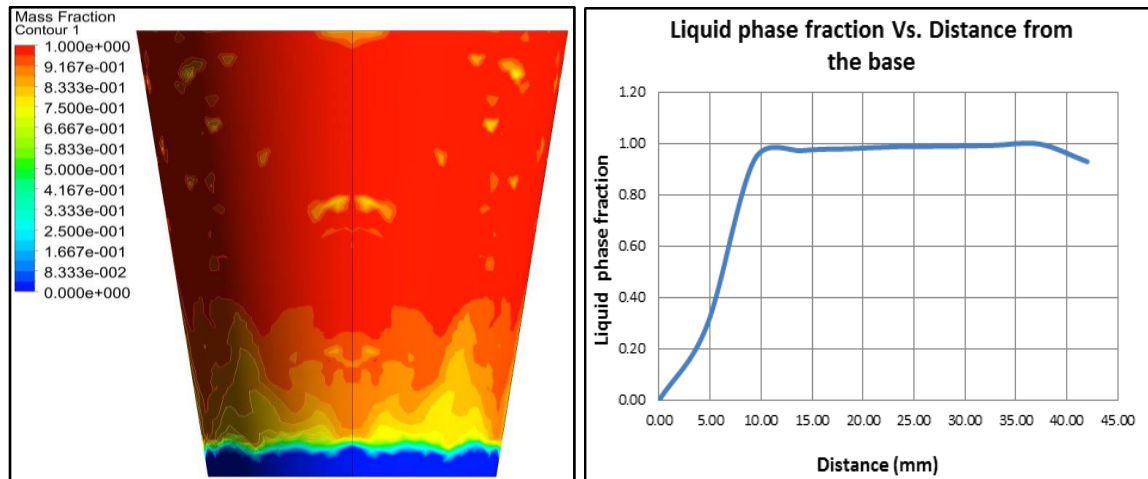
Figure 3-5: (a) Liquid phase fraction contours (left) and (b) liquid phase fraction vs. distance from the base (right) after 30 minutes of real time freezing [12]

Figure 3-6(a) shows the salt water contours in the container after 30 minutes of freezing, while Figure 3-6(b) displays the salt water concentration with distance from the container base at mid-section. It is clear from this figure that at the top edge of the ice layer (4mm) the concentration is 1.2%. However, as the distance from the ice top edge increases, the brine concentration increases to reach maximum of about 5.8%. Thermal and solutal buoyancies cause the variations in the brine concentration as shown in the figure for the rest of the solution. [12]
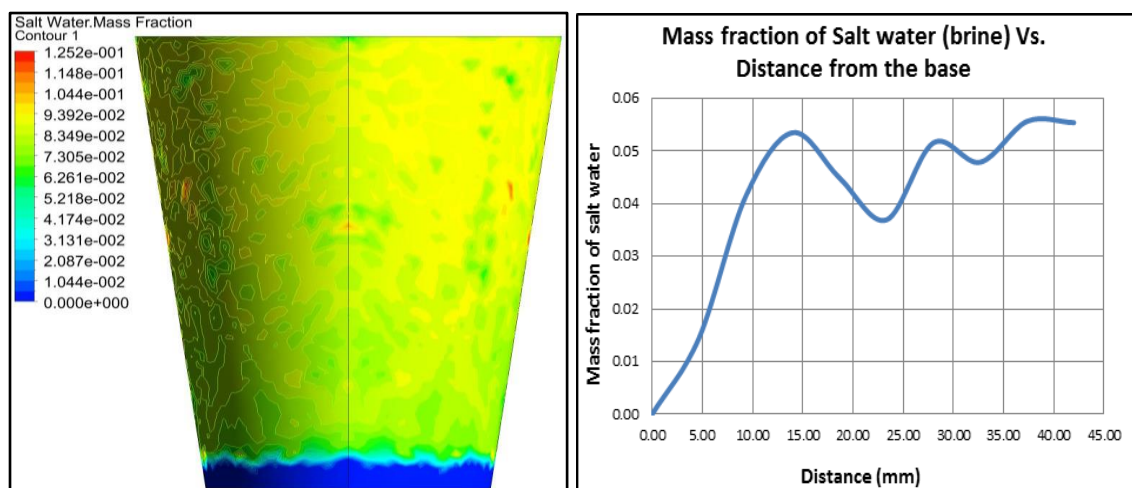
Figure 3-6: (a) Salt water mass fraction contours (left) and (b) salt water mass fraction vs. distance from the base (right) after 30 minutes of real time freezing [12]

Figure 3-7(a) exhibits the pure water contours in the container after 30 minutes of freezing, while Figure 3-7(b) displays the mass fraction of pure water with distance from the container base at mid-section. It is apparent from this figure that close to the container base where ice is formed, maximum concentration of pure water exists. Above the ice layer of 4mm thickness, pure water mass fraction decreased to reach a value of 0.946 at height of 13mm and remain at an average value of 0.95. Again, the variations in the mass fraction of pure water for the rest of the solution, displayed in the figure, are caused due to buoyancies. [12]
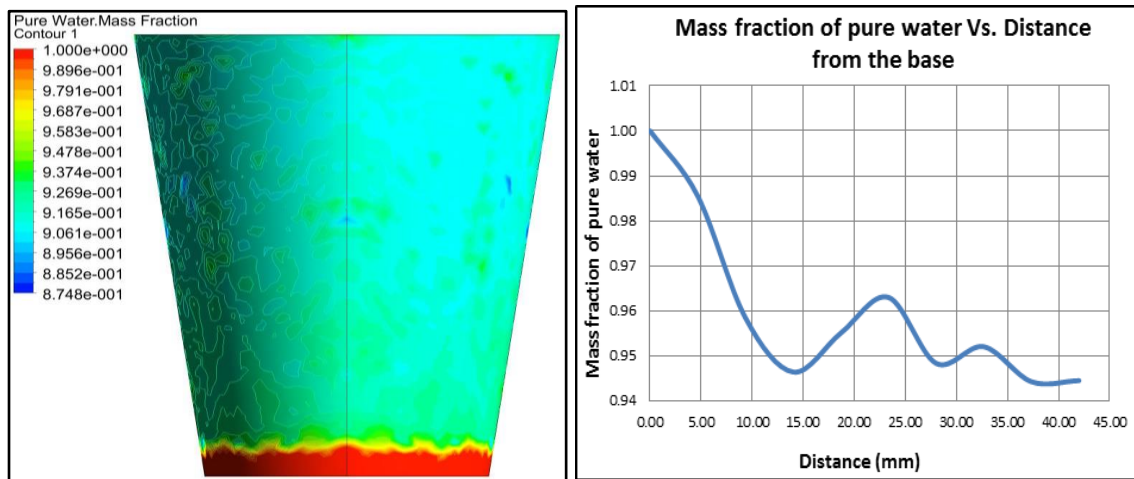
Figure 3-7: (a) Pure water mass fraction contours (left) and (b) pure water mass fraction vs. distance from the base (right) after 30 minutes of real time freezing [12]

Figure 3-8 shows the average temperature, liquid phase fraction and mass fraction variations of ice and brine with time. The gradual decrease in temperature is shown in Figure 3-8(a) as the solution freezes. Figure 3-8(b) shows the average solution liquid phase fraction decreasing with time; it starts at 1 as full liquid state and then slowly reduces as the solution freezes. Figure 3-8(c) shows the mass fraction of the remaining brine increasing from 35g/L to about 65g/L. This is due to the fact that as the pure water freezes to form ice, the concentration of the remaining brine solution increases. Figure 3-8(d) shows the decrease in the average mass fraction of pure water as the freezing process progresses. [12]
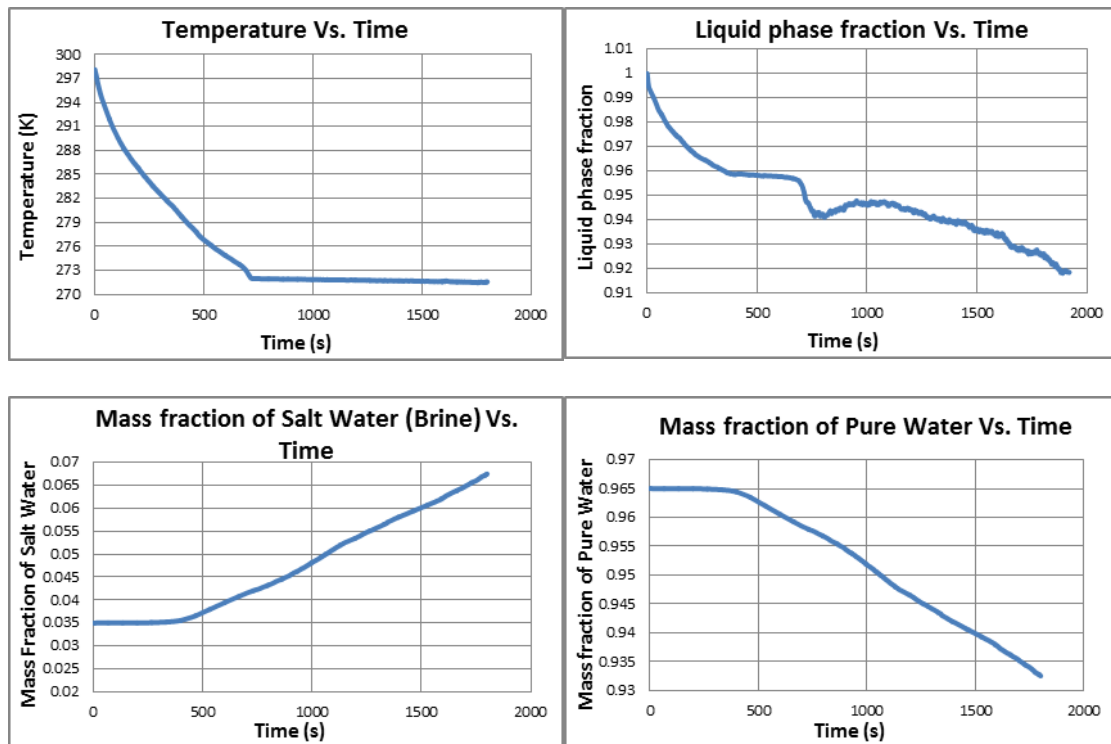
Figure 3-8: Variation with time for average (a) temperature (top left), (b) liquid phase fraction (top right), (c) mass fraction of salt water (bottom left) and (d) mass fraction of pure water (bottom right) [12]

3.5 Experimental test facility

A test facility was developed to understand the freeze desalination process and also to validate the CFD model. A small stainless steel cup has been used as a container to undertake the freezing process, where a 55x55mm Peltier cooling device was used to freeze the bottom of the container. Thermocouples have been placed at different locations such as; the surface of the cup, surface of the Peltier cooling device and where the ice is forming. The ice formation is investigated; where the volume of ice formed and the ice and brine salinities were also measured.

3.5.1 Layout of the test facility

Figure 3-9 shows a schematic diagram of the experimental facility consisting of a stainless steel cup, a Peltier device, a heat sink and a cooling fan, thermocouples, a power supply, a data logger and a computer. The stainless steel cup is a conical frustum shaped cup with a base diameter of 20mm, a top diameter of 36mm and a height of 42mm. It was used to contain the saline water and was cooled from the base using a 55x55mm Peltier device producing a maximum cooling capacity of 128.7W. The Peltier device was connected to a high performance combined heat sink and fan assembly with a maximum cooling capacity of 250W. Thermal paste was used to ensure good contact between the Peltier device and the heat sink as well as the container base. Thermocouples were used to measure the temperature at the cold side of the Peltier cooling device and at various locations inside the stainless steel container. The temperature values were continuously recorded using a data logger and a personal computer [12]. An insulation material was used to cover the sides and the top of the container as shown in Figure 3-9. The thermal conductivity of the used insulating material is 0.034 W/m.K. During testing, the cold side temperature of the Peltier device was controlled to stay at 260K with a variation of less than ± 3K. [12]
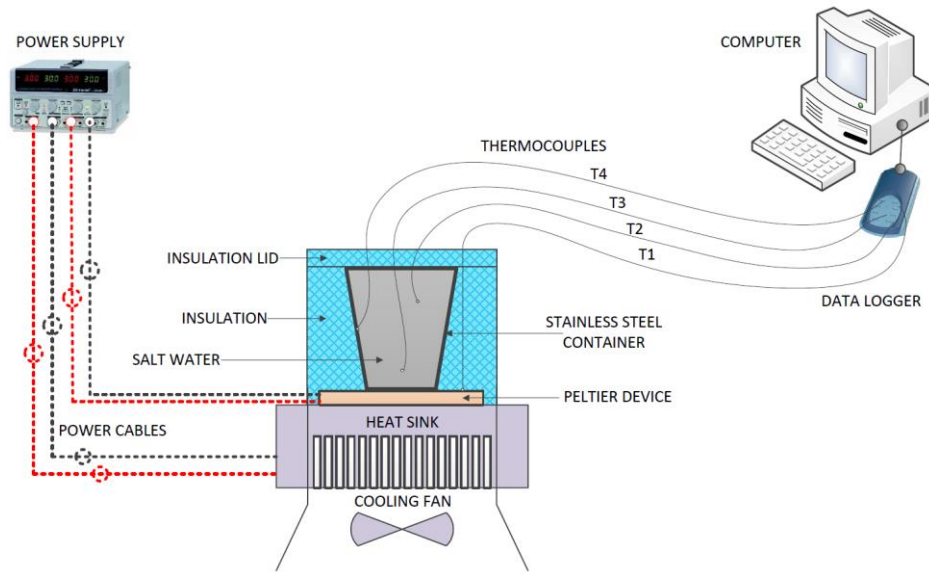
Figure 3-9: Schematic diagram of the experiment [12]

3.5.2 Measuring devices and calibration

A salinity meter and thermocouples were used in this experimental work as the measuring devices to measure salinity of saline water and reject brine, and temperatures at various positions.

Thermocouples

Four thermocouples were used to measure the temperature at different locations in this experiment. One thermocouple was used to measure the temperature at the (cold) surface of the Peltier device where the sensor tip of this thermocouple was pasted onto the Peltier device's cold surface using aluminium tape in order to allow effective contact. Another thermocouple was used to measure the temperature at the surface of the stainless steel container, while two other thermocouples were used to measure the temperature at two different locations inside the stainless steel cup to measure the salt water temperature and the temperature of the ice forming. These were all type-K thermocouples which can

measure temperatures as low as 73.15K. The thermocouples were passed through holes made in the insulation material and connected to a 'TC-08 PICO' data logger which was connected to a computer in order to monitor and record the temperature measurements during the experiment.

Thermocouples calibration

Calibrating thermocouples allows to draw the connection between the actual data point and the measured data point. The standard actual value was taken using a thermometer and plotted against the measured reading from the thermocouple. Figure 3-10 displays the calibration set-up used where the thermocouples were immersed in a water flask at the same level as the sensing end of the thermometer. A controlled heater was used to control the heat delivered to the water and this permitted to set the temperature of water at various values reaching 100°C using a thermostat. After the temperatures reach steady state, they were recorded using data loggers connected to a computer, along with the thermometer readings. Using the ice/water flask, the initial point of 0°C was enabled.

For the experimental work conducted in chapter 5 of this thesis, cryogenic temperatures were being used, therefore cryogenic temperatures were included in the calibration process where the thermocouples were placed inside the LN_2 thermo-flask and their reading was compared to the boiling point of liquid nitrogen at atmospheric pressure of -195.79°C [139]. The data recorded in the computer were then used to plot the calibration curves for all thermocouples. In the experimental work described in this thesis, a total of 12 thermocouples were used, of which ten were of surface K-type (5TC-TT-KI-36-1M) and two were of probe K-type (TJ2-CPSS-1M15E-150). The calibration curves for one of the

surface thermocouples (used in all three experiments) and one of the thermocouple probes (used in experiment conducted in chapter 5) are shown in Figure 3-11.
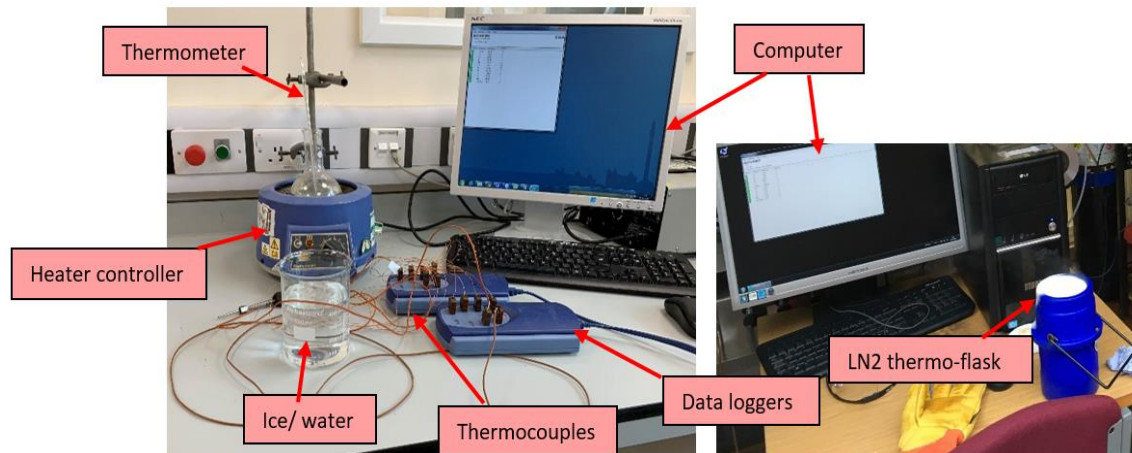
Figure 3-10: Thermocouple calibration set-up
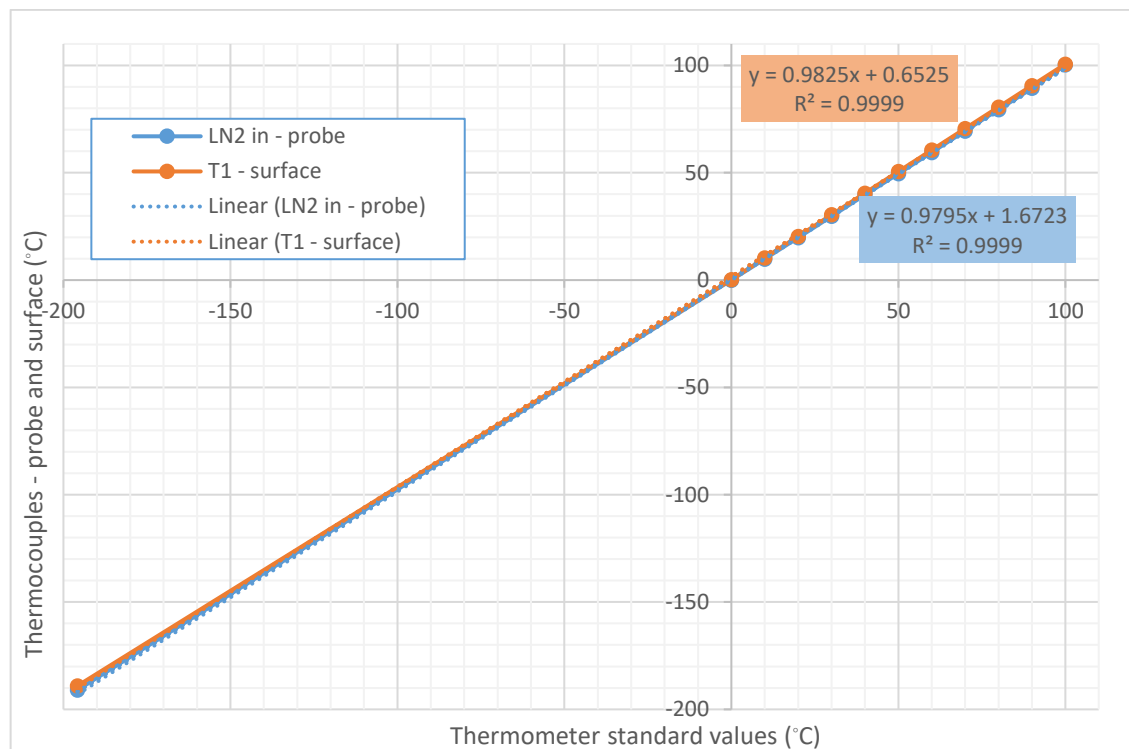
Figure 3-11: Thermocouple calibration curve for one probe and one surface thermocouple

Uncertainty analysis

Uncertainty analysis has been conducted for the thermocouples in order to determine the accuracy of the results. The results obtained from experiments are affected by the instruments that measure the different parameters (X_i). Deviation of the results from the true values occurs due to the errors in measuring these parameters [140].

$$Results = f(X_1, X_2, X_3, \dots X_n) \qquad \text{3-14}$$

Random (precision) errors and systematic (bias) errors are the two types of errors in any measuring device. Random errors or repeatability errors are numerical in nature and they are triggered by unpredictable variations in the experiment. They are acquired from the average standard deviation with 95% confidence level as shown in equation (3-15) [140].

$$U_{random} = t_{N-1,95\%} S_{\hat{x}} \qquad \text{3-15}$$

where, N is the number of data points in the sample and $t_{N-1,95\%}$ is the student distribution factor for a degree of freedom N-1. $S_{\hat{x}}$ is the mean standard deviation which is obtained from equation (3-16).

$$S_{\hat{x}} = \frac{1}{\sqrt{N}} \sqrt{\frac{\sum_{i=1}^{N}(X_i - \overline{X})^2}{N-1}} \qquad \text{3-16}$$

Systematic errors includes hysteresis errors, data acquisition errors and calibration errors [140] and it is calculated by equation (3-17).

$$U_{systematic} = \sqrt{\sum_{i=1}^{M} U_{i,systematic}^2} \qquad \text{3-17}$$

where, M is the number of systematic error sources. Laboratory calibration or manufacturer data (if available) is the source for $U_{systematic}$.

The overall uncertainty for the measuring instruments is calculated using the root square sum (RSS) of systematic and random errors as shown in equation (3-18).

$$U_{overall} = \pm \sqrt{U_{systematic}^2 + U_{random}^2}$$

3-18

The uncertainty analysis is conducted for all the thermocouples and it is thoroughly explained for one of the surface thermocouples, T2. Firstly, the calibration curve of the surface thermocouple T2 is plotted and the linear equation for the trend line is found as shown in Figure 3-12.
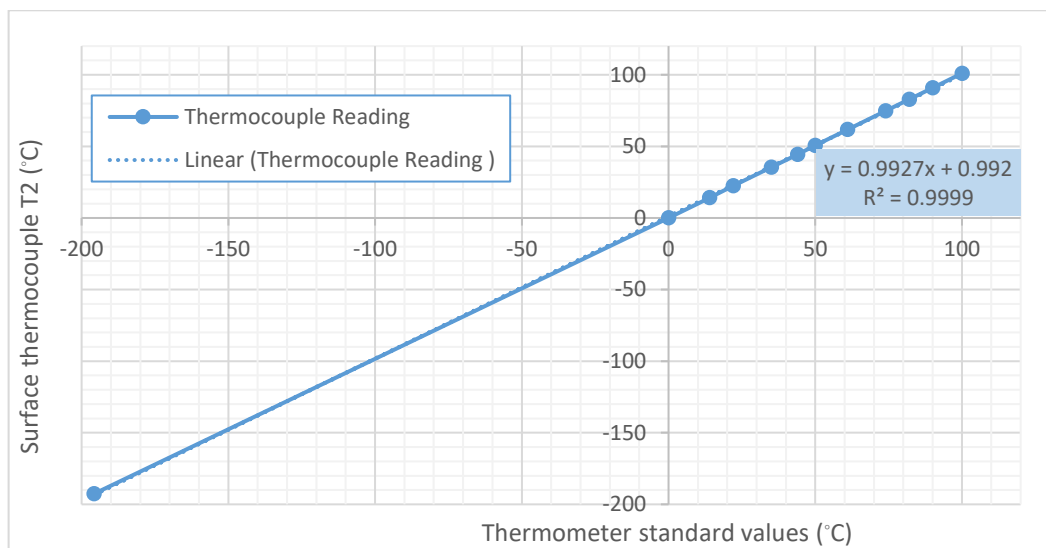
Figure 3-12: Thermometer calibration for surface thermocouple T2

Then the trend line linear equation values and the deviations for different temperature points are calculated as shown in Table 3-5.

Table 3-5: Deviations for different temperature points for surface thermocouple T2

N	Thermometer Reading (X_i)	Thermocouple Reading	Trend line linear Equation $\overline{X}= 0.9927x + 0.992$	Deviation $(X_i - \overline{X})^2$
1	-195.79	-192.64	-193.37	5.86
2	0.00	0.00	0.99	0.98
3	14.00	14.12	14.89	0.79
4	22.00	22.36	22.83	0.69
5	35.00	35.38	35.74	0.54
6	44.00	44.41	44.67	0.45
7	50.00	50.62	50.63	0.39
8	61.00	61.69	61.55	0.30
9	74.00	74.78	74.45	0.20
10	82.00	82.81	82.39	0.15
11	90.00	90.85	90.34	0.11
12	100.00	100.97	100.26	0.07

Finally, the uncertainty calculations for the surface thermocouple T2 is calculated as follows:

- The summation of deviation points $\sum_{i=1}^{N}(X_i - \overline{X})^2$ is 10.55374.

- The degree of freedom N-1 is 11.

- The standard deviation is 0.28276.

- The student distribution factor for a degree of freedom N-1, $t_{N-1,95\%}$ is 2.200985.

- The total random errors U_{random} is 0.622348.

- The total uncertainty of the thermocouple $\pm\sqrt{U_{systematic}^2 + U_{random}^2}$ is $\pm0.62285°C$.

Table 3-6 displays the uncertainty values and their trend line linear equations for all the thermocouples used in all the experimental work carried out in chapters 3, 4 and 5 in this thesis and Appendix A shows the calibration graphs for all the thermocouples used.

Table 3-6: Uncertainty analysis for all the thermocouples used in this thesis

Thermocouple Type	Trend Line Equation	R^2	Uncertainty (°C)
LN2 In – Probe	$\overline{\overline{X}} = 0.9825x + 0.6525$	0.9999	± 0.868
T1 - Surface	$\overline{\overline{X}} = 0.9795x + 1.6723$	0.9999	± 1.235
T2 - Surface	$\overline{\overline{X}} = 0.9927x + 0.992$	0.9999	± 0.622
T3 - Surface	$\overline{\overline{X}} = 0.9941x + 0.7721$	1	± 0.491
T4 - Surface	$\overline{\overline{X}} = 0.9877x + 0.9752$	0.9999	± 0.730
T5 - Surface	$\overline{\overline{X}} = 0.9912x + 1.2996$	0.9999	± 0.801
T6 - Surface	$\overline{\overline{X}} = 0.9887x + 1.7115$	0.9998	± 1.059
T7 - Surface	$\overline{\overline{X}} = 0.9938x + 0.8894$	1	± 0.565
T8 - Surface	$\overline{\overline{X}} = 0.9808x + 0.8778$	0.9999	± 0.964
T9 - Surface	$\overline{\overline{X}} = 0.9916x + 0.9826$	0.9999	± 0.649
T10 - Surface	$\overline{\overline{X}} = 0.9839x + 2.2046$	0.9998	± 1.351
LN2 Out – Probe	$\overline{\overline{X}} = 0.9907x + 0.2408$	1	± 0.461

Salinity meter

An Omega handheld salinity meter as shown in Figure 3-13 [141] was used to measure the salinity of the salt water mixtures. This has a range of 0.1% to 10% salinity measurements and can function at temperatures from -5°C to 60°C [141]. The salinity meter was used to measure the salinity of ice and brine after the freeze desalination process and also to measure the salinity when making salt water solutions before the experiment.

Figure 3-13: Omega handheld salinity meter [12]

Table 3-7 shows the accuracy levels of the calibrated salinity meter given in the salinity meter manual [141].

Table 3-7: Calibrated accuracy levels of the salinity meter [141]

Salinity levels	Accuracy
0 to 0.9%	±0.1
1.0 to 1.9%	±0.2
2.0 to 2.9%	±0.3
3.0 to 4.9%	±0.5
5.0 to 7.9%	±1.0
8.0 to 10.0%	±1.5

Salinity meter calibration

The calibration process was conducted by measuring salt on a weighing scale and adding de-ionised water to create a salt water mixture. This salt water mixture was measured by inserting the salinity meter probe into the mixture as shown in Figure 3-14. The salinity level percentage is calculated by equation (3-19) and the results are shown in

Table 3-8 and Figure 3-15 for different salt water mixtures. The manufacturer's accuracy is taken from Table 3-7. It can be seen that the measured accuracy is lower than those given by the manufacturer.
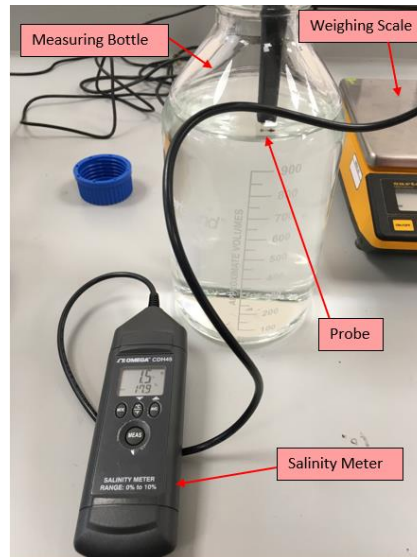
Figure 3-14: Calibrating the salinity meter

$$Salinity\ Level\ (\%) = \frac{Salt\ mass}{Volume\ of\ Deionised\ water} \times 100 \qquad 3\text{-}19$$

Table 3-8: Salinity calibration

Salt mass (g)	De-ionised water (ml)	Salinity level % (calculated value)	Salinity level % (measured value)	Measured Accuracy	Manufacture's Accuracy [141]
3	1000	0.3	0.3	0	±0.1
4	1000	0.4	0.4	0	±0.1
5	1000	0.5	0.5	0	±0.1
8	1000	0.8	0.8	0	±0.1
9	1000	0.9	0.9	0	±0.1
10	1000	1	1	0	±0.2
11	1000	1.1	1.1	0	±0.2
15	1000	1.5	1.5	0	±0.2
25	1000	2.5	2.4	-0.1	±0.3
35	1000	3.5	3.3	-0.2	±0.5
45	1000	4.5	4.3	-0.2	±0.5
55	1000	5.5	5.2	-0.3	±1.0
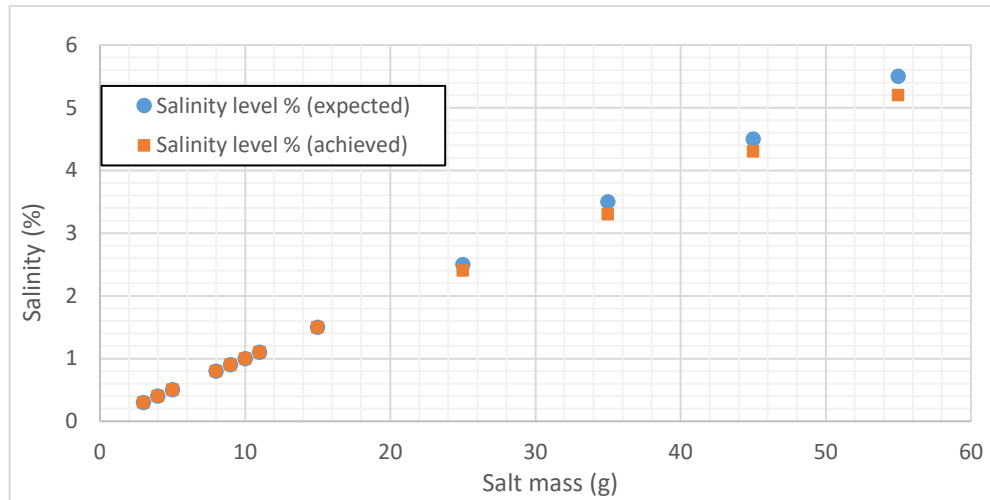
Figure 3-15: Salinity calibration graph

3.6 Experimental methodology

3.6.1 Experimental procedure

A stainless steel container was used to freeze a salt water solution to study the freeze desalination process and to validate the CFD model discussed in section 3.3 of this chapter. The steps of the experimental methodology are summarised as follows:

1. Saline water was prepared using 100ml of de-ionised water mixed with 3.5g of salt in order to create a mixture with a concentration of 35g/L as calculated using equation (3-19). The salinity of this mixture was measured using the Omega salinity meter (shown in Figure 3-13) giving a reading of 3.5% [12].

2. A known volume of the prepared salt water solution made was then poured into the stainless steel container.

3. The insulation material was placed around the sides and the top of the container as shown in Figure 3-9.

4. The data logger and the personal computer were started to record and monitor the thermocouple temperature readings till all the temperatures were stable at room temperature.

5. The power supply was turned on to the Peltier and the heat sink/cooling fan to cool the bottom of the stainless steel frustum. During testing, the cold side temperature of the Peltier device was controlled to remain at 260K with ± 3K using the power supply.

6. A stopwatch was used to measure the time taken to generate ice and then the power supply was turned off when the ice was generated.

7. At the end of the experiment, the generated ice was separated from the remaining concentrated brine. The ice obtained was washed to remove any brine attached to its outer surface, then melted and its salinity was measured. The salinity of the remaining brine solution was also measured. [12]

8. The volume and mass of ice, the volume of remaining brine and the salinities of ice and brine were all measured.

In each test, two experiments have been conducted at the same conditions in order to calculate the amount of brine washed off during the cleaning of ice. In the first experiment, the ice was washed and the salinity was measured and in the second experiment, the ice was not washed and the salinity was measured. Therefore, the salinity of brine washed away in the first experiment can be calculated by equation (3-20) and the total brine salinity can be calculated using equation (3-21). [12]

$$Ice\ Salinity\ (Ex2) - Ice\ Salinity\ (Ex1) = Excess\ brine\ stuck\ to\ the\ ice\ surface \qquad 3\text{-}20$$

$$Excess\ brine + Brine\ Salinity\ (Ex1) = Total\ Brine\ Salinity\ (Ex1) \qquad 3\text{-}21$$

Hence, the salinity of the ice was obtained from experiment 1, where the ice was washed, while the salinity of the brine was taken from experiments 1 and 2 where the total brine salinity was calculated [12].

Six tests were conducted of the same initial salinity of salt water and the results were averaged and analysed. Parametric study was then conducted by changing the initial salinity of salt water, where the same steps described above were repeated with different initial salt water salinities.

3.7 Experimental results

Table 3-9 shows results obtained after conducting two experiments where the ice was washed and not washed. A salt water concentration of 35g/L (3.5%) was frozen indirectly at a freezing temperature of 260K for 30 minutes. Generally, salt water concentration of 35g/L (3.5%) represents the average sea water salinity.

Table 3-9: Experimental results [12]

Experiment	1 (ice washed)	2 (ice not washed)
Time (minutes)	30	30
Initial Mass Fraction of Sea Water (g/L)	35	35
Initial Salinity (%)	3.5	3.5
Salinity of Ice formed (%)	1.4	3.0
Salinity of Brine remaining (%)	3.8	3.7
Mass of Ice Before Washing (g)	3.55	3.61
Mass of Ice After Washing (g)	2.14	-
Mass of ice washed off when cleaning (g)	1.41	-

Equation (3-20) and (3-21) were used to calculate the final ice and brine salinities. From Table 3-9, the excess brine stuck to the ice surface and the total brine salinity were

calculated using equations (3-20) and (3-21) to be 1.6% and 5.4% respectively [12]. Parametric study was then carried out by conducting more experiments with salt solutions of different salinities i.e. 25g/l, 35g/l and 45g/l to study the effects of initial salinity on the quality of water produced and brine output. Therefore, results showed that the increase in initial salinity increased the salinity of ice produced and reduced the volume of ice produced.

3.8 CFD modelling validation

The CFD results in terms of salt water temperature, cooling device temperature and salinity were compared to those from the experimental measurements [12]. Figure 3-16 shows the temperature variation with time for salt water temperature T3 and the Peltier cooling device cold side temperature T1 as obtained from CFD modelling and experimental measurements (for 35g/L salt water solution) with an average deviation of ±0.495K and ±0.115K respectively. [12]
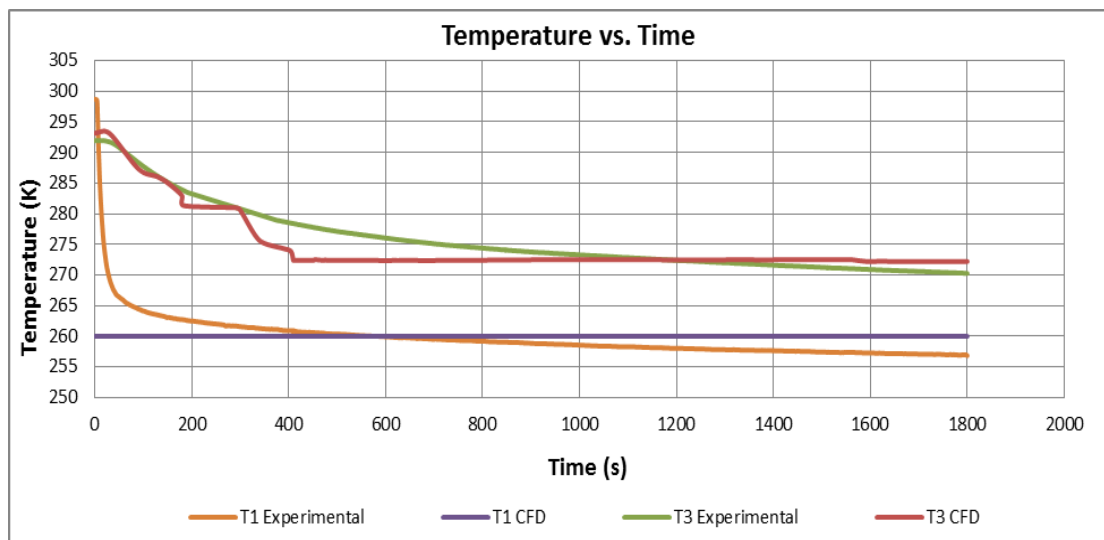
Figure 3-16: Temperature vs. time comparison for experimental and CFD results for 35g/L salt water solution [12]

Figure 3-17 shows the temperature variation with time for salt water temperature T3 from CFD and experimental measurements carried out for tests at different initial salinity levels of 25g/L and 45g/L. It is shown that both the experimental and the CFD results follow a similar pattern and reach similar final temperatures with an average deviation of ±3.07K for 25g/L and ±2.82K for 45g/L [12].
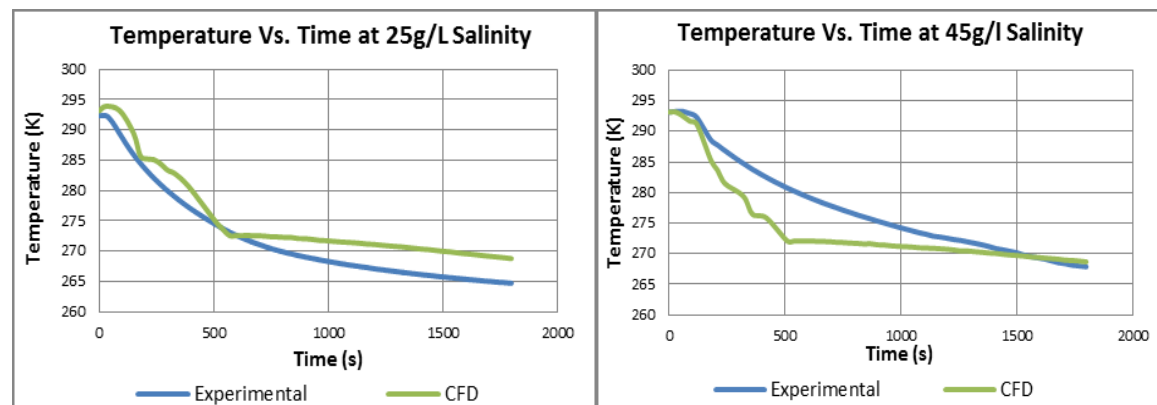
Figure 3-17: Temperature vs. time graphs for salinity levels of (a) 25g/L (left) and (b) 45g/L (right) [12]

Table 3-10 shows the comparison between the CFD model and the experimental measurements for salinity after 30 minutes of real time experiment. It is clear from this table that the produced ice salinity from both experimental testing and CFD modelling shows good agreement, 1.4% for experimental and 1.43% for the CFD, giving a percentage error of 2.10%. Similarly the remaining brine salinity from both experimental testing and CFD modelling shows good agreement, 5.4% for experimental and 6.5% for the CFD, giving a percentage error of 16.9. [12]

Table 3-10: CFD and Experimental results comparison [12]

Comparison	Experimental	CFD
Time (minutes)	30	30
Initial Mass Fraction of Sea Water (g/L)	35	35
Initial Salinity (%)	3.5	3.5
Salinity of Ice formed (%)	1.4	1.43
Salinity of Brine remaining (%)	5.4	6.5
Percentage error of ice salinity (%)	2.10	
Percentage error of brine salinity (%)	16.9	

3.9 CFD parametric analysis

The developed CFD model was then used to carry out parametric analysis to predict the effects of freezing temperature, solution salinity and the direction of freezing; on the freezing time, ice production and its salinity. Table 3-11 displays the different cases run with different parameters and the boundary conditions used. [12] Various cooling temperatures namely 230, 250, 260 and 270K; various initial salinity levels 35, 45 and 55g/L and various freezing directions top surface, bottom surface and lateral surfaces were investigated.

Table 3-11: Parametric analysis cases with input, output and boundary conditions [12]

Temperature Cases			
Cases	*Input*	*Constants and Boundary Conditions*	*Output*
Temp 230K	Freezing temp. 230K	Initial salinity 35g/L, Non-slip stationary walls. All other walls with heat flux (W/m^2) = 0.	Total ice production (mm^3) - 7067.7
Temp 250K	Freezing temp. 250K	Initial salinity 35g/L, Non-slip stationary walls. All other walls with heat flux (W/m^2) = 0.	Total ice production (mm^3) - 3721.0
Temp 260K	Freezing temp. 260K	Initial salinity 35g/L, Non-slip stationary walls. All other walls with heat flux (W/m^2) = 0.	Total ice production (mm^3) - 1513.3
Temp 270K	Freezing temp. 270K	Initial salinity 35g/L, Non-slip stationary walls. All other walls with heat flux (W/m^2) = 0.	Total ice production (mm^3) - 81.3
Salinity Cases			
Cases	*Input*	*Constants and Boundary Conditions*	*Output*
Salinity 35g/L	Initial Salinity 35g/L	Freezing temp. 260K, Non-slip stationary walls. All other walls with heat flux (W/m^2) = 0.	Total ice production (mm^3) - 1513.3
Salinity 45g/L	Initial Salinity 45g/L	Freezing temp. 260K Non-slip stationary walls. All other walls with heat flux (W/m^2) = 0.	Total ice production (mm^3) - 1109.9
Salinity 55g/L	Initial Salinity 55g/L	Freezing temp. 260K Non-slip stationary walls. All other walls with heat flux (W/m^2) = 0.	Total ice production (mm^3) - 882.1
Freezing Direction Cases			
Cases	*Input*	*Constants and Boundary Conditions*	*Output*
Top	Freezing from top surface	Initial salinity 35g/L, Freezing temp. 260K, Non-slip stationary walls. Bottom and Lateral walls with heat flux (W/m^2) = 0.	Ice production *per unit surface area (mm^2)* - 4.50
Lateral	Freezing from lateral surfaces	Initial salinity 35g/L, Freezing temp. 260K, Non-slip stationary walls. Top and Bottom walls with heat flux (W/m^2) = 0.	Ice production *per unit surface area (mm^2)* - 4.20
Base	Freezing from base/bottom surface	Initial salinity 35g/L, Freezing temp. 260K, Non-slip stationary walls. Top and Lateral walls with heat flux (W/m^2) = 0.	Ice production *per unit surface area (mm^2)* - 3.97

3.9.1 Effect of freezing temperature

The effect of changing the base freezing temperature from 230K, 250K, 260K and 270K was investigated. Figure 3-18 shows the variation of the average solution temperature and the solidification (liquid phase fraction) with time at various freezing temperatures. It is evident from Figure 3-18(a) that as the base freezing temperature decreases, the average solution temperature decreases at a faster rate leading to an increased solidification rate as shown in Figure 3-18(b); where at 230K a liquid phase fraction of 0.61 was achieved at the end of 30 minutes compared to 0.78, 0.87 and 0.99 for 250K, 260K and 270K respectively. [12]
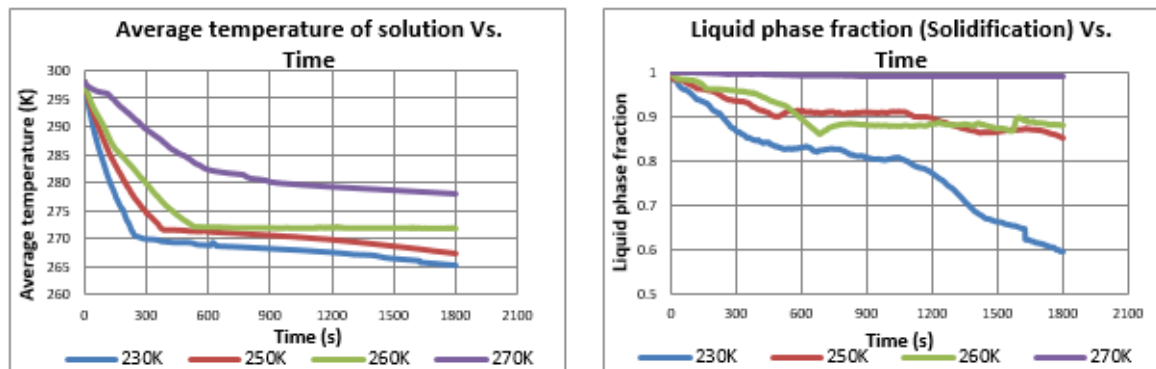
Figure 3-18: (a) Average temperature of solution (left) and (b) liquid phase fraction (right) vs. time graphs for different freezing temperatures [12]

Figure 3-19 displays the contours for the solution temperature and solidification (liquid phase fraction) at freezing temperatures of 230K, 250K, 260K and 270K. The solidification of pure water varies with temperature and it is seen in the contours after 30 minutes of freezing. It is apparent from this figure that as the freezing temperature is reduced; the cold region and the frozen layer are increased, while the overall container temperature is more uniform. Regarding the solidification, as the freezing temperature is decreased the volume of ice produced is increased.
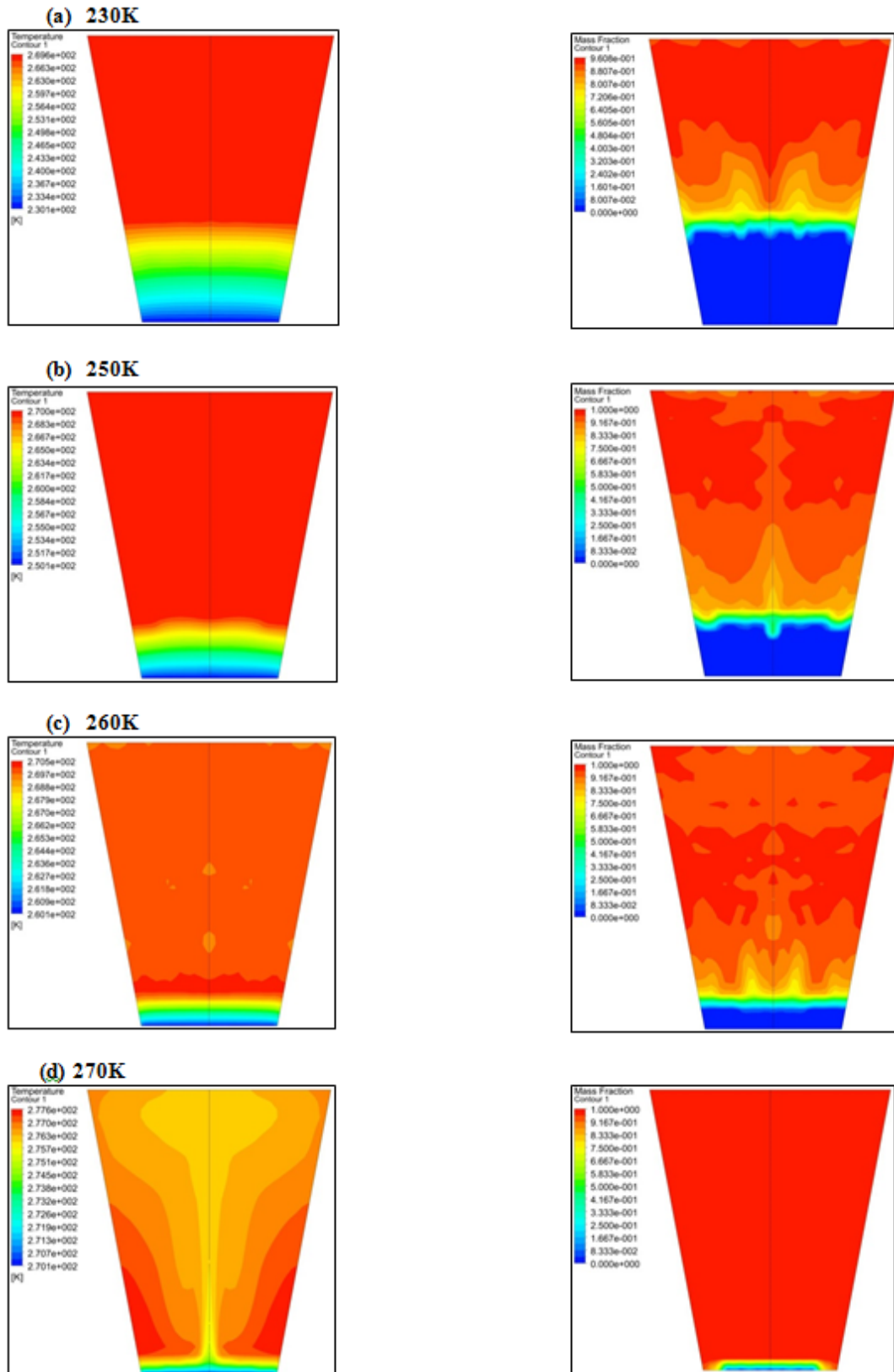
Figure 3-19: Contours for temperature (left) and liquid phase fraction (right) for base freezing temperatures of (a) 230K (b) 250K, (c) 260K and (d) 270K [12]

The produced ice volumes at base temperatures of 230K, 250K, 260K, and 270K are 7067.7, 3721.0, 1513.3, and 81.3mm^3 respectively, proving the significant effect of the freezing temperature on ice production. Figure 3-19 also indicates that as the freezing temperature decreases, ice formation increases and the mass fraction of the remaining brine is increasing. [12]

3.9.2 Effect of salinity

The effect of initial salt water concentration on the remaining brine concentration and ice production was investigated. Figure 3-20 shows the contours of liquid phase fraction at 260K freezing temperature using initial solution concentration levels of 35g/L, 45g/L and 55g/L at the end of 30 minutes freezing time. It is evident from this figure that as the initial solution salinity increases, the ice production is reduced and the remaining brine concentration increases. Thus, the volumes of ice produced at concentrations of 35g/L, 45g/L and 55g/L are 1513.3mm^3, 1109.9mm^3 and 882.1mm^3 respectively. [12]
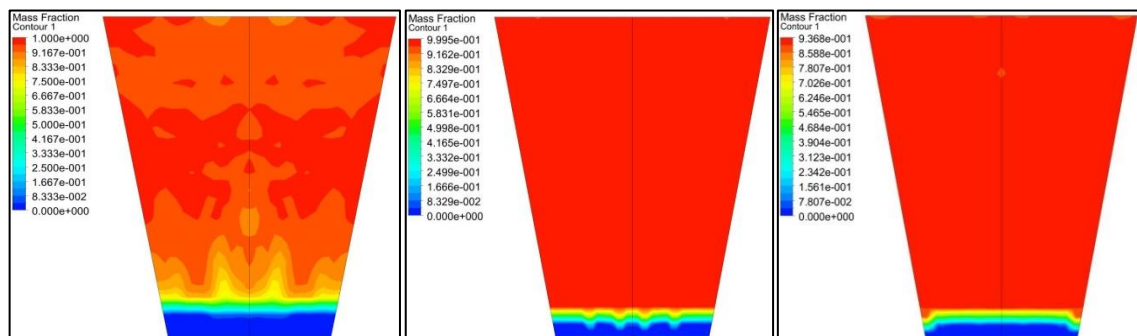
Figure 3-20: Liquid phase fraction contours for concentrations of (a) 35g/L (left), (b) 45g/L (middle) and (c) 55g/L (right) [12]

3.9.3 Effect of direction of freezing

The developed CFD model was used to investigate the effect of freezing direction on ice production. Figure 3-21 displays the effect of cooling the container from different directions (top, sides and base); on the solution temperature, solidification (liquid phase fraction) and velocity streamlines. The volumes of ice produced per unit surface area (mm^2) for freezing directions from top, lateral and base are 4.50, 4.20 and 3.97mm^3 respectively. It is clear from these figures that freezing from the top direction allows maximum ice production, while freezing from the bottom produces the lowest amount of ice. Freezing from the top enables a convection movement, where thermal and solutal buoyancies are acting in opposite directions forming a natural source of hydrodynamic instability; which leads to better mixing, enabling more freezing. As for freezing from the bottom, the thermal and solutal buoyancies are acting in the same direction; leading to limited mixing and reduced freezing rate. Regarding the lateral freezing, the thermal and solutal buoyancies are acting in perpendicular directions; leading to lower mixing levels than freezing from the top, but higher than freezing from the bottom. Presenting the velocity streamlines is useful since low velocity streamlines indicate regions where ice has formed, while high velocity streamlines indicate regions with high brine solution. It can also be seen from Figure 3-21 that the distribution of streamlines velocities varies significantly according to the freezing direction. [12]
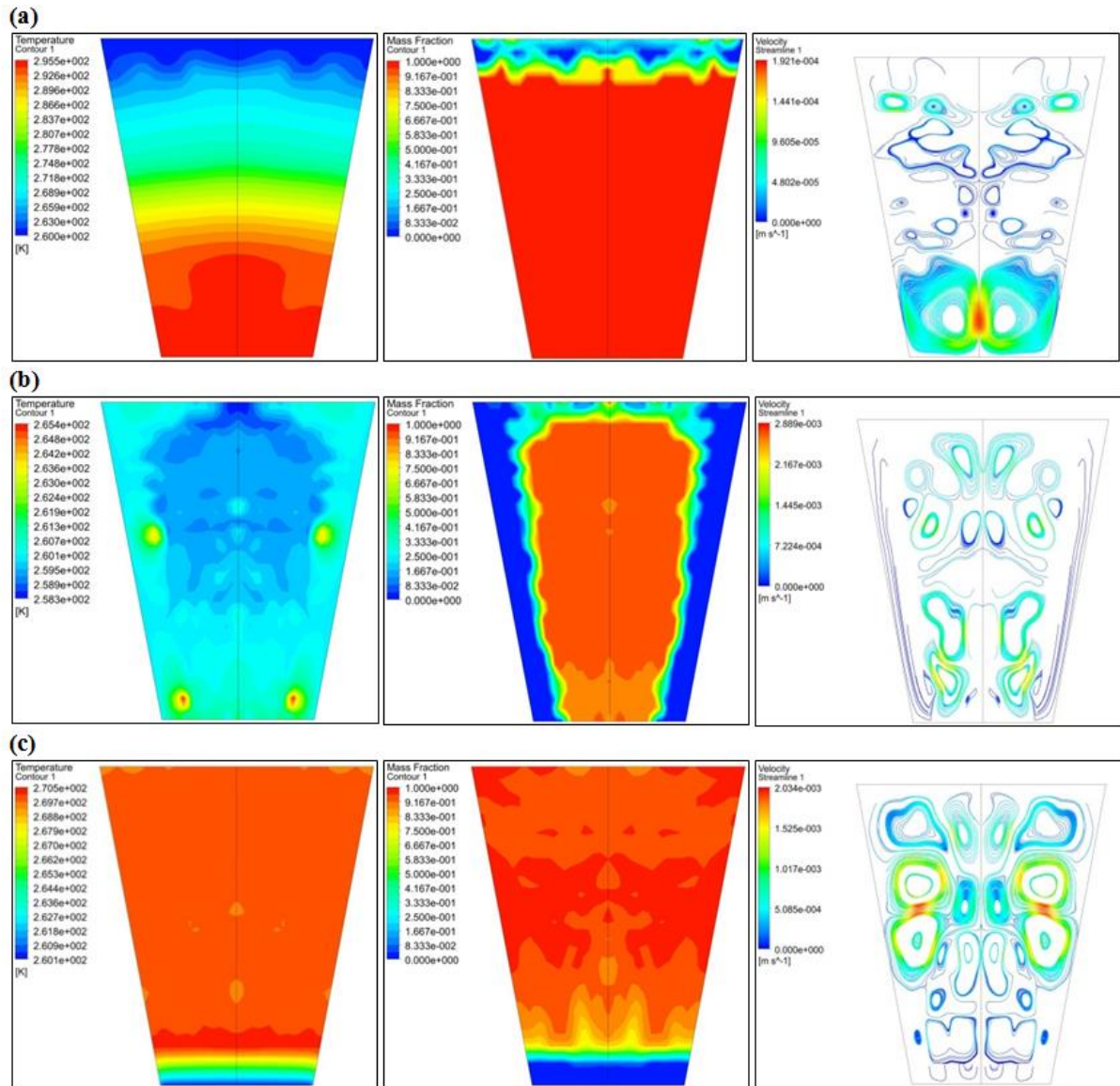
Figure 3-21: Temperature contours (left), liquid phase fraction contours (middle) and velocity streamlines (right) for (a) freezing from the top (b) lateral freezing and (c) freezing from the bottom [12]

3.10   Summary

Using the species transport, solidification/melting and energy modules in ANSYS Fluent software; a 3D CFD model was developed for the indirect freeze desalination process. The CFD model was validated through experimental testing, where the ice salinity and salt water temperatures from the experimental results were compared with the CFD simulation; the former giving a percentage deviation of 2.10 and the latter giving an average deviation of ±0.495K. Results also indicated that as solidification process has occurred; the ice temperature is increasing from the lower edge of the ice layer (in contact with the freezing surface) to the upper edge (in contact with brine solution), and then it remains constant through the brine solution. Also, at the top edge of the ice layer, the brine concentration is very low by approximately 1.2%, but as the distance from the ice top edge increases, the brine concentration increases to reach maximum of about 5.8%. [12]

Parametric analysis were carried out to predict the effects of freezing temperature, solution salinity and the direction of freezing; on the freezing time, ice production and its salinity. Results showed that lower temperatures enabled faster freezing and more ice produced; where at 230K freezing temperature, 4.67 times more ice was obtained compared to the 260K freezing temperature. The higher the salinity of sea water, the less pure the ice crystals become and slower the freezing process, where for 55g/L of initial salt water concentration, 58.3% less ice was produced compared to 35g/L of initial salt water concentration. [12] Regarding the effects of freezing direction; results showed that the volumes of ice produced per unit surface area (mm^2) for freezing directions from top, lateral and base were 4.50, 4.20 and 3.97mm^3 respectively. Freezing from the top is more efficient, where thermal and solutal buoyancies act in opposite directions; leading to enhanced

mixing and thus enabling more freezing. However, for freezing from the bottom, the thermal and solutal buoyancies are acting in the same direction; allowing minimum mixing and a reduced freezing rate. As for the lateral freezing, the thermal and solutal buoyancies are acting in perpendicular directions; leading to moderate mixing levels and thus lower ice production than the top surface freeze condition. [12]

Freeze desalination process was then investigated using a commercially available ice maker machine to assess the feasibility of using such device for portable water production and the results are discussed in chapter 4. Exploiting cryogenic energy for freeze desalination was then investigated and discussed in chapter 5.

CHAPTER 4

4. INDIRECT FREEZE DESALINATION USING AN ICE MAKER MACHINE

4.1 Introduction

This chapter is solely based on the published papers "Numerical Investigation of Indirect Freeze Desalination using an Ice Maker Machine" by Jayakody et al [7] and "Indirect contact freeze water desalination for an ice maker machine – CFD simulation" by Jayakody et al [14]. Contents such as texts, figures, graphs and tables are taken from the above mentioned papers [7], [14].

In this chapter, the feasibility of using a commercially available ice maker machine for freeze desalination is investigated, where Computational Fluid Dynamics (CFD) have been used to model the salt separation process of freeze desalination and validated using a commercially available ice maker machine. Although several experimental studies were carried out regarding freeze desalination [32], [35], [41]–[45], [53], [54], they are mostly aimed at large scale production of potable water. Developing a small scale portable desalination system can offer potential in applications like domestic houses, schools, local shops and hospitals. Only Williams et al [98] conducted a research on using an ice maker machine for desalting brine; where experimental work was done by using an ice maker machine to assess the technical viability of using the ice maker as a treatment system for salt water. It was concluded that the feed salt water concentration had a considerable effect

on the rejection of salt and the water recovery ratios. [7] In this chapter, the feasibility of using a small ice-maker for indirect freeze desalination is investigated using experimental testing and numerical modelling.

4.2 Experimental test facility

A commercially available ice maker ('Klarstein' [142]) was used to assess the feasibility of using an ice maker machine for the freeze desalination process to produce potable water. This commercially available ice maker was used to study the freeze desalination process and to validate the CFD model. The ice maker was instrumented with thermocouples connected to its freezing tubes in order to measure the temperatures at different locations. The formation of ice is analysed; where the volume of ice formed and the ice and brine salinities were also measured.

4.2.1 Layout of the test facility

Figure 4-1 shows the experimental facility used, consisting of the 'Klarstein' [142] ice maker, data logger and personal computer. An ice maker machine type 'Klarstein' [142] with 10 freeze tubes was used in the experimental work; it runs for about 8 minutes to produce 10 ice units in a single run and due to the characteristics of the machine, each ice unit has a volume of about 4000mm^3. Type-K surface thermocouples were placed at different locations on the freeze tubes of the ice maker to monitor the freeze tube surface temperature as shown in Figure 4-1. Furthermore, an additional type-K surface thermocouple was placed near the freeze tubes in order to monitor the temperature variation

during the ice forming process. These thermocouples were connected to a data logger to record the temperatures with time by the computer. The temperature of the freeze tubes was maintained constant at 257.15K with ± 3K fluctuation. A 1000ml of de-ionised water was thoroughly mixed with 35g of salt in order to get a salt water concentration of 3.5% (or 35g/l) to match the average sea water salinities. Consequently, 1000ml of salt water was poured into the ice maker machine and the freezing process was carried out for 8 minutes. Figure 4-2 shows a single ice block generated at the end of the freezing process to be measured for its mass and dimensions. The ice blocks were then melted to measure total volume and salinity. The remaining brine was also collected to measure its salinity. [7]
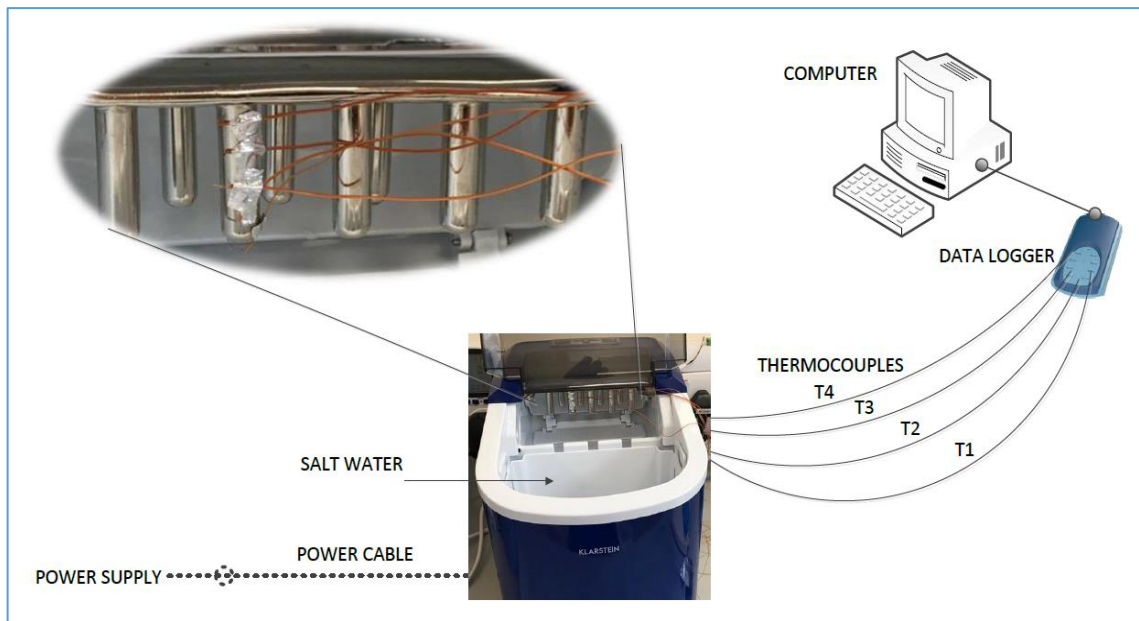
Figure 4-1: Experimental schematic diagram [7]

Figure 4-2: A single ice unit formed from the ice maker [7]

4.2.2 Measuring devices and calibration

Thermocouples and a salinity meter were used in this experiment to measure temperatures and salinity respectively.

Thermocouples

Four thermocouples have been used to measure the temperatures at the surface of the freezing tubes and also at locations where the ice is forming. These were type-K thermocouples able to measure temperatures down to 73.15K. Sensor tips of these thermocouples were pasted into the stainless steel freezing tubes using aluminium tape in order to allow effective contact. The thermocouples were connected to a 'TC-08 PICO' data logger, which was connected to a computer to record the temperature measurements during the experiment. The thermocouples were calibrated in order to evaluate their accuracy using the process described in section 3.5.2.

Salinity meter

The Omega handheld salinity meter [141] described in section 3.5.2 was used to measure the salinity of the salt water mixtures. This has a range of 0.1% to 10% salinity measurements and can operate at temperatures from -5°C to 60°C [141]. The salinity meter was used to measure salt water solutions made before the experiment and also to measure the salinity of ice and brine after freeze desalination process.

4.3 Experimental methodology

A commercially available ice maker was used to investigate the feasibility of using an ice maker machine to conduct freeze desalination as a portable application. The steps of the experimental methodology are explained as follows:

1. A salt water mixture was created by mixing salt with de-ionised water and this solution's salinity was measured by the Omega Handheld salinity meter [12].

2. A known volume of the salt water solution was then poured into the ice maker.

3. The 'Klarstein' [142] ice maker machine was then turned on and a stop watch was used to measure the time taken to produce one batch of ice.

4. Once the first batch of ice was produced, the machine was turned off, the stop watch was stopped and the ice was collected.

5. Several ice cubes were then taken and their dimensions were measured using a Vernier calliper.

6. The ice cubes were left to melt and then the mass and volume of the melted ice were measured.

7. The salinity of the melted ice was measured.

8. The remaining brine collected from the ice maker, was poured to a beaker and its volume and salinity were measured.

Four tests were conducted at the same initial salinity of salt water and the results were averaged and analysed. Parametric study was then conducted by changing the initial salinity of the salt water and the testing procedure was repeated. The salt solutions were produced by measuring the mass of salt and mixing it with 1000ml of de-ionised water and the salinity of the produced solution was calculated using equation (3-19). The salinity meter was also used to measure and confirm the salinity of salt water solution.

4.3.1 Energy and efficiency calculations

The total energy lost by water was calculated using equation (4-1), consisting of four terms; firstly, the energy lost from the remaining brine and secondly, the energy lost from water when ice was formed which was calculated from the initial conditions to the freezing point (F.P) of salt water. Thirdly, the energy gained by ice which was calculated from the freezing point (F.P) of salt water to the final temperature of ice and finally, the latent heat of fusion.

$$Q_{total\ water} = Q_{brine} + Q_{water\ to\ F.P} + Q_{F.P\ to\ ice} + mL_f \qquad \text{4-1}$$

where, L_f is the latent heat of fusion for sea water and m is the mass. Equation (4-2) was used to find the energy for ice, water and brine.

$$Q_{ice/water/brine} = m(Cp_2 T_2 - Cp_1 T_1) \qquad \text{4-2}$$

where, Cp_1 and Cp_2 are the initial and final specific heat capacities of water respectively. T_1 and T_2 are the initial and final temperatures respectively.

The overall efficiency of the freezing process was calculated using equation (4-3).
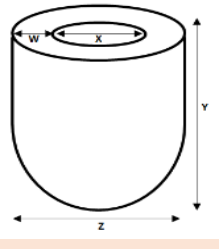
$$Eff_{ice-maker} = \frac{Q_{total\,water}}{Q_{ice-maker}}$$
<div align="right">4-3</div>

where, $Q_{total\,water}$ is the total energy lost by water calculated using equation (4-1) and $Q_{ice-maker}$ is the total energy output of the ice maker calculated using the measured power output, number of freezing steps and time.

4.4 Experimental results

In the primary case, a salt water concentration of 35g/L (3.5%) that represents the average sea water salinity, was used in the ice maker. From this experiment, after 8 minutes of freezing, 10 ice cubes were obtained with a volume and a mass of 33000mm^3 and 34.08g respectively. The average salinity of the melted ice was 3.0% and of the remaining brine was 3.6%. The dimensions of a single ice unit was measured and shown in Table 4-1. Parametric study was then carried out experimentally by conducting more experiments with salt solutions of different salinities i.e. 1.5%, 2.5%, 3.5% and 4.5% to study the effect of initial salinity on the quality of ice produced and brine output as shown in Table 4-6. The results showed that when the salt solutions' initial salinity was decreased, the volume of ice produced increased and the quality of ice increased, meaning that the salinity of ice formed decreased.

Table 4-1: Recorded results from the experiment [7]

Parameters		Results
Salt (g)		35
De-ionised Water (mm³)		1000000
Initial Salinity (%)		3.5
Time (min)		8
Volume of Ice Obtained (mm³)		33000
Mass of Ice Obtained (g)		34.08
	W (mm)	4.3
	X (mm)	10
	Y (mm)	21.3
	Z (mm)	18.2
Ice Salinity (%)		3.0
Brine Salinity (%)		3.6

The overall efficiency was 0.42 to freeze a 3.5% salt water solution to produce one batch of ice using the ice maker machine, which was calculated using equations (4-1) to (4-3). In order to determine the efficiency, the total energy output of the ice maker must be calculated. Hence, it must be noted that the experimental power consumption in the ice maker does not mirror the actual power consumption due to many factors such as having many components in the ice maker that is not required for the desalination process as confirmed by Williams et al. [98].

4.5 CFD Modelling

CFD software ANSYS Fluent version 16.2 [129] has been used to model the freeze desalination process of a commercially available ice maker machine. A single freeze tube of the 'Klarstein' [142] ice maker has been modelled using ANSYS Fluent to model the indirect contact freeze desalination process where the ice formed on the surface of the cold tubes of the ice maker is formed primarily of pure water and the brine is rejected to the remaining water solution. [7]

4.5.1 Geometry generation

The geometry has been modelled using ANSYS geometry modeller to the exact dimensions of a single freeze tube out of the 10 freeze tubes present in the 'Klarstein' [142] ice maker. Due to its symmetrical nature, only a quarter of the 3D circular tube has been modelled on CFD in order to reduce the computational time. Figure 4-3 shows the CFD geometry of the freeze tube that has been modelled using ANSYS Fluent geometry modeller. The measured freeze tube diameter and the length are 10.8mm and 20.6mm respectively. The surrounding salt water region is taken to be of 46.8mm diameter due to the fact that the distance between the outside edges of two freezing tubes is 18mm. The length of the region is taken to be 45mm to allow for enough ice formation to be seen and to clearly observe the freezing process surrounding the freeze tube as shown in Figure 4-3 and in the schematic shown in Figure 4-5.
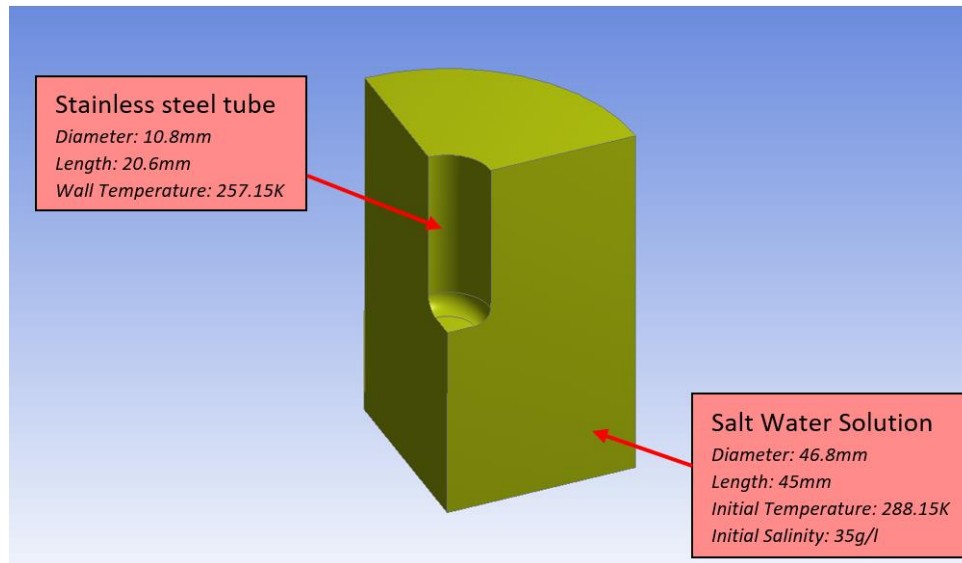
Figure 4-3: Geometry of CFD model

4.5.2 Mesh

The 3D geometry is then imported to 'ANSYS Meshing' where a fine tetrahedral mesh was implemented to create a mesh with 9946 nodes and 5911 elements as shown in Figure 4-4(a). Edge sizing was used to optimise the mesh as shown in Figure 4-4(b). Mesh independency study was carried out by using edge sizing to give coarser and finer meshes. The predicted ice salinity from CFD was compared to experimental values with three different types of meshes. The salt water with an initial salinity of 1.5% has been desalinated to experimentally produce ice with a salinity of 1.1%. This has been compared with a coarse, a medium and a fine mesh. Table 4-2 shows the effect of mesh types on the percentage error where the difference between the error produced using fine mesh and that of using medium mesh is small. However, the use of fine mesh resulted in a significant time consumed in the simulation. Therefore, medium mesh is used in further simulations.

Table 4-2: Mesh Independency [7]

Mesh Type	Nodes	Elements	Simulation Time (hours)	Salinity-Experimental (%)	Salinity-CFD (%)	Percentage of Error (%)
Coarse	7447	4543	16	1.1	1.3500	22.73
Selected Mesh	9946	5911	24	1.1	1.0800	1.82
Fine	17252	10188	36	1.1	1.0824	1.60
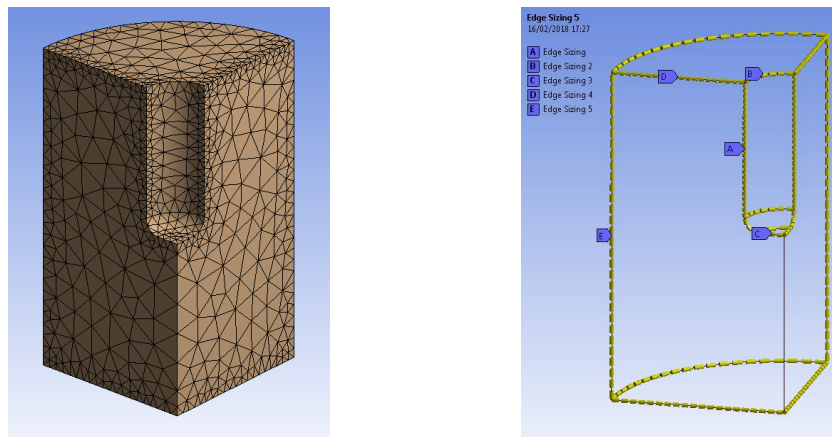
Figure 4-4: Tetrahedral mesh (left) (a) and edge sizing used (right) (b) [7]

4.5.3 Set-up

The selected mesh was then imported into 'ANSYS Fluent Setup' to set the materials, modules/equations, boundary conditions, solution methods, discretization settings, etc. A pressure-based solver has been used with laminar incompressible flow conditions through a transient solving process in order to run the simulations to achieve 8 minutes of real time. A laminar viscous model has been exploited to solve the computational fluid dynamics model. The main physics models used were energy, species transport and solidification/melting modules. [7]

Figure 4-5 displays a schematic diagram of the CFD model and Table 4-4 summarises the boundary conditions and the assumptions made. Sea water with an initial salt concentration of 35g/L has been modelled with a fixed initial temperature of 288.15K. The freezing tube with a temperature of 257.15K has been used to freeze the sea water solution. The rest of the walls have been regarded as adiabatic as indicated in Figure 4-5. [7]

In order to simulate the freezing process and the pure water (as ice) separation from the rejected brine solution, Energy (heat transfer), Species Transport and Solidification/Melting modules were utilised. In ANSYS Fluent, the solidification process is modelled using an enthalpy – porosity technique, where a porous zone is incorporated at the liquid-solid mushy zone, using liquid fraction corresponding to the porosity value [133]–[135]. A pressure drop occurs when the water freezes and solidifies and in order to predict this pressure drop, momentum sink terms are incorporated in the momentum equation [7], [136]. The physics and the theory of the CFD modelling process is thoroughly discussed in sections 3.2 in chapter 3.
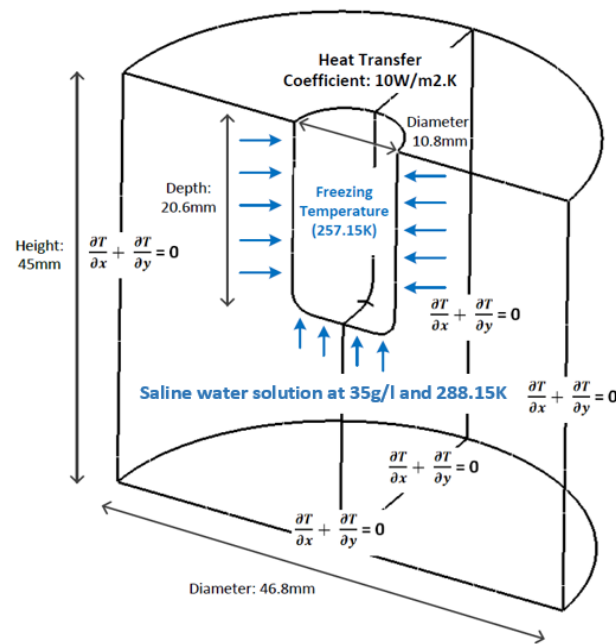
Figure 4-5: Schematic diagram of the modelled freeze tube in the ice maker [7]

Firstly, the working fluid of salt water is created by using the 'Species Transport' and 'Solidification/Melting' modules; where the mass fraction is automatically integrated into the module in order to generate a mixture of two species which are 'Pure water' and 'Salt water'. These are in two different concentrations and by mixing the two; a salt water mixture is made with an identifiable concentration. In the ANSYS Fluent material set-up, the properties of water to create the two concentrations for 'Pure water' and 'Salt water' can be inputted. Table 4-3 shows how the properties such as thermal conductivity, viscosity, specific heat, density, etc. are entered as a piecewise-linear function of temperature in ANSYS Fluent material set-up. After freezing, this allows the separation of pure water as ice and salt water as brine from the mixture. [7]

Table 4-3: Input of Properties for Pure Water and Salt Water [7]

Properties	Pure Water	Salt Water
Viscosity (kg/m.s)	Piecewise-linear	Piecewise-linear
Thermal Conductivity (W/m.K)	Piecewise-linear	Piecewise-linear
Cp Specific Heat (J/kg.K)	Piecewise-linear	Piecewise-linear
Density (kg/m³)	Piecewise-linear	Piecewise-linear
Molecular Weight (kg/kgmol)	18.02	18.63

Table 4-4: Boundary conditions with assumptions [7]

Boundaries	Conditions	Assumptions
Freeze tube	• Wall temperature - 257.15K • Non-slip stationary walls • Wall thickness – 5mm • Material – Aluminium	• Constant wall temperature at the freeze tube.
Container walls	• Adiabatic (Heat flux (W/m²) = 0) • Non-slip stationary walls	• Walls are assumed to be adiabatic with no heat transfer.
Top surface	• Natural convection • Heat transfer coefficient – 10 (W/m²K) • Non-slip stationary walls	• Natural convection for water to be in contact with air
Symmetry	• Symmetry has been set to only model $1/4^{th}$ of the geometry to decrease the computational time	• Solidification is assumed to occur evenly around the freeze tube

A coupled scheme has been used in the solution and the discretization settings are displayed in Table 4-5. The residual monitors used for energy was 1×10^{-11} and for continuity, velocity and saltwater mass fraction were 1×10^{-9}. A time step size of 0.001 with 20 iterations per time step was used for 480000 time steps to simulate the process for 8 minutes. The maximum time step size used was 0.001 after conducting time step size independency tests. [7]

Table 4-5: Discretization settings [7]

Spatial Discretization	Solution Method
Gradient	Least squares cell based
Pressure	PRESTO!
Momentum	Second order upwind
Energy	Second order upwind
Salt-water	Second order upwind
Transient formulation	First order implicit

The flow diagram of the CFD simulation process is shown in Figure 4-6 [7].
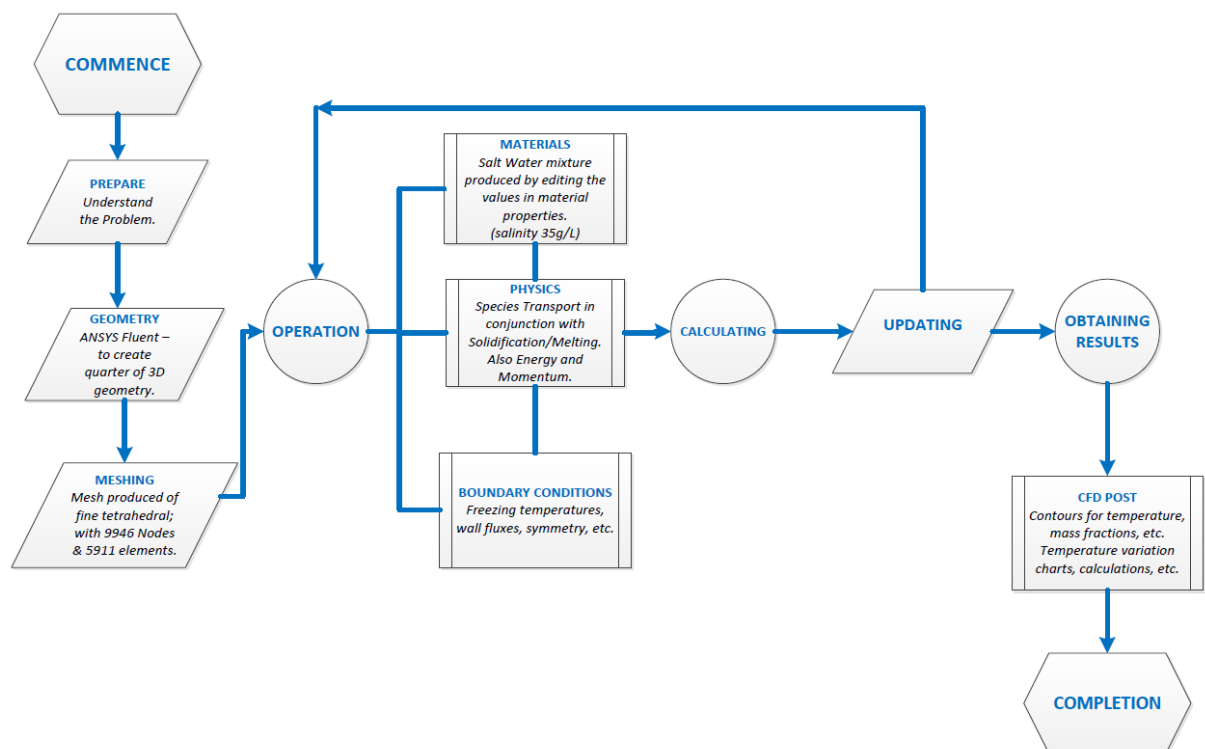
Figure 4-6: Flow diagram of the CFD simulation process [7]

4.6 CFD Results

Figure 4-7, Figure 4-8, Figure 4-9 and Figure 4-10 show the variation of temperature, liquid phase fraction, salt water mass fraction (salinity) and pure water mass fraction (salinity) respectively. The 3D contours and 2D variations from the edge of the freezing tube to the rest of the solution for 257.15K freezing temperature and 35g/L initial salt concentration (3.5% salinity) are displayed. The 2D variations are taken as the horizontal distance at the midpoint edge of the freezing tube to the rest of the solution. It is clear from Figure 4-7(a) that through the first 9mm distance from the tube edge the ice temperature is increasing at a faster rate than that through the second 9mm to reach 273.15K at 18mm indicating the end of the freezing zone. The distribution of temperature is clearly shown from the beginning of the ice layer to the rest of the solution in Figure 4-7(b) after 8 minutes of freezing. An ice layer of thickness 4.5mm is formed from each side and at the bottom of the ice layer, the temperature is recorded to be 257.15K while at the top edge of the ice layer, the temperature is about 265K. The temperature of the ice layer is rising from the bottom edge of the ice layer which is in contact with the freezing tube to the top edge of the ice layer which is in contact with the brine solution. Further away from the ice layer, the temperature rises to become constant throughout the rest of the brine solution. [7]
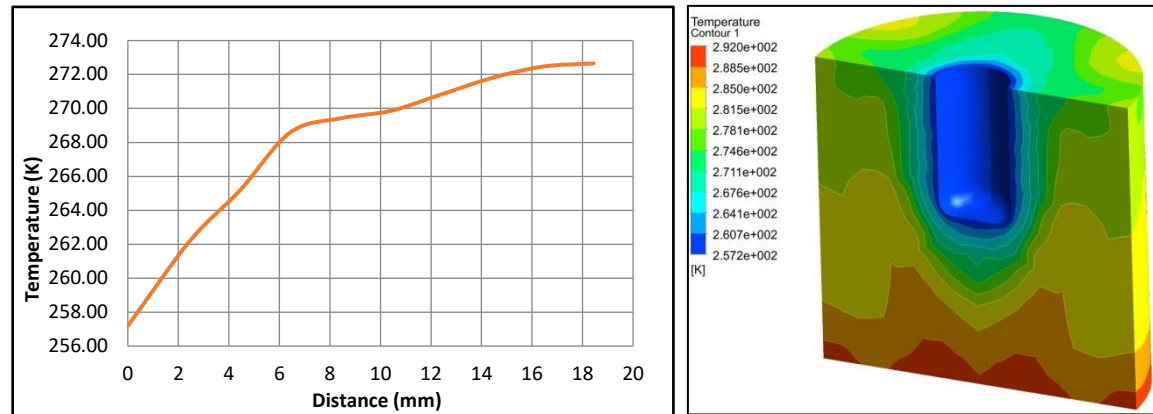
Figure 4-7: Water temperature variation against distance from the freezing tube edge (a) and temperature contours (b) [7]

The liquid phase fraction contours are displayed in Figure 4-8(b) and the formation of ice around the freezing tube is indicated by the blue region. The remaining brine is denoted by the red region while the liquid/solid mushy zone is shown by the intermediate colours in the contours. Hence the liquid fraction is defined by the solidification of water where the blue layer denotes minimum liquid fraction thus indicating a solidified section. The red region indicates the rest of the brine solution where a high amount of liquid fraction is seen, thus indicating a liquid region. Figure 4-8(a), displays the liquid phase fraction versus the distance from the edge of the freezing tube; where the solidification is distributed from the ice layer to the rest of the solution and from Figure 4-8(b) the measured thickness of ice obtained was 4.5mm. [7]
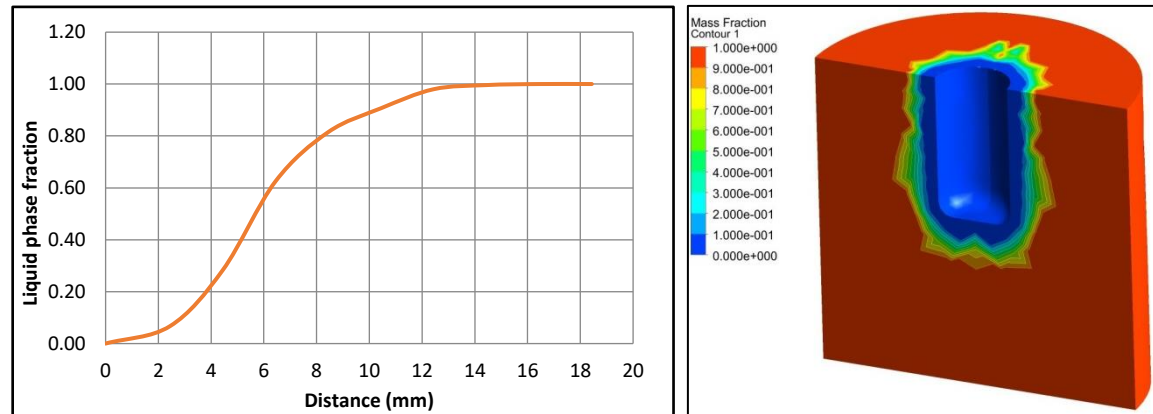
Figure 4-8: Liquid phase fraction against the distance from the freezing tube edge (a) and liquid phase fraction contours (b) [7]

After 8 minutes of freezing; the mass fraction of salt water contours is shown in Figure 4-9(b) where it can be seen that in the ice layer, the salt water mass fraction is minimal and in the rest of the solution it is high. The salt water mass fraction (salinity) distribution for the distance from the beginning of ice layer to the rest of the solution is shown in Figure 4-9(a). It is quite apparent from this figure that at the edge of the ice layer, the salt water salinity is about 2% and it increases to a maximum value of about 4.2% in the rest of the solution. The deviations seen in the salt water mass fraction are due to the thermal and solutal buoyancies. [7]
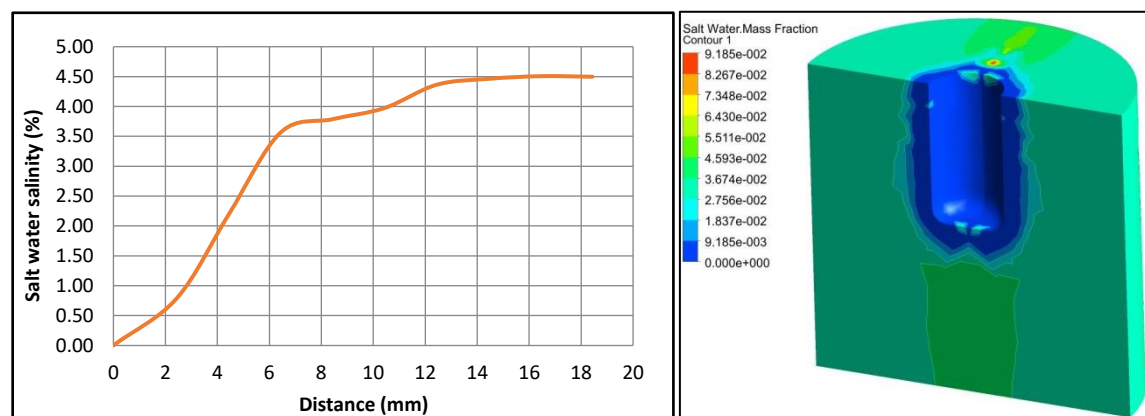
Figure 4-9: Salt water salinity against the distance from the freezing tube edge (a) and salt water mass fraction contours (b) [7]

In contrast to the mass fraction of salt water contours, the mass fraction of pure water contours is displayed in Figure 4-10(b) where in the ice layer, the pure water mass fraction is high and in the rest of the solution it is low. The pure water mass fraction distribution for the distance from the beginning of the ice layer to the rest of the solution is shown in Figure 4-10(a). It is clear that at the ice layer, the pure water mass fraction is very high, and it drops for the rest of the solution. The buoyancies cause the variation seen on the pure water mass fraction contours in Figure 4-10. [7]
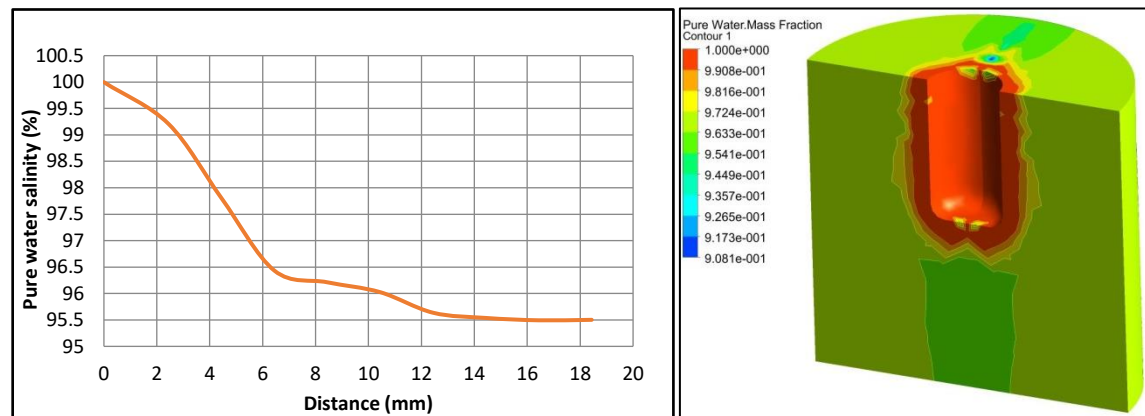
Figure 4-10: Pure water salinity against the distance from the freezing tube edge (a) and pure water mass fraction contours (b) [7]

4.7 CFD modelling validation

Figure 4-11 displays the temperatures measured using the thermocouples T1, T2 and T3 which were placed at different locations at the freezing tubes' surface. The average of these temperatures was then used as the set temperature for the CFD simulations. The thermocouple T4 is the temperature at which the ice was forming, and it was compared with the CFD results. Figure 4-11 shows the comparison between the measured and

modelled freezing tube surface temperatures (T1, T2 and T3) and the temperature change during the ice forming process (T4) with a maximum deviation value of 0.93% for temperature T4. [7]
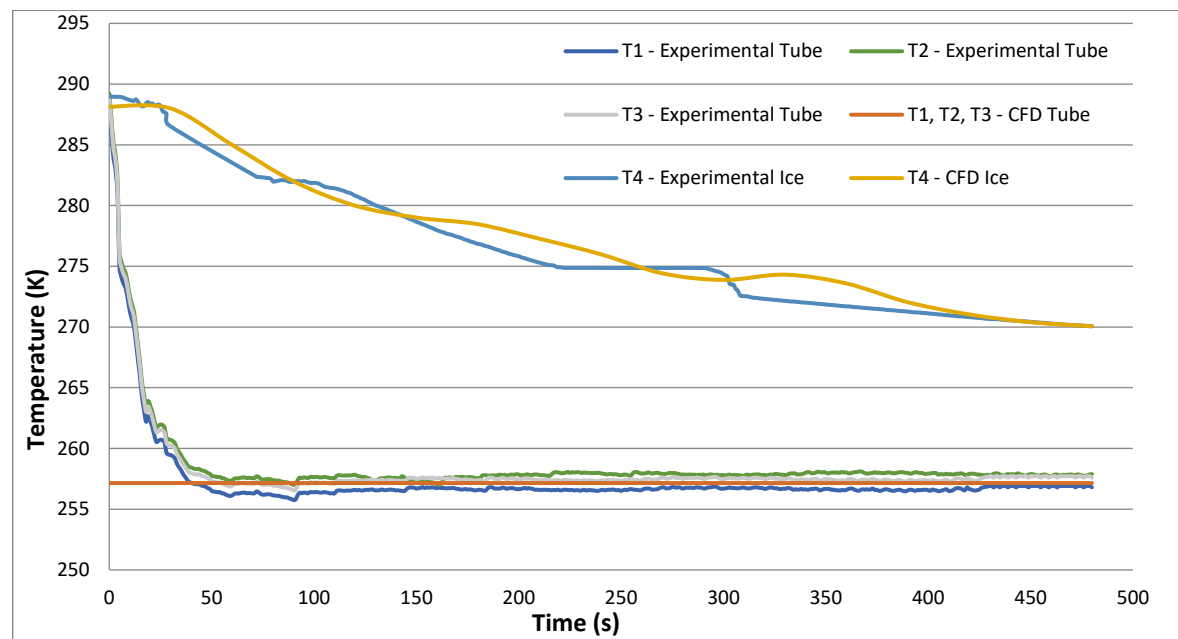
Figure 4-11: CFD and experimental comparison of temperature vs. time [7]

Table 4-6 compares the CFD and experimental results for ice and brine salinities obtained after freezing with different initial salt water salinities, 1.5%, 2.5%, 3.5% and 4.5% showing minimal percentage errors between the two to conclude the validation of the model. The volumes and the masses of ice obtained are also compared. It is quite apparent from Table 4-6, that the comparison between the CFD and experimental results shows good agreement. [7]

Table 4-6: CFD and experimental comparison for different initial salinity levels [7]

Parameters	Initial Salinity of Sea Water (%)											
	1.5			2.5			3.5			4.5		
	Exp.	CFD	% Error	Exp.	CFD	% Error	Exp.	CFD	% Error	Exp.	CFD	% Error
Ice Salinity (%)	1.1	1.08	1.82	2.1	1.88	10.48	3.0	2.55	15.00	3.6	3.11	13.61
Brine Salinity (%)	1.6	1.80	12.50	2.6	2.94	13.08	3.6	3.98	10.50	4.6	5.11	11.09
Volume per ice unit (mm³)	3900	4500	15.38	3600	4264	18.40	3300	3421	3.60	2700	2795	3.518
Mass per ice unit (g)	4.008	4.554	13.62	3.750	4.351	16.03	3.408	3.514	3.11	2.840	2.896	1.97

In order to reduce the ice salinity from 1.5% to below 0.1% which is recommended as safe to drink by the WHO [13], four freezing stages were carried out. Figure 4-12 displays the CFD and experimental comparison on ice salinity for each freezing stage.
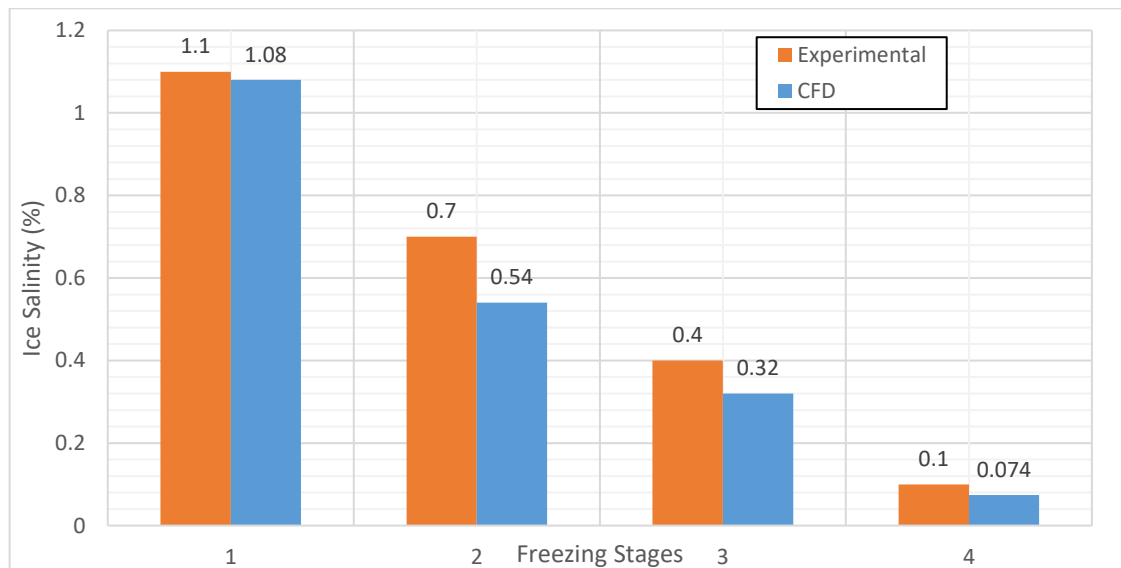
Figure 4-12: Freezing stages carried out to reduce ice salinity below 0.1%

4.8 CFD parametric analysis

In theory, the freeze desalination process is predicted to produce ice crystals which are pure but the ice quality is affected by many aspects during the freezing process. It was suggested that the ions could be expelled into brine of slight quantities of moderately frozen or completely unfrozen. Occasionally, these ions do get trapped into the ice crystal, in qualitative concurrence with the low solubility of salts in ice [53]. Luo et al [54] conducted a research on factors that affected the ice crystal quality during freezing where it was concluded that the rate of freezing, solid fraction, temperature of freezing and the concentration of the solution affected the ice quality. [7] Therefore, parametric study was carried out using the validated CFD model in order to investigate the effects of the freeze tube temperature and the initial salinity of salt water on ice production and the final salinities of ice and brine. [7] Parametric study has also been done on the geometry of the freezing tubes of the ice maker machine to investigate the effect of geometry on ice production. Table 4-7 and Table 4-8 display the volume of ice produced and the required energy calculated using equations (4-1) and (4-2) at various freeze tube temperatures and various initial salinities of the salt water respectively.

Table 4-7: Case studies with input, output and boundary conditions for different freezing temperatures [7]

Parametric Analysis for Different Freezing Temperatures				
Jobs	**Input data**	**Boundary Conditions and Factors**	**Energy Required (J)**	**Output Results**
270K	270K of freezing temp.	Adiabatic (Heat flux (W/m^2) = 0) and non-slip stationary walls. Initial Sea water temperature = 288.15K and salinity = 3.5%.	618.75	Volume of ice produced (mm^3) - 0
265K	265K of freezing temp.	Adiabatic (Heat flux (W/m^2) = 0) and non-slip stationary walls. Initial Sea water temperature = 288.15K and salinity = 3.5%.	1419.90	Volume of ice produced (mm^3) - 1235.79
257.15K	257K of freezing temp.	Adiabatic (Heat flux (W/m^2) = 0) and non-slip stationary walls. Initial Sea water temperature = 288.15K and salinity = 3.5%.	4004.06	Volume of ice produced (mm^3) - 3421.04
245K	245K of freezing temp.	Adiabatic (Heat flux (W/m^2) = 0) and non-slip stationary walls. Initial Sea water temperature = 288.15K and salinity = 3.5%.	5898.53	Volume of ice produced (mm^3) - 7189.83
235K	235K of freezing temp.	Adiabatic (Heat flux (W/m^2) = 0) and non-slip stationary walls. Initial Sea water temperature = 288.15K and salinity = 3.5%.	6762.44	Volume of ice produced (mm^3) - 8093.43
225K	235K of freezing temp.	Adiabatic (Heat flux (W/m^2) = 0) and non-slip stationary walls. Initial Sea water temperature = 288.15K and salinity = 3.5%.	10223.71	Volume of ice produced (mm^3) - 17315.42

It is seen in Table 4-7 that when the freezing temperature is reduced, the volume of ice obtained increases, and also the energy required to reduce the temperature increases. In Table 4-8, it is evident that increasing the initial salinity of the salt water would reduce the amount of ice produced. Since the temperature is constant when varying the initial salinity of salt water, the energy required does not change to a great deal.

Table 4-8: Case studies with input, output and boundary conditions for different initial salt water concentrations [7]

Parametric Analysis for Different Initial Salinities			
Jobs	**Input data**	**Boundary Conditions and Factors**	**Output Results**
15g/L	1.5% of initial salinity	Adiabatic (Heat flux $(W/m^2) = 0$) and non-slip stationary walls. Initial Sea water temperature = 288.15K. Freeze tube temperature = 257.15K.	Volume of ice produced (mm^3) - 4500.21
25g/L	2.5% of initial salinity	Adiabatic (Heat flux $(W/m^2) = 0$) and non-slip stationary walls. Initial Sea water temperature = 288.15K. Freeze tube temperature = 257.15K.	Volume of ice produced (mm^3) - 4264.04
35g/L	3.5% of initial salinity	Adiabatic (Heat flux $(W/m^2) = 0$) and non-slip stationary walls. Initial Sea water temperature = 288.15K. Freeze tube temperature = 257.15K.	Volume of ice produced (mm^3) - 3421.04
45g/L	4.5% of initial salinity	Adiabatic (Heat flux $(W/m^2) = 0$) and non-slip stationary walls. Initial Sea water temperature = 288.15K. Freeze tube temperature = 257.15K.	Volume of ice produced (mm^3) - 2795.99

4.8.1 Effect of freezing temperature

The contours for the salt water temperature, liquid phase fraction and the mass fraction of salt water are presented in Figure 4-13 for the various freezing temperatures of 265K, 257.15K, 245K, 235K and 225K.
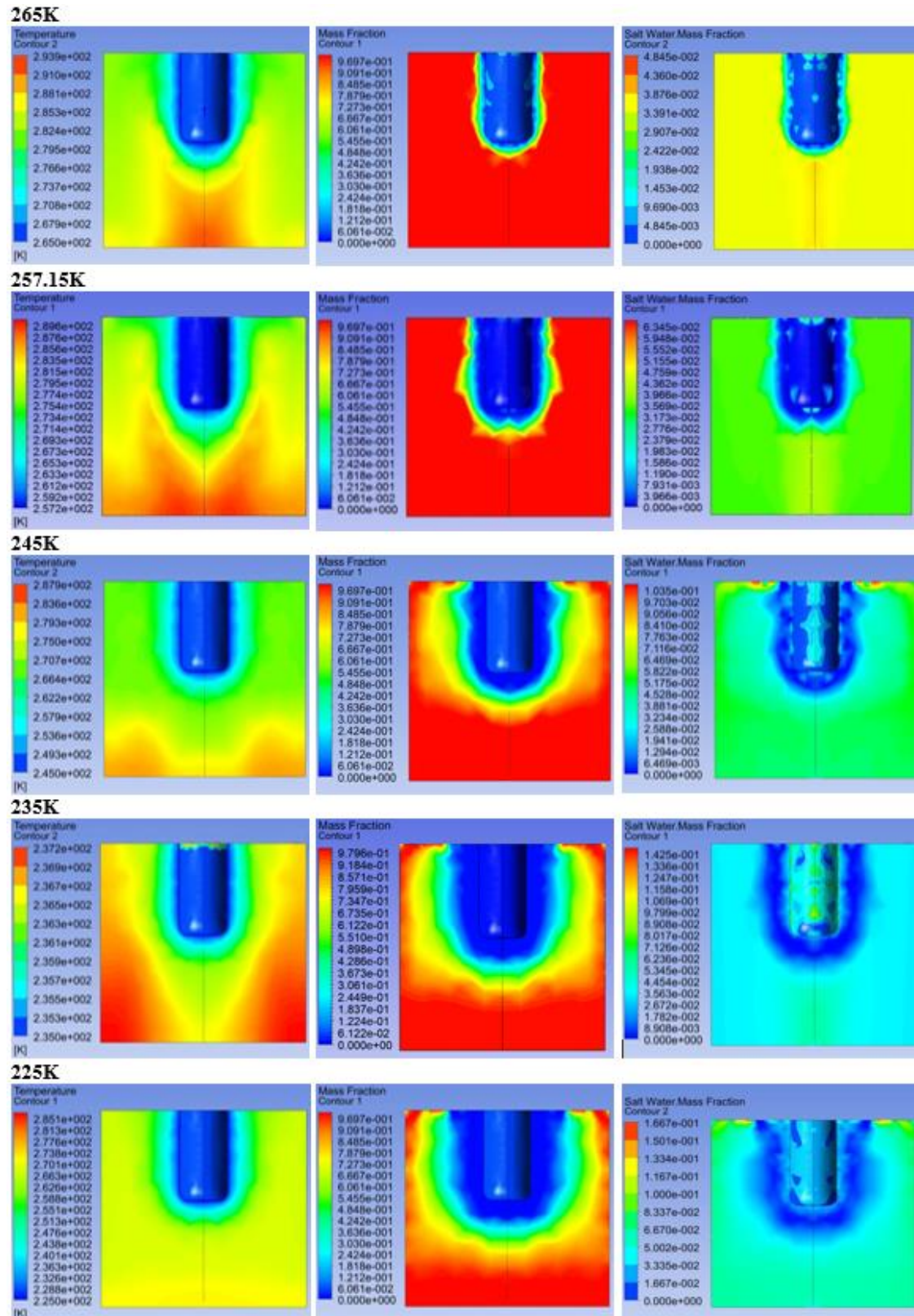
Figure 4-13: Temperature (left), liquid phase fraction (middle) and salt water mass fraction (right) contours for freezing temperatures of 265K, 257.15K, 245K, 235K and 225K [7]

It can be seen that decreasing the freezing temperature increases the solidification of water, also the size of liquid phase fraction regions (blue layer) are increasing as the freezing temperatures decreases leading to larger volumes of produced ice. Hence, 265K, 257.15K, 245K, 235K and 225K freezing temperatures produced 1235.79, 3421.04, 7189.83, 8093.43 and 17315.42 mm^3 of ice respectively after 8 minutes of freezing, as presented in Figure 4-14. It is clear from this figure that 225K freeze tube temperature produced about 5 times more ice than the 257.15K freeze tube temperature that the ice maker usually operates at. [7]
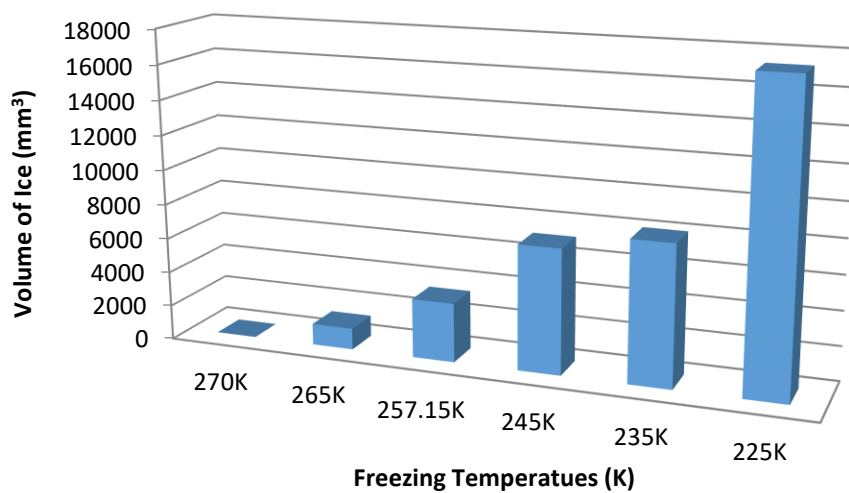
Figure 4-14: Volume of ice obtained at different freezing temperatures [7]

The salinities of the ice and brine after the freezing process have been compared for different freezing temperatures in Figure 4-15. The ice salinities obtained for the freezing temperatures of 265K, 257.15K, 245K, 235K and 225K were 2.29%, 2.55%, 2.63%, 2.77% and 3.02% respectively. It is seen that at higher freezing temperatures, the produced ice is with lower salinities; where 225K freezing temperature produced 18.43% less purer ice compared to the standard freezing temperature of 257.15K. This trend can be explained

because at lower freezing temperatures, the difference in temperature between the salt water and the freezing tube increases. This gradually surges the heat transfer and enables the formation of ice much faster, thus causing less time for the salt in the water to be detached from the ice. This therefore ensures that more salt remains in the ice that is formed around the freezing tube [11]. Figure 4-15 also compares the salinities of the remaining brine at the various freezing temperatures mentioned above. It was shown in Figure 4-13 that as the freezing temperature is reduced, the mass fraction of brine increases in the remaining solution while the ice production rises. Hence, the final brine salinities for the freezing tube temperatures of 265K, 257.15K, 245K, 235K and 225K become 3.45%, 3.98%, 4.52%, 5.18% and 5.51% respectively. The reason behind this being; as the freezing tube temperature decreases, the volume of ice produced increases, thus only a small volume of liquid or brine which is of high concentration remains. [7]
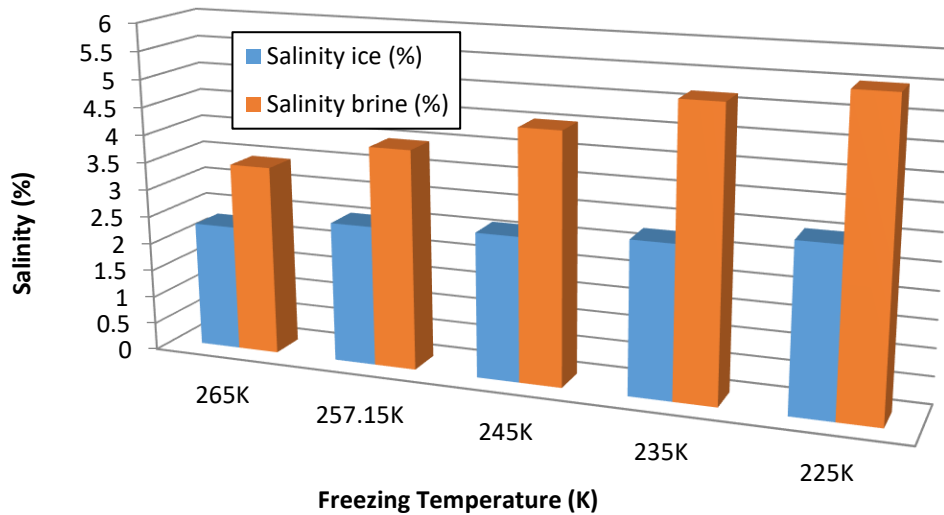
Figure 4-15: Ice and brine salinities obtained at different freeze tube temperatures [7]

4.8.2 Salinity

Parametric study was then conducted by changing the initial salt water salinity from 1.5%, 2.5%, 3.5% and 4.5% to observe the effect of ice production and the salinities of ice and brine. The volumes of ice produced for 1.5%, 2.5%, 3.5% and 4.5% salt water concentrations were 4500.21, 4264.04, 3421.04 and 2795.99mm^3 respectively (as shown in Table 4-6) which indicates that as the initial salt water concentration decreases, the volumes of ice produced increases. This can be explained as at higher salt water concentrations the ice crystals become less pure and slow the freezing process. It is also reported by Williams et al [98] that the initial concentration of the salt water had a considerable effect on rejecting salt and the water recovery ratios. [7]

Figure 4-16, Figure 4-17 and Figure 4-18 show the variation of temperature, liquid phase fraction and salt water mass fraction (salinity) versus the distance from the surface of the freezing tube. In Figure 4-16, the first 9mm distance from the tube edge appears to have a greater increase in rate of temperature compared to the second 9mm. The ice layer thickness is high for lower freezing temperatures and the increase in temperature from the bottom of the ice layer to the top of the ice layer for all freezing temperatures follows a similar pattern. The temperature appears to be constant for the rest of the brine solution away from the ice layer. Figure 4-17 displays the liquid phase fraction at different freezing temperatures where the ice layer thickness increases for lower freezing temperatures, thus it can be concluded that lower freezing temperatures would generate a larger volume of ice. Figure 4-18 displays the salt water mass fraction (salinity) for the distance from the edge of the freezing tube and it is seen that at higher freezing temperatures, the salinity of ice is low in comparison to when freezing at lower temperatures. [7]
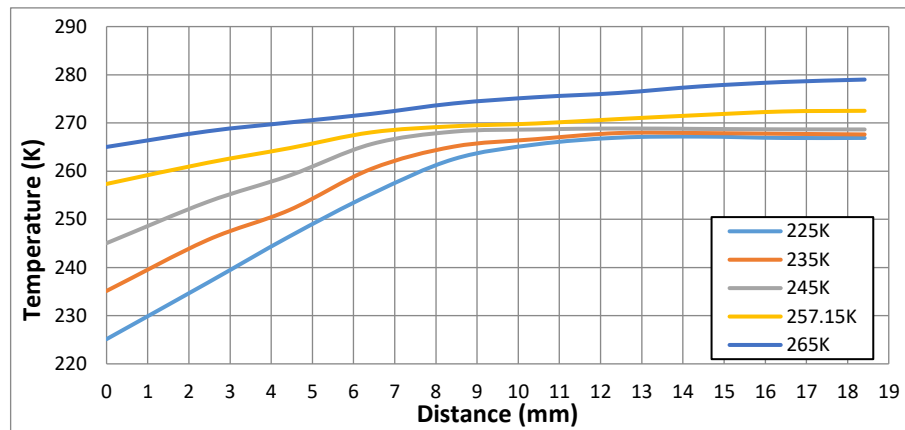
Figure 4-16: Water temperature variation against distance from the freezing tube edge for different freezing temperatures [7]
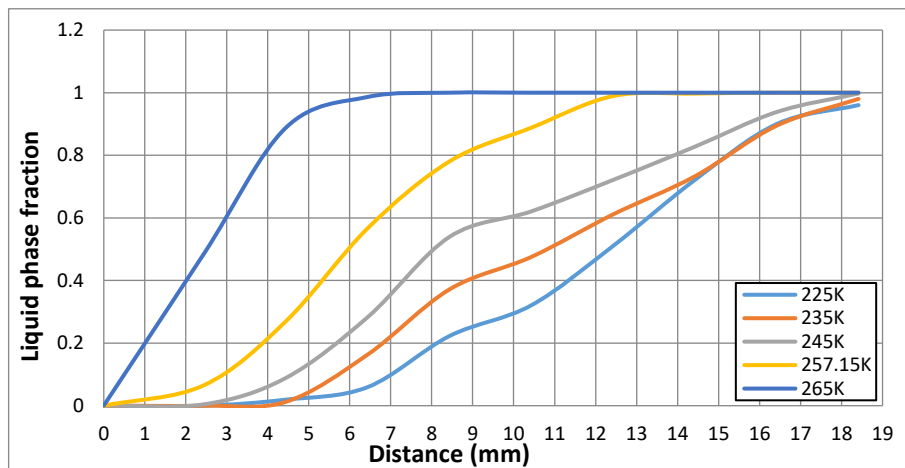
Figure 4-17: Liquid phase fraction against the distance from the freezing tube edge for different freezing temperatures [7]

4.8.3 Second stage of freezing

It is clear from Figure 4-18, that freezing temperatures of 245K, 257.15K and 265K seem

to produce ice with lower average salinities of 0.50, 0.53 and 0.48% at a thickness of 3.3,

2.5 and 0.7mm respectively from the freezing tube as shown in Figure 4-19. Therefore,

Figure 4-19 displays the thickness of ice for ice salinities below 1.0% for freezing

temperatures from 245K to 265K.
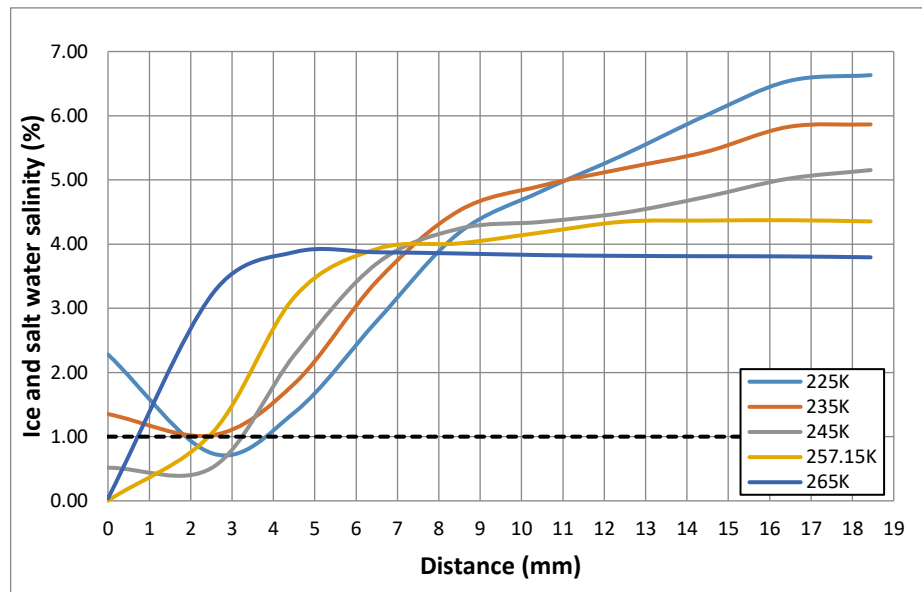
Figure 4-18: Ice and salt water salinity against the distance from the freezing tube edge for different freezing temperatures (3.5% initial salinity) [7]
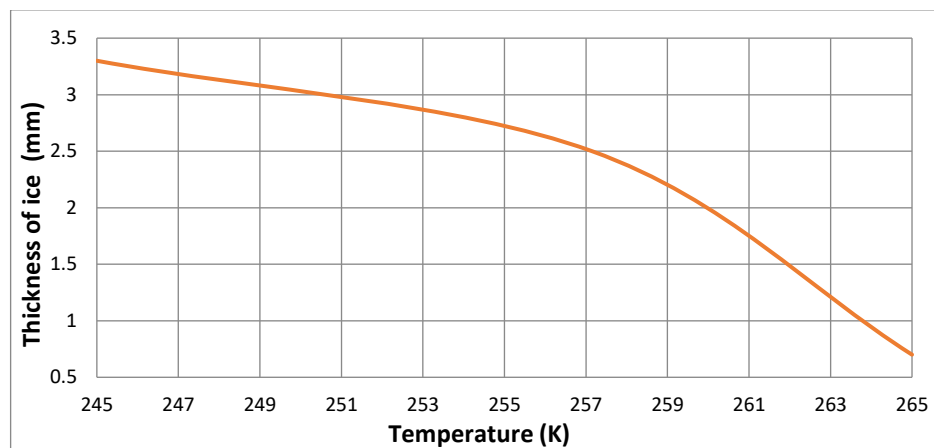
Figure 4-19: Thickness of ice for ice salinities below 1.0% vs. temperature [7]

Although such salinity levels are low but they are still higher than the accepted salinity levels of 0.1% regarded as fresh and safe to drink by the WHO [13]. As displayed in Figure 4-18, the average salinity of ice achieved was about 0.5%, so in order to produce purer ice with accepted salinity level of less than 0.1%, then the produced water of 0.5% salinity was used to conduct a second stage of freeze desalination using the freezing temperatures of

215K, 225K, 235K and 245K. The 245K freezing temperature was chosen as it gave the least average ice salinity below the 1.0% salinity mark and therefore, freezing temperatures below 245K were then taken in order to quickly desalinate the 0.5% salinity of sea water to give a larger volume of ice. Figure 4-20 shows the output salinity levels from the edge of freezing tube at temperatures of 215K, 225K, 235K and 245K using initial salt water salinity of 0.5%. It is clear from this figure that salinity of 0.1% was achieved at temperatures of 215K, 225K, 235K and 245K giving an ice thickness of 7.3, 7.6, 6.8 and 5.4mm respectively. The volumes of this pure ice (below 0.1%) are shown in Figure 4-21 with highest ice volume of 12329.24mm^3 achieved at 225K. Figure 4-22 shows the average ice salinities over the whole region starting from the freezing surface up to the 0.1% mark for the temperatures shown in Figure 4-20. It is clear from this figure that all the average salinities are below 0.05% (500mg/l) which is regarded as good quality drinking water by the WHO [13]. [2]
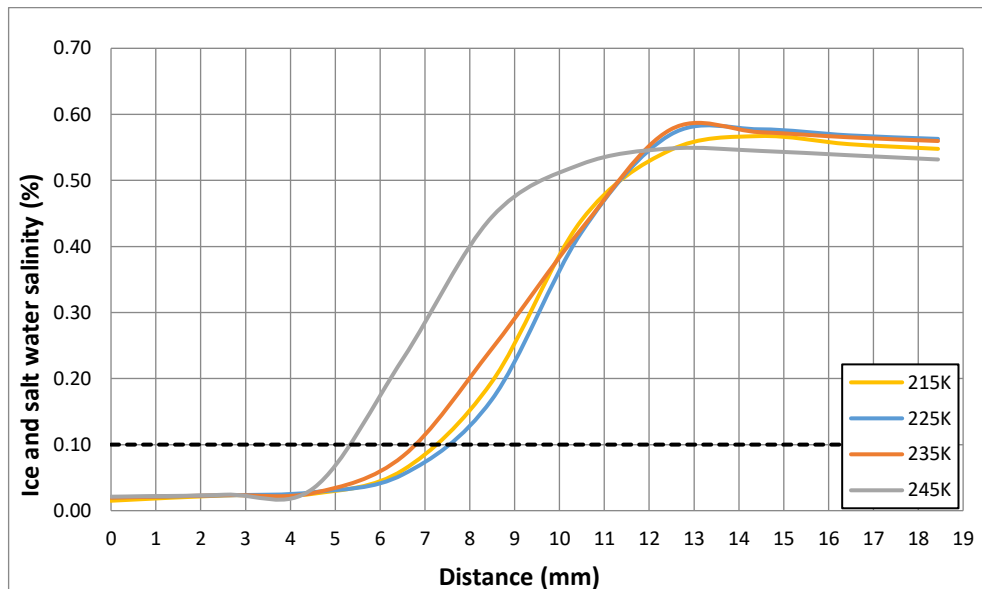
Figure 4-20: Ice and salt water salinity from the edge of the freezing tube at different freezing temperatures (0.5% initial salinity) [7]
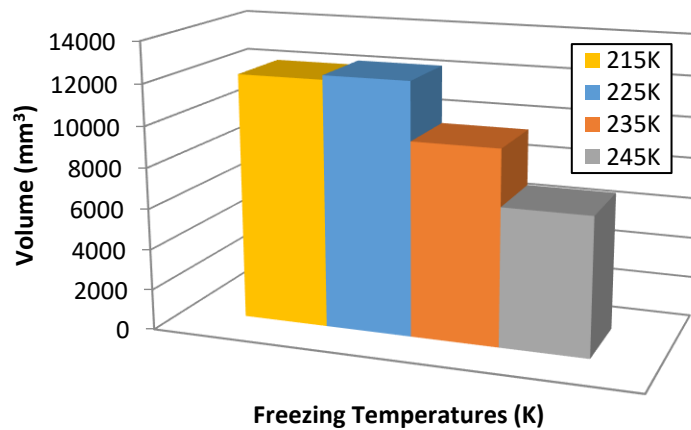
Figure 4-21: Volume of ice obtained below 0.1% salinity for different freezing temperatures [7]
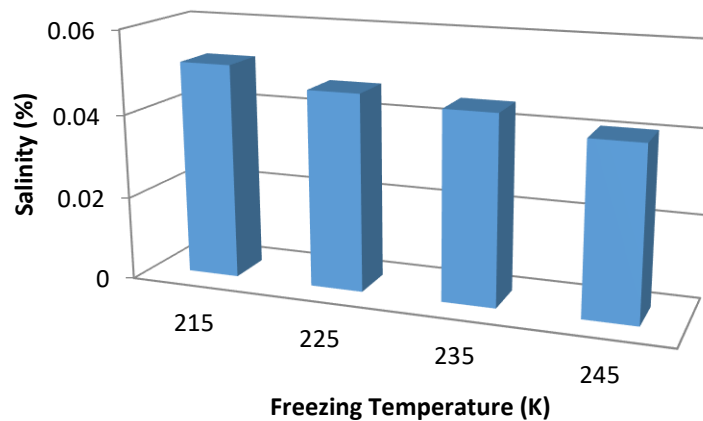
Figure 4-22: The average salinity of ice formed at different freezing temperature [7]

4.8.4 Geometry of the freezing tube

The geometry of the freezing surface of a single freezing tube has been changed to investigate the effect on ice production. The freezing temperature was constant at 260K and the initial salinity was 35g/L. Changing the diameter and the length of the freezing tube have been investigated and the performance of this study is summarised in Figure 4-23. The liquid phase fraction contours are shown in Figure 4-24 and Figure 4-25 for the change

in diameter and length respectively for a single freezing tube. The produced ice volumes for freezing tube diameters 5mm and 20mm were 842mm^3 and 3188mm^3 respectively. Increasing the length of the freezing tube generated more ice, where a 10mm and a 20mm length produced 1267mm^3 and 2770mm^3 of ice respectively. Increasing the diameter and the length of the freezing tube, increased the volume of ice produced as this increased the total freezing surface area [14]. The heat transfer rate in the freeze tube is proportional to the power consumption; therefore, the geometry must be selected with a low heat transfer rate and a high volume of ice. Hence, it is seen that, the 20mm diameter with a 15mm length is the best geometry to use and it is 2.8 times better in terms of heat transfer rate over ice production compared to the 5mm diameter with a 15mm length geometry. Furthermore, the design of the ice maker and the space allocated for the freezing tubes must also be taken into consideration when choosing the best geometry. Having 5 freezing tubes of 10mm diameter with a 20mm length dimensions would produce 9.3% more water than having 10 freezing tubes of 10mm diameter with a 10mm length.
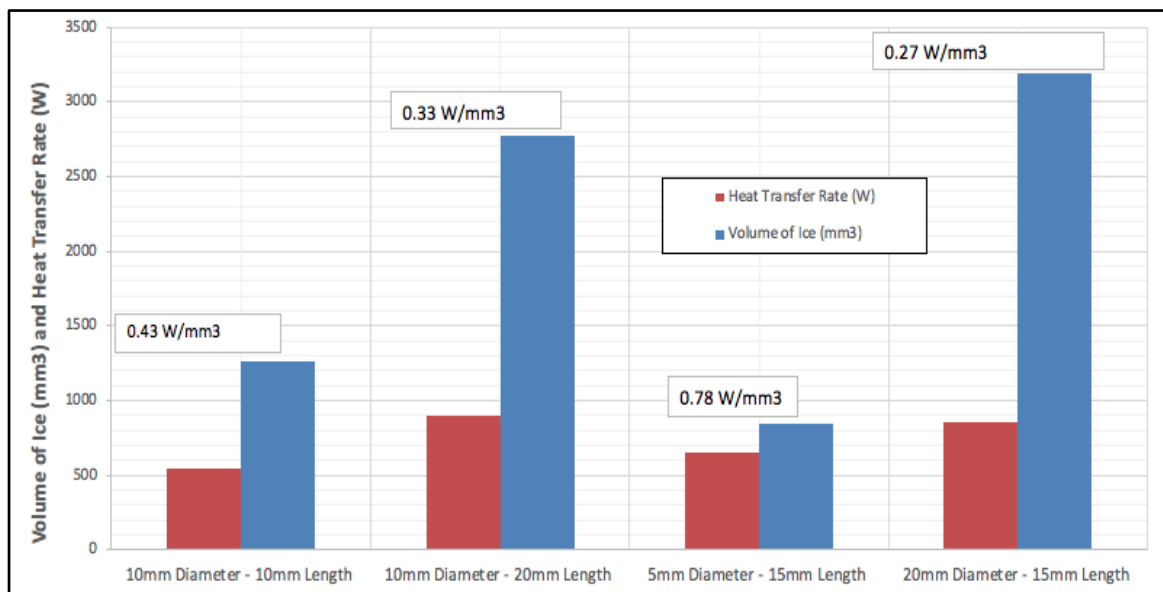
Figure 4-23: Performance of the geometry of the freezing tubes
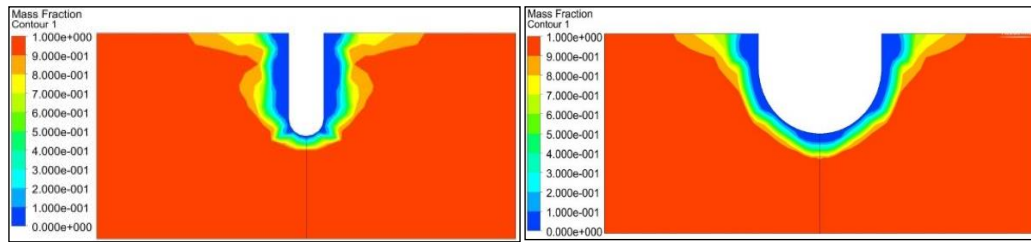
Figure 4-24: Liquid phase fraction contours for 5mm diameter (left) and 20mm diameter (right) [14]
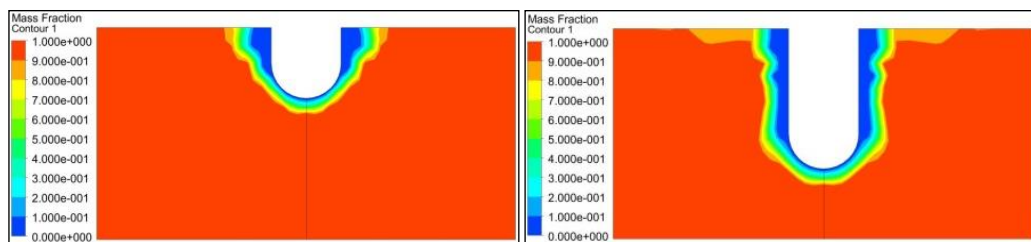
Figure 4-25: Liquid phase fraction contours for 10mm length (left) and 20mm length (right) [14]

4.9 Summary

The feasibility of using an ice maker machine as a portable application to produce potable water is investigated. The ice maker offers potential as a small scale desalination system in portable applications such as domestic houses, schools, local shops and hospitals. Experimental testing has been conducted using a commercially available ice maker machine and numerical modelling has been done on CFD to carry out parametric study on temperature, salinity and the geometry of the ice maker machine. The overall efficiency was 0.42 to freeze a 3.5% salt water solution to produce one batch of ice using the ice maker machine. In the validation process of experimental and CFD, the results showed average deviations of $\pm 4.6K$ and $\pm 0.56K$ for the freezing tube temperature and the temperature

change of the ice forming respectively. Additionally, the percentage errors obtained for the salinities of ice and brine obtained were 15% and 10.5% respectively indicating good agreement between the two. [7]

Parametric analysis was then carried out using the validated CFD model in order to observe the effects of the freeze tube temperature and the initial salinity of salt water on ice production and the final salinities of ice and brine. Results showed that as the freezing temperature decreases, the production of ice increases due to low temperature causing a faster rate of freezing and an improved solidification rate for salt water. At 225K freeze tube temperature, 5 times more ice was produced in comparison to the standard 257.15K freeze tube temperature that the ice maker usually operates at. Additionally, the lowest average salinity achieved was 0.5% at 245K freezing temperature for an ice thickness of 3.3mm, which is higher than the 0.1% recommended by the WHO as safe to drink water [13]. Therefore, a second stage of freezing process was applied to this 0.5% to produce a salinity level below the required 0.1%. Results showed that salinity of 0.1% was achieved at temperatures of 215K, 225K, 235K and 245K with pure ice volumes of 12114.40, 12329.24, 9516.39 and 6785.36mm^3 respectively. Results also showed that the average ice salinity for the second stage of freezing was below 0.05% which is regarded as good quality drinking water. Such results highlight the potential of using freeze desalination to produce drinking water. [7] Parametric study has also been conducted on the geometry of the freezing tubes of the ice maker machine on the volume of ice produced. It is observed that, increasing the diameter and the length of the freezing tube, generated more ice due to the increase in freezing surface area. The 20mm diameter with a 15mm length is the best freezing tube geometry and it is 2.8 times better in terms of heat transfer rate over ice

production compared to the 5mm diameter with a 15mm length geometry. Additionally, having 5 freezing tubes of 10mm diameter with a 20mm length dimensions would produce 9.3% more water than having 10 freezing tubes of 10mm diameter with a 10mm length.

Further research using cryogenic energy storage such as that of liquefied natural gas (LNG) and stored liquefied LN_2/L_{air} for the process of freeze desalination is investigated, as this shows great potential to obtain fresh water efficiently. This process is explored by evaporating LN_2 to N_2 while concurrently freezing sea water to attain fresh water as this proves to be a promising technique. This method has been implemented and further discussed in chapter 5.

CHAPTER 5

5. EVAPORATION OF LIQUID NITROGEN FOR FREEZE DESALINATION

5.1 Introduction

In this chapter, the use of liquid nitrogen for freeze desalination has been studied. Many researchers have looked into the use of cryogenics as a source of energy for many applications such as cooling for domestic and industrial processes and driving turbines and engines for power generation [144]–[148]. Cryogenic energy has also been utilised in freeze desalination by few researchers [11], [32], [35]. However numerical modelling of using cryogenic energy for freeze desalination has not yet been investigated and the use of the evaporation of liquid nitrogen for indirect contact freeze desalination has not yet been investigated. Therefore, this chapter focuses on the evaporation of liquid nitrogen for indirect contact freeze desalination. Computational fluid dynamics (CFD) analysis of this process is carried out and an experimental test rig has been built to further understand this process and validate the CFD model. This chapter consists of two sections, firstly the CFD modelling and secondly, the experimental testing to validate the CFD model.

Literature on CFD modelling of the evaporation of liquid nitrogen is very limited. Therefore, CFD modelling of the evaporation of liquid nitrogen as a source of cooling for the freeze desalination process was established. Firstly, the theoretical background of the CFD simulation of the evaporation of LN_2 processes is described in this chapter.

5.2 CFD theory of the evaporation of liquid nitrogen process

The liquid nitrogen turns from liquid to nitrogen gas in the evaporation process of LN_2. Therefore, for modelling the evaporation process where the fluid changes phase (liquid to gas); the multiphase model in ANSYS is used. Additionally, the energy and the turbulent models were used to determine temperature variation during the turbulent flow of the fluid. In the ANSYS multiphase module, three different 'Euler-Euler multiphase' models are offered: the Eulerian model, the mixture model and the volume of fluid (VOF) model [136]. All of these 'Euler-Euler multiphase' models can be used to model the evaporation of liquid nitrogen. However, only the volume of fluid (VOF) can be used in conjunction with the solidification/melting model that is used to model the freeze desalination process. Therefore, when simulating the evaporation of liquid nitrogen simultaneously with the freeze desalination modelling, only the VOF option in the multiphase model can be used.

5.2.1 Euler-Euler multiphase models

Multiphase mixture model

This multiphase model is able to model multiphase flows where the phases travel at various speeds, but assume local equilibrium over short spatial length scales [136]. Homogeneous multiphase flows where the phases move at the same speeds and with very strong coupling can also be modelled [136]. By solving energy, momentum and continuity equations for the mixture, algebraic expressions for the relative speeds, and volume fraction equations for the secondary phases is the approach that the mixture model can model phases. Key processes that the mixture model is able to model are: bubbly flows where the gas volume fraction stays low, cyclone separators, sedimentation, and particle-laden flows with low

loading [136]. When using the mixture model, it is able to run the model with more than one domain, without causing any major issues. Conversely, in order to obtain results close to the experimental results, the evaporation frequency must be altered by trial and error. Additionally, the Lee model is used to model the interphase mass transfer through evaporation-condensation [136].

In the mixture model, the continuity equation is denoted by equation (5-1) [136].

$$\frac{d}{dt}(\rho_m) + \nabla \cdot (\rho_m \overrightarrow{v_m}) = 0 \qquad \text{5-1}$$

where, the mixture density ρ_m is denoted by equation (5-2) and α_k is the volume fraction of phase k,

$$\rho_m = \sum_{k=1}^{n} \alpha_k \rho_k \qquad \text{5-2}$$

and the mass-averaged velocity $\overrightarrow{v_m}$ is denoted by equation (5-3).

$$\overrightarrow{v_m} = \frac{\sum_{k=1}^{n} \alpha_k \rho_k \vec{v}_k}{\rho_m} \qquad \text{5-3}$$

In the mixture model, the momentum equation can be obtained by adding all the individual momentum equations for all phases, as shown in equation (5-4) [136].

$$\frac{d}{dt}(\rho_m \overrightarrow{v_m}) + \nabla \cdot (\rho_m \overrightarrow{v_m} \, \overrightarrow{v_m}) = -\nabla_p + \nabla \cdot [\mu_m (\nabla \overrightarrow{v_m} + \nabla \vec{v}_m^T)] + \rho_m \vec{g} + \vec{F} +$$

$$\nabla \cdot (\sum_{k=1}^{n} \alpha_k \, \rho_k \vec{v}_{dr,k} \vec{v}_{dr,k}) \qquad \text{5-4}$$

where, μ_m is the mixture viscosity denoted by equation (5-5), $\vec{F}$ is the body force and n is the number of phases.

$$\mu_m = \sum_{k=1}^{n} \alpha_k \mu_k \qquad \text{5-5}$$

For the secondary phase k, the drift velocity $\vec{v}_{dr,k}$ is found by equation (5-6).

$$\vec{v}_{dr,k} = \vec{v}_k - \vec{v}_m \qquad\qquad 5\text{-}6$$

In the mixture model, the energy equation is shown in equation (5-7) [136].

$$\frac{d}{dt}\sum_{k=1}^{n}(\alpha_k \rho_k E_k) + \nabla.\sum_{k=1}^{n}\left(\alpha_k \vec{v}_k(\rho_k E_k + p)\right) = \nabla.\left(k_{eff}\nabla T\right) + S_E \qquad\qquad 5\text{-}7$$

where, the effective conductivity is denoted as k_{eff} which is $(\sum \alpha_k(k_k + k_t))$. k_t is the turbulent thermal conductivity. S_E represents any other volumetric heat sources and for a compressible phase E_k is denoted in equation (5-8).

$$E_k = h_k - \frac{p}{\rho_k} + \frac{v_k^2}{2} \qquad\qquad 5\text{-}8$$

$\frac{v_k^2}{2}$ denotes the energy transfer due to conduction. For an incompressible phase, equation (5-8) simplifies to $E_k = h_k$, where h_k is the sensible enthalpy for phase k.

In the mixture model, for volume fraction equation for secondary phase p can be obtained from the continuity equation, as shown in equation (5-9) [136].

$$\frac{d}{dt}\left(\alpha_p \rho_p\right) + \nabla.\left(\alpha_p \rho_p \vec{v}_m\right) = -\nabla.\left(\alpha_p \rho_p \vec{v}_{dr,p}\right) + \sum_{q=1}^{n}(\dot{m}_{qp} - \dot{m}_{pq}) \qquad\qquad 5\text{-}9$$

In the mixture model for the evaporation of liquid nitrogen, the evaporation-condensation model is enabled. The Lee model is used to model the interphase mass transfer through evaporation-condensation and liquid-vapour mass transfer is directed by the vapour transport equation (5-10) [136].

$$\frac{d}{dt}\left(\alpha_v \rho_v\right) + \nabla.\left(\alpha_v \rho_v \vec{V_v}\right) = \dot{m}_{lv} - \dot{m}_{vl} \qquad\qquad 5\text{-}10$$

where, α_v is the vapour volume fraction, ρ_v is the vapour density, v is the vapour phase and $\vec{V_v}$ is the vapour phase velocity. $\dot{m}_{lv}$ and $\dot{m}_{vl}$ are the rates of mass transfer due to evaporation and condensation respectively.

The mass transfer can be explained as shown in equation (5-11), for evaporation.

If $T_l > T_{sat}$ (evaporation):

$$\dot{m}_{lv} = coeff * \alpha_l \rho_l \frac{T_l - T_{sat}}{T_{sat}} \qquad 5\text{-}11$$

where, $coeff$ is a coefficient given in equation (5-12) but should be fine-tuned and can be deduced as a relaxation time. The phase volume fraction and density are denoted by α and ρ respectively.

$$coeff = \frac{6}{d_b} \beta \sqrt{\frac{M}{2\pi R T T_{sat}}} L \left(\frac{\alpha_v \rho_v}{\rho_l - \rho_v} \right) \qquad 5\text{-}12$$

where, R is the universal gas constant, L is the latent heat, d_b is the bubble diameter, T is the temperature and β is the accommodation coefficient that indicates the portion of vapour molecules moving into the liquid surface and adsorbed by this surface [136].

When, modelling the evaporation of liquid nitrogen, the liquid nitrogen (LN$_2$) was the primary phase and the nitrogen gas (N$_2$) was the secondary phase. Subject to different temperatures and pressures, the properties of the primary (LN$_2$) and secondary (N$_2$) phases varied. This data was collected from the property tables and charts shown in Appendix B.

Multiphase volume of fluid (VOF) model

By solving a single set of momentum equations and tracking the volume fraction of each of the fluids in the field, the VOF model is able to model two or more immiscible fluids

[136]. Key processes that the VOF model is able to model are: steady/transient tracking of any liquid-gas interface, motion of bubbles in a liquid, prediction of jet breakup, etc. [136]. In the VOF model, the tracking of the interfaces between the phases is achieved by using the continuity equation for the volume fraction of one or more of the phases. Hence, equation (5-13) represents this for the qth phase [136].

$$\frac{1}{\rho_q}\left[\frac{d}{dt}\left(\alpha_q\rho_q\right) + \nabla.\left(\alpha_q\rho_q\vec{v}_q\right) = S_{\alpha_q} + \sum_{p=1}^{n}\left(\dot{m}_{pq} - \dot{m}_{qp}\right)\right]$$

5-13

where, the mass transfer from phase p to phase q is denoted as $\dot{m}_{pq}$ and the mass transfer from phase q to phase p is denoted as $\dot{m}_{qp}$. S_{α_q} is a source term which is zero by default but a user-defined mass source for each phase can be specified.

For the primary phase, the volume fraction equation will not be solved; based on the following constraint, the primary-phase volume fraction will be calculated:

$\sum_{q=1}^{n}\alpha_q = 1$. Through implicit or explicit time discretization, the volume fraction equation is solved [136].

In the VOF model, a single momentum equation is solved and the subsequent velocity field is shared amid the phases. The momentum equation is dependent on the volume fractions of all phases via the properties μ and ρ, as shown in equation (5-14) [136].

$$\frac{d}{dt}(\rho\vec{v}) + \nabla.(\rho\vec{v}\vec{v}) = -\nabla_p + \nabla.[\mu(\nabla\vec{v} + \nabla\vec{v}^T)] + \rho\vec{g} + \vec{F}$$

5-14

In the VOF model, the energy equation (5-15), is shared among the phases [136].

$$\frac{d}{dt}(\rho E) + \nabla.\left(\vec{v}(\rho E + p)\right) = \nabla.\left(k_{eff}\nabla T\right) + S_h$$

5-15

Energy E (equation (5-16)) and temperature T are treated as mass-averaged variables in the VOF model.

$$E = \frac{\sum_{q=1}^{n} \alpha_q \rho_q E_q}{\sum_{q=1}^{n} \alpha_q \rho_q}$$ 5-16

where, the specific heat of that phase and the shared temperature are what E_q for each phase is based on [136]. The effective thermal conductivity k_{eff} and ρ are shared by the phases. Influences from radiation and any other volumetric heat sources are what the source term S_h comprises [136].

When modelling the evaporation of liquid nitrogen in conjunction with the freeze desalination process, the VOF model has been utilised.

Multiphase Eulerian model

The Eulerian model can be used only in the evaporation of liquid nitrogen process separately and this model has not been used in this research. Modelling of multiple separate but interacting phases can be done by the Eulerian model. The phases can be solids, liquids or gases in almost any arrangement. The convergence behaviour and memory requirements are the only factors that would limit the number of secondary phases in the Eulerian multiphase model because any number of secondary phases can be modelled. However, memory requirements and convergence behaviour could limit the solution [136]. This is the most complicated model as it takes into account the effect of most parameters that affect the boiling process like; drag coefficient, lift force, bubble departure, mass transfer, transient and film boiling, heat transfer mechanism during nucleate boiling and wall lubrication [149].

5.3 CFD modelling process – evaporation of liquid nitrogen for freeze desalination

The computational fluid dynamics (CFD) modelling process of the evaporation of liquid nitrogen to provide the cooling for freeze desalination contains two different processes. Firstly, the evaporation of liquid nitrogen process discussed in section 5.2 of this chapter and secondly, the freeze desalination process discussed in section 3.2 of chapter 3. Therefore, the CFD modelling of the evaporation of liquid nitrogen to conduct freeze desalination, was done in two scenarios. In the first scenario, when modelling the evaporation of liquid nitrogen to simultaneously conduct freeze desalination, both the processes of freeze desalination and liquid nitrogen evaporation occurred in parallel. In the second scenario, the evaporation of liquid nitrogen was done first, where the surface temperatures were taken as a temperature profile and inputted into the freeze desalination model and both were run separately. There are benefits and drawbacks for doing this simulation in both scenarios.

When modelling both the processes together, the results can be more accurate due to this method being very similar to the actual experimental tests. However, this scenario uses many models simultaneously, including multiphase, solidification/melting, species transport, energy, laminar/turbulent flow. This brought out many problems including very long computational time. Additionally, only the VOF option in the multiphase model can be used and this is a simpler solving technique in comparison to Mixture and Eulerian techniques.

When modelling the two processes separately, the evaporation of liquid nitrogen was done first and then the temperatures obtained at the surface were taken and then imported into the freeze desalination process as a temperature profile. In this scenario, the number of models used at once was less and did not give many errors and the computational time was not very long. Additionally, more complex options for the multiphase model such as mixture and Eulerian can be used. However, an assumption has been made that the temperature profile imported is accurate and does not change with time.

Therefore, for the CFD modelling of the evaporation of liquid nitrogen for freeze desalination, the VOF multiphase model has been used initially but due to the very lengthy computational times and due to solutions crashing, it has not been used for further results. Consequently, the Mixture Multiphase model has been used to carry out the CFD simulations as it still gave accurate results to validate with the experimental work and with shorter computational times.

5.4 CFD modelling and methodology

In this section, computational fluid dynamics (CFD) was used to model the evaporation of liquid nitrogen to simultaneously conduct freeze desalination of saline water using the software ANSYS Fluent version 19.1 [129].

5.4.1 Evaporation of liquid nitrogen process

When modelling the evaporation of liquid nitrogen process, two phase flow exist with liquid nitrogen evaporating to nitrogen gas and this cryogenic fluid evaporation has been observed by many researchers by conducting experiments or by using mathematical modelling [150]–[156]. Accordingly, it is found that this process of boiling is split into three forms of which are nucleate boiling, transient boiling and film boiling which are all reliant on the temperature of the wall as shown in Figure 5-1.

When liquid nitrogen passes through a tube, heated up and evaporated, the process is called cryogenic chill down where the subcooled liquid nitrogen is converted into superheated gas. In the cryogenic chill down process; free convection, nucleate, transition and film boiling processes occur. Starting with film boiling at the initial stages when the heat transfer surface temperature is at ambient, followed by transient boiling due to the reduction in temperature of the tube and lastly, nucleate boiling and free convection when the tube surface temperature decreases near to about LN_2 saturated temperature.
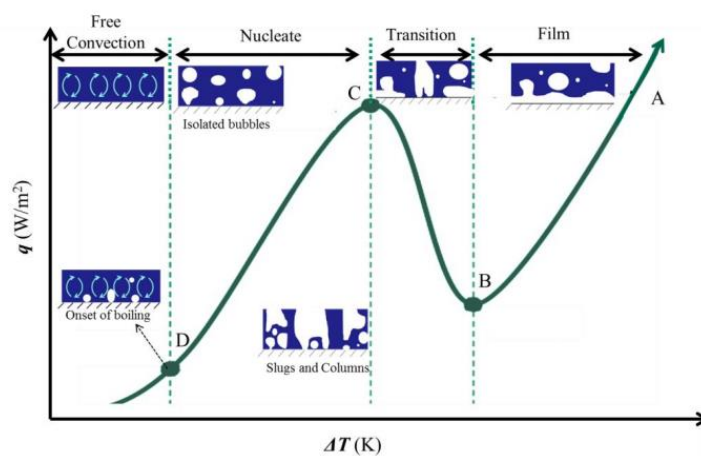
Figure 5-1: Boiling curve and flow patterns [153]

5.4.2 Geometry

The geometry has then been modelled using ANSYS geometry modeller of the CFD software, to the exact dimensions of the experimental test rig which was designed based on results obtained for the cryogenic chill down process studied by Hartwig et al. [152]. Figure 5-2 shows the 3D geometry modelled using ANSYS geometry modeller consisting of two concentric tubes where the inner one is made of copper with a 6mm diameter and it is surrounded by a Pyrex glass tube with a 15mm diameter. The thickness of the copper tube and the glass tube were 0.5mm and 3mm respectively with a total length of 1000mm. Liquid nitrogen flows through the inner tube, while the sea water stays stationary in the glass tube surrounding the copper tube. Only half of the geometry has been modelled due to the symmetrical nature of the pipes as shown in Figure 5-3, in order to reduce the computational time.
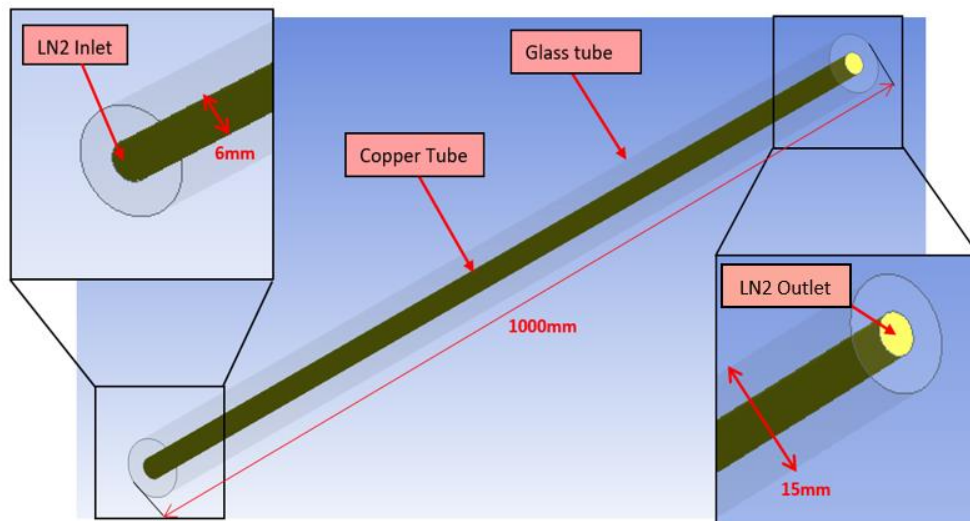
Figure 5-2: The geometry of the heat exchanger
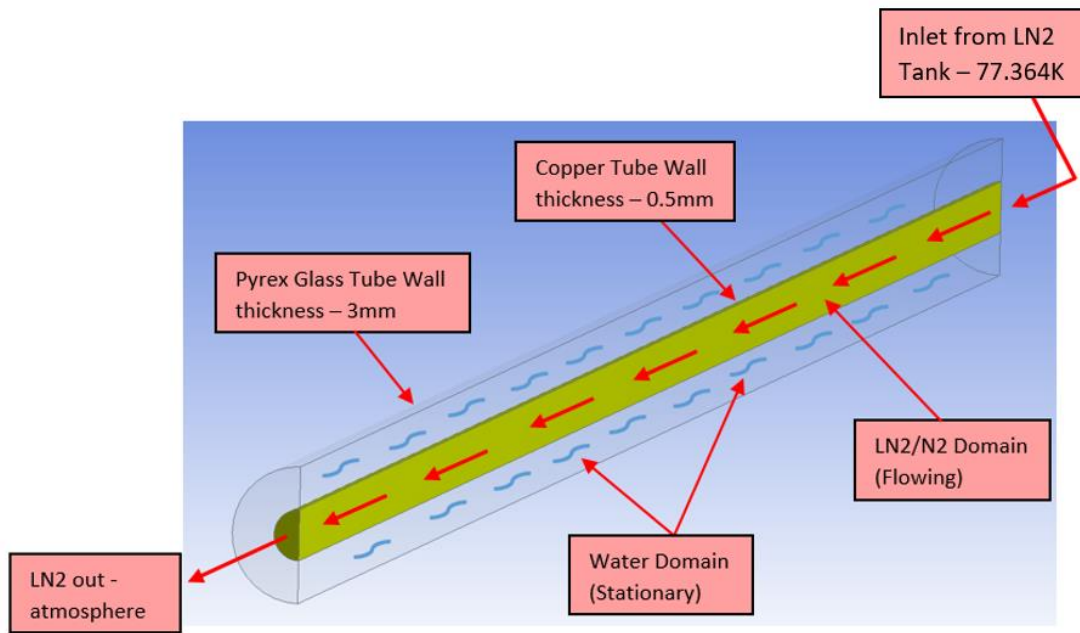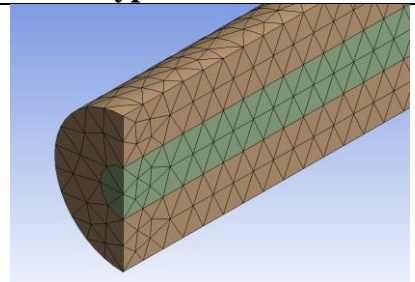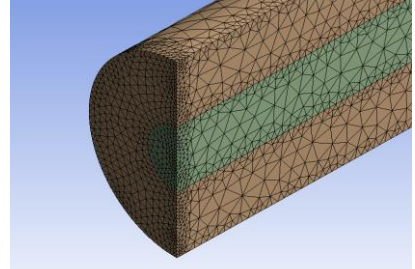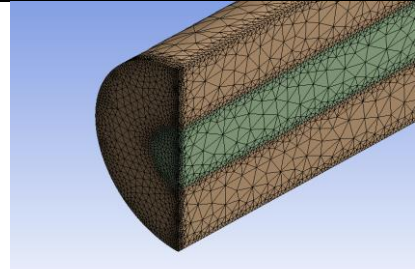
Figure 5-3: Heat exchanger domains and flow directions – cross-sectional view

5.4.3 Mesh

'ANSYS Meshing' was used to create the 3D mesh of the geometry where a tetrahedral mesh has been created with edge sizing in order to optimise the mesh. Mesh independency study was conducted by using finer and coarser meshes with different edge sizing in order to select a suitable mesh as shown in Table 5-1. The predicted salinity of ice was compared with the measured salinity of ice (0.9%) and the percentage errors are shown in Table 5-1. The quality of all the three meshes were good, however increasing the density of the mesh requires longer computational time but produces more accurate results [7]. Further increase in the mesh density did not improve the results to a great deal, thus a medium mesh has been chosen.

Table 5-1: Mesh types used

Mesh Types	Description
	- Coarse mesh without edge sizing. - Nodes: 16750 - Elements: 10461 - Salinity of ice (%): 0.65 - Percentage error (%): 27.8% - Total Running Time: 2 Days
	- Medium mesh with edge sizing. - Nodes: 101081 - Elements: 64517 - Salinity of ice (%): 0.73 - Percentage error (%):18.9% - Total Running Time: 6 Days
	- Fine mesh with edge sizing. - Nodes: 194542 - Elements: 123550 - Salinity of ice (%): 0.75 - Percentage error (%):16.7% - Total Running Time: 10 Days

5.4.4 Set-up

'ANSYS Fluent-Setup' was used to define the solvers, materials, modules, boundary conditions, solution methods and discretization settings for the imported mesh. A transient solving process was selected due to time variation of the wall temperature during the cryogenic chill down process. A pressure-based solver was used with absolute velocity formulation enabled.

The primary physics modules used were energy, multiphase, viscous, species transport and solidification/melting in order to simulate the evaporation of liquid nitrogen and

simultaneously conduct freeze desalination. These modules are thoroughly discussed in section 3.2 in Chapter 3 and section 5.2 in this chapter, where the theory of the CFD simulation process is explained.

The boundary conditions are set to match the experimental test rig and Figure 5-3 displays the labelled cross-sectional view of the CFD model. The system is divided into two sections where, the evaporation of liquid nitrogen domain is inside the copper tube while the surrounding glass tube contains the salt water mixture domain to be frozen. Initially, the system is at ambient of 293.15K. Then, liquid nitrogen enters the tube at a temperature of 77.364K, evaporates inside the tube and leaves as nitrogen gas. The inlet is set as velocity inlet where the velocity of liquid nitrogen entering the system was 0.0006m/s and the outlet was set as a pressure outlet at atmospheric pressure. The surrounding salt solution is of 15g/l concentration (1.5%) with an initial temperature of 293.15K. This salt solution is present inside the surrounding Pyrex glass tube where the copper tube makes contact with the salt solution to indirectly freeze and desalinate the solution.

The discretization settings used in this model are shown in Table 5-2 and a coupled scheme was implemented as a solving algorithm. Continuity, velocity and saltwater mass fraction's residual monitors were 1×10^{-9} and for energy was 1×10^{-11}. In order to obtain the most accurate results in less computational time, a suitable time step must be selected by conducting time step size independency tests. Therefore, it is understood that increasing the time step size, decreased the computational time; however, decreasing the time step size, improved the results' accuracy and avoided many errors in the ANSYS Fluent software. After conducting time step size independency tests by trial and error, a time step

of 0.0001s was used with 20 iterations per time step, thus 5400000s of time steps were required to run the simulation for 9mins real time. This was the optimum time step size that could be used; where increasing this time step size produced less accurate results and decreasing this time step resulted in longer computational time. Increasing this time step also produced many errors such as 'floating point exception' to appear in the 'ANSYS Fluent Solution', resulting in the system crashing. With this time step size, it took about 6 days to complete one run with the mesh nodes and elements stated above in Table 5-1. The computer used has a 48GB RAM with an i7 Intel® Core™ processor @ 3.70GHz.

Table 5-2: Discretization settings

Spatial Discretization	Solution Method
Gradient	Least squares cell based
Pressure	PRESTO!
Momentum	Second order upwind
Volume Fraction	First order upwind
Turbulent Kinetic Energy	Second order upwind
Turbulent Dissipation Rate	Second order upwind
Energy	Second order upwind
Salt-water	Second order upwind
Transient formulation	First order implicit

5.5 CFD results

The temperature distribution of the liquid nitrogen in the copper tube is shown in Figure 5-4, where only the beginning of the tube is at very low temperatures due to the very low velocity of LN_2. The temperature distribution of the salt water surrounding the copper tube is shown in Figure 5-5.
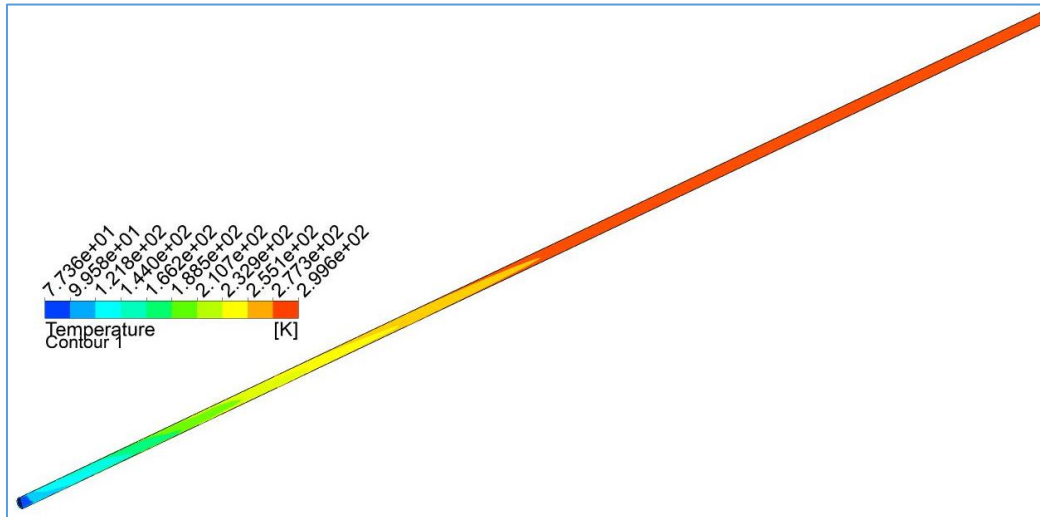
Figure 5-4: Temperature distribution of the LN$_2$ copper tube
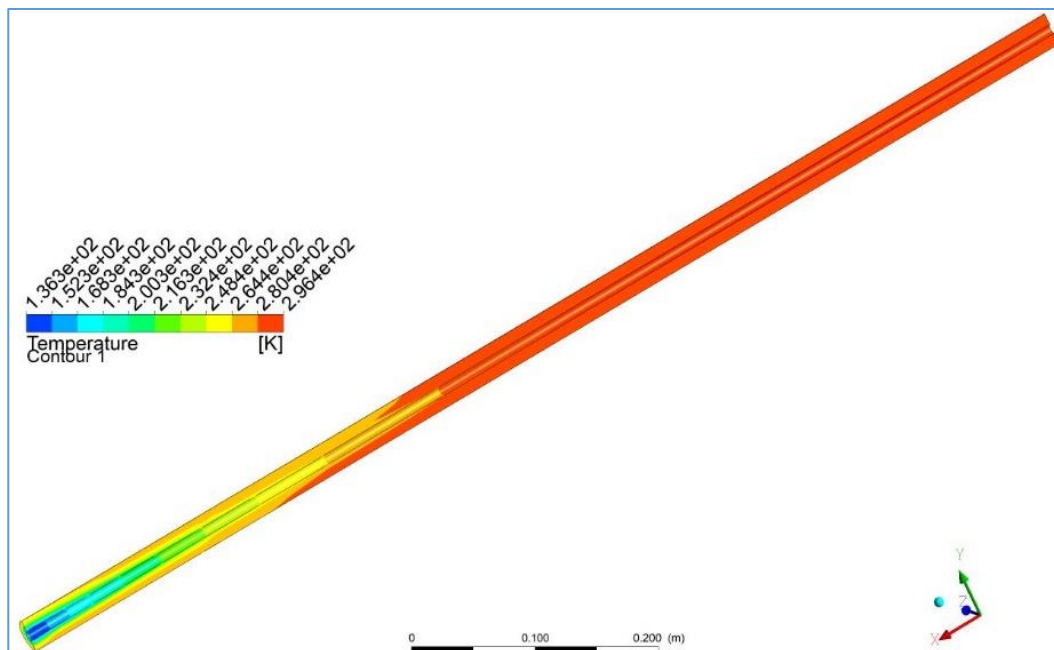
Figure 5-5: Temperature distribution of the salt water surrounding the copper tube

Figure 5-6 displays the liquid phase fraction contours, where the formation of ice is shown. The blue region indicates the ice formed, the brine remaining is indicated by the red region and the intermediate colours denotes the liquid/solid mushy zone. Also, these contours go from 0 to 1 where 1 means it's is pure liquid, 0 means it is pure solid and the intermediate

numbers represent the mushy regions. Liquid phase fraction contours in Figure 5-6 shows that ice was formed only at the beginning of the tube due to the low velocity of LN_2. The volume of ice formed was 46.71 ml.
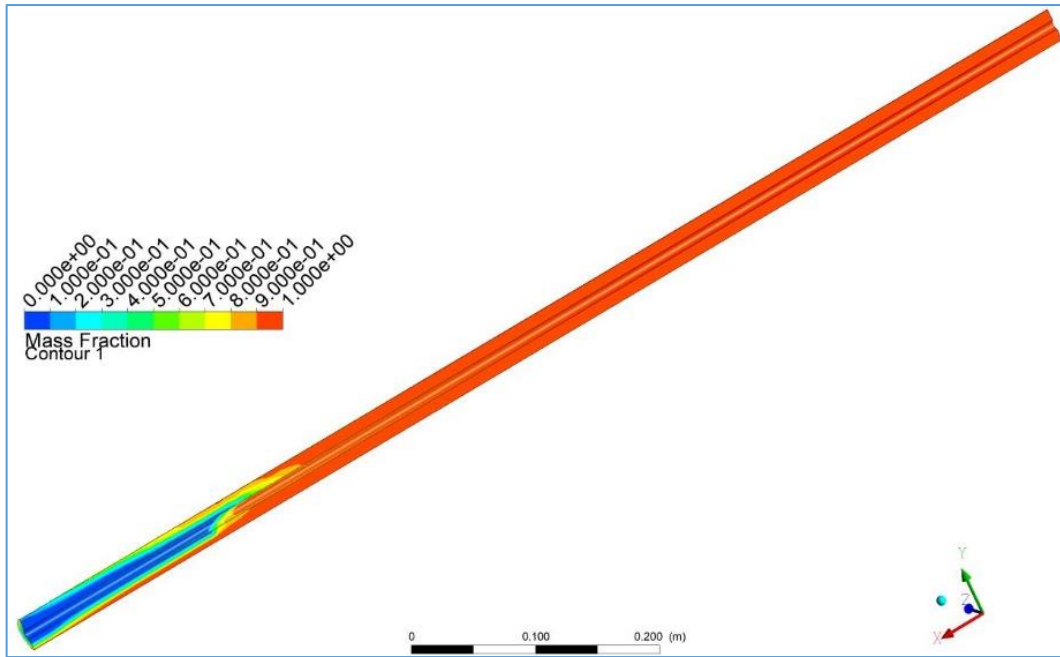
Figure 5-6: Liquid phase fraction contours

Figure 5-7 and Figure 5-8 shows the salt water mass fraction and pure water mass fraction contours respectively. The salt water mass fraction is minimal in the regions where the ice is formed as shown in Figure 5-7 and the pure water mass fraction is very high in these regions as shown in Figure 5-8. Hence, the salinity of ice formed was 0.73% and the salinity of the remaining brine was 1.70% and it is calculated by taking the volume average over the whole domain.

Figure 5-7: Salt water mass fraction contours
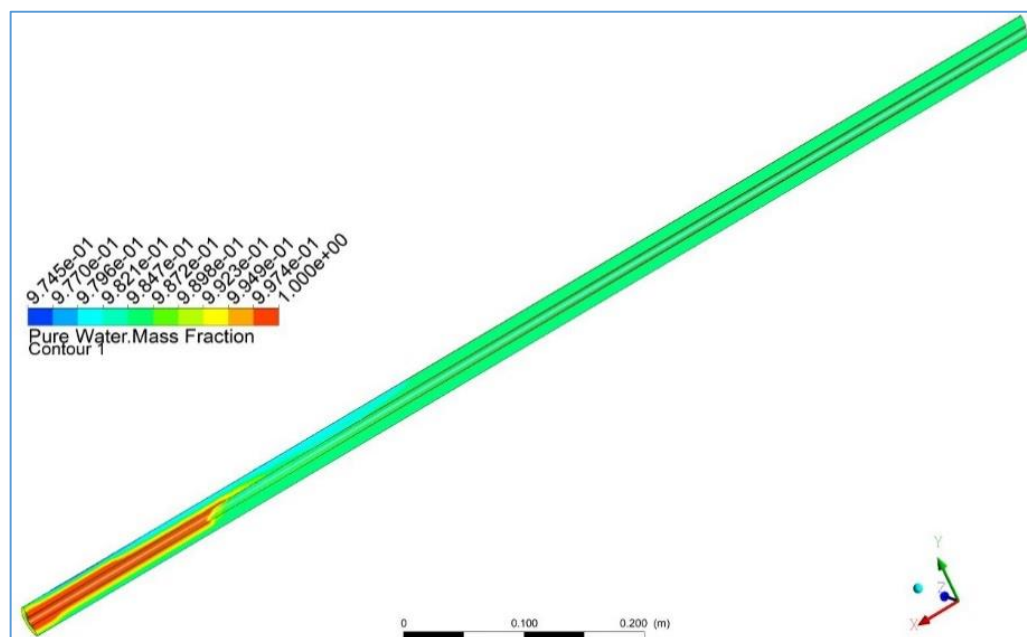
Figure 5-8: Pure water mass fraction contours

5.6 Experimental test facility

This test rig was constructed to develop a system where the evaporation of liquid nitrogen would simultaneously desalinate sea water. The primary objective of this test rig was to understand the evaporation process of liquid nitrogen to be used for desalinating sea water. The heat transfer process was also examined where a method for enhancement of heat transfer was implemented in order to capitalize on the cold energy stored in liquid nitrogen. Detailed description of the test rig with all the important components and measuring devices is given in the following subsections.

5.6.1 Layout of the test facility

The experimental test facility's schematic diagram is shown in Figure 5-9. This test rig is divided into two circuits; the evaporation of liquid nitrogen circuit and the freeze desalination one which are connected by a heat exchanger. The concentric tube heat exchanger consists of a copper tube for the evaporation of LN_2 which is surrounded by a glass tube that contains stationary sea water. A glass tube was chosen to store sea water in order to observe the formation of ice and a copper tube was used for the LN_2 evaporation process to ensure effective heat transfer between the evaporating nitrogen and the saline water.
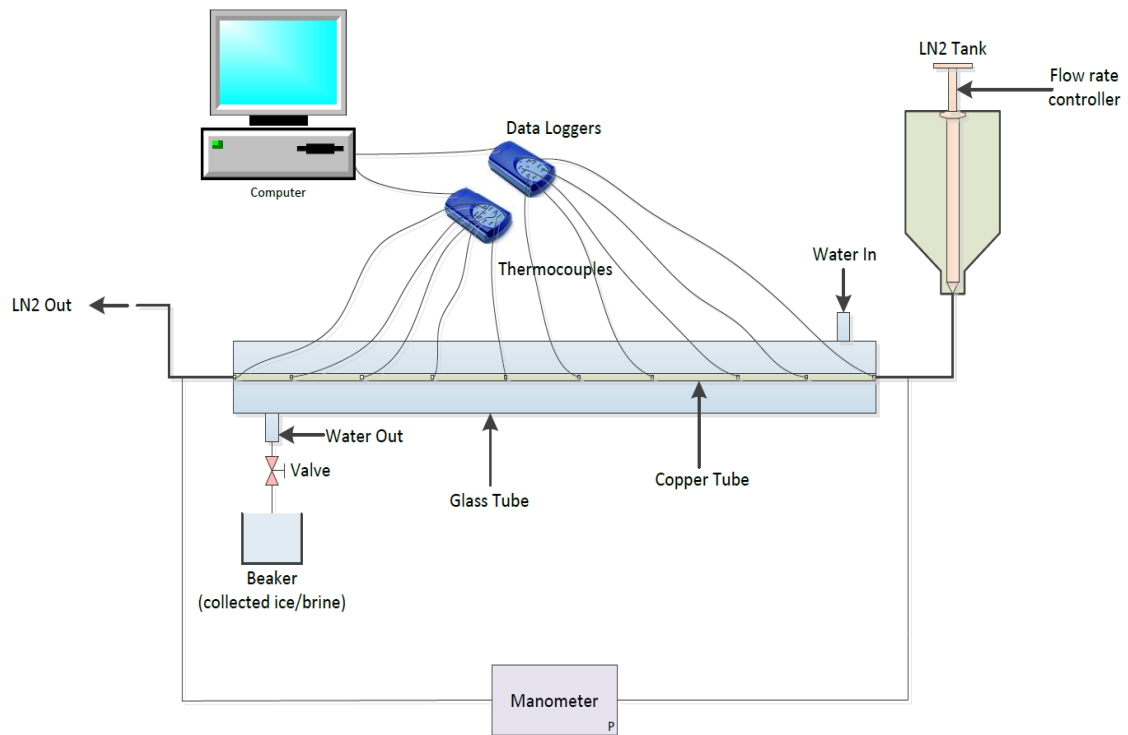
Figure 5-9: Schematic diagram of the experimental test facility
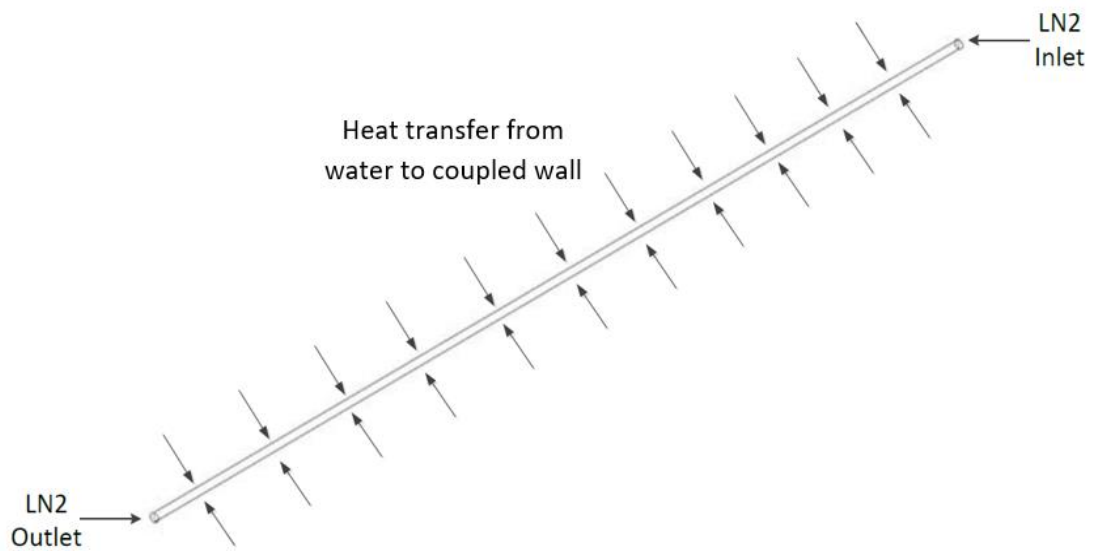
Figure 5-10: Schematic diagram of the LN$_2$ tube
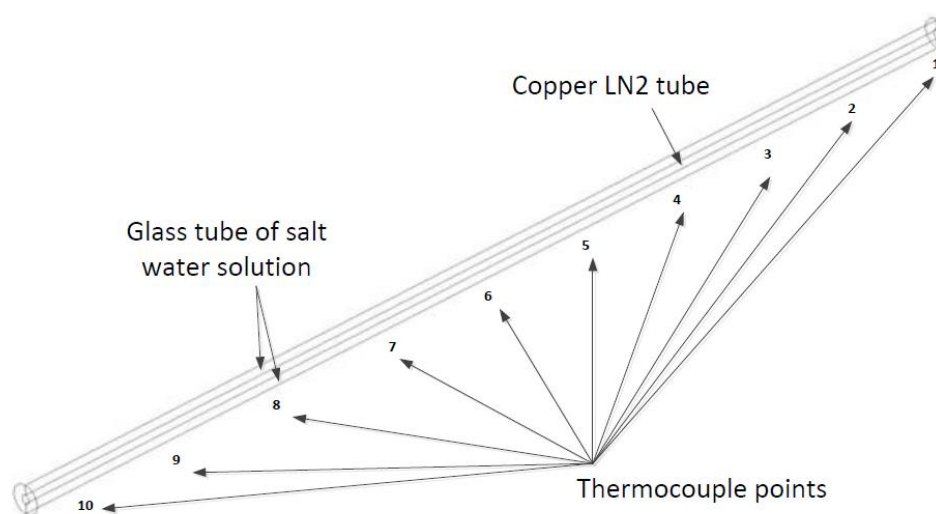
Figure 5-11: Schematic diagram showing the test rig with the thermocouple points

In the first circuit, the liquid nitrogen was poured into an insulated LN$_2$ tank and it was circulated through an 8mm diameter copper tube as shown in Figure 5-10 and into the atmosphere at moderately higher temperature. The LN$_2$ flow rate was measured and cryogenic thermocouples were placed at the inlet and outlet of the heat exchanger and as well as at different locations at the surface of the copper tube to measure the temperatures as shown in Figure 5-11. The pressure difference between the inlet and outlet was measured using a manometer. Insulation sheets and aluminium foil has been used to insulate the LN$_2$ tank and the joining copper tubes.

In the second circuit, sea water of known salinity is poured into the glass tube which is surrounding the copper tube. This stationary sea water is cooled down by the evaporation of LN$_2$. The temperature was measured at different locations at the surface of the copper tube using thermocouples. The temperature sensors were all connected to two data loggers

146

that are connected to a computer to record the data. The complete test rig is shown photographically in Figure 5-12 with all its main components labelled.
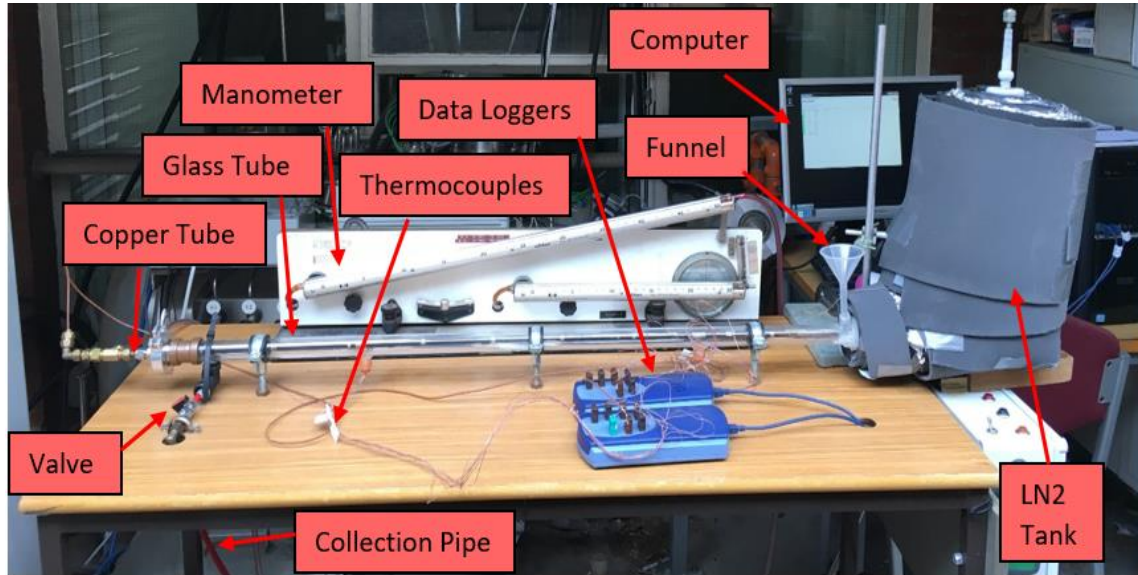
Figure 5-12: The developed test rig

Certain experiments were carried out with a copper mesh inserted into the copper tube to increase the heat transfer. The copper mesh is inserted into the copper tube using a metal bar, where the copper mesh is wrapped around and once the mesh is inserted, the metal bar is taken out. The inserted copper mesh has a wire diameter of 0.5mm and is shown in Figure 5-13.

Figure 5-13: Copper Mesh

5.6.2 Heat exchanger - desalination test rig

A detailed CAD drawing of the designed concentric heat exchanger is shown in Figure 5-14, where the inner copper tube and the outer glass tube are clearly seen with the fittings. The overall length of this heat exchanger is 1000mm. The copper tube has an inner diameter of 8mm with a 0.5mm wall thickness and the glass tube has an inner 28mm diameter with a 3mm wall thickness. The outer tube was made from glass that can handle cryogenic temperatures and this allows the ice formation to be seen clearly. Copper fittings with rubber sealing has been used at both ends to connect the glass tube to the copper tube. In order to prevent any leakage during testing when the copper tube expands or shrinks; KF fittings were used to join the tube feed through and copper fittings with plastic sealing.
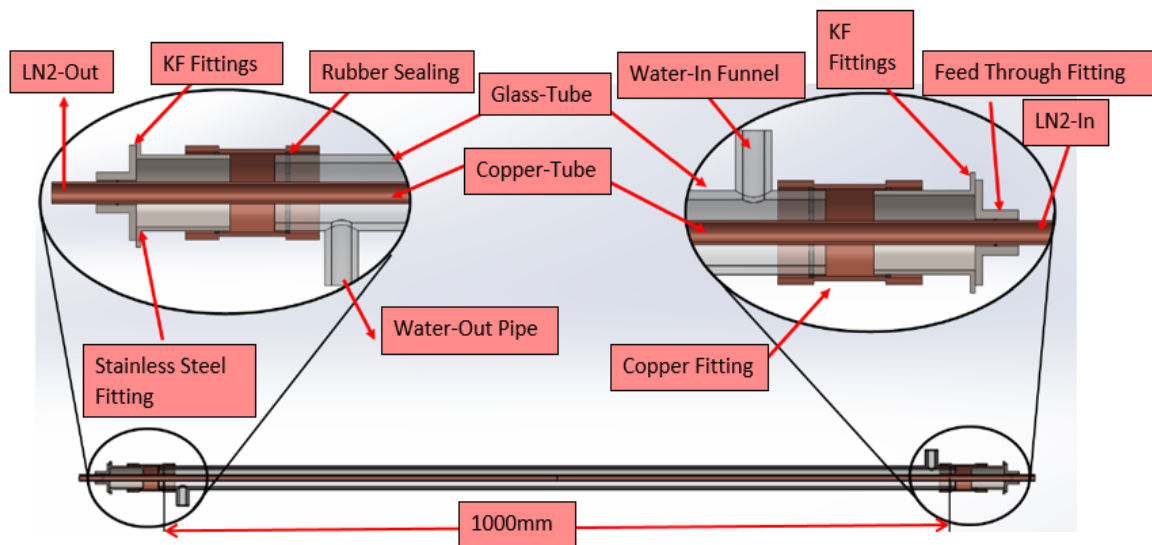
Figure 5-14: CAD drawing of the heat exchanger

5.6.3 Cryogenic tank

The liquid nitrogen cryogenic tank is made of copper which has a total volume of 0.51litres. The 54mm diameter tank with a 207mm length is connected to a reducer from 54mm to 15mm by a copper push fitting. This is then welded to another reducer to decrease the diameter to 8mm. In order to minimize heat transfer from the surrounding to the LN_2 in the tank, 21 insulation sheets were wrapped around it. Also aluminium foil was used between the insulation layers to reduce radiation heat transfer. 21 layers of insulation sheets were selected as the temperature of the last insulation sheet was measured and it was close to ambient temperature. These insulation sheets has a thermal conductivity of 0.035W/m.K and of 3mm thickness. Therefore, the total diameter with the insulation sheets converts to 230mm. Figure 5-15 shows the entire tank with its components.
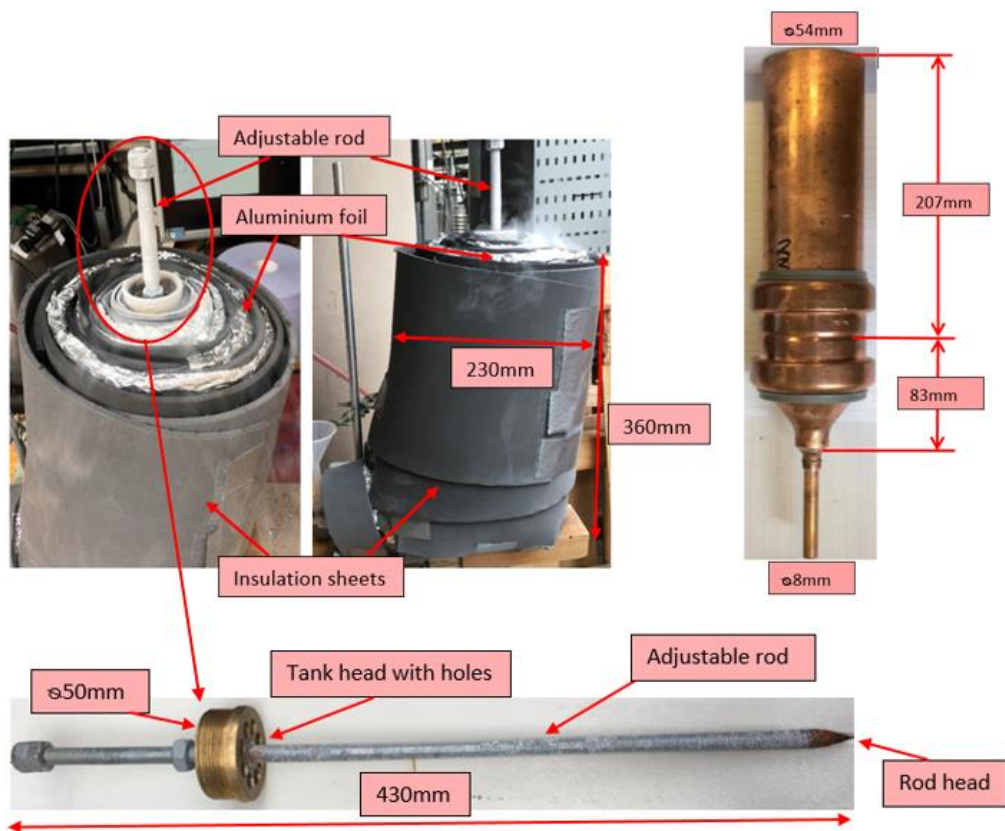
Figure 5-15: LN_2 tank with its components

The liquid nitrogen flow rate is controlled using an adjustable rod that is placed inside the tank as shown in Figure 5-15. The 430mm rod works similar to a valve, where it is rotated to open and close at the rod head. The adjustable rod has several holes seen in Figure 5-15 and when it is inserted into the tank and placed at the tank head, it is used to prevent any build-up of pressure due to the evaporation of liquid nitrogen in the tank.

5.6.4 Measuring devices and calibration

Thermocouples, a salinity meter and a manometer were used in this experiment to measure temperatures, salinity and pressure difference respectively.

Thermocouples

In total, 12 thermocouples were used to measure the temperature at different locations in the test rig. Out of the 12, two of them were used to measure the temperature at the inlet and outlet of the liquid nitrogen copper tube. These two were thermocouple probes of type-K, which were used to measure the inlet temperature of LN_2 and the outlet temperature of N_2. The rest of the 10 thermocouples were cement-on surface thermocouples of type-K and were fitted at the outer surface of the copper tube to measure the temperature of the surface. These 10 thermocouples were equidistant from each other as shown in Figure 5-16, where T1 is closest to the LN_2 inlet and T10 is closest to the N_2 outlet. They are self-adhesive and are able to measure temperatures down to 73.15K. The sensor tip of the thermocouples were pasted into the copper tube using aluminium tape in order to allow effective contact. The thermocouples were connected to two data loggers by passing them through two holes made in the glass tube with two rubber bongs to avert any leakage of water. The two 'TC-

08 PICO' data loggers as shown in Figure 5-17 were connected to a computer to record the temperature measurements during the experiment.

| LN2 OUT | T10 | T9 | T8 | T7 | T6 | T5 | T4 | T3 | T2 | T1 | LN2 IN |

Figure 5-16: Thermocouple distribution
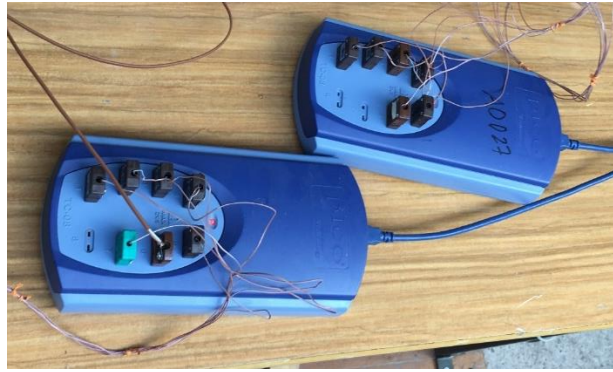
Figure 5-17: TC-08 PICO data loggers to measure temperature

The thermocouples were first calibrated in order to assess the temperature measurement's accuracy. Calibrating thermocouples allows to draw the relation between the actual data point and the measured data point. In this experiment, two types of thermocouples have been used of which 2 were thermocouple probes of type-K and the other 10 were surface thermocouples of type-K. The thermocouple calibration process is explained in section 3.5.2 of chapter 3.

Manometer

The pressure difference between inlet and outlet of the evaporation of liquid nitrogen was measured using an inclined differential manometer as shown in Figure 5-18. Two silicon tubes were used to connect the ends of the manometer to the inlet and the outlet of LN_2

tube. An inclined differential manometer was used to enable measuring the expected pressure drop of the LN$_2$ flow. The measured pressure difference was calculated using equation (5-17).

$$\Delta P = \rho g l \, sin\theta \hspace{6cm} \text{5-17}$$

where, l is the level of fluid in the inclined ruler and θ is the angle of inclination which was 38°. g is gravitational acceleration and ρ is the density of the manometer fluid which was 0.748. The manometer has been calibrated using a pressure gauge comparator.

Figure 5-18: Manometer

Salinity meter

In order to measure the salinity of the saline water, an Omega handheld salinity meter [141] was used. This has a range of 0.1% to 10% salinity and can operate at temperatures from -5°C to 60°C [141]. The salinity meter was used to measure the salinity of ice and brine after the freeze desalination process and also to measure the salinity when making salt water solutions before the experiment. Table 3-7 shows the accuracy levels of the calibrated salinity meter given in the salinity meter manual [141]. The calibration process of the salinity meter is explained further in the experimental section 3.5.2 – 'Salinity Meter Calibration' of chapter 3 [141].

5.7 Experimental methodology

5.7.1 Experimental procedure

This test rig was built to study the evaporation of liquid nitrogen process for freeze desalination. CFD modelling conducted in section 5.4 of this chapter was also validated using this test rig. In the first set of tests, the copper tube was kept as it is and the flow rates were changed. In the second set of tests, a copper mesh was inserted into the copper tube in order to increase the transfer of heat and to improve the freezing rate. The experimental steps are stated as follows:

1. A known solution of salt water was made by mixing salt with de-ionised water and its salinity was measured.

2. The manometer was fixed to the inlet and outlet of the copper tube.

3. The thermocouples were connected to the data logger and the data logger was connected to a computer to record and monitor temperature changes. The temperature measurements were at the inlet and outlet of the copper tube and also at the outer surface of the copper tube. The temperature was then monitored to be stable at room temperature.

4. Liquid nitrogen was then poured down the LN_2 tank and due to the very low temperatures of LN_2, excessive boiling occurred inside the tank and it slowly decreased, as the temperature inside the tank became steady.

5. Liquid nitrogen was then again poured down the LN_2 tank and filled to the top to start recording the data.

6. The measured salt water solution was then poured using a small funnel into the glass tube surrounded by the copper tube.

7. A stop watch was used to time the evaporation of liquid nitrogen in conjunction with freeze desalination until the LN_2 tank was empty.

8. Once the LN_2 tank was empty, the stopwatch was stopped and the remaining brine was collected into a beaker by opening the valve. The volume and salinity of brine collected were measured.

9. 30ml of wash water was poured to wash away the brine remaining in the test rig due to stagnation.

10. The ice formed was then left to melt inside the test rig. Once all ice had melted, the pure water was then collected into another beaker and its volume and salinity were measured.

The measured ice salinity was then created using salt and de-ionised water solution using step 1 to start the second stage of freezing and similarly the third stage of freezing in order to reduce the final ice salinity below 0.1%. Additionally, other tests were conducted with different LN_2 flow rates by rotating the adjustable rod. A copper mesh was then inserted into the copper tube and the experiment was repeated in order to evaluate the improvement in heat transfer in terms of better freezing rate giving a higher volume of ice.

5.7.2 Energy calculations

The energy balance for the hot stream of saline water and the cold stream of LN_2 passing through the heat exchanger was evaluated. The total energy lost by salt water to form ice was calculated using equation (4-1) and equation (4-2) and the energy calculations are explained in section 4.3.1.

In order to find the percentage of energy lost by water to form ice from liquid nitrogen, first the energy in liquid nitrogen is calculated using equation (5-18).

$$E_{LN2} = \text{Energy Density of } LN_2 \times \text{Volume of } LN_2 \qquad\qquad 5\text{-}18$$

The energy density of LN_2 was calculated using H_1 and H_2 which are the inlet and outlet enthalpies obtained from thermodynamic property tables for nitrogen [157] (Appendix B). The volume of LN_2 used depended on how many freezing stages were carried out.

Then the percentage of energy lost by water to form ice (overall efficiency) from liquid nitrogen was calculated using equation (5-19).

$$\% \, of \, Energy \, lost \, by \, water = \frac{Q_{total\,water}}{E_{LN2}} \times 100 \qquad\qquad 5\text{-}19$$

where, $Q_{total\,water}$ is the total energy lost by water calculated using equation (4-1) and equation (4-2).

5.7.3 Salinity calculations

The salt solutions were created by measuring the mass of salt and mixing it with 1000ml of de-ionised water and calculated using equation (3-19). The salinity meter was then used to measure the salinity of these salt water solutions.

5.7.4 Heat exchanger effectiveness

When designing a heat exchanger, the two primary approaches are the Log Mean Temperature Difference (LMTD) method and the effectiveness Number of Thermal Units

(NTU) method. The heat exchanger effectiveness was calculated as follows. Firstly, the

LMTD was calculated using equation (5-20).

$$\Delta T_{LMTD} = \frac{\Delta T_2 - \Delta T_1}{\ln\frac{\Delta T_2}{\Delta T_1}}$$

5-20

where, ΔT_1 and ΔT_2 are the difference in temperatures at the ends of the heat exchanger and

it is calculated by equations (5-21) and (5-22).

$$\Delta T_1 = T_{W1} - T_{N1}$$

5-21

$$\Delta T_2 = T_{W2} - T_{N2}$$

5-22

T_{W1} and T_{W2} are the water inlet and outlet temperatures and T_{N1} and T_{N2} are the nitrogen

inlet and outlet temperatures.

In order to calculate the effectiveness; the NTU, was calculated using equation (5-23).

$$NTU = \frac{UA}{C_{min}}$$

5-23

C_{min} is the smaller heat capacity and it is calculated by equation (5-24). A is the surface

area of the copper tube and U is the overall heat transfer coefficient calculated by equation

(5-25).

$$C_{min} = \dot{m}C_p$$

5-24

$$U = \frac{\dot{Q}}{A\Delta T_{LMTD}}$$

5-25

When phase change evaporation occurs in the heat exchanger, then the behaviour of the

heat exchanger is independent of flow arrangement. Therefore, the effectiveness of the heat

exchanger is calculated using equation (5-26).

$$\varepsilon = 1 - e^{-NTU}$$

5-26

5.8 Experimental results

5.8.1 Effect of test conditions on temperature and energy

Four tests were conducted, and the first two tests were conducted by evaporating LN_2 in a smooth copper tube with two different flow rates. In the third and fourth tests, a copper mesh has been inserted in order to increase the heat transfer with two different flow rates. The four tests were analysed in terms of the inlet and outlet temperatures of liquid nitrogen, the temperature of ice forming at the surface of the copper tubes and the volume and salinity for the ice and brine. All the four tests had an initial salt water salinity of 1.5% and three stages were conducted in order to desalinate the salt water to below 0.1% which is regarded as safe to drink by the WHO [13].

In the first test, liquid nitrogen passed through the copper tube and evaporated at a flow rate of 8.69×10^{-4} kg/s, simultaneously freezing the saline water surrounding the copper tube. Figure 5-19 shows the temperature distribution of liquid nitrogen at inlet and outlet and the initial and final water temperatures. The inlet temperature of LN_2 was 77.15K and the outlet temperature was 199.15K indicating that energy has been lost by water for ice formation and a considerable amount of energy has been lost to the surroundings. The initial temperature of salt water was 291.15K and the average temperature for ice formed and brine remaining were 269.74K and 283.8K respectively.
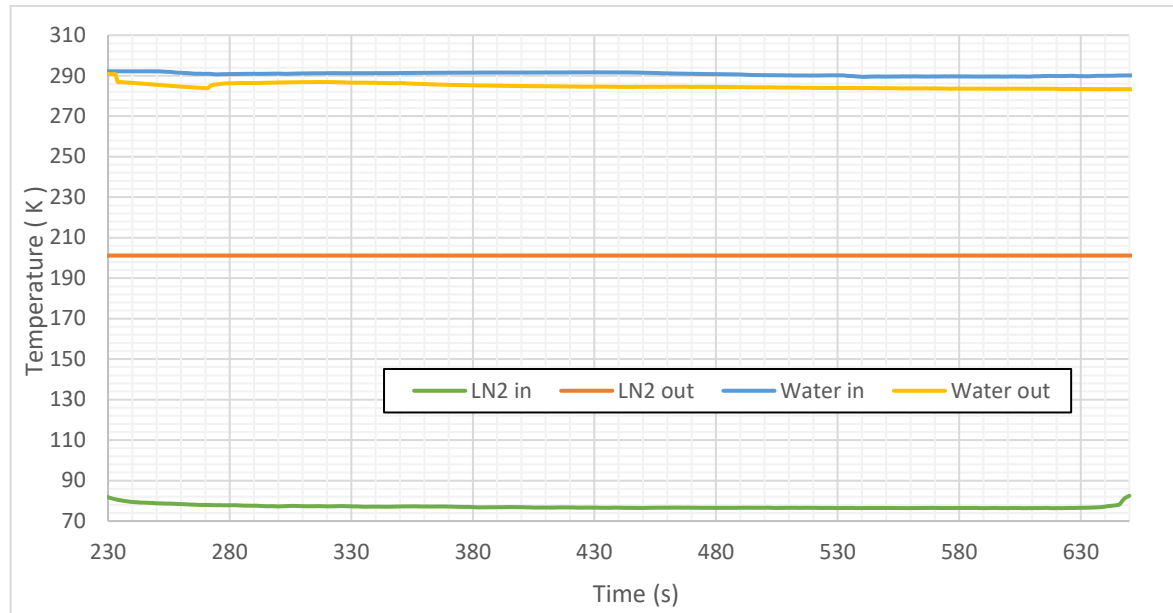
Figure 5-19: Test 1 - LN$_2$ and water temperature distribution

The surface temperatures at the copper tube surface T1 to T10 were monitored and are displayed in Figure 5-20. It is seen in this figure that the temperature increases from T1 which is closest to the LN$_2$ inlet to T10 which is closest to the LN$_2$ outlet. The decrease in temperature at the inlet causes the water to freeze and to form ice. Hence, it is clear that ice is only formed at locations T1 to T3 where the surface temperature is below 273.15K. This ice is of low salinity compared to the rest of the remaining brine solution. The mean temperature at the tube surface was calculated to be 275.14K.
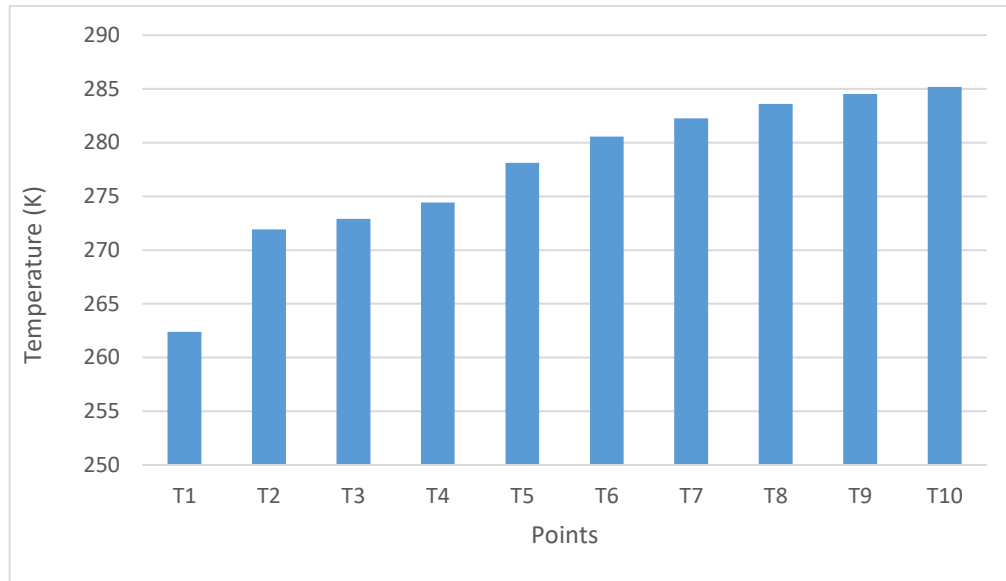
Figure 5-20: Test 1 - Temperature at copper tube surface T1-T10

The pressure difference was also monitored using the manometer and calculated using equation (5-17) to be 255Pa. The energy calculations were calculated using equations (4-1), (4-2), (5-18) and (5-19) and they are summarised in Table 5-3. It can be seen that only 21.42% of energy was absorbed in order to form ice.

Table 5-3: Test 1 - Energy calculations

Total energy lost by water (kJ)	31.81
Total energy in LN_2 (kJ)	149.41
Percentage of energy lost by water from LN_2 to form ice (%)	21.42

In the second test, the flow rate of liquid nitrogen was reduced to 7.45×10^{-4} kg/s and the water remained at stationary. The initial temperature of water was 289.15K and that of LN_2 entering the tube at 78.15K and left the system at 243.15K as shown in Figure 5-21. Thus, energy was still lost to the surroundings as the nitrogen left at a temperature significantly lower than the ambient temperature. The ice formed from this process had a temperature of 267.15K and the remaining brine had a temperature of 281.15K. The average temperature

of the tube wall was calculated to be 277.75K. Lower flow rate of LN_2 meant that the outlet LN_2 temperature and the average wall temperature were higher compared to the first test indicating that the heat loss was smaller compared to test 1 as shown in Table 5-4. Figure 5-22 shows the tube surface temperature distribution from T1-T10 and it is seen that ice is formed at the locations of T1-T3.
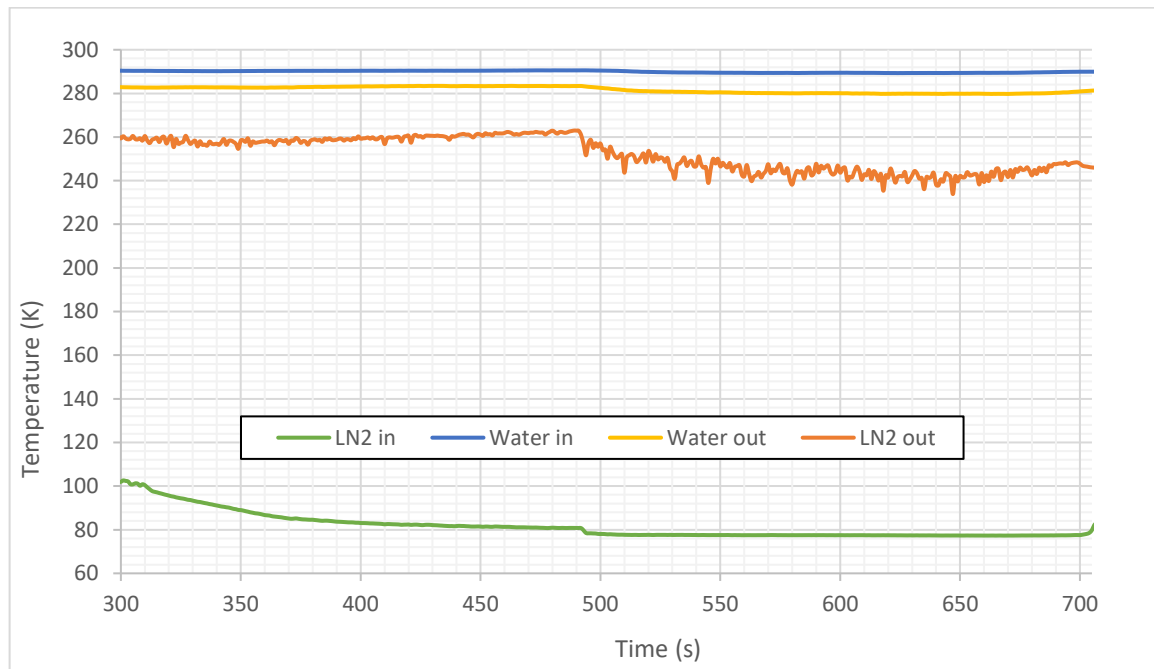
Figure 5-21: Test 2 - LN_2 and water temperature distribution
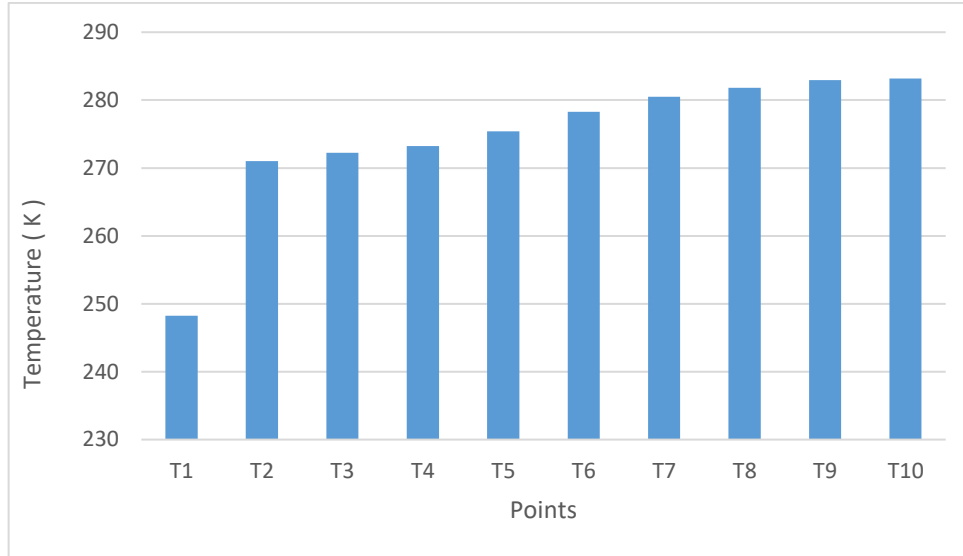
Figure 5-22: Test 2 - Temperature at copper tube surface T1-T10

The average pressure difference was calculated to be about 212Pa. Considerable amount of energy was lost to the surroundings but lower compared to test 1, as shown in Table 5-4. It is seen that 25.43% of energy has been lost by water to form ice from liquid nitrogen and it is about 18.78% more than test 1.

Table 5-4: Test 2 - Energy calculations

Total energy lost by water (kJ)	37.79
Total energy in LN_2 (kJ)	149.41
Percentage of energy lost by water from LN_2 to form ice (%)	25.43

In the third and fourth tests, a copper mesh (Figure 5-13) was inserted halfway through the copper tube in order to increase the heat transfer between the fluids and these two tests vary due to different flow rates of LN_2. The mesh was only inserted at the halfway point of the tube due to the fact that; there is a considerable amount of freezing seen at the beginning of the tube where the liquid nitrogen is entering, therefore adding a mesh here would mean

161

that there would be an uncontrollable amount of freezing, causing the surrounding glass tube to crack at the beginning of the tube.

In the third test, the LN_2 flow rate was 5.96×10^{-4} kg/s and the water remained still. The inlet LN_2 temperature was 77.15K and the outlet LN_2 temperature was 273.88K as shown in Figure 5-23. A very high outlet temperature indicates that lower amount of energy was lost to the surroundings and more energy has been transferred from water to the LN_2. The initial temperature of water was 291.15K and the average temperature of the ice formed and remaining brine were 262.3K and 279.63K respectively. The average surface temperature was calculated to be 271.34K. The temperature distribution is very different to the first two tests as shown in Figure 5-24. This can be explained as follows, since the copper mesh was inserted up to the half way point of the tube, a considerable amount of heat transfer is seen at the beginning of the mesh, leading to low temperature, at points T5-T7.
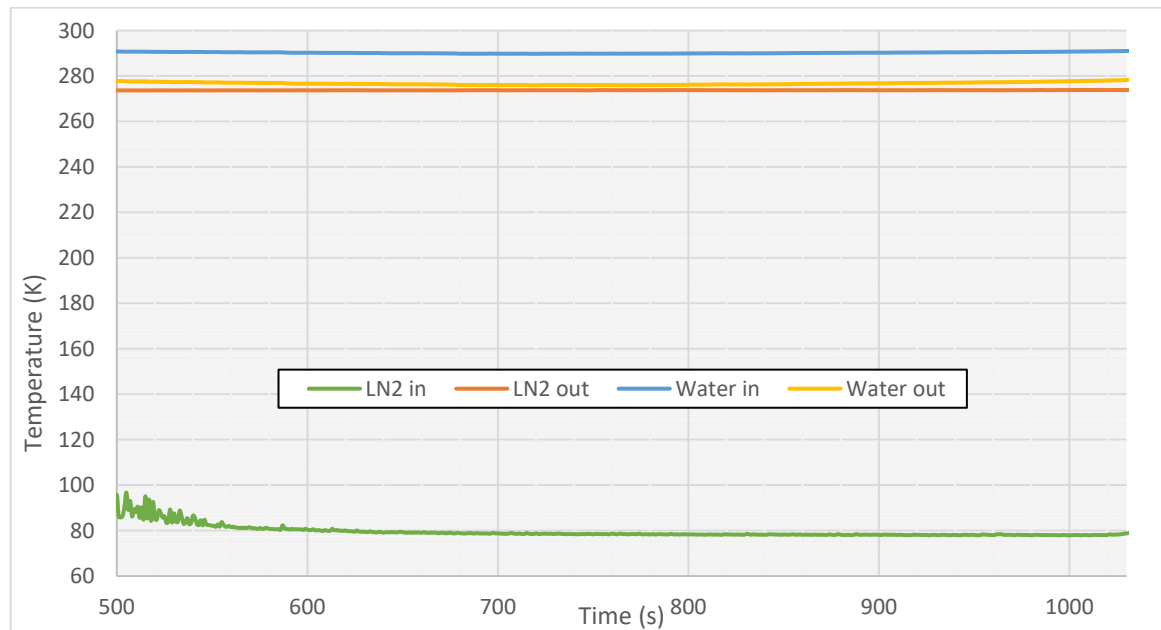
Figure 5-23: Test 3 - LN_2 and water temperature distribution
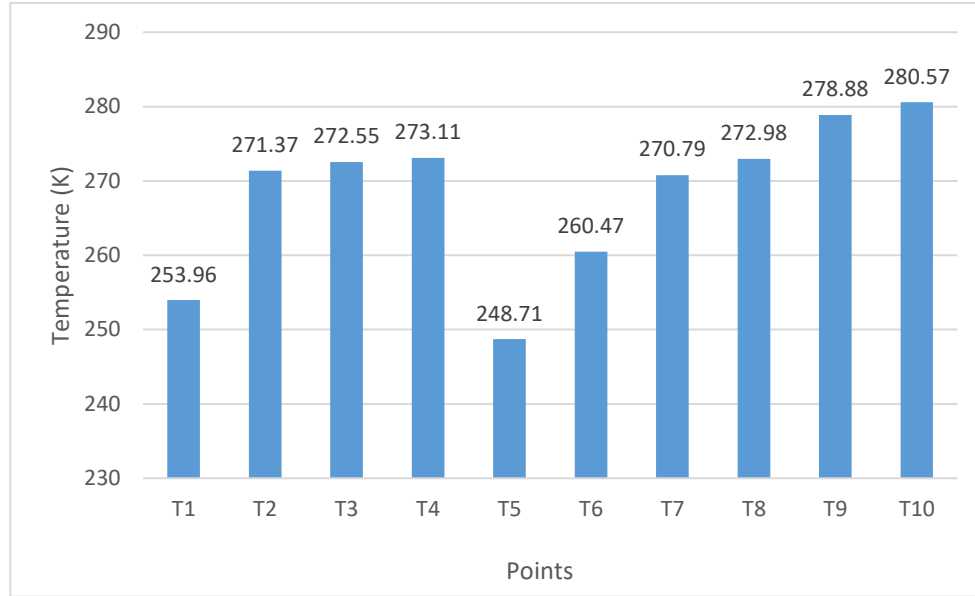
Figure 5-24: Test 3 - Temperature at copper tube surface T1-T10

The pressure difference was much higher of about 988Pa due to the presence of the wire mesh. Table 5-5 shows the energy calculation results and it is seen that about 62.91% of energy has been lost by water to form ice from liquid nitrogen. Overall, in test 3 using a copper mesh, the heat transfer rate increased significantly and more volume of ice was formed, thus indicating a high desalination rate.

Table 5-5: Test 3 - Energy calculations

Total energy lost by water (kJ)	93.74
Total energy in LN_2 (kJ)	149.41
Percentage of energy lost by water from LN_2 to form ice (%)	62.91

In the final test, the flow rate has been reduced to 5.55×10^{-4} kg/s and the water remained stationary. The LN_2 inlet and outlet temperatures were 79.15K and 276.5K respectively as shown in Figure 5-25. The initial temperature of saline water was 291.15K and the produced ice had a temperature of 261.15K and the remaining brine with temperature of 278.47K.
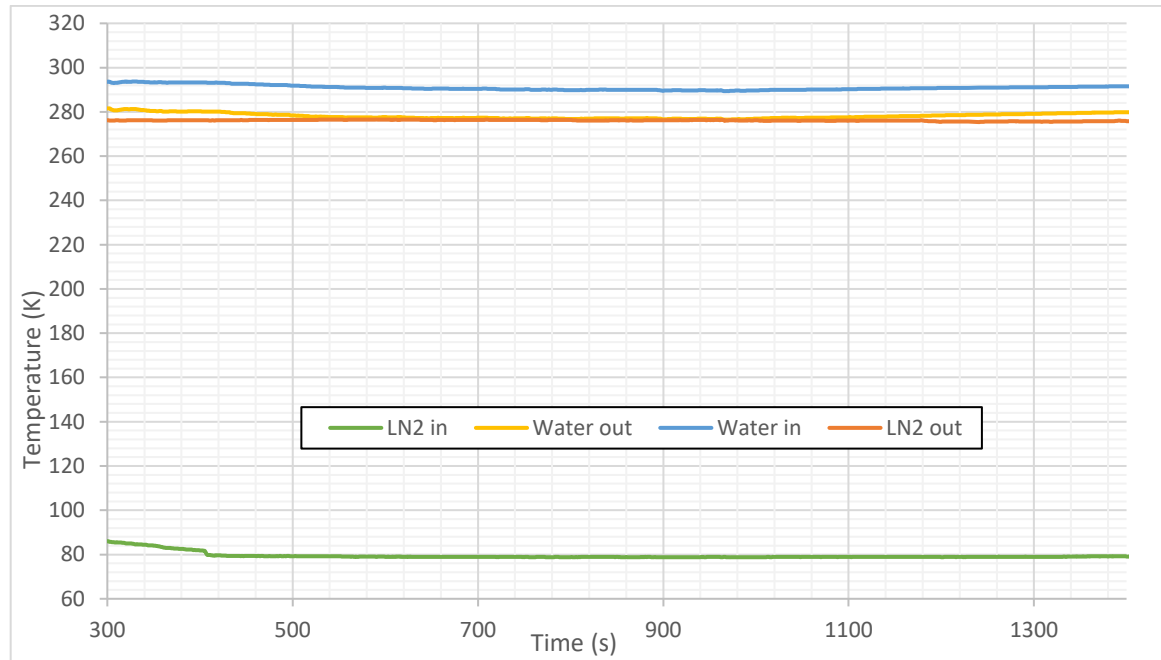
Figure 5-25: Test 4 - LN$_2$ and water temperature distribution

The mean temperature at the surface walls was calculated to be 273.55K. The temperature distribution is quite similar to test 3 with the mesh inserted, however the temperatures at T1-T3 are slightly lower compared to test 3 as shown in Figure 5-26.
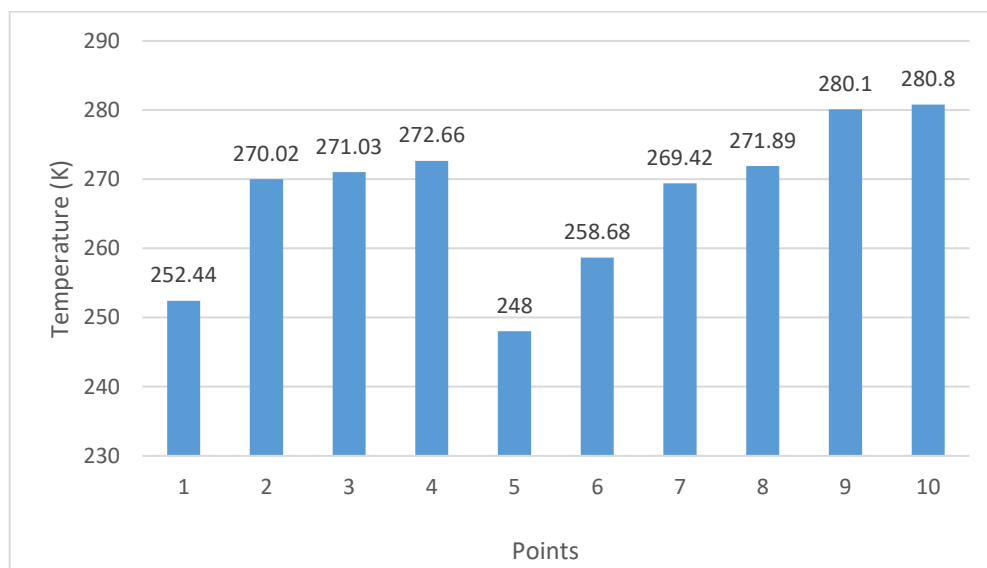
Figure 5-26: Test 4 - Temperature at copper tube surface T1-T10

164

Due to the lower flow rate, the pressure difference was lower compared to test 3 and it was 950.16Pa. Therefore, 69.61% of energy has been lost by water to form ice from liquid nitrogen and it was 10.65% more than in test 3 due to the lower flow rate.

Table 5-6: Test 4 - Energy calculations

Total energy lost by water (kJ)	102.65
Total energy in LN_2 (kJ)	149.41
Percentage of energy lost by water from LN_2 to form ice (%)	69.61

5.8.2 Comparison of results with and without mesh

The first two tests had higher liquid nitrogen flow rates due to the absence of the copper mesh and resulted in most of the energy being wasted into the atmosphere as the nitrogen leaves at low temperature with trapped liquid droplets. The copper mesh enhanced the heat transfer rate at a great deal resulting in more ice production. The percentage of energy lost by water to form ice is shown in Figure 5-27, where it is seen that the mesh improved the percentage of energy lost by water significantly.
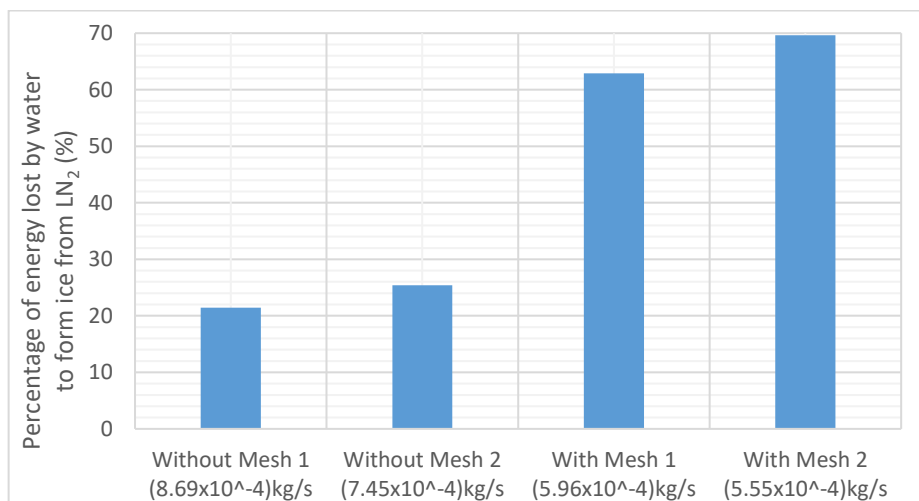
Figure 5-27: Percentage of energy lost by water to form ice from LN_2

The heat exchanger effectiveness has been calculated using equations (5-20) to (5-26) and displayed in Figure 5-28. The two lowest effectiveness values are for the tests conducted without the mesh and the lowest one (test 1) being with a higher flowrate. This means that the energy loss is greater in the tests conducted without the mesh and the highest energy loss is for the test with a higher flowrate out of the two. The two tests with a mesh being inserted showed greater effectiveness and less energy loss. The highest heat exchanger effectiveness is obtained for the test with a lower flow rate out of the two.
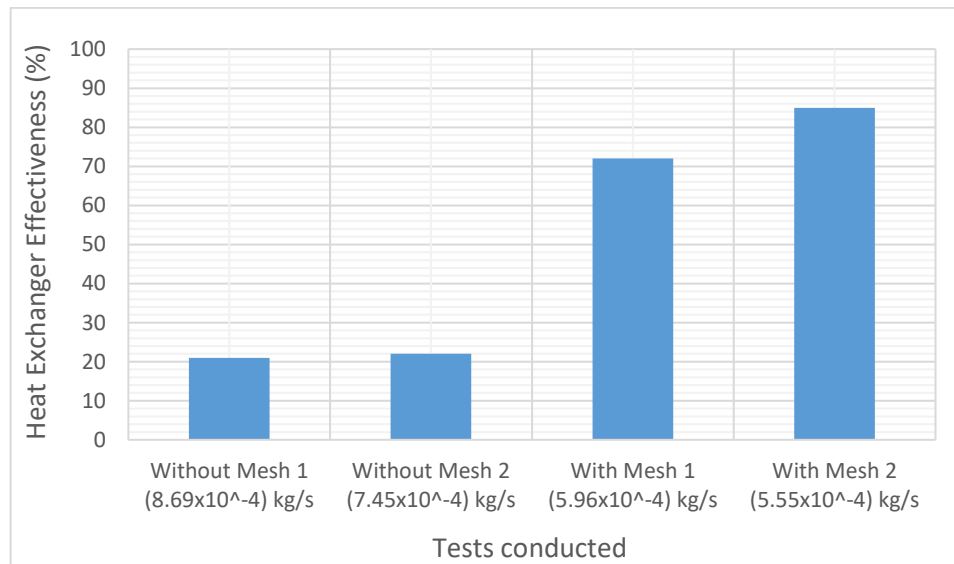
Figure 5-28: Heat exchanger effectiveness for the 4 tests conducted

5.8.3 Effect of test conditions on salinity and volume of ice

A salt solution of 1.5% salinity was indirectly freeze desalinated by the evaporation of liquid nitrogen. Three stages of freezing were conducted in order to bring 1.5% salt water salinity to 0.1%, which is recommended as safe to drink by the WHO [13]. In order to obtain accurate results by undergoing repeatability, three experiments were conducted of

the same initial conditions, where 1.5% salinity has been desalinated in three stages for each experiment as shown in Figure 5-29. In the first experiment the salinity dropped to 1.0% in the first stage and then after freezing the 1.0% salinity solution in the second stage, it dropped to 0.5%. The 0.5% solution was then taken to conduct freezing in the final stage and it dropped to 0.2%, which however is still above the recommended 0.1% salinity. In experiment two, the 1.5 % saltwater salinity decreased to 0.9% then to 0.4% and finally to 0.1%, which is within the acceptable limits of safe to drink water by the WHO [13]. In the third experiment, similar to experiment 2, the salinity of 1.5% saltwater solution first decreased to 0.9% and then to 0.4%. The 0.4% solution was further desalinated to decrease to 0.1% which is recommended as safe to drink by the WHO [13]. Figure 5-29 shows three experiments done for repeatability and the average deviation for the salinity levels are ±0.1.
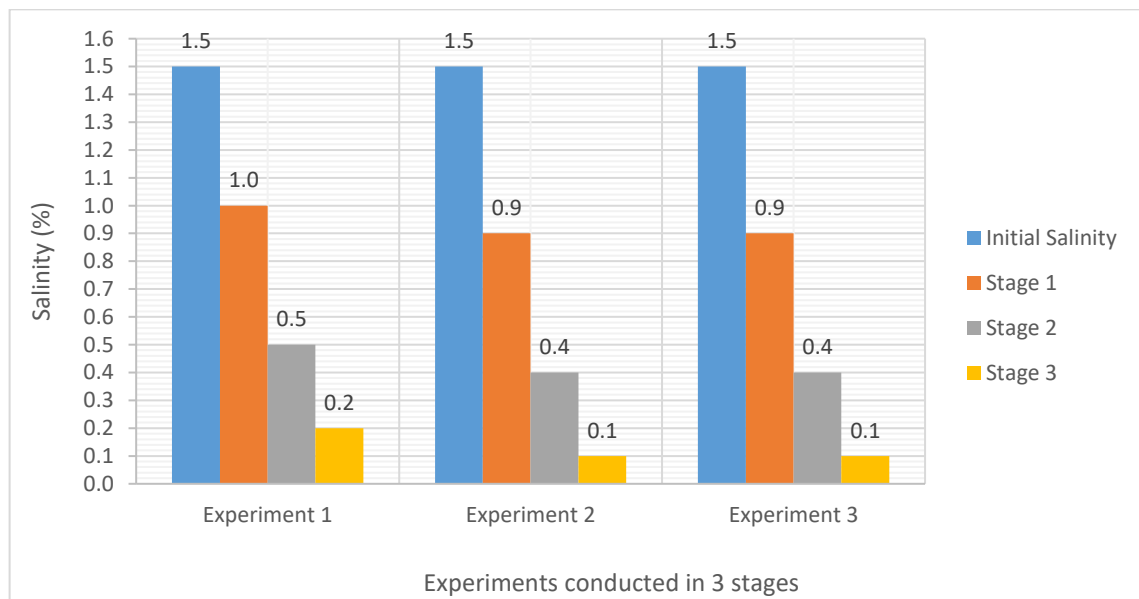
Figure 5-29: Three experiments conducted in 3 freezing stages

Figure 5-30 shows the average volume of ice obtained at each freezing stage for all the experiments conducted with a mesh being inserted. Therefore, it is seen that in the first

stage, the volume of ice obtained is low and it increases as the salinity of the initial salt solution decreases. Jayakody et al [7] explained that the ice crystals become less pure at higher initial salt water concentrations. William et al [98] proved that the initial salt water salinity had a significant effect on salt rejection and water recovery ratios.
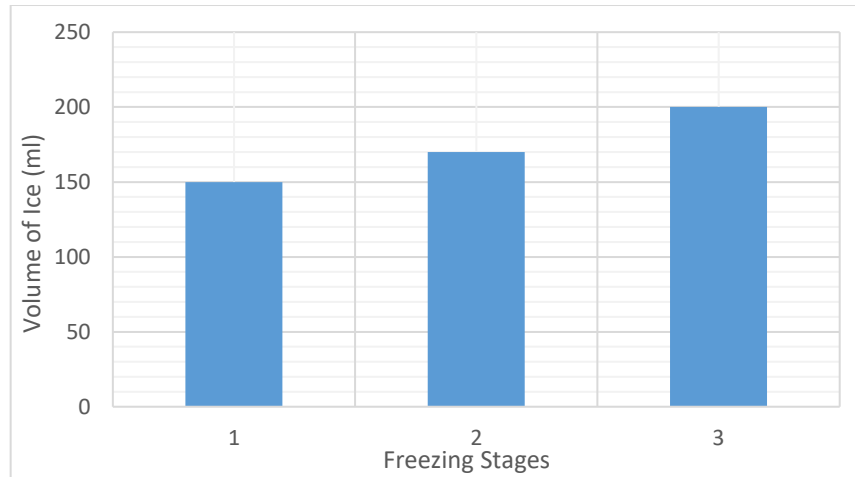
Figure 5-30: Volume of ice for different freezing stages on average for the 3 experiments conducted for the tests done with the mesh

5.9 CFD modelling validation

The CFD model presented in section 5.4 was validated using experimental work, where the operating conditions of the experiment were inputted in the CFD model as boundary conditions. The validation process was only carried out to the cases without the mesh as including a mesh inside the copper tube would require an excessively large computational time. The validation process was carried out in terms of the temperatures at the outer surface of the copper tube, volume of ice formed and also the ice and brine salinities.

Figure 5-31 compared the CFD predicted temperatures to their corresponding measured values at various locations on the copper tube surface at 9 minutes of real time. In this

figure, the experimental (case with a mass flowrate of 7.45×10^{-4} kg/s) temperature from T1-T10 were compared with those predicted by CFD, showing good agreement. The deviation from the experimental values was minimal with maximum deviation were at T3 and T9 of 9.9K and 9.2K respectively. Additionally, the average deviation of all the points were 6.3K. The average wall temperature of the experimental work was 277.75K and that of the CFD was 275.25K indicating good agreement.
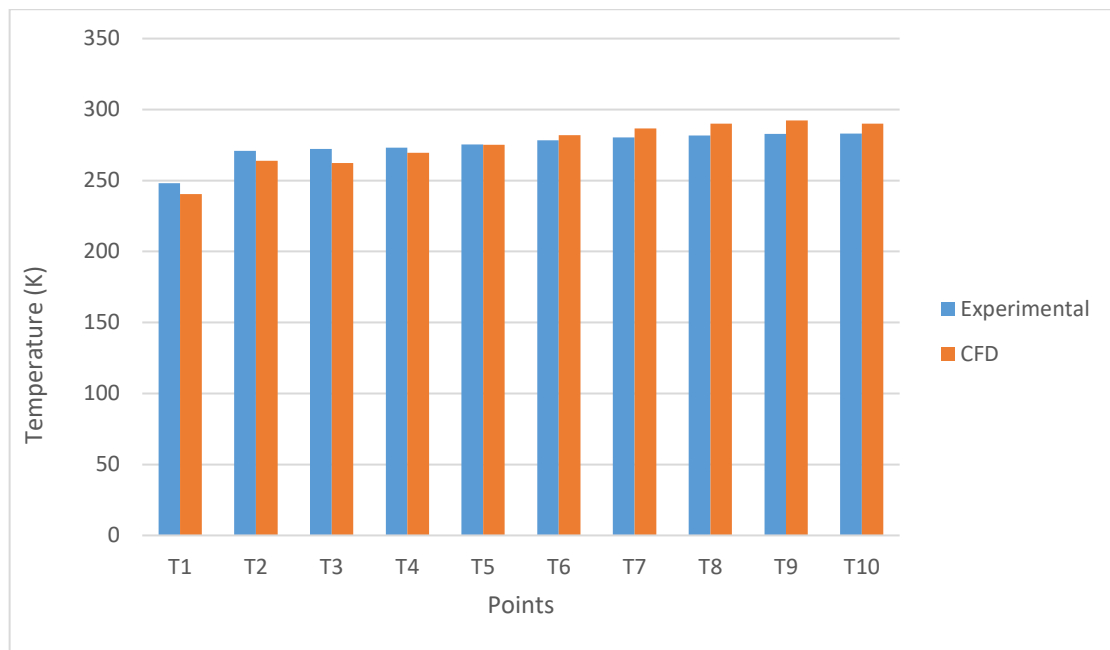
Figure 5-31: Temperature comparison at different locations of the copper tube

The CFD predicted volume of ice formed, and the ice and brine salinities were compared to the experimental values for each stage of freezing as shown in Table 5-7. It is apparent that the ice and brine salinities and the volumes of ice formed at each stage of freezing show good agreement.

Table 5-7: Salinity and volume for each stage of freezing for CFD and Experimental without mesh

Parameters	Initial Salinity of Sea Water (%) at Each Stage of Freezing								
	Stage 1 - 1.5% Salinity			Stage 2 - 0.9% Salinity			Stage 3 - 0.4% Salinity		
	Exp.	CFD	% Error	Exp.	CFD	% Error	Exp.	CFD	% Error
Ice Salinity (%)	0.90	0.73	18.78	0.40	0.33	17.75	0.10	0.08	17.00
Brine Salinity (%)	1.50	1.70	13.60	0.90	0.96	6.56	0.40	0.43	6.62
Volume Ice (ml)	55.00	46.71	15.07	70.00	64.29	8.16	75.00	72.73	3.03

It is also seen in Figure 5-30 and Table 5-7 for cases done with and without the mesh respectively; that in the third stage of freezing, 2.6 times more volume of ice was produced for the case with the mesh in comparison to the case without the mesh.

5.10   CFD parametric analysis – flow rate

The validated CFD model was used to carry out parametric analysis to investigate the effect of LN_2 flow rate on the produced volume of ice. Figure 5-32 shows the volume of ice at various inlet LN_2 velocities ranging from 0.0001 to 0.016m/s. It can be seen that the volume of ice increased with the increase of LN_2 velocity.
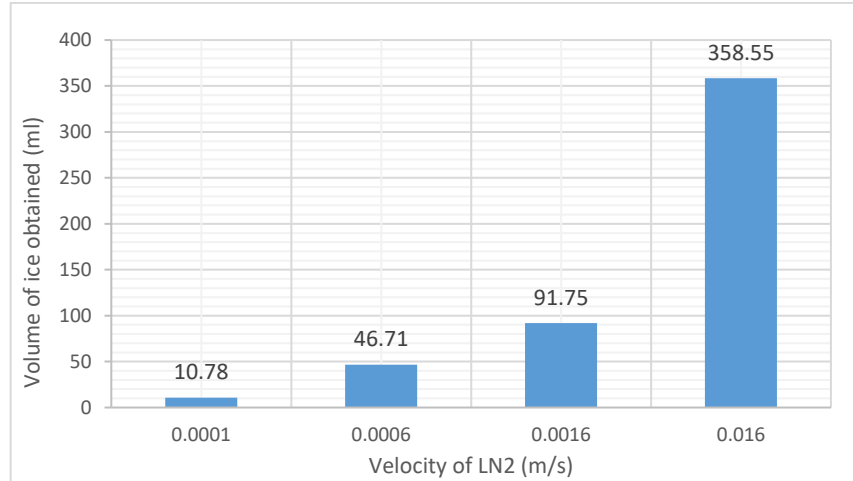
Figure 5-32: Volume of ice obtained at different LN_2 velocities

Figure 5-32 shows that for 0.0001m/s and 0.0006m/s of LN_2 velocities, a volume of 10.78ml and 46.71ml of ice were obtained respectively. Therefore, increasing the velocity of LN_2 by 6 times, increased the volume of ice by about 4.3 times. For 0.0016m/s velocity of liquid nitrogen, the volume of ice obtained was 91.75ml, where it produced 96.42% more ice in comparison to the 0.0006m/s velocity of LN_2. And for 0.016m/s velocity of LN_2, it is seen that a greater volume of ice of about 358.55ml was obtained, which is about 3.91 times more than the volume obtained at 0.0016m/s velocity of LN_2. This is due to the fact that, as the flow rate is increased, LN_2 travels further along the copper tube before being fully evaporated and thus reducing the temperature at a large area of the copper tube. Figure 5-33, Figure 5-34, Figure 5-35 and Figure 5-36 displays the temperature contours and the liquid phase fraction contours for 0.0001, 0.0006, 0.0016 and 0.016m/s of LN_2 velocity respectively.
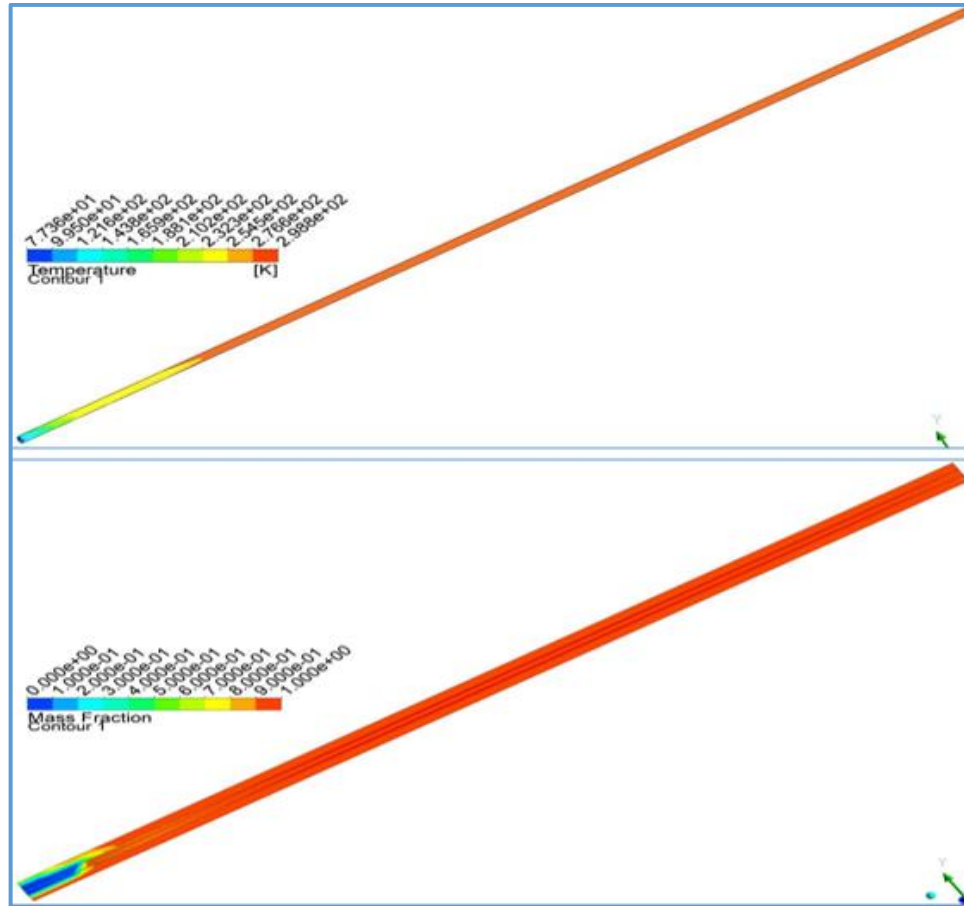
Figure 5-33: 0.0001m/s LN_2 velocity: a) temperature contours (top) b) liquid phase

fraction contours (bottom)
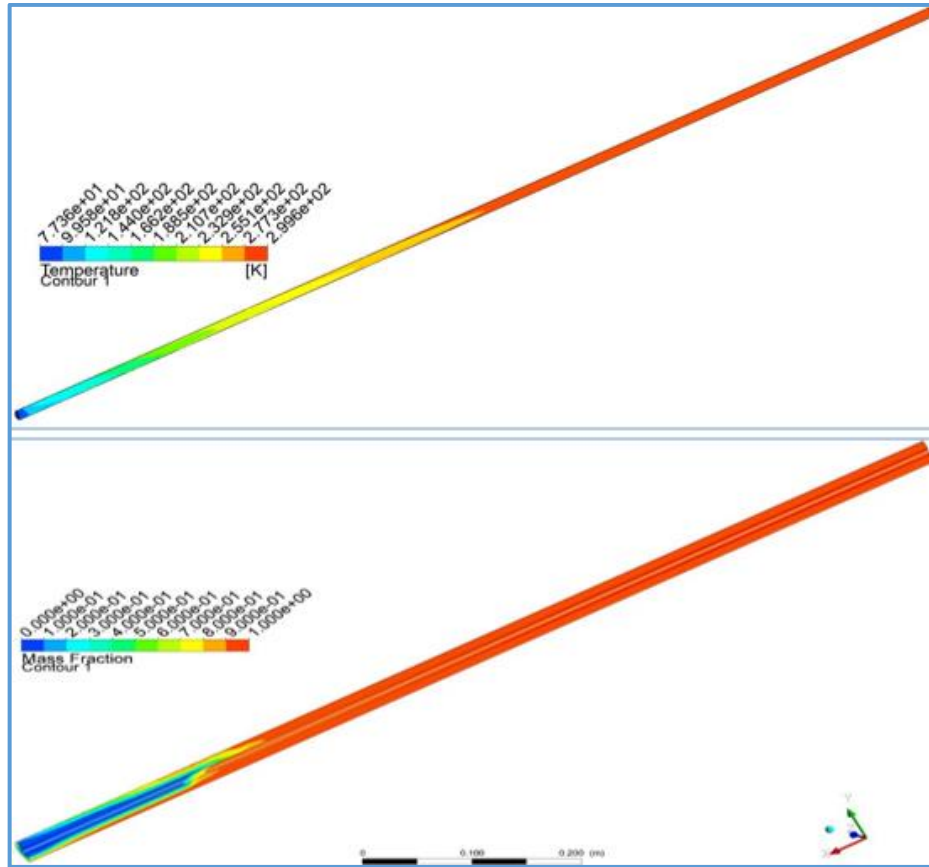
Figure 5-34: 0.0006m/s LN$_2$ velocity: a) temperature contours (top) b) liquid phase fraction contours (bottom)
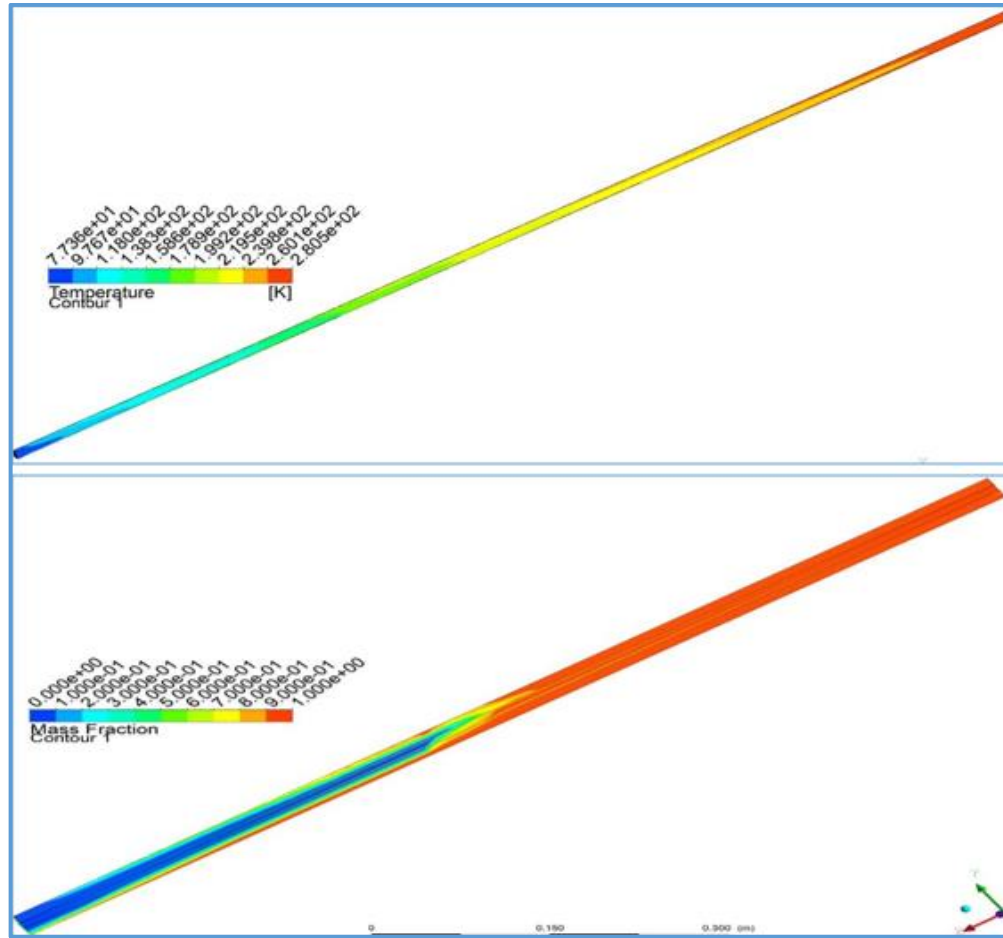
Figure 5-35: 0.0016m/s LN$_2$ velocity: a) temperature contours (top) b) liquid phase fraction contours (bottom)
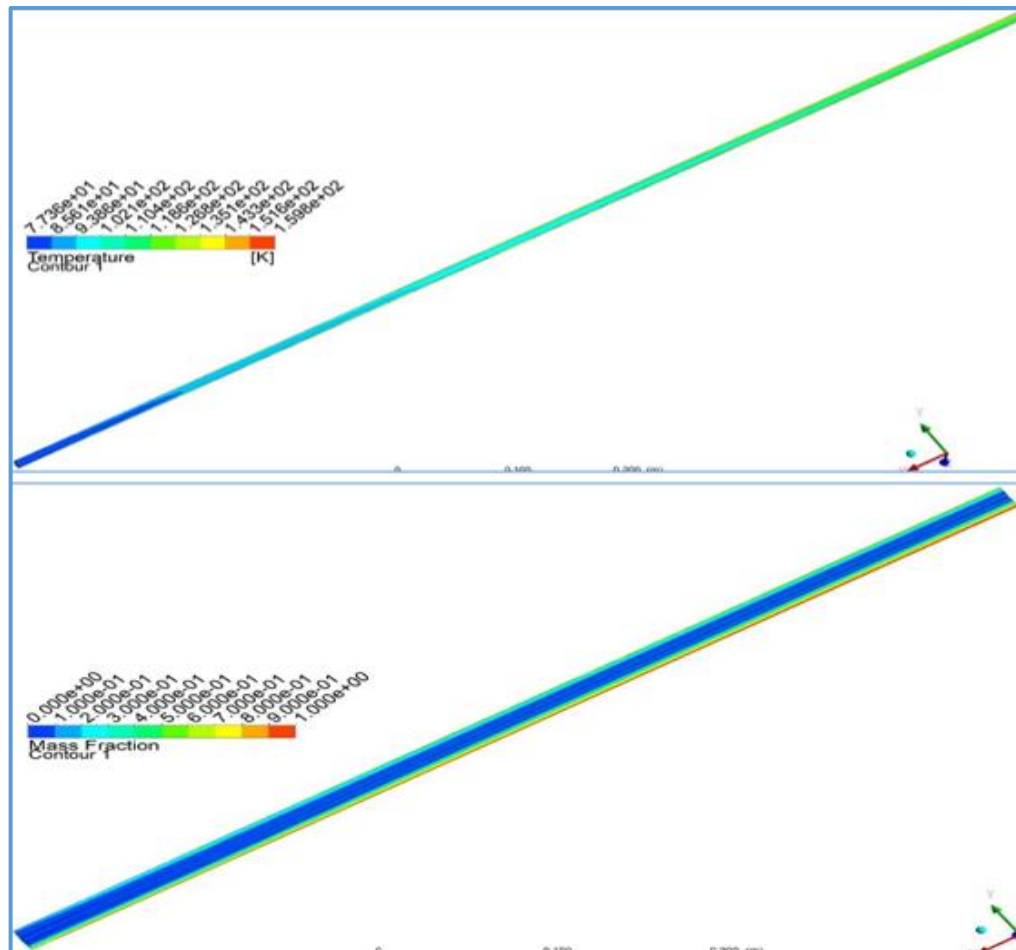
Figure 5-36: 0.016m/s LN$_2$ velocity: a) temperature contours (top) b) liquid phase fraction contours (bottom)

Therefore, it can be concluded that, by increasing the velocity of LN$_2$, more ice would be generated, and thus more water could be desalinated due to the fact that the LN$_2$ travels further along the copper tube before being evaporated. However, increasing the velocity means that the N$_2$ outlet conditions will have higher amount of cold energy.

5.11   Summary

Evaporation of liquid nitrogen to provide the cooling required for freeze desalination is discussed in this chapter. Firstly, CFD analysis have been presented where a CFD model for the evaporation of liquid nitrogen was developed. This CFD model was then validated using experimental testing. The temperatures at the surface of the copper tube, the volume of ice obtained, and the ice and brine salinities were compared using an experimental test rig that matches the CFD model.

Secondly, the developed experimental test rig was discussed. The test rig was built to evaporate liquid nitrogen while simultaneously freezing sea water in order to validate the CFD model. The layout of the test rig, the main components and the measuring devices were described. The experimental procedure, heat exchanger effectiveness and energy and salinity calculations were also explained. Four experiments were conducted with different flow rates of LN_2. The first two experiments had no mesh inserted while the other 2 had a copper mesh inserted in order to enhance the heat transfer. Inserting the copper mesh improved the heat transfer to a great deal, producing more ice and more desalinated water. Then the percentage of energy lost by water (overall efficiency) from liquid nitrogen to form ice increased significantly for the cases with the mesh; where it was 70% and 63% for the cases with the mesh and it was only 25% and 21% for the cases without the mesh. The heat exchanger effectiveness improved considerably when the mesh was inserted as it increased by about 3.65 times for the cases with the mesh in comparison to the cases carried out without using a mesh.

Three stages of freezing were done in order to bring the ice salinity of 1.5% down to 0.1% which is stated as safe to drink by the WHO [13]. It was also concluded that, the initial salinity of salt water had a significant effect on the volume of ice produced and the rate of freezing. 0.5litres of liquid nitrogen was evaporated with 104kJ of energy consumption to freeze 450ml of salt water in order to obtain a volume of 150ml, 170ml and 200ml of pure water in the first, second and third freezing stages respectively, to bring the ice salinity below 0.1%.

The CFD model was then compared with the results obtained from experimental testing where the temperatures at the outer surface of the copper tube, volume of ice obtained, and ice and brine salinities were compared to show good agreement between the two. Parametric study was then carried out by changing the liquid nitrogen flow rate to observe the volume of ice obtained. When increasing the velocity of LN_2 by 6 times, the volume of ice obtained increased by 4.3 times. It was concluded that by increasing the constant velocity of LN_2, more volume of ice was generated due to LN_2 travelling further along the copper tube before being evaporated leading to lower surface temperatures and higher rate of freezing.

CHAPTER 6

6. CONCLUSIONS AND RECOMMENDATIONS FOR FUTURE

In the conclusions chapter, certain information and outcomes are taken from the published papers; "Computational Fluid Dynamics Investigation on Indirect Contact Freeze Desalination" by Jayakody et al [12], "Numerical Investigation of Indirect Freeze Desalination using an Ice Maker Machine" by Jayakody et al [7] and "Indirect contact freeze water desalination for an ice maker machine – CFD simulation" by Jayakody et al [14].

6.1 Introduction

The basic substance for life is water and it progressively becoming a scarce resource. The world population is affected by the shortage of water; as many deaths and diseases are caused by poor water quality and this is expected to increase in the next 25 years. The increasing need for fresh water can be facilitated by desalination technologies which have been continuously developing. Majority of the desalination processes use evaporative methods where a vast amount of energy is used with high amounts of CO_2 emissions. Freeze desalination offers the benefit of lower energy consumption, due the latent heat of fusion being approximately one-seventh that of the latent heat of vaporisation. Computational fluid dynamics (CFD) is a powerful method that enables to investigate thermodynamic

178

processes, such as freeze desalination. Literature on computational fluid dynamics studies for freeze desalination is very limited and therefore the use of CFD to model and simulate the freeze desalination process was carried out. Cryogenic energy offers potential for enhancing renewable energy utilisation, due to the fact that liquid nitrogen and liquid air have high energy density. Therefore, the vast amount of cold energy obtained from regasification of LNG and liquid nitrogen/air (cryogenic energy) has the potential to be used for freeze desalination, as most of this cold energy has not been exploited today. Therefore, this high-quality energy supply can be used to cool sea water in the freeze desalination process. Due to the on-going energy supply-demand disparity, augmenting these technologies can assist in providing solutions for this, and in bettering the economics of the renewable energy powered desalination systems, as desalination capacity is growing worldwide.

6.2 Conclusions

Computational Fluid Dynamics modelling has been carried out to simulate the freeze desalination process where the salt separation and the dynamics of ice layer growth has been investigated to study the amount of ice formed and salinity of the remaining brine at different operating conditions. The CFD model has been validated using experimental testing and the feasibility of using an ice maker machine for freeze desalination was investigated by using a commercially available ice maker machine. The use of cryogenics for freeze desalination shows potential, where the use of cryogenic energy by the evaporation of liquid nitrogen to carry out freeze desalination was investigated. The aim

and objectives described in section 1.2 of chapter 1 have been achieved and the main outcomes are as follows:

6.2.1 Literature review outcomes:

✓ Due to the rapid shortage in water, desalination offers a solution to obtain potable water from seawater.

✓ Freeze desalination is an important process due to the lower energy consumption compared to other desalination processes; as the latent heat of freezing is low (333.5 kJ/kg) in comparison to the latent heat of evaporation (2256.7 kJ/kg).

✓ Cryogenic energy storage using liquid nitrogen and liquid air offers a solution for the intermittent nature of renewable energy sources because of its high energy density. The application of cryogenic energy for the freeze desalination process shows prospective due to the lower energy consumption.

6.2.2 CFD modelling outcomes:

✓ Computational fluid dynamics is an effective technique that enables the comprehensive analysis of thermodynamic processes like freeze desalination. Using the species transport, solidification/melting and energy modules in ANSYS Fluent software; a 3D CFD model was developed of the freeze desalination process that enabled the salt separation from saline water during the freezing process.

✓ The developed CFD model was validated using a Peltier cooling device and an ice maker machine. Using the Peltier device, the ice salinity and salt water temperatures from the experimental results were compared with the CFD simulation; the former

giving a percentage deviation of 2.10 and the latter giving an average deviation of ±0.495K [12]. Using the ice maker machine, the validation results showed average deviations of ±4.6K and ±0.56K for the freezing tube temperature and the temperature change of the ice forming respectively. Additionally, the percentage errors obtained for the salinities of ice and brine were 15% and 10.5% respectively indicating good agreement between the two. [7]

✓ Using the Peltier cooling device, the validated CFD model was used to investigate the effect of temperature, initial salinity and direction of freezing on ice production and ice salinity. Results showed that lower temperatures enabled faster freezing and more ice produced; where at 230K freezing temperature, 4.67 times more ice was obtained compared to the 260K case. Also, the higher the initial salinity of sea water, the less pure the ice crystals become and slower the freezing process, where for 55g/L of salt water concentration, 58.3% less ice was produced compared to 35g/L of salt water concentration. [12]

✓ Using the ice maker machine, validated CFD model was used for parametric analysis to observe the effects of the freeze tube temperature and the initial salinity of salt water on ice production and the final salinities of ice and brine. Results showed that as the freezing temperature decreases, the production of ice increases due to low temperature causing a faster rate of freezing and an improved solidification rate of salt water. At 225K freeze tube temperature, 5 times more ice was produced in comparison to the standard 257.15K freeze tube temperature that the ice maker usually operates at. [7]

✓ The lowest average salinity achieved was 0.5% at 245K freezing temperature for an ice thickness of 3.3mm, which is higher than the 0.1% recommended by the WHO

as safe to drink water [13]. Therefore, a second stage of freezing process was applied to this 0.5% to produce a salinity level below the required 0.1%. Results showed that salinity of 0.1% was achieved at temperatures of 215K, 225K, 235K and 245K with pure ice volumes of 12114.40, 12329.24, 9516.39 and 6785.36mm^3 respectively. Results also showed that the average ice salinity for the second stage of freezing was below 0.05% which is regarded as good quality drinking water. Such results highlight the potential of using the ice maker for freeze desalination to produce drinking water. [7]

✓ Parametric study was also carried out by changing the geometry of the freezing tubes where increasing the diameter and the length of the freezing tube, increased the volume of ice produced as this increased the total freezing surface area but this also increased the heat transfer rate and power consumption. It is seen that, the 20mm diameter with a 15mm length is the best geometry to use with a low heat transfer rate producing a higher volume of ice. Having 5 freezing tubes of 10mm diameter with a 20mm length dimensions would produce 9.3% more water than having 10 freezing tubes of 10mm diameter with a 10mm length.

6.2.3 Cryogenic energy storage for freeze desalination outcomes:

✓ The validated CFD model for freeze desalination was integrated with CFD modelling of liquid nitrogen evaporation to investigate the feasibility of using cryogenic energy for freeze desalination. This CFD model was then validated using experimental test facility constructed to evaporate liquid nitrogen to supply the cooling required for freezing.

✓ The temperatures at the surface of the copper tube, the volume of ice obtained, and the ice and brine salinities were compared using an experimental test rig that matches the CFD model. In the validation process, the average deviation for all the temperature points were only 6.3K and the percentage errors for salinity of ice, brine and volume of ice were 17%, 6.6% and 3% respectively, showing good agreement.

✓ Experimental heat exchanger test facility based on using liquid nitrogen to provide the cooling required for freeze desalination was constructed. Four experiments were conducted with different flow rates of LN_2. The first two experiments had no mesh inserted while the other 2 had a copper mesh inserted in order to enhance the heat transfer between the saline water and liquid nitrogen. Inserting the copper mesh improved the heat transfer significantly, producing 2.6 times more ice in comparison to without using a mesh. The percentage of energy lost by water to form ice (overall efficiency) from liquid nitrogen increased significantly for the cases with the mesh; where it was 70% and 63% for the cases with the mesh and it was only 25% and 21% for the cases without the mesh. The heat exchanger effectiveness improved considerably when the mesh was inserted as it was about 3.65 times more for the cases with the mesh in comparison to the cases carried out without using a mesh.

✓ Parametric study proved that, the initial salinity of salt water had a significant effect on the volume of ice produced and the output salinity. Therefore, to bring saline water with an initial salinity of 1.5% down to 0.1% which is stated as safe to drink water by the WHO [13], requires three stages of freezing.

✓ Parametric study was then carried out on CFD by changing the liquid nitrogen flow rate to observe the volume of ice obtained. When increasing the velocity of LN_2 by

6 times, the volume of ice obtained increased by 4.3times. It was concluded that by increasing the constant velocity of LN_2, more volume of ice was generated due to LN_2 travelling further along the copper tube before being evaporated.

Overall, the fundamentals of CFD modelling of the freeze desalination process was carried out and was validated using experimental work. This model was then improved and developed for an ice maker machine to assess the feasibility of using an ice maker for freeze desalination as a domestic application. This CFD model was also combined with the CFD modelling of the LN_2 evaporation process to assess the feasibility of using cryogenic energy for freeze desalination. Experimental work has been carried out using an ice maker machine and a constructed cryogenic test-rig to validate the developed CFD models. Furthermore, the overall efficiencies were investigated for the ice maker machine and for the cryogenic test-rig in order to reduce the ice salinity below 0.1% as regarded by the WHO as safe to drink [13]. Due to the requirement of reducing the ice salinity from 1.5% down to 0.1%, a number of freezing steps were required. Therefore, this meant that the energy requirement was also repeated for the number of steps carried out. Therefore, the overall efficiency was 0.12 for the ice maker machine to reduce the ice salinity from 1.5% to less than 0.1%. In the cryogenic desalination test rig, approximately 1.35 litres of liquid nitrogen was required to reduce the ice salinity from 1.5% to less than 0.1% with an overall efficiency of 0.23. Therefore, it can be concluded that the cryogenic test rig had a better efficiency. This highlights the potential of using the available cryogenic energy storage including the regasification of LNG or LN_2/L_{Air}, for freeze desalination, as most cold energy during LNG regasification, has been unexploited today.

6.3 Recommendations for future work

The freeze desalination process still remains to be a complex process consisting of a high capital cost. Therefore, the process is minimally used in the desalination industry. Regardless, freeze desalination plays an important role in the food industry, as well as in other areas as there are several industrial plants that use this method. Overall, further research should be performed in order to acquire a greater efficiency, as this form of desalination is considered as a promising technique, due to low energy consumption and the use of low temperature. Accordingly, the use of cryogenic energy proves to be an encouraging technique to conduct freeze desalination.

The research conducted in this thesis was to study the indirect contact freeze desalination technique and also to investigate the feasibility of using a commercially available ice maker machine to conduct freeze desalination. The use of cryogenic energy to effectively conduct freeze desalination is also investigated in this thesis. In order to increase the effectiveness of this process, further research must be conducted, such as:

➢ The test-rigs developed can be effectively improved to generate more desalinated ice with lower amount of energy consumed.

➢ The test facility developed is based on a batch process, therefore future developments should be carried out to ensure continuous production of desalinated ice.

➢ Investigate the effect of heat exchanger geometry to improve the heat transfer coefficient between LN_2 and the salt water.

➢ A stirrer can be included in the test rig that allows to stir the ice and create a slurry, which would reduce the amount of salt being trapped in ice layers, thus giving better quality ice.

➢ A washing system can be developed to systematically wash the ice obtained, where the ice can be cleaned thoroughly to produce ice with much lower salinities.

➢ The use of liquid air instead of liquid nitrogen can be investigated to conduct freeze desalination due to the many advantages of using liquid air over liquid nitrogen.

➢ The cryogenic test rig can be improved by having different mesh thicknesses along the copper tube to have a constant freezing temperature at the copper tube to generate a constant amount of ice along the tube to generate lower ice salinities.

REFERENCES

[1] E. Mathioulakis, V. Belessiotis, and E. Delyannis, "Desalination by using alternative energy: Review and state-of-the-art," *Desalination*, vol. 203, no. 1–3, pp. 346–365, 2007.

[2] J. E. Miller, "Review of water resources and desalination techniques," *Sand Rep.*, 2003.

[3] J. W. R. Engelman, R.P. Cincotta, B. Dye, T. Gardner-Outlaw, *People in the Balance: Population and Natural Resources at the Turn of the Millennium*, Population. Washington, D.C., 2000.

[4] M. Barlow and T. Clarke, "Blue Gold: The Fight to Stop the Corporate Theft of the World's Water," *Contemp. Hum. Ecol.*, vol. 11, no. 1, pp. 67–71, 2004.

[5] P. H. Gleick, "Water in crisis: a guide to the world's fresh water resources," *International Affairs*. 1993.

[6] H. March, "The politics, geography, and economics of desalination: a critical review," *Wiley Interdiscip. Rev. Water*, vol. 2, no. 3, pp. 231–243, 2015.

[7] H. Jayakody, R. Al-Dadah, and S. Mahmoud, "Numerical investigation of indirect freeze desalination using an ice maker machine," *Energy Convers. Manag.*, vol. 168, pp. 407–420, 2018.

[8] S. Burn, M. Hoang, D. Zarzo, F. Olewniak, E. Campos, B. Bolto, and O. Barron, "Desalination techniques - A review of the opportunities for desalination in agriculture," *Desalination*, vol. 364, pp. 2–16, 2015.

[9] H. M. Curran, "Water desalination by indirect freezing," *Desalination*, vol. 7, no. 3, pp. 273–284, 1970.

[10] P. G. Youssef, R. K. Al-Dadah, and S. M. Mahmoud, "Comparative analysis of desalination technologies," in *Energy Procedia*, 2014, vol. 61, pp. 2604–2607.

[11] W. Lin, M. Huang, and A. Gu, "A seawater freeze desalination prototype system utilizing LNG cold energy," *Int. J. Hydrogen Energy*, vol. 42, no. 29, pp. 18691–18698, 2017.

[12] H. Jayakody, R. Al-Dadah, and S. Mahmoud, "Computational fluid dynamics investigation on indirect contact freeze desalination," *Desalination*, vol. 420, pp. 21–33, 2017.

[13] US Environmental Protection Agency, "Water-quality criteria, standards, or recommended limits for selected properties and constituents," 1994. [Online]. Available: https://pubs.usgs.gov/wri/wri024094/pdf/mainbodyofreport-3.pdf. [Accessed: 14-Dec-2017].

[14] H. Jayakody, R. Al-Dadah, and S. Mahmoud, "Indirect contact freeze water desalination for an ice maker machine - CFD simulation," in *E3S Web of Conferences*, 2017, vol. 22.

[15] J. Liu, Y. Wang, Z. Yu, X. Cao, L. Tian, S. Sun, and P. Wu, "A comprehensive analysis of blue water scarcity from the production, consumption, and water transfer perspectives," *Ecol. Indic.*, vol. 72, pp. 870–880, 2017.

[16] M. Pedro-Monzonís, A. Solera, J. Ferrer, T. Estrela, and J. Paredes-Arquiola, "A review of water scarcity and drought indexes in water resources planning and management," *J. Hydrol.*, vol. 527, pp. 482–493, 2015.

[17] C. Charcosset, "A review of membrane processes and renewable energies for desalination," *Desalination*, vol. 245, no. 1–3, pp. 214–231, 2009.

[18] T. I. E. Veldkamp, Y. Wada, H. de Moel, M. Kummu, S. Eisner, J. C. J. H. Aerts,

REFERENCES

and P. J. Ward, "Changing mechanism of global water scarcity events: Impacts of socioeconomic changes and inter-annual hydro-climatic variability," *Glob. Environ. Chang.*, vol. 32, pp. 18–29, 2015.

[19]   I. C. Karagiannis and P. G. Soldatos, "Water desalination cost literature: review and assessment," *Desalination*, vol. 223, no. 1–3, pp. 448–456, 2008.

[20]   O. Sahin, R. A. Stewart, and M. G. Porter, "Water security through scarcity pricing and reverse osmosis: A system dynamics approach," *J. Clean. Prod.*, vol. 88, pp. 160–171, 2015.

[21]   D. Lawala, M. Antara, A. Khalifaa, S. Zubaira, and F. Al-Sulaimana, "Humidification-dehumidification desalination system operated by a heat pump," *Energy Convers. Manag.*, vol. 161, pp. 128–140, 2018.

[22]   O. Sahin, R. S. Siems, R. A. Stewart, and M. G. Porter, "Paradigm shift to enhanced water supply planning through augmented grids, scarcity pricing and adaptive factory water: A system dynamics approach," *Environ. Model. Softw.*, vol. 75, pp. 348–361, 2016.

[23]   "World Economic Forum, 2014. 'Global Risks 2014, Ninth ed.'"

[24]   United Nations Educational Scientific and Cultural Organization (UNESCO), *Water in a changing world. The United Nations World Water Development Report 2 (WWDR2). World Water Assessment Programme (WWAP).* 2009.

[25]   Y. Ramírez, L. A. Cisternas, and A. Kraslawski, "Application of House of Quality in assessment of seawater pretreatment technologies," *J. Clean. Prod.*, vol. 148, pp. 223–232, 2017.

[26]   R. Clayton, "A Review Of Current Knowledge: Desalination For Water Supply. 3rd ed. Marlow, Buckinghamshire: Foundation for Water Research, Print.," 2015.

REFERENCES

[27]   M. C. Fragkou and J. McEvoy, "Trust matters: Why augmenting water supplies via desalination may not overcome perceptual water scarcity," *Desalination*, vol. 397, pp. 1–8, 2016.

[28]   A. Al-Karaghouli and L. L. Kazmerski, "Energy consumption and water production cost of conventional and renewable-energy-powered desalination processes," *Renewable and Sustainable Energy Reviews*, vol. 24. pp. 343–356, 2013.

[29]   H. Cooley, P. H. Gleick, and G. Wolff, *Desalination with a grain of salt - a California Perspective*. 2006.

[30]   A. D. Khawaji, I. K. Kutubkhanah, and J. M. Wie, "Advances in seawater desalination technologies," *Desalination*, vol. 221, no. 1–3, pp. 47–69, 2008.

[31]   M. S. Rahman, M. Ahmed, and X. D. Chen, "Freezing-melting process and desalination: I. review of the state-of-the-art," *Sep. Purif. Rev.*, vol. 35, no. 2, pp. 59–96, 2006.

[32]   J. Chang, J. Zuo, K. J. Lu, and T. S. Chung, "Freeze desalination of seawater using LNG cold energy," *Water Res.*, vol. 102, pp. 282–293, 2016.

[33]   C. Li, S. Besarati, Y. Goswami, E. Stefanakos, and H. Chen, "Reverse osmosis desalination driven by low temperature supercritical organic rankine cycle," *Appl. Energy*, vol. 102, pp. 1071–1080, 2013.

[34]   D. Han, W. F. He, C. Yue, and W. H. Pu, "Study on desalination of zero-emission system based on mechanical vapor compression," *Appl. Energy*, vol. 185, pp. 1490–1496, 2017.

[35]   W. Cao, C. Beggs, and I. M. Mujtaba, "Theoretical approach of freeze seawater desalination on flake ice maker utilizing LNG cold energy," *Desalination*, vol. 355, pp. 22–32, 2014.

REFERENCES

[36] A. Brunetti, F. Macedonio, G. Barbieri, and E. Drioli, "Membrane engineering for environmental protection and sustainable industrial growth: Options for water and gas treatment," *Environ. Eng. Res.*, vol. 20, no. 4, pp. 307–328, 2015.

[37] A. Chafidz, E. D. Kerme, I. Wazeer, Y. Khalid, A. Ajbar, and S. M. Al-Zahrani, "Design and fabrication of a portable and hybrid solar-powered membrane distillation system," *J. Clean. Prod.*, vol. 133, pp. 631–647, 2016.

[38] A. Shahmansouri, J. Min, L. Jin, and C. Bellona, "Feasibility of extracting valuable minerals from desalination concentrate: A comprehensive literature review," *Journal of Cleaner Production*, vol. 100. pp. 4–16, 2015.

[39] H. Jafari Mosleh, S. J. Mamouri, M. B. Shafii, and A. Hakim Sima, "A new desalination system using a combination of heat pipe, evacuated tube and parabolic through collector," *Energy Convers. Manag.*, vol. 99, pp. 141–150, 2015.

[40] B. Kalista, H. Shin, J. Cho, and Am Jang, "Current development and future prospect review of freeze desalination," *Desalination*, vol. 447, pp. 167–181, 2018.

[41] Z. Lu and L. Xu, "Freezing Desalination Process," *Desalin. Water Resour.*, vol. 2, pp. 275–290, 2014.

[42] D. G. and J. N. Randall, "A Succinct Review Of The Treatment Of Reverse Osmosis Brines Using Freeze Crystallization," *J. Water Process Eng.*, vol. 8, pp. 186–194, 2015.

[43] R. Fujioka, L. P. Wang, G. Dodbiba, and T. Fujita, "Application of progressive freeze-concentration for desalination," *Desalination*, vol. 319, pp. 33–37, 2013.

[44] A. A. A. Attia, "New proposed system for freeze water desalination using auto reversed R-22 vapor compression heat pump," *Desalination*, vol. 254, no. 1–3, pp. 179–184, 2010.

REFERENCES

[45] P. M. Williams, M. Ahmad, B. S. Connolly, and D. L. Oatley-Radcliffe, "Technology for freeze concentration in the desalination industry," *Desalination*, vol. 356. pp. 314–327, 2015.

[46] Y. Rogers, G. and Mayhew, "Thermodynamic and transport properties of fluids. Oxford, UK: B. Blackwell," 1995.

[47] V. G. Gude, "Energy storage for desalination processes powered by renewable energy and waste heat sources," *Appl. Energy*, vol. 137, pp. 877–898, 2015.

[48] H. J. Dakkama, P. G. Youssef, R. K. Al-Dadah, and S. Mahmoud, "Adsorption ice making and water desalination system using metal organic frameworks/water pair," *Energy Convers. Manag.*, vol. 142, pp. 53–61, 2017.

[49] M. Hasan, R. Filimonov, J. Chivavava, J. Sorvari, M. Louhi-Kultanen, and A. E. Lewis, "Ice growth on the cooling surface in a jacketed and stirred eutectic freeze crystallizer of aqueous Na2SO4solutions," *Sep. Purif. Technol.*, vol. 175, pp. 512–526, 2017.

[50] W. M. Haynes, Ed., *CRC Handbook Of Chemistry And Physics. 95th ed. Boca Raton: CRC Press*. 2015.

[51] P. Pronk, "Fluidized Bed Heat Exchangers To Prevent Fouling In Ice Slurry Systems And Industrial Crystallizers," 2006.

[52] P. Pronk, C. A. Infante Ferreira, and G. J. Witkamp, "Influence of solute type and concentration on ice scaling in fluidized bed ice crystallizers," *Chem. Eng. Sci.*, vol. 61, no. 13, pp. 4354–4362, 2006.

[53] L. Vrbka and P. Jungwirth, "Brine rejection from freezing salt solutions: A molecular dynamics study," *Phys. Rev. Lett.*, vol. 95, no. 14, pp. 1–4, 2005.

[54] C. S. Luo, W. W. Chen, and W. F. Han, "Experimental study on factors affecting the

quality of ice crystal during the freezing concentration for the brackish water," *Desalination*, vol. 260, no. 1–3, pp. 231–238, 2010.

[55] T. Bartholin, P. Haubold, M. Godicchen, and E. Bartholin, "Thomae Bartholini de nivis usu medico observationes variae.," *Hafniae: Typis Matthiae Godicchii, Sumptibus Petri Haubold, Bibl.*, 1661.

[56] R. Boyle and C. Merret, "New experiments and observations touching cold, or, An experimental history of cold begun.," *London Print. John Crook*, 1665.

[57] A. Kircheri, "Mundus subterraneus, inXIIlibros digestus.," *2nd ed. Amsterdam*, 1668.

[58] A. Lorgna, "Nuove Sperienze intorno alla Dolcivicazione dell'Acqua del Mare.," *Mem. Mat. Fis. Soc. Ital. Sci. Modena, 3*, 1786.

[59] G. Nebbia and G. N. Menozzi, "Early experiments on water desalination by freezing," *Desalination*, vol. 5, no. 1, pp. 49–54, 1968.

[60] H. Hendrickson and R. Moulton, "Research and development of processes for desalting water by freezing.," *Washington, D.C. U.S. Dept. Inter.*, 1956.

[61] G. Karnofsky, "Saline water conversion by direct freezing with butane.," *Res. Dev. Prog. Rep. No. 40. Washingt. US Dept. Commer.*, 1960.

[62] H. Wiegandt, P. Harriott, and J. Leinroth, "Desalting of seawater by freezing.," *Washingt. U.S. G.P.O.*, 1968.

[63] Dravo Corp., "10, 000,000 gallon per day secondary refrigerant freeze desalting plant.," *Rep. PB251906, Off. Saline Water US dept. Inter.*, 1973.

[64] W. H. Denton, M. J. S. Smith, J. T. Klaschka, R. Forgan, H. R. Diffey, C. H. Rumary, and R. W. Dawson, "Experimental studies on washing and melting ice crystals in the immiscible refrigerant freezing process," *Desalination*, 1974.

REFERENCES

[65] H. F. Wiegandt and R. L. Von Berg, "Myths about freeze desalting," *Desalination*, vol. 33, no. 3, pp. 287–297, 1980.

[66] J. Rosen, "Freeze concentration beats the heat. (FC may save energy compared to conventional freezing processes).," *Mech. Eng.*, vol. 112, no. 12, pp. 46–50, 1990.

[67] J. Sánchez, Y. Ruiz, J. M. Auleda, E. Hernández, and M. Raventós, "Review. Freeze concentration in the fruit juices industry," *Food Sci. Technol. Int.*, vol. 15, no. 30, pp. 45–26, 2009.

[68] J. Rosen, "Freeze concentration beats the heat.," *New York Am. Soc. Mech. Eng.*, 1990.

[69] N. J. J. Huige and H. A. C. Thijssen, "Production of large crystals by continuous ripening in a stirrer tank," *J. Cryst. Growth*, vol. 13–14, pp. 483–487, 1972.

[70] R. W. Hartel, "Evaporation and freeze concentration.," *Handb. Food Eng. Heldman, D.R. Lund, D.B. (eds.), Marcel Dekker New York*, pp. 341–392.

[71] W. Gibson, D. Emmermann, G. Grossman, R. Johnson, A. Modica, and A. Pallone, "Spray freezer and pressurized counterwasher for freeze desalination," *Desalination*, vol. 14, no. 3, pp. 249–262, 1974.

[72] Y. Spiegler, K. and El-Sayed, "A desalination primer," *St. Maria Imbaro, Italy Balaban Desalin. Publ.*, 1994.

[73] W. Rice and D. S. C. Chau, "Freeze desalination using hydraulic refrigerant compressors," *Desalination*, vol. 109, no. 2, pp. 157–164, 1997.

[74] L. C. Dickey, "Evaporation of water from agitated freezing slurries at low pressure," *Desalination*, vol. 104, no. 3, pp. 155–163, 1996.

[75] M. V. Rane and Y. S. Padiya, "Heat pump operated freeze concentration system with tubular heat exchanger for seawater desalination," *Energy Sustain. Dev.*, vol. 15, no.

2, pp. 184–191, 2011.

[76]   P. Brian, "Potential advantages and development problems in water desalination by freezing.," *Chem. Engr. May*, vol. 78, pp. 191–197, 1971.

[77]   A. . Barduhn, "The freezing process for water conversion in the United States.," *Sel. Pap. Desalin. Ocean Technol. Levine, S.N. (ed.), Dover New York, 414.*, 1968.

[78]   R. Barduhn, A., Rose, A. and Sweeny, "Waste-water renovation," *Cincinnati, Ohio U.S. Dept. Heal. Educ. Welfare, Public Heal. Serv. Div. Water Supply Pollut. Control*, 1963.

[79]   J. B. Pangborn, "Observations of the eutectic freezing of salt solutions," *Dep. Chem. Eng. Report, Syracuse Univ.*, 1963.

[80]   A. Schroeder, P., Chan, A. and Rashid Khan, "Freezing processes-the standard of the future," *Desalination*, vol. 21, no. 2, pp. 125–136, 1977.

[81]   F. Van Der Ham, G. J. Witkamp, J. De Graauw, and G. M. Van Rosmalen, "Eutectic freeze crystallization: Application to process streams and waste water purification," *Chem. Eng. Process. Process Intensif.*, vol. 37, no. 2, pp. 207–213, 1998.

[82]   G. L. Stepakoff, D. Siegelman, R. Johnson, and W. Gibson, "Development of a eutectic freezing process for brine disposal," *Desalination*, vol. 15, no. 1, pp. 25–38, 1974.

[83]   F. Van Der Ham, G. J. Witkamp, J. De Graauw, and G. M. Van Rosmalen, "Eutectic freeze crystallization simultaneous formation and separation of two solid phases," *J. Cryst. Growth*, vol. 198/199, pp. 744–748, 1999.

[84]   F. van der Ham, M. M. Seckler, and G. J. Witkamp, "Eutectic freeze crystallization in a new apparatus: The cooled disk column crystallizer," *Chem. Eng. Process. Process Intensif.*, vol. 43, no. 2, pp. 161–167, 2004.

REFERENCES

[85]   C. Himawan, R. J. C. Vaessen, H. J. M. Kramer, M. M. Seckler, and G. J. Witkamp, "Dynamic modeling and simulation of eutectic freeze crystallization," *J. Cryst. Growth*, vol. 237–239, pp. 2257–2263, 2002.

[86]   H. Thijssen, "Apparatus for separation and treatment of solid particles from a liquid suspension," U.S. Patent 3,872,009.

[87]   K. El Kadi and I. Janajreh, "Desalination by Freeze Crystallization : An Overview," *Int . J . Therm. Environ. Eng.*, vol. 15, no. 2, pp. 103–110, 2017.

[88]   J. Amran N, Samsuri S, Safiei N, Yamani Z, Zakaria and M., "Review: Parametric Study on the Performance of Progressive Cryoconcentration System," *Chem. Eng.*, 2014.

[89]   P. Wang and T. S. Chung, "A conceptual demonstration of freeze desalination-membrane distillation (FD-MD) hybrid desalination process utilizing liquefied natural gas (LNG) cold energy," *Water Res.*, vol. 46, no. 13, pp. 4037–4052, 2012.

[90]   O. Miyawaki, S. Kato, and K. Watabe, "Yield improvement in progressive freeze-concentration by partial melting of ice," *J. Food Eng.*, vol. 108, no. 3, pp. 377–382, 2012.

[91]   M. Gunathilake, M. Dozen, K. Shimmura, and O. Miyawaki, "An apparatus for partial ice-melting to improve yield in progressive freeze-concentration," *J. Food Eng.*, vol. 142, pp. 64–69, 2014.

[92]   L. Liu, O. Mjyawaki, and K. Nakamura, "Progressive Freeze-Concentration of Model Liquid Food," *Food Sci. Technol. Int. Tokyo*, vol. 3, no. 4, pp. 348–352, 1997.

[93]   P. A. Weiss, "Desalination by freezing. Practice of Desalination," *(ed. R Bakish), New Jersey Noyes Data Corp. New Jersey*, pp. 260–270, 1973.

[94]   W. Johnson, "State-of-the-art of freezing processes, their potential and future,"

Desalination, vol. 19, no. 1–3, pp. 349–358, 1976.

[95] N. Akhtar, L. McGrath, and P. Roberts, "Dynamic modelling and partial simulation of a pilot scale column crystallizer," *Desalination*, vol. 28, no. 1, pp. 1–11, 1979.

[96] O. Miyawaki, L. Liu, and K. Nakamura, "Effective partition constant of solute between ice and liquid phases in progressive freeze-concentration," *J. Food Sci.*, vol. 63, no. 5, pp. 756–758, 1998.

[97] A. Rich, Y. Mandri, D. Mangin, A. Rivoire, S. Abderafi, C. Bebon, N. Semlali, J. P. Klein, T. Bounahmidi, A. Bouhaouss, and S. Veesler, "Sea water desalination by dynamic layer melt crystallization: Parametric study of the freezing and sweating steps," *J. Cryst. Growth*, vol. 342, no. 1, pp. 110–116, 2012.

[98] P. M. Williams, M. Ahmad, and B. S. Connolly, "Freeze desalination: An assessment of an ice maker machine for desalting brines," *Desalination*, vol. 308, pp. 219–224, 2013.

[99] Y. Lim, M. Al-Atabi, and R. A. Williams, "Liquid air as an energy storage: A review," *J. Eng. Sci. Technol.*, vol. 11, no. 4, pp. 496–515, 2016.

[100] M. Antonelli, U. Desideri, R. Giglioli, F. Paganucci, and G. Pasini, "Liquid air energy storage: A potential low emissions and efficient storage system," *Energy Procedia*, vol. 88, pp. 693–697, 2016.

[101] R. Morgan, S. Nelmes, E. Gibson, and G. Brett, "Liquid air energy storage - Analysis and first results from a pilot scale demonstration plant," *Appl. Energy*, vol. 137, pp. 845–853, 2015.

[102] Tom Lombardo, "Cryogenic Energy Storage," 2013. [Online]. Available: https://www.engineering.com/ElectronicsDesign/ElectronicsDesignArticles/Article ID/5780/Cryogenic-Energy-Storage.aspx.

REFERENCES

[103] D. Strahan, "Liquid Air in the energy and transport systems: Opportunities for industry and innovation in the UK," *Centre for Low Carbon Futures*, 2013. [Online]. Available: http://dearman.co.uk/wp-content/uploads/2016/05/Liquid-air-in-the-energy-transport-systems.pdf.

[104] H. Chen, Y. Ding, Y. Li, X. Zhang, and C. Tan, "Air fuelled zero emission road transportation: A comparative study," *Appl. Energy*, vol. 88, no. 1, pp. 337–342, 2011.

[105] C. Knowlen, J. Williams, A. T. Mattick, H. Deparis, and A. Hertzberg, "Quasi-Isothermal Expansion Engines for Liquid Nitrogen Automotive Propulsion," *SAE Electr. Veh. Altern. Powerplants, Energy Manag. Batter. Technol. - SP-1284*, 1997.

[106] R. M. Skobel and D. Davey, "Liquid nitrogen cooled beverage dispenser US20080289357A1," 2012.

[107] F. Dakhil, "Air conditioning apparatus using liquid nitrogen US5960635A," 1999.

[108] M. Watanabe, H. Yumura, H. Hirota, T. Masuda, M. Shimoda, R. Ohno, M. Ikeuchi, H. Yaguchi, H. Ichikawa, T. Mimura, S. Honjo, and T. Hara, "Recent progress of Liquid nitrogen cooling system (LINCS) for Yokohama HTS cable project," *Phys. Procedia*, vol. 36, pp. 1313–1318, 2012.

[109] J. Wang, W. Xu, S. Ding, Y. Shi, M. Cai, and A. Rehman, "Liquid air fueled open-closed cycle Stirling engine and its exergy analysis," *Energy*, vol. 90, pp. 187–201, 2015.

[110] D. Strahan, "Liquid Air on the European Highway, The economic and environmental impact of zero-emission transport refrigeration," *Dearman*, 2015. [Online]. Available: https://www.airqualitynews.com/wp-content/uploads/2015/09/Liquid-Air-on-the-European-Highway.pdf.

[111] B. Ameel, C. T'Joen, K. De Kerpel, P. De Jaeger, H. Huisseune, M. Van Belleghem, and M. De Paepe, "Thermodynamic analysis of energy storage with a liquid air Rankine cycle," *Appl. Therm. Eng.*, vol. 52, no. 1, pp. 130–140, 2013.

[112] H. Liu and L. You, "Characteristics and applications of the cold heat exergy of liquefied natural gas," *Energy Convers. Manag.*, vol. 40, no. 14, pp. 1515–1525, 1999.

[113] T. Miyazaki, Y. T. Kang, A. Akisawa, and T. Kashiwagi, "A combined power cycle using refuse incineration and LNG cold energy," *Energy*, vol. 25, no. 7, pp. 639–655, 2000.

[114] A. Messineo and D. Panno, "Potential applications using LNG cold energy in Sicily," *Int. J. Energy Res.*, vol. 32, no. 11, pp. 1058–1064, 2008.

[115] D. Strahan, "World Changing Refrigeration www.dearman.co.uk Powered by the revolutionary Dearman engine, and fuelled by liquid nitrogen for sustainable clean cool energy," *Dearman*, 2017. [Online]. Available: https://dearman.co.uk/wp-content/uploads/2018/09/Dearman-Hubbard-Transport-Refrigeration-Unit.pdf.

[116] W. Xu, J. Wang, M. Cai, and Y. Shi, "Liquid air fueled open–closed cycle Stirling engine," *Energy Convers. Manag.*, vol. 94, pp. 210–220, 2015.

[117] C. A. Ordonez, "Liquid nitrogen fueled, closed Brayton cycle cryogenic heat engine," *Energy Convers. Manag.*, vol. 41, no. 4, pp. 331–341, 2000.

[118] M. C. Plummer, C. P. Koehler, D. R. Flanders, R. F. Reidy, and C. A. Ordonez, "Cryogenic Heat Engine Experiment," *Adv. Cryog. Eng.*, vol. 43, pp. 1245–1252, 1998.

[119] M. D. Newman and S. A. McCormick, "LNG (liquefied natural gas) and LIN (liquid nitrogen) in transit refrigeration heat exchange system US8763409B2," 2014.

[120] R. Garlov, V. Saveliev, K. Gavrylov, L. Golovin, and H. Pedolsky, "Refrigeration of a food transport vehicle utilizing liquid nitrogen US6345509B1," 2002.

[121] C. A. Ordonez and M. C. Plummer, "Cold thermal storage and cryogenic heat engines for energy storage applications," *Energy Sources*, vol. 19, no. 4, pp. 389–396, 1997.

[122] S. K. Ratkje and O. Flesland, "Modelling the freeze concentration process by irreversible thermodynamics," *J. Food Eng.*, vol. 25, no. 4, pp. 553–568, 1995.

[123] F. G. F. Qin, X. D. Chen, and M. M. Farid, "Growth kinetics of ice films spreading on a subcooled solid surface," *Sep. Purif. Technol.*, vol. 39, no. 1–2 SPEC. ISS., pp. 109–121, 2004.

[124] F. G. F. Qin, X. D. Chen, and K. Free, "Freezing on subcooled surfaces, phenomena, modeling and applications," *Int. J. Heat Mass Transf.*, vol. 52, no. 5–6, pp. 1245–1253, 2009.

[125] F. G. F. Qin, J. Zhao, A. Russell, X. Chen, J. Chen, and L. Robertson, "Simulation And Experiment Of The Unsteady Heat Transport In The Onset Time Of Nucleation And Crystallization Of Ice From The Subcooled Solution," *Int. J. Heat Mass Transf.*, vol. 46, no. 17, pp. 3221–3231, 2003.

[126] J. Chivavava, M. Rodriguez-Pascual, and A. E. Lewis, "Effect of operating conditions on ice characteristics in continuous eutectic freeze crystallization," *Chem. Eng. Technol.*, vol. 37, no. 8, pp. 1314–1320, 2014.

[127] F. E. Genceli, M. Rodriguez Pascual, S. Kjelstrup, and G.-J. Witkamp, "Coupled Heat and Mass Transfer during Crystallization of $MgSO_4 \cdot 7H_2O$ on a Cooled Surface," *Cryst. Growth Des.*, vol. 9, no. 3, pp. 1318–1326, 2009.

[128] A. J. and M. J. S. Abid, "Simulation Of Binary Mixture Freezing: Application To

Seawater Desalination," *Int. J. Eng. Sci. Innov. Technol.*, vol. 4, no. 6, pp. 158–163, 2015.

[129] "ANSYS Fluent," 2018. [Online]. Available: https://www.ansys.com/en-gb/products/fluids/ansys-fluent.

[130] Aroussia Jaouahdou and Mohamed Safi, "Experimental and Numerical study of Freezing Water around a cylindrical tube: application to desalination," in *12th International Conference on Heat Transfer, Fluid Mechanics and Thermodynamics*, 2016, pp. 456–461.

[131] L. Vrbka and P. Jungwirth, "Molecular dynamics simulations of freezing of water and salt solutions," *J. Mol. Liq.*, vol. 134, no. 1–3 SPEC. ISS., pp. 64–70, 2007.

[132] A. Junkratuek, J. Srudhiprom, and T. Srinophakun, "Computational fluid dynamics of a horizontal hydrocyclone for freezing desalination," *Asia-Pacific J. Chem. Eng.*, vol. 12, no. 5, pp. 765–774, 2017.

[133] V. R. Voller, "Modeling Solidification Processes. Technical report. Mathematical Modeling of Metals," *Process. Oper. Conf. Palm Desert, CAAmerican Metall. Soc.*, 1987.

[134] V. R. Voller, A. D. Brent, and K. J. Reid, "A Computational Modeling Framework for the Analysis of Metallurgical Solidification Process and Phenomena," *Conf. Solidif. Process. Ranmoor House, Sheffield, Engl.*, 1987.

[135] V. R. Voller and C. Prakash, "A fixed grid numerical modelling methodology for convection-diffusion mushy region phase-change problems," *Int. J. Heat Mass Transf.*, vol. 30, no. 8, pp. 1709–1719, 1987.

[136] I. Ansys, "ANSYS FLUENT theory guide 15th ed," *Knowl. Creat. Diffus. Util.*, vol. 15317, no. November, pp. 724–746, 2013.

REFERENCES

[137] V. R. Voller and C. R. Swaminathan, "General source-based method for solidification phase change," *Numer. Heat Transf. Part B Fundam.*, vol. 19, no. 2, pp. 175–189, 1991.

[138] V. R. Voller, A. D. Brent, and C. Prakash, "The modelling of heat, mass and solute transport in solidification systems," *Int. J. Heat Mass Transf.*, vol. 32, no. 9, pp. 1719–1731, 1989.

[139] R. F. Barron, *Cryogenic Systems*. Oxford University Press, 1985.

[140] A. M. Elsayed, "Heat transfer in helically coiled small diameter tubes for miniature cooling systems," University of Birmingham, 2011.

[141] "Handheld Meter, O.M.E.G.A. Engineering, Handheld Salinity Meter," 2017. [Online]. Available: Omega.co.uk.

[142] "Tequila Ice Maker Machine 12kg / 24h Blue | Klarstein," *Klarstein.co.uk.*, 2017. [Online]. Available: https://www.klarstein.co.uk/Home-appliances/Ice-cube-machines/Tequila-Ice-Maker-Machine-12kg-24h-Blue.html.

[143] "Salinity." [Online]. Available: http://www.epa.sa.gov.au/environmental_info/water_quality/threats/salinity. [Accessed: 14-Dec-2017].

[144] A. Ahmad, R. Al-Dadah, and S. Mahmoud, "Liquid nitrogen energy storage for air conditioning and power generation in domestic applications," *Energy Convers. Manag.*, vol. 128, no. 15, pp. 34–43, 2016.

[145] K. M. Khalil, A. Ahmad, S. Mahmoud, and R. K. Al-Dadah, "Liquid air/nitrogen energy storage and power generation system for micro-grid applications," *J. Clean. Prod.*, vol. 164, no. 15, pp. 606–617, 2017.

[146] A. Ahmad, R. Al-Dadah, and S. Mahmoud, "Liquid air utilization in air conditioning

and power generating in a commercial building," *J. Clean. Prod.*, vol. 149, no. 15, pp. 773–783, 2017.

[147] A. Ahmad, R. Al-Dadah, and S. Mahmoud, "Air conditioning and power generation for residential applications using liquid nitrogen," *Appl. Energy*, vol. 184, no. 15, pp. 630–640, 2016.

[148] D. Strahan, "Dearman," *Dearman*, 2017. [Online]. Available: http://dearman.co.uk/wp-content/uploads/2017/11/Dearman_Company_brochure_301017_web.pdf. [Accessed: 31-Oct-2018].

[149] ANSYS, "ANSYS Fluent User Guide 18.2," 2017.

[150] D. Deng, S. W. Xie, and R. S. Wang, "Two-phase flow pressure drop of liquid nitrogen boiling in the straight section downstream of U-bend," *J. Shanghai Jiaotong Univ.*, vol. 19, no. 4, pp. 495–501, 2014.

[151] J. N. Chung and K. Yuan, "Recent progress on experimental research of cryogenic transport line chilldown process," *Front. Heat Mass Transf.*, vol. 6, no. 1, pp. 1–17, 2015.

[152] J. Hartwig, H. Hu, J. Styborski, and J. N. Chung, "Comparison of cryogenic flow boiling in liquid nitrogen and liquid hydrogen chilldown experiments," *Int. J. Heat Mass Transf.*, vol. 88, pp. 662–673, 2015.

[153] M. Ahammad, T. Olewski, Y. Liu, S. Rahmani, S. Mannan, L. Vechot, and M. O. Kay, "Guidelines for simulating cryogenic film boiling using volume of fluid (VOF) method," *Symp. Ser. No 160*, vol. 25, pp. 1–10, 2015.

[154] S. Wang, J. Wen, Y. Li, H. Yang, Y. Li, and J. Tu, "Numerical prediction for subcooled boiling flow of liquid nitrogen in a vertical tube with MUSIG Model,"

Chinese J. Chem. Eng., vol. 21, no. 11, pp. 1195–1205, 2013.

[155] S. R. Darr, H. Hu, R. Shaeffer, J. Chung, J. W. Hartwig, and A. K. Majumdar, "Numerical Simulation of the Liquid Nitrogen Chilldown of a Vertical Tube," in *53rd AIAA Aerospace Sciences Meeting*, 2015, pp. 1–13.

[156] H. Hu, J. N. Chung, and S. H. Amber, "An experimental study on flow patterns and heat transfer characteristics during cryogenic chilldown in a vertical pipe," *Cryogenics (Guildf).*, vol. 52, no. 4–6, pp. 268–277, 2012.

[157] American Society of Heating Refrigerating and Air-Conditioning Engineers, "2009 Ashrae Handbook: Fundamentals, S-I Edition," *ASHRAE J.*, 2009.

APPENDIX A – Thermocouple calibration

The thermocouple calibration graphs for all the thermocouples used in the three experiments carried out in this research are displayed; this calibration procedure is discussed in section 3.5.2 - 'Thermocouples calibration', in chapter 3.
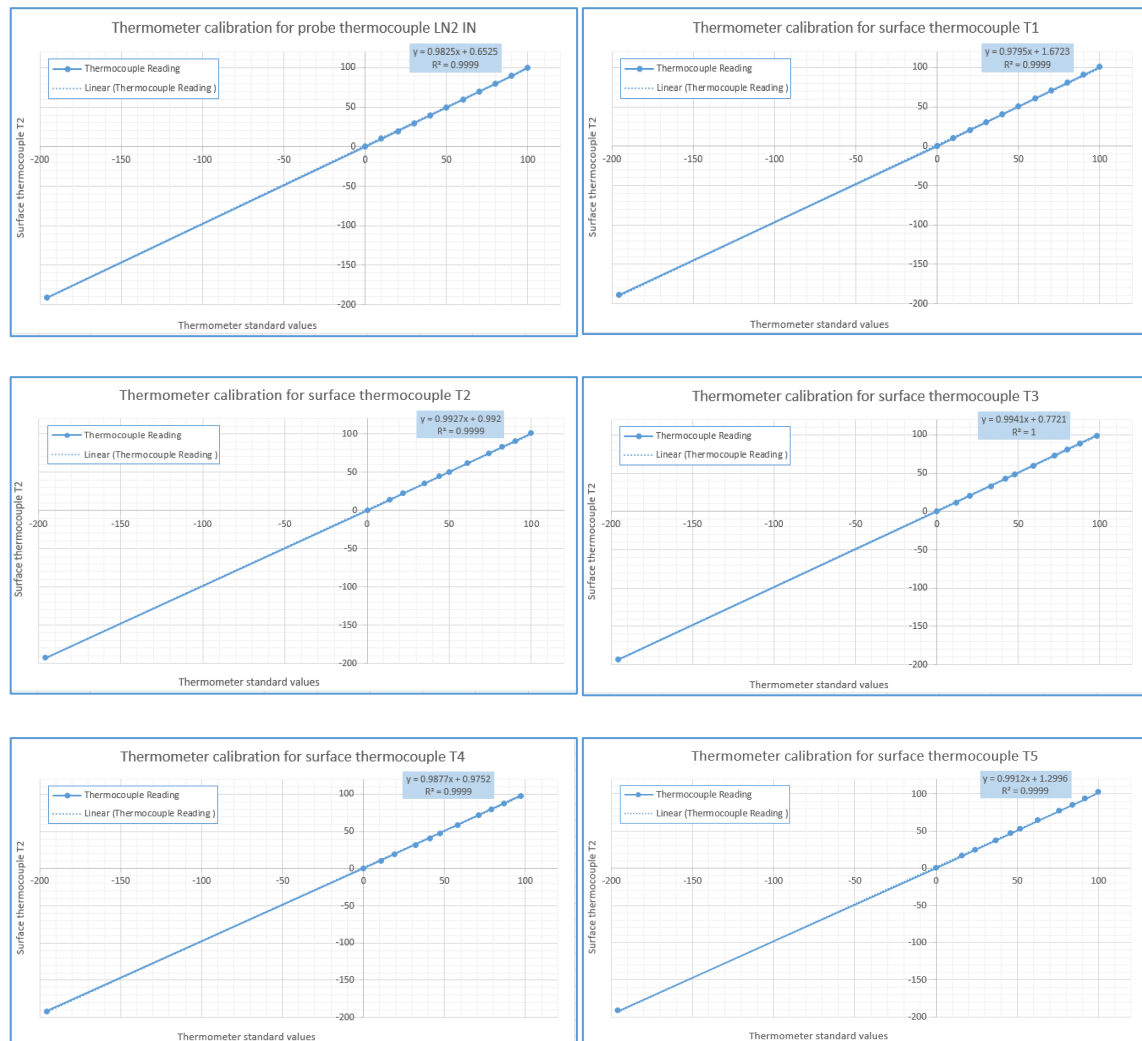

Figure A-0-1: Thermocouple calibration curves for LN_2 IN probe and surface thermocouples T1 to T5
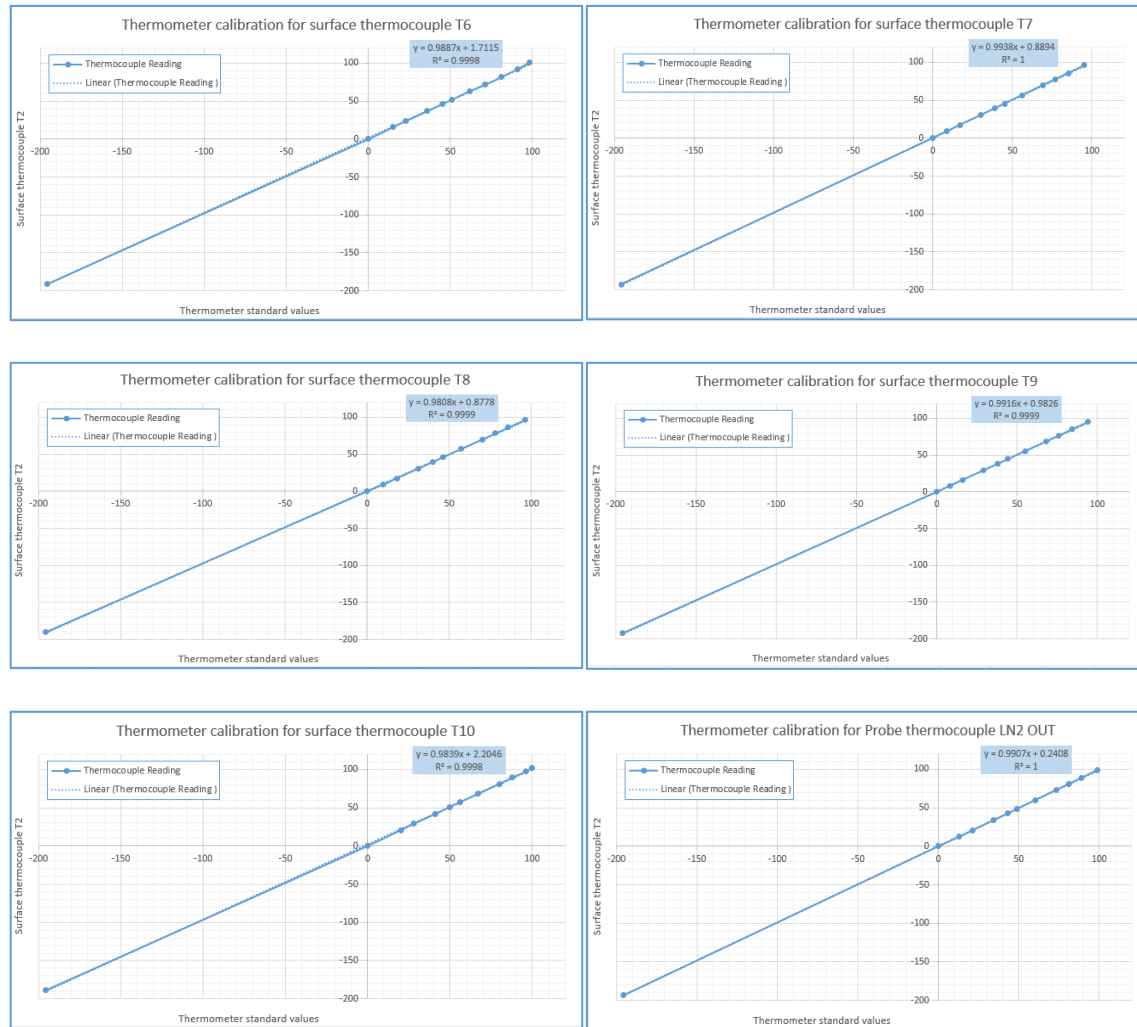
Figure A-0-2: Thermocouple calibration curves for surface thermocouples T6 to T10 and LN$_2$ OUT probe

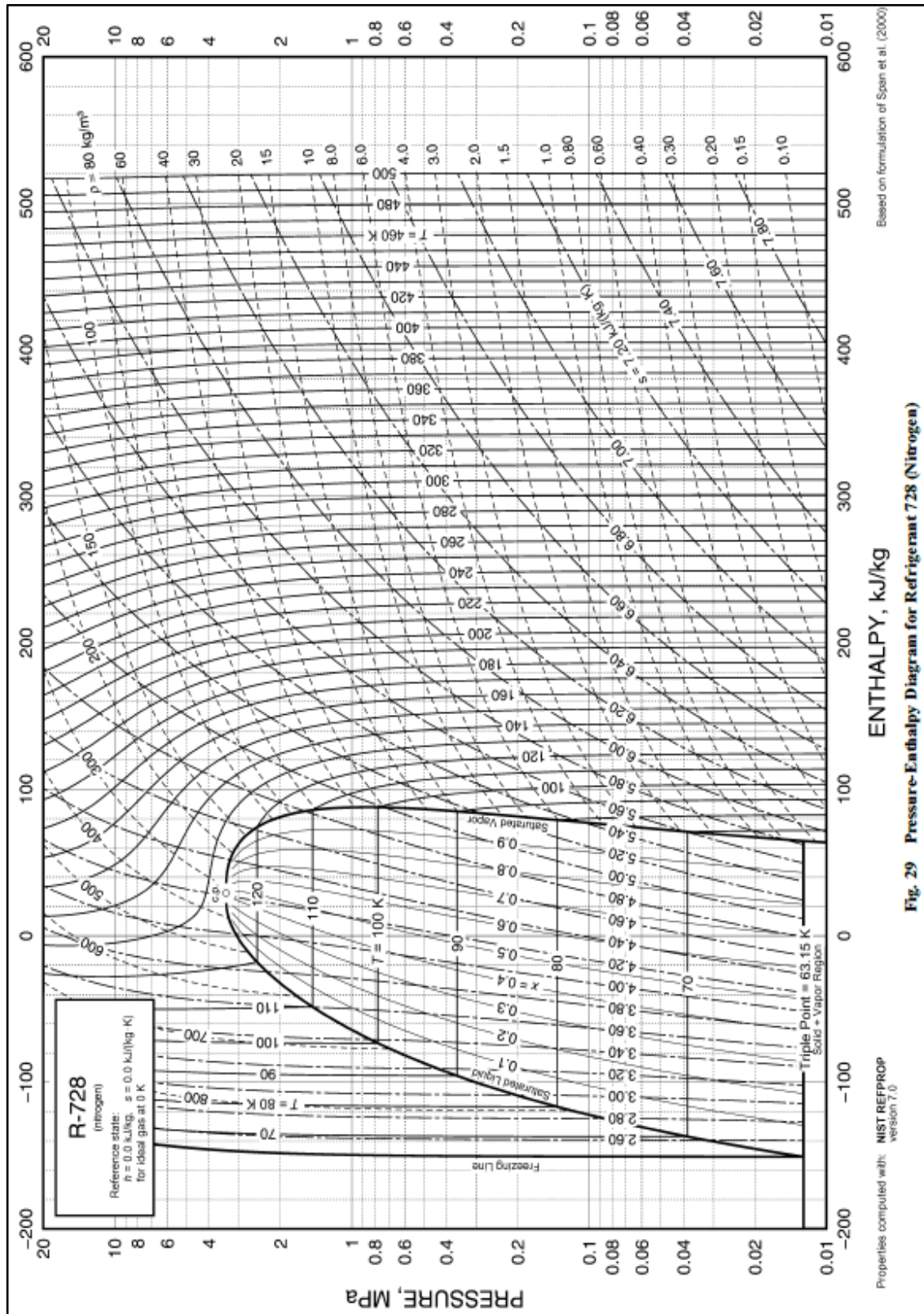# APPENDIX B – Thermophysical properties of Nitrogen

Figure B-0-1: Pressure-enthalpy diagram for Nitrogen [157]

Table B-1: Thermophysical properties of Nitrogen [157]

Thermophysical Properties of Refrigerants 30.61

Refrigerant 728 (Nitrogen) Properties of Saturated Liquid and Saturated Vapor

Temp., K	Absolute Pressure, MPa	Density, kg/m³ Liquid	Volume, m³/kg Vapor	Enthalpy, kJ/kg Liquid	Enthalpy, kJ/kg Vapor	Entropy, kJ/(kg·K) Liquid	Entropy, kJ/(kg·K) Vapor	Specific Heat c_p, kJ/(kg·K) Liquid	c_p Vapor	c_p/c_v Vapor	Velocity of Sound, m/s Liquid	Velocity of Sound, m/s Vapor	Viscosity, μPa·s Liquid	Viscosity, μPa·s Vapor	Thermal Cond., mW/(m·K) Liquid	Thermal Cond., mW/(m·K) Vapor	Surface Tension, mN/m	Temp., K
63.15[a]	0.01252	867.2	1.48310	−150.73	64.78	2.4257	5.8383	2.000	1.058	1.411	995	161.1	311.6	4.38	173.2	5.62	12.24	63.15
64	0.01460	863.7	1.28720	−149.03	65.59	2.4524	5.8059	2.002	1.061	1.413	987	162.1	297.5	4.44	171.5	5.71	12.03	64
66	0.02062	855.4	0.93698	−145.02	67.47	2.5140	5.7336	2.005	1.066	1.417	966	164.3	267.8	4.59	167.5	5.92	11.55	66
68	0.02848	847.0	0.69642	−141.00	69.31	2.5739	5.6667	2.010	1.073	1.421	946	166.4	242.3	4.73	163.5	6.14	11.07	68
70	0.03854	838.5	0.52743	−136.97	71.10	2.6321	5.6045	2.014	1.082	1.427	926	168.4	220.2	4.88	159.5	6.35	10.59	70
72	0.05121	829.9	0.40625	−132.93	72.83	2.6889	5.5466	2.020	1.091	1.433	906	170.3	201.1	5.03	155.5	6.58	10.12	72
74	0.06691	821.1	0.31772	−128.87	74.50	2.7442	5.4925	2.027	1.102	1.441	885	172.1	184.3	5.19	151.5	6.80	9.65	74
76	0.08610	812.2	0.25192	−124.79	76.11	2.7983	5.4417	2.035	1.114	1.450	865	173.8	169.6	5.34	147.5	7.03	9.19	76
77.35[b]	0.10132	806.1	0.21682	−122.02	77.16	2.8342	5.4090	2.041	1.124	1.457	851	174.8	160.7	5.44	144.8	7.19	8.87	77.35
78	0.10926	803.1	0.20226	−120.70	77.64	2.8511	5.3939	2.045	1.129	1.461	845	175.3	156.6	5.49	143.5	7.26	8.73	78
80	0.13687	793.9	0.16422	−116.58	79.10	2.9028	5.3487	2.056	1.145	1.473	824	176.7	145.1	5.65	139.5	7.51	8.27	80
82	0.16947	784.6	0.13470	−112.43	80.47	2.9534	5.3059	2.068	1.163	1.487	804	178.0	134.8	5.81	135.6	7.76	7.83	82
84	0.20757	775.0	0.11152	−108.26	81.75	3.0031	5.2651	2.083	1.184	1.503	783	179.2	125.6	5.97	131.6	8.01	7.38	84
86	0.25174	765.2	0.09310	−104.05	82.93	3.0520	5.2262	2.099	1.208	1.521	762	180.2	117.2	6.14	127.7	8.29	6.94	86
88	0.30251	755.2	0.07831	−99.81	84.01	3.1000	5.1888	2.119	1.235	1.542	741	181.0	109.7	6.31	123.7	8.57	6.51	88
90	0.36046	745.0	0.06632	−95.52	84.97	3.1473	5.1527	2.141	1.266	1.567	719	181.8	102.8	6.48	119.8	8.87	6.09	90
92	0.42616	734.5	0.05651	−91.18	85.81	3.1940	5.1178	2.166	1.300	1.594	697	182.4	96.5	6.66	115.9	9.19	5.67	92
94	0.50020	723.8	0.04842	−86.79	86.52	3.2401	5.0839	2.196	1.341	1.626	675	182.8	90.7	6.84	111.9	9.53	5.25	94
96	0.58316	712.7	0.04169	−82.34	87.10	3.2858	5.0507	2.231	1.387	1.664	652	183.1	85.4	7.03	108.0	9.89	4.84	96
98	0.67565	701.2	0.03605	−77.81	87.51	3.3311	5.0181	2.271	1.440	1.707	629	183.3	80.4	7.23	104.0	10.29	4.44	98
100	0.77827	689.4	0.03129	−73.21	87.77	3.3761	4.9858	2.318	1.503	1.758	605	183.3	75.8	7.43	100.1	10.73	4.05	100
105	1.08330	657.5	0.02224	−61.27	87.56	3.4882	4.9055	2.479	1.714	1.931	543	182.5	65.3	7.98	90.3	12.04	3.10	105
110	1.46580	621.5	0.01598	−48.49	85.84	3.6015	4.8226	2.743	2.062	2.221	476	180.8	56.0	8.63	80.4	13.83	2.21	110
115	1.93700	578.7	0.01146	−34.39	81.91	3.7198	4.7311	3.240	2.749	2.778	403	177.7	47.3	9.44	70.6	16.58	1.39	115
120	2.51060	523.4	0.00799	−17.87	74.17	3.8514	4.6185	4.508	4.631	4.216	317	172.6	38.4	10.62	61.0	21.72	0.66	120
125	3.20690	426.1	0.00487	6.40	55.03	4.0373	4.4263	16.720	23.740	16.930	195	160.3	26.9	13.33	56.4	41.54	0.08	125
126.19[c]	3.39580	313.3	0.00319	29.23	29.23	4.2149	4.2149	∞	∞	∞	0	0.0	—	—	∞	∞	0.00	126.19

*Temperatures on ITS-90 scale   [a]Triple point   [b]Normal boiling point   [c]Critical point

Refrigerant 728 (Nitrogen) Properties of Gas at 0.101 325 MPa (one standard atmosphere)

Temp., °C	Density, kg/m³	Enthalpy, kJ/kg	Entropy, kJ/(kg·K)	c_p, kJ/(kg·K)	c_p/c_v	Vel. of Sound, m/s	Visc., μPa·s	Thermal Cond., mW/(m·K)	Temp., °C	Density, kg/m³	Enthalpy, kJ/kg	Entropy, kJ/(kg·K)	c_p, kJ/(kg·K)	c_p/c_v	Vel. of Sound, m/s	Visc., μPa·s	Thermal Cond., mW/(m·K)
−195.8[b]	4.6121	77.16	5.4090	1.124	1.457	174.8	5.44	7.19	150	0.8065	439.66	7.2005	1.047	1.397	419.0	23.14	34.30
−180	3.7571	94.51	5.6133	1.081	1.432	194.0	6.51	8.72	160	0.7879	450.14	7.2249	1.048	1.396	423.8	23.53	34.93
−160	3.0593	115.90	5.8213	1.061	1.419	215.2	7.81	10.63	170	0.7701	460.62	7.2489	1.049	1.396	428.6	23.92	35.56
−140	2.5858	137.02	5.9932	1.052	1.412	234.2	9.06	12.49	180	0.7531	471.12	7.2723	1.050	1.395	433.3	24.31	36.18
−120	2.2414	158.02	6.1402	1.048	1.409	251.6	10.27	14.28	190	0.7368	481.62	7.2952	1.051	1.394	438.0	24.69	36.80
−100	1.9789	178.95	6.2687	1.045	1.406	267.9	11.42	16.03	200	0.7212	492.14	7.3177	1.053	1.394	442.6	25.07	37.42
−90	1.8696	189.40	6.3273	1.045	1.405	275.6	11.99	16.88	210	0.7063	502.67	7.3397	1.054	1.393	447.1	25.44	38.03
−80	1.7719	199.85	6.3829	1.044	1.405	283.1	12.54	17.71	220	0.6920	513.22	7.3613	1.055	1.392	451.6	25.81	38.63
−70	1.6839	210.28	6.4355	1.043	1.404	290.4	13.08	18.54	230	0.6782	523.78	7.3825	1.057	1.391	456.0	26.18	39.23
−60	1.6043	220.71	6.4857	1.043	1.404	297.5	13.61	19.35	240	0.6650	534.36	7.4033	1.059	1.390	460.4	26.54	39.83
−50	1.5320	231.14	6.5335	1.042	1.403	304.4	14.14	20.15	250	0.6523	544.95	7.4238	1.060	1.389	464.7	26.90	40.42
−40	1.4659	241.56	6.5791	1.042	1.403	311.2	14.65	20.94	260	0.6401	555.56	7.4439	1.062	1.389	468.9	27.26	41.01
−30	1.4053	251.98	6.6229	1.042	1.403	317.9	15.16	21.72	270	0.6283	566.19	7.4636	1.064	1.388	473.2	27.62	41.59
−20	1.3496	262.40	6.6649	1.042	1.402	324.4	15.66	22.49	280	0.6169	576.84	7.4831	1.066	1.387	477.3	27.97	42.17
−10	1.2981	272.82	6.7053	1.042	1.402	330.7	16.15	23.25	290	0.6060	587.50	7.5022	1.068	1.386	481.5	28.32	42.75
0	1.2504	283.23	6.7441	1.041	1.402	337.0	16.63	24.00	300	0.5954	598.19	7.5210	1.070	1.385	485.5	28.66	43.32
10	1.2061	293.65	6.7815	1.041	1.402	343.1	17.10	24.74	310	0.5852	608.90	7.5395	1.072	1.384	489.6	29.00	43.89
20	1.1648	304.06	6.8177	1.041	1.401	349.1	17.57	25.47	320	0.5753	619.62	7.5577	1.074	1.383	493.6	29.35	44.46
30	1.1263	314.47	6.8526	1.041	1.401	355.0	18.03	26.20	330	0.5658	630.37	7.5757	1.076	1.381	497.5	29.68	45.02
40	1.0903	324.89	6.8864	1.041	1.401	360.8	18.49	26.91	340	0.5565	641.14	7.5934	1.078	1.380	501.4	30.02	45.58
50	1.0565	335.30	6.9191	1.042	1.401	366.5	18.94	27.62	350	0.5476	651.93	7.6109	1.080	1.379	505.3	30.35	46.13
60	1.0247	345.72	6.9509	1.042	1.400	372.1	19.38	28.32	360	0.5390	662.74	7.6281	1.082	1.378	509.1	30.68	46.69
70	0.9948	356.14	6.9817	1.042	1.400	377.7	19.82	29.01	370	0.5306	673.58	7.6451	1.085	1.377	512.9	31.01	47.23
80	0.9666	366.56	7.0117	1.042	1.400	383.1	20.25	29.69	380	0.5225	684.44	7.6618	1.087	1.376	516.7	31.34	47.78
90	0.9399	376.99	7.0408	1.043	1.400	388.5	20.68	30.37	390	0.5146	695.32	7.6783	1.089	1.375	520.4	31.66	48.33
100	0.9147	387.42	7.0691	1.043	1.399	393.7	21.10	31.04	400	0.5069	706.22	7.6947	1.092	1.374	524.1	31.98	48.87
110	0.8908	397.85	7.0967	1.044	1.399	398.9	21.52	31.70	420	0.4923	728.10	7.7267	1.096	1.371	531.4	32.62	49.94
120	0.8681	408.30	7.1236	1.044	1.398	404.0	21.93	32.36	440	0.4785	750.08	7.7580	1.101	1.369	538.6	33.24	51.00
130	0.8466	418.74	7.1498	1.045	1.398	409.1	22.34	33.01	460	0.4655	772.15	7.7885	1.106	1.367	545.6	33.87	52.06
140	0.8261	429.20	7.1755	1.046	1.397	414.1	22.74	33.66	480	0.4531	794.32	7.8183	1.111	1.365	552.6	34.48	53.10
									500	0.4414	816.59	7.8475	1.116	1.363	559.4	35.08	54.14

[b]Saturated vapor at normal boiling point